



HAL
open science

Design and test of a readout ASIC for a SiPM - based camera : ALPS (ASIC de lecture pour un photodétecteur SiPM)

Fatima Mehrez

► **To cite this version:**

Fatima Mehrez. Design and test of a readout ASIC for a SiPM - based camera : ALPS (ASIC de lecture pour un photodétecteur SiPM). Micro and nanotechnologies/Microelectronics. Université Grenoble Alpes, 2015. English. NNT : 2015GREAT131 . tel-01399631

HAL Id: tel-01399631

<https://theses.hal.science/tel-01399631>

Submitted on 20 Nov 2016

HAL is a multi-disciplinary open access archive for the deposit and dissemination of scientific research documents, whether they are published or not. The documents may come from teaching and research institutions in France or abroad, or from public or private research centers.

L'archive ouverte pluridisciplinaire **HAL**, est destinée au dépôt et à la diffusion de documents scientifiques de niveau recherche, publiés ou non, émanant des établissements d'enseignement et de recherche français ou étrangers, des laboratoires publics ou privés.

THÈSE

Pour obtenir le grade de

DOCTEUR DE L'UNIVERSITÉ GRENOBLE ALPES

Spécialité : **Nano Electronique Nano Technologie (NENT)**

Arrêté ministériel : 7 août 2006

Présentée par

Fatima Mehrez

Thèse dirigée par **Sylvie Rosier-Lees**
et codirigée par **Richard Hermel**

préparée au sein du **Laboratoire d'Annecy-Le-Vieux de Physique des Particules**
et de l'**Ecole Doctorale Electronique, Electrotechnique, Automatique et Traitement du Signal (EEATS)**

Design and Test of a Readout ASIC for a SiPM-based Camera: ALPS (ASIC de Lecture Pour un Photodé- tecteur SiPM)

Thèse soutenue publiquement le **19 Novembre 2015**,
devant le jury composé de :

M. Giovanni Lamanna

Directeur de Recherche, LAPP - CNRS, Président

Mme. Nicoleta Dinu Jaeger

Ingénieur de Recherche, ARTEMIS, Rapporteur

M. Jean-François Glicenstein

Directeur de Recherche, CEA - Saclay, Rapporteur

M. Pascal Vincent

Professeur, LPNHE, Examinateur

Mme. Sylvie Rosier-Lees

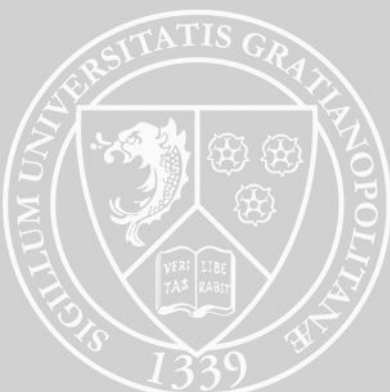
Directeur de Recherche, LAPP - CNRS, Directeur de thèse

M. Richard Hermel

Ingénieur de Recherche, LAPP - CNRS, Co-Directeur de thèse

M. Eric Delagnes

Ingénieur de Recherche, CEA - Saclay, Invité



to my parents

*"Nous sommes condamnés à espérer. Ce qui se passe aujourd'hui ne peut pas être la fin
de l'Histoire"*
Saadallah Wannous, (1941–1997) un critique littéraire et dramaturge syrien.

"We are condemned to hope. What is going on today can not be the end of the History"
Saadallah Wannous, (1941–1997) Syrian playwright.

Contents

Introduction	1
1 Introduction to high energy gamma-rays astronomy	3
1.1 Introduction	5
1.2 Cosmic ray	5
1.2.1 Energy spectrum	7
1.3 Gamma rays	8
1.3.1 Production mechanisms	9
1.3.2 Detection mechanisms	9
1.3.3 Cherenkov light	11
1.4 Cherenkov Telescope Array (CTA)	11
1.5 Large Size Telescope (LST)	13
1.5.1 First generation camera of the LST	14
1.5.2 Second generation LST camera	16
1.6 Conclusion	18
2 SiPM based camera	21
2.1 Introduction	23
2.2 Photo detection principle	23
2.3 Photomultiplier tube (PMT)	25
2.4 Semiconductor photodetectors	28
2.4.1 PN junction	29
2.4.2 PIN junction	29
2.4.3 Avalanche Photodiode (APD)	30
2.4.4 Geiger-Mode Avalanche Photodiode (G-APD)	31
2.5 Silicon Photo-Multiplier (SiPM)	33
2.5.1 SiPM industrial variety	36
2.5.2 Multi-pixel Silicon photo multiplier (SiPM matrix)	36
2.5.3 SiPM in astrophysics instruments	37
2.6 4×4 SiPM matrix characterization	38
2.6.1 Test bench	39
2.6.2 Temperature Measurement	43
2.6.3 Pedestals	44
2.6.4 Gain variation with over voltage	47
2.6.5 Optimum operating point	48
2.6.6 Gain dispersion among the 16 pixels	49

2.6.7	Noise in SiPM	59
2.7	SiPM Modeling	60
2.8	Conclusion	63
3	ALPS Design	65
3.1	Introduction	67
3.2	State of the art in readout-electronics	67
3.3	Readout chip, block diagram development	70
3.4	The preamplifier	73
3.4.1	Interface with the detector - Input stage	74
3.4.1.1	Transimpedance amplifier	74
3.4.1.2	Current amplifier (current conveyor)	75
3.4.2	Gain stage	79
3.4.3	Current mirror choice	80
3.4.3.1	Simple current mirror	81
3.4.3.2	Cascode current mirror	83
3.5	Proposed preamplifier and simulation results	85
3.5.1	Symmetric currents (transimpedance gain)	87
3.5.2	Symmetric loads (current gain)	89
3.5.3	Combination of transimpedance and current adjustment	91
3.5.4	Response speed	91
3.5.5	Dynamic range, Linearity	93
3.5.6	Signal to noise ratio	95
3.5.7	Power consumption	98
3.6	Slow control	98
3.6.1	8-bit DAC for per-pixel over-voltage control	99
3.6.2	Preamplifier gain correction	100
3.6.3	Noisy channel elimination function	101
3.7	Analog sum function	103
3.8	Trigger	104
3.9	Overall chip and layout	104
3.10	Single-ended to differential converter	107
3.11	Conclusion	107
4	ALPS experimental results and measurements	109
4.1	Introduction	111
4.2	Test board design	111
4.2.1	Labview slow control interface	113
4.3	Test bench of Electrical tests	115
4.4	Preamplifier tests	118
4.4.1	Linearity and dynamic range	119
4.4.2	Signal shape	121
4.5	Slow control tests	123
4.5.1	Residual pedestal	123
4.5.2	Gain control	124
4.5.3	Gain equalization	126
4.5.4	Noisy channel suppression	130

4.5.5	Bypassing gain control	131
4.6	Sum function	133
4.6.1	The shape of output signal	133
4.6.2	Sum as a function of the controlled gain	134
4.6.3	Sum of different signals	137
4.6.4	Sum as a function of the input level	137
4.7	Test bench for ALPS test with SiPM	139
4.8	Signal shape	141
4.9	Conclusion	143
Summary		145
A Terminology of photodetector devices		149
B Electrical tests (continuation)		155
B.1	Residual pedestal	155
B.2	Gain control	156
B.3	Gain equalization	158
B.4	Sum as a function of the input level	161
C ALPS tests with SiPM (Specification)		163
C.1	Light emitting diode LED	163
C.2	Optical filters	164
C.3	Preamplifier test	164
C.4	Sum Function	165
References		167

List of Figures

- 1.1 Nuclear abundance: cosmic rays compared to the solar system. Source: <http://w3.iihe.ac.be/~aguilar/PHYS-467/PA3.html>. 6
- 1.2 The journey of the cosmic rays from their source to their detection[13]. 6
- 1.3 Energy spectrum of cosmic rays. Source of the figure:<http://www.physics.utah.edu/~whanlon/spectrum.html>. 7
- 1.4 On top: Different components of the electromagnetic spectrum where gamma rays occupy the upper part. Bottom: Energy range of gamma rays. 8
- 1.5 Indirect γ - ray detection scenarios. Right: air shower particle detector (detects cascade particles that can reach the ground). Left: Cherenkov telescope (images Cherenkov light emitted by secondary gamma-ray induced particles that do not reach the ground).<http://astronomy.nmsu.edu/tharriso/ast536/ast536lecture3.html> 10
- 1.6 Integral sensitivity for CTA from MC simulations, together with the sensitivities in comparable conditions (50 h for IACTs, 1 year for Fermi-LAT and HAWC) for some gamma-ray observatories[3]. 11
- 1.7 Dynamic range of CTA telescopes. Thin lines with small symbols illustrate the limited impact of a reduced dynamic range of the readout electronics (clipped at 1000 photoelectrons). The dashed black line with diamonds, shows the sensitivity if there was no electron background[3]. 13
- 1.8 Three clusters of the first generation camera of the LST. Each cluster is composed of 7 PMT modules and the cluster electronics[26]. 15
- 1.9 Photograph of one cluster to be installed in the camera of the first LST. 7 PMT modules in the cluster share the same readout board. The core of the readout system is based on the Domino Ring Sampler chip (DRS4), which is based on switched capacitor arrays (SCAs)[29][30]. 15
- 1.10 Bloc diagram of one cluster of the first LST camera[29]. 16
- 1.11 Spectrum of Cherenkov light in blue, night sky background (NSB) spectrum in red. 16

- 2.1 Left: Transitions between energy band extremes. a) Semiconductor with a direct gap, vertical transitions with photon absorption/emission (radiative). b) Semiconductor with indirect gap, oblique transition (non radiative). c) Semiconductor with indirect gap, stimulated vertical-transition then transition to the minimum of the conductance band: direct absorption of the photon[33]. 24

2.2	Dispersion curves: a) photon in the space and inside a semiconductor. b) Electron in the space. c)Electrons in a semiconductor with a direct gap. d)Electrons in a semiconductor with an indirect gap[33].	24
2.3	Photomultiplier tube.	26
2.4	Typical drawbacks of PMT. Source: http://www.hamamatsu.com/us/en/support/	27
2.5	PN operation principle[40].	29
2.6	PIN photodiode: structure and linearity limits for different bias voltages. .	30
2.7	APD structure and gain.	31
2.8	Two different structures of the G-APD	32
2.9	Operation principle of a G-APD.	33
2.10	SiPM structure: Source: http://www.hamamatsu.com/us/en/community/optical_sensors/tutorials/physics_of_mppc/	34
2.11	Photon counting with a SiPM[50].	35
2.12	Methods for estimating number of detected Photon by a SiPM[50].	35
2.13	Discrete SiPM arrays (fabricated by from left to right: Hamamatsu, FBK, Sensl). Pixels are assembled on a printed circuit.	37
2.14	Monolithic SiPM arrays (left form Hamamatsu, right from Sensl). Pixels are integrated on the same substrate.	37
2.15	[56]	38
2.16	SiPM array under test.	39
2.17	SiPM characterization test bench (I).	41
2.18	SiPM characterization test bench(II).	41
2.19	Example of test configuration via labview interface.	42
2.20	Temperature characteristics of one SiPM[49].	43
2.21	Temperature variation measurement during tests.	44
2.22	Pedestals measured on the high gain of each SiPM of the array (for 15 macro pixels). Pixel number 16 was connected to the oscilloscope which explains its distribution.	45
2.23	Pedestals measured on the low gain of each SiPM of the array (for 15 macro pixels). Pixel number 16 was connected to the oscilloscope which explains its distribution	46
2.24	Charge spectrum of one pixel biased with 72V measured on the high gain: LED was controlled by a pulse of 2.35 V amplitude, 5 ns width with repetition of 300 Hz. We can see the pedestal represented by the 0pe peak, the peaks of the single photo electron, two photo electrons, three photo electrons, respectively. The red arrow points out the position of the single photo electron in respect to the pedestal.	47
2.25	Shift of the photo electron peak position as a function of bias voltage for one pixel.	48
2.26	Charge distribution measured on the high gain for each pixel. SiPM array was biased at 71.3V and received light from a LED controlled by a pulse of 2.35 V amplitude, 5 ns width with repetition of 300 Hz.	50
2.27	Charge distribution measured on the low gain for each pixel. SiPM array was biased at 71.3V and received light from a LED controlled by a pulse of 2.35 V amplitude, 5 ns width with repetition of 300 Hz.	51

2.28	Charge distribution, measured on the high gain, of 15 macro pixels of the SiPM array. The matrix was biased at 72V and received light from a LED controlled by a pulse of 2.35V amplitude, 5ns width with repetition of 300 Hz. Plots are organized in the same connection order of array elements and readout channels.	52
2.29	Charge distribution, measured on the low gain, of 15 macro pixels of the SiPM array. The matrix was biased at 72V and received light from a LED controlled by a pulse of 2.35V amplitude, 5ns width with repetition of 300 Hz. Plots are organized in the same connection order of array elements and readout channels.	53
2.30	Charge distribution of 16 macro pixel of the SiPM array. The matrix was biased at 72V and received light from a LED controlled by a pulse of 2V amplitude, 5ns width with repetition of 300 Hz. Plots are organized in the same mapping of the SiPM array. Less luminosity was applied here that can be noticed from short spectra containing one or two photoelectron peaks at most. Test iterated with 11000 events.	54
2.31	Spectrum of one macro pixel approximated to a fit function. Dots are measured data points, continued red line is the fit function.	55
2.32	Spectra of 15 elements of SiPM array illuminated by blue LED controlled with a 300Hz pulse of 2.3V amplitude and 5ns wide.	56
2.33	Single photo-electron position distribution among the 16 macro pixel of the SiPM array fed by $V_{Bias} = 72V$. Position parameter is extracted from fitted spectra in Fig.2.32.	57
2.34	SiPM output signal (blue line). At $t = \tau = 45ns$, $V(\tau) = V_0/e$. The green part is the sum of the $N_L = 16$ samples being read in charge reading mode (i.e, $Q_{16\ samples}$).	58
2.35	Dark current rate measurement with temperature for $1 \times 1\ mm^2$ SiPM. <i>Source: La photo-détection avec les SiPM dans le cadre du CTA, R. Kosakowski - presentation CL, LAPP 2011.</i>	60
2.36	Electrical model of one SiPM. This model of photodetector is used in the design and simulation of the front-end electronics in the next chapter. . . .	61
2.37	Output signal form of a SiPM ($3.5 \times 3.5\ mm^2$, 3600 cells, N-on-P structure)[63].	62
2.38	SiPM signal shape. Result from simulating the model shown in Fig.2.36 with a current pulse I_{event} of: Amplitude= $231.15\ \mu A$, rise time = $1ns$ = fall time, $499ps$ pulse width at FWHM.	62
2.39	Output signal of the SiPM sixteen measured on the oscilloscope (yellow signal). Output pulse integration during the reading window, gives the charge distribution spectrum that represents the photon counting and that is shown in orange.	63
3.1	Preliminary block diagram of ALPS (presented in the SiPM advanced workshop - July 2013).	71
3.2	Block diagram of ALPS	72
3.3	Input stage candidates	75
3.4	Example of transimpedance amplifier	75
3.5	Building the input common base current conveyor with bipolar transistor. .	76

3.6	PMOS input stage.	77
3.7	Small signal model of the super common gate input stage. Where V_{in} is an input voltage applied at the node IN of Fig.3.6b, V_{out} is the voltage at the drain of the transistor M_1 of the same figure. Z_{in} formula is found by analyzing the circuit to find the relation V_{in}/I_{in}	78
3.8	Simulation plot (by Cadence) of the input impedance of the input stage built with a super common gate current conveyor.	79
3.9	Gain stage, current mirror choice	81
3.10	Output characteristics of a simple current mirror and an ideal current mirror. <i>Source: Design analogique en technologies fines, lecture by Marc Pastre from EPFL, IN2P3 summer school 2013. http://www.in2p3.fr/actions/formation/microelectronique13/Pastre.pdf.</i>	82
3.11	Simulated response to 1 photo electron (pe) signal measured at simple current mirror high gain output. Response time represents the rising time of this output signal calculated between the base line and the maximum of the front edge.	83
3.12	Simulated response of the preamplifier built with a simple current mirror preamplifier.	84
3.13	Cascode current mirror - small signal model	85
3.14	Improved current mirror	85
3.15	Pre-amplifier, final scheme. MP_1 , R_1 , MP_2 , MN_2 forms the general polarization circuit that is common for all the sixteen preamplifiers.	86
3.16	Simulation of high gain response to one photo electron signal according to the symmetric currents scenario.	88
3.17	Symmetric currents (transimpedance gain) scenario, preamplifier simulated results of the high gain response (blue), low gain response (green) to input signals ranging from 1 to 7000 photo electrons.	88
3.18	High gain response to one photo electron signal according to Symmetric loads scenario.	90
3.19	Symmetric loads (current adjustment) scenario, preamplifier simulated results: (blue) on high gain, (green) on low gain. Input signals range from 1 to 7000 photo electrons.	90
3.20	Current pulse <i>simulated</i> at the output of the SiPM-model for one photo electron equivalent input pulse.	92
3.21	Voltage signal <i>simulated</i> at high gain output as a response to one photo electron response of the SiPM model.	92
3.22	Preamplifier simulated results on dynamic range for the transimpedance and current adjustment scenario.	93
3.23	Linearity error on the high gain can be seen about 8% at the beginning of the covered range. The error stays in the range of 3% for inputs between 20 <i>pe</i> and 125 <i>pe</i> which is the maximum covered by the HG before it gets saturated.	94
3.24	Linearity error on the low gain is about 3% for an input of 125 <i>pe</i> , it increases to 10% before drawing back to 3% for an input of 1000 <i>pe</i>	94

3.25	Noise simulated on the high gain output of the preamplifier. RMS noise is the square root of the integration of this plot over the same frequency range. RMS noise is found to be 2.3 mV	96
3.26	Controlling the applied voltage at the anode of one macro pixel (SiPM).	99
3.27	Adjusting a channel's gain by R-2R ladder	100
3.28	(a)Analog switch, (b) 1 to 2 Multiplexer	102
3.29	The generation of the command bit <i>cmd</i> for one multiplexer.	102
3.30	Summing the sixteen controlled signals after the preamplifier gain correction.	103
3.31	A block diagram of the trigger function integrated inside ALPS.	105
3.32	Preamplifier layout parts	106
3.33	ALPS layout	106
3.34	Single ended to differential conversion of the high gain sum output on the test board. The same scheme is used for the sum signal on the low gain. Conversion functionality will be integrated inside the chip in a forthcoming version.	107
4.1	The first test board. a)analog inputs leading electrical signals into the ASIC, b) SiPM connector, c)interface connector, d) chip socket, e)analog outputs, f) FPGA, g) USB connector	112
4.2	The second test board. a)analog inputs , b) SiPM connector, c) ALPS chip, d) digital slow control probes, e)analog output probes, f)analog outputs (lemos), g) FPGA, h) USB connector	112
4.3	Labview interface(I). a) 8-bit words for overvoltage adjustment by per macro-pixel DAC 8-bit, b) 8-bit words for high/low gain adjustment via R-2R blocks, c) high/low gain noisy channel suppression (<i>no_CB</i> bits), d) 10-bit word to the DAC 10-bit for discriminator threshold adjustment.	114
4.4	Labview interface(II). a) bypassing the gain control process with active <i>gain_fix</i> bit, b) probing a selected channel preamplifier outputs.	115
4.5	Test bench for chip electrical tests.	116
4.6	(a)Input circuit configuration, (b) Input signal form.	117
4.7	High gain output of the preamplifier for one photo electron equivalent signal. In red, when a voltage source of $385\text{ }\mu\text{V}$ amplitude, rising time of 2 ns is used as input. In blue, when SiPM model is used as input.	118
4.8	Preamplifier output on both high gain and low gain for different input signals. The high gain seems to be less than what was found by simulation while low gain is higher than predicted.	119
4.9	Non-linearity on the HG of the preamplifier shows a similar pattern to what was found in simulation. The error in linearity stays in the range of 3% for a dynamic range that goes between 11 pe and 193 pe excepting the second point corresponding to 34 pe where the non-linearity is about 4%.	120
4.10	Non linearity on the LG of the preamplifier is within the desired value 3% for a dynamic range between 171.7 pe and 337.7 pe	120
4.11	Preamplifier output signal seen on high gain (blue), and on low gain (orange) for an input of $V_{in} = 1.28\text{ mV} \equiv 3.3\text{ photo electrons}$	121

-
- 4.12 Elementary current pulses produced by the SiPM for BW=300 MHz and different values of R_{in} and L the inductive element added by the connector between the SiPM and the readout electronics[65]. 122
- 4.13 The effect of a parasitic capacitive load due to lemo connectors (estimated by 10 pF) at the input and on the preamplifier high gain output (in red). Output of the preamplifier with no capacitive loads (in blue). Input signal is the equivalent of 1 photo electron voltage being simulated as a pulse of $385\text{ }\mu\text{V}$ amplitude and 2 ns leading edge. 123
- 4.14 Residual pedestal measured on the SUM_LG_SE for different input levels. The dispersion found to be 4.7%, 4.6% and 6% for the used input levels of 36.9 mV , 75 mV and 146 mV (equivalent to 95.8, 194.8, and 379.22 photo electrons) respectively. 124
- 4.15 Dispersion among the sixteen channels for $V_{in} = 3.69\text{ mV}$ is about 3.6%, 3.7%, 3.4% and 3.8% respectively for R-2R-gain 0.5, 1, 1.5 and 2. 125
- 4.16 Linearity of gain control process on high gain path for two different inputs. Each point is the mean of the sixteen channels outputs for the given input and gain-control code. In blue, plot represents average outputs of the sixteen channels for $V_{in} = 3.69\text{ mV}$. In red, plot represents average outputs of the sixteen channels for $V_{in} = 13.2\text{ mV}$ 126
- 4.17 Linearity of gain control process on low gain path for two different inputs. Each point is the mean of the sixteen channels outputs for the given input and gain-control code. In blue, plot represents average outputs of the sixteen channels for $V_{in} = 75\text{ mV}$. In red, plot represents average outputs of the sixteen channels for $V_{in} = 146\text{ mV}$ 126
- 4.18 The procedure of gain correction after the HG pre-amplifier for an input signal of 3.69 mV : a) measuring the pedestal of each channel and fixing the standard output (here it was put to 200 mV), b) digitally control the gain of each channel via programming the switches of each R-2R bloc, c) measuring the output which at this step includes the pedestal and here we can notice the 2.1% dispersion of the output value, d) the sixteen outputs after residual pedestal subtraction from measured data. We can notice a dispersion of about 0.24% among the sixteen channels. The gain is now homogeneous for almost all the channels and the small dispersion (less than 1%) is better than expected. 128
- 4.19 Gain equalization on high gain path for two other different input signals $V_{in} = 8\text{ mV}$ and $V_{in} = 21\text{ mV}$ (equivalent to 20.78 photo electrons, 54.5 photo electrons). That reduces gain dispersion in the sixteen readout channels to less than 1% (about 0%, and 0.2% respectively). 128
- 4.20 Gain equalization on low gain path for two different input signals $V_{in} = 146\text{ mV}$, and $V_{in} = 292\text{ mV}$ (equivalent to 379.2 photo electrons, 758.4 photo electrons). That reduces gain dispersion in the sixteen readout channels to less than 1% (about 0.48%, and 0.25% respectively). 129

-
- 4.21 Each high gain output is the mean of the 16-channel outputs measured for only one channel fed at a time. Left: high-gain output vs V_{in} after pedestal subtraction, for different R-2R gains (i.e, for different gain control codes which are unique for the sixteen channel each time). Right: high-gain output vs V_{in} after gain equalization including pedestal subtraction. 129
- 4.22 Left: low gain sum output of channel 15 when receiving an input of $V_{in} = 100\text{ mV} \cong 259.7\text{ photo electrons}$ and passing through R-2R block that was programmed according to the code 128. Right, the output at the same point if channel 15 was suppressed by activating the bit labeled *no_CB*. The signal that appears on the output is a residual pedestal. This result was obtained with the first test board. 130
- 4.23 Low gain sum output when channel 15 is suppressed while receiving an input of 100 mV and gain control code of 255. The same output level is noticed as when the gain control code was set to 128 in Fig.4.22. This result was obtained with the first test board. 131
- 4.24 Left: high gain sum output of channel 15 when receiving an input of $V_{in} = 100\text{ mV}$ and passing through R-2R block that was programmed according to the code 255. Right, the output at the same point if channel 15 was suppressed by activating the bit labeled *no_CB*. This result was obtained with the first test board. 131
- 4.25 Using the first test board, for an input signal of 100 mV : Left, high gain output when signal is treated by the gain control whose code is fixed to full scale (255). Right, the same output when the signal bypasses the control step (active *gain_fix*). 132
- 4.26 Using the first test board, for an input signal of 100 mV : Left, low gain output when signal is treated by the gain control code of 255. Right, the same output when the signal bypasses the control step (active *gain_fix*). 132
- 4.27 ASIC outputs (from left to right)of *ch5*, *ch16* and *ch5+ch16* for $V_{in} = 21\text{ mV}$ when: a) R-2R gain = 0, which is also the residual pedestal discussed in section4.5.1; b) R-2R gain = 0.5, c) R-2R gain = 1, d) R-2R gain =1.5. 134
- 4.28 Sum measured on the single ended high gain output of the chip when two identical inputs are applied on two channels for different controlled gains. 135
- 4.29 Sum measured on the single ended low gain output of the chip when two identical inputs are applied on two channels for different controlled gains. 136
- 4.30 Left: sum of two different inputs where the plots include the residual pedestal. Right: corrected plots after pedestal subtraction. For both sides, in blue is the output when only *ch5* receives an input signal of 146 mV . In red is the output when only *ch16* receives an input signal of 74 mV . The x plot labeled *ch5+ch16-c* is the expected sum of these two outputs in blue and in red. While the green plot labeled *ch5+ch16-m* is the measured output when simultaneously $V_{in,ch5} = 146\text{ mV}$ and $V_{in,ch16} = 74\text{ mV}$ 137

4.31	Sum on high gain path of two signals as a function of the level of these input signals. Here the R2R gain was set to 1 and in Fig.B.9, measurements are shown for different R-2R controlled gains. Results are after pedestal correction. In blue is the output when only <i>ch5</i> receives an input signal. In red, is the output when only <i>ch16</i> receives an input signal. In green, the plot labeled <i>ch5+ch16-m</i> is the measured sum output when both <i>ch5</i> and <i>ch16</i> are fed by identical inputs. The x plot labeled <i>ch5+ch16-c</i> is the arithmetic sum of the measured outputs when input signal is applied only on <i>ch5</i> and the measured output when the same input signal is applied only on <i>ch16</i> . For input signals that cause saturation on the high gain path, the output should be measured on the low gain path.	138
4.32	Sum on low gain path of two signals as a function of the level of these input signals. Here the R2R gain was set to 1 and in Fig.B.10, measurements are shown for different R-2R controlled gains. Results are pedestal free. <i>ch5+ch16-m</i> is the plot of the measured sum output when both <i>ch5</i> and <i>ch16</i> are fed by identical input. <i>ch5+ch16-c</i> is the plot of the manual sum of the measured output when input signal is applied only on <i>ch5</i> and the measured output when the same input signal is applied only on <i>ch16</i>	138
4.33	Test bench for tests with SiPM	139
4.34	High gain preamplifier output of channel 6 reading a signal produced by the corresponding macro pixel (SiPM) when the SiPM matrix is illuminated with the full LED intensity.	142
4.35	Sum signal shape measured at the single ended output of the high gain, slew rate effect can be noticed.	142
A.1	PDE as a function of wavelength for different device sizes. Left, from Sensl[116]. Right, from Hamamatsu[49].	151
A.2	Pulses of the incident light on top. On the bottom: In black, pulses due to light at the output of the photodetector (of type MPPC: Multi Pixel Photon Counter) and red pulses are dark induced pulses[50].	151
A.3	Oscilloscope shot showing dark counts and we can see the crosstalk effect[116].	152
B.1	Residual pedestal measured on the <i>SUM_HG_SE</i> for different input levels. The dispersion found to be 4.8%, 2% and 2.7% for the used input levels of 3.69 mV, 13.2 mV and 21 mV respectively.	155
B.2	Dispersion among the sixteen channels for $V_{in} = 13.2mV$ is about 3%, 3%, 3.9% and 3.7% respectively for R-2R-gain 0.5, 1, 1.5 and 2.	156
B.3	Dispersion among the sixteen channels for $V_{in} = 75mV$ is about 5.5%, 4.9%, 4.7% and 5.2% respectively for R-2R-gain 0.5, 1, 1.5, 2.	157
B.4	Dispersion among the sixteen channels for $V_{in} = 146mV$ is about 5%, 4.3%, 4.2% and 4.2% respectively for R-2R-gain 0.5, 1, 1.5, 2.	157
B.5	High gain equalization for an input of 8 mV, the standard output was defined to 400 mV. The result shows zero dispersion among the sixteen channels.	158
B.6	High gain equalization for an input of 21 mV, the standard output was defined to 1.138 V. The result shows a dispersion of about 0.2% among the sixteen channels.	159

B.7	Low gain equalization for an input of 146 mV , the standard output was defined to 100 mV . The result shows 0.48% of dispersion among the sixteen channels.	159
B.8	Low gain equalization for an input of 292 mV , the standard output was defined to 200 mV . The result shows a dispersion of about 0.25% among the sixteen channels.	160
B.9	Sum on high gain path of two signals as a function of the level of these input signals. Measurements are shown for different R-2R controlled gains. Results are after pedestal correction. In blue is the output when only <i>ch5</i> receives an input signal. In red, is the output when only <i>ch16</i> receives an input signal. In green, the plot labeled <i>ch5+ch16-m</i> is the measured sum output when both <i>ch5</i> and <i>ch16</i> are fed by identical inputs. The x plot labeled <i>ch5+ch16-c</i> is the arithmetic sum of the measured output when input signal is applied only on <i>ch5</i> and the measured output when the same input signal is applied only on <i>ch16</i> . For input signals that cause saturation on the high gain path, the output should be measured on the low gain path.	161
B.10	Sum on low gain path of two signals as a function of the level of these input signals for different R-2R controlled gain. Results are pedestal free. <i>ch5+ch16-m</i> is the plot of the measured sum output when both <i>ch5</i> and <i>ch16</i> are fed by identical input. <i>ch5+ch16-c</i> is the plot of the manual sum of the measured output when input signal is applied only on <i>ch5</i> and the measured output when the same input signal is applied only on <i>ch16</i>	162
C.1	Relative intensity as a function to the emitted wave length (http://html.alldatasheet.com/html-pdf/157144/HP/HLMP-DB45-N00DD/108/3/HLMP-DB45-N00DD.html).	163
C.2	Preamplifier output signals for three light intensities. Each point is the mean of the sixteen preamplifiers outputs for the considered intensity. Left, measurements on the low gain. Right, measurements on the high gain. . .	164
C.3	Single ended sum output signals for a range of relative light intensities starting with 0.675 without an optical filter down to 0.0675 with the most opaque filter. Left, measurements on the low gain output. Right, measurements on the high gain output.	165
C.4	Single ended sum output signals ratio over a range of light intensities from 0.675 down to 0.068.	166

List of Tables

1.1	Main characteristics of the Hamamatsu R11920-100-20 developed for CTA project[26].	14
1.2	Effective quantum efficiency of the PMT and that of the SiPM for both the Cherenkov light and the night sky background (NSB) respectively. SiPM effectively collects 1.6 times more Cherenkov photons and 4.4 times more NSB photons than that collected by the PMT[31].	17
2.1	[56]	38
2.2	Left: One pixel of the FACT camera. We can see a hexagonal entrance window of the light guide that concentrates light onto the square sensor. Right:Parameters of the SiPMs chosen for the FACT project: Hamamatsu S10362-33-050C[56].	38
2.3	Specifications of the tested array.	39
2.4	Source: Product information of <i>Monolithic MPPC array with FPC (S11829-3344MF, S11830-3344MF)</i>	39
2.5	Used model parameters for one micro cell in a SiPM.	61
2.6	Comparison of the critical characteristics of photo-multiplier tubes and the tested array of SiPM.	64
3.1	Some examples of the readout electronic chips that read different types of photo detectors.	68
3.2	Device parameters of the input stage as drawn in Fig.3.6b.	77
3.3	List of simple current mirror parameters for a gain ratio $HG/LG = 100$. R_{HG} and R_{LG} are respectively the high gain load and the low gain load.	82
3.4	List of devices' dimensions for the transimpedance gain scenario.	87
3.5	List of devices' dimensions for the current gain scenario.	89
3.6	List of preamplifier component parameters and DC operating point.	91
3.7	Noise summary showing the contribution of each device in the preamplifier. id is the drain-source resistance thermal noise, rn is the noise due to the physical resistor (i.e, thermal noise), rs is the source parasitic thermal noise, fn is the flicker noise.	97
3.8	Power consumption calculation	98
3.9	Gain control and noisy channel suppression function, in short.	103
4.1	Power supply list	117

4.2	Gain control configuration with an active <i>no_CB</i> bit that leads to delete the low gain path of the corresponding channel (channel 15 here) even if the gain control was set to 128 (i.e, $G_{R2R} = 1$).	130
4.3	Gain control configuration with an active <i>no_CB</i> bit that leads to delete the low gain path of the corresponding channel (channel 15 here) even if the gain control was set to 255 (i.e, $G_{R2R} = 2$).	131
4.4	Gain control configuration with an active <i>gain_fix</i> bit.	132
4.5	Gain control configuration for the four cases considered in the signal shape test of the sum output.	133
4.6	LED control pulse	140
4.7	Light intensities at the output of each used optical filter (losses in optical connection and fiber optic were ignored).	141

Introduction

Cosmic rays are particles that are believed to carry lot of responses to the questions about the history and may be the future of our universe. Even though composition and propagation mechanisms of these rays are now defined, most of their sources are still veiled. Several instruments were sent to space, built on the ground trying to track back these rays to their origins, studying their properties and to find out the hidden blocks of the energy and matter edifices.

Cherenkov Telescope Array (CTA) is a project of building ground-based high-energy gamma ray observatory[1]. This project aims to cover a wide energy range: *some* $10\text{ GeV} - 300\text{ TeV}$ with improved performance in terms of sensitivity, resolution, and field of view[2]. For this aim, two sites of different-size telescopes will be constructed in both northern (La Palma in Spain) and southern (Paranal in Chile) hemispheres¹. Three types of telescopes are being studied and developed for a data taking launch by the year 2020: Large Size Telescope (LST), Medium Size Telescope (MST), and Small Size Telescope (SST)[3].

The motivation of this thesis goes in the interest of a new camera for the LST using more efficient photodetector device. The ameliorated sensitivity sought demands devices with higher photon detection efficiency. A proposal is introduced to build a second generation camera based on the last photodetection technology with its adapted fast front-end electronics.

Four Large size Telescopes (LST)s are planned to be constructed in both CTA sites. LSTs are the lower energy instrumentation. Each LST is planned to detect the lower range of energy between 20 GeV and $\sim a\text{ hundred of GeV}$. This makes it more sensitive than any other existing ground-based gamma ray instrument.

Some principles of gamma rays astrophysics and some details about the CTA project are introduced in the first chapter.

The first generation of LST camera will use photo multiplier tubes (PMT)s that have been efficient photodetectors used in most current instruments. However, an emerging technology represented by the Silicon PhotoMultipliers (SiPM) seems to be able to solve some of the PMTs drawbacks and to reach even lower energy ($\sim 10\text{ GeV}$). SiPMs are serious candidates to replace PMTs in the second generation camera dedicated to the LSTs. SiPM is a small size photodetector robust to magnetic field and high light intensities. It operates at lower voltages comparing to the PMT and provides almost close gain with higher quantum efficiency. The First G-APD Cherenkov Telescope (FACT)[4][5] is a successful and encouraging experience of exploiting these detectors in such instruments.

A review of the photodetection principles and detector's evolution are introduced in the second chapter. PMTs advantages and disadvantages are underlined before investi-

¹Decision was made in 2015 <https://portal.cta-observatory.org/Pages/News.aspx>.

gating the characteristics of the emerging SiPM detectors. SiPM technology is showing the possibility of building a large surface photodetector in the form of matrix. An array of sixteen macro pixels of the type SiPM is being tested and characterized. Results are discussed and specifications are summarized in order to design appropriate readout electronics. This part of the project started on February 2013 and its results were presented on July in the first SiPM workshop in Munich[6].

The motivation of this thesis is to prove the feasibility of such SiPM-based camera. A demonstrator readout electronic chip was proposed. This demonstrator can interface a 4×4 SiPM array fabricated by Hamamatsu to the current acquisition system represented by NECTAR[7] or DRAGON[8]. Design process, circuit solutions, choices, and control facilities are explained in the third chapter. Simulation results and expected performance are also presented.

Design and simulation took place between August 2013 and March 2014. Simulation results were presented in the second SiPM workshop in Geneva on March 2014[9] and in the LST general meeting in Padua on July 2014. The readout chip is labeled ALPS that stands for *ASIC de Lecture Pour SiPM* was designed using AMS $0.35 \mu m$ BiCMOS - SiGe technology. It was fabricated as a part of a multi project circuit (CMP) run between March and August 2014.

Five packaged samples with 25 non-packaged dies of ALPS were received at the end of July 2014. Test benches and Labview slow control interface are described in the fourth chapter. ALPS performance was measured using electrically generated signals and with SiPM generated signals. Test environment, problems and results are discussed in this last chapter. Some results of the electrical tests were presented in the LST meeting in Annecy on February 2015[10] and in the 34th ICRC conference on 2015[11].

Finally, achievements and perspectives are proposed in the conclusion.

Chapter 1

Introduction to high energy gamma-rays astronomy

Contents

1.1	Introduction	5
1.2	Cosmic ray	5
1.2.1	Energy spectrum	7
1.3	Gamma rays	8
1.3.1	Production mechanisms	9
1.3.2	Detection mechanisms	9
1.3.3	Cherenkov light	11
1.4	Cherenkov Telescope Array (CTA)	11
1.5	Large Size Telescope (LST)	13
1.5.1	First generation camera of the LST	14
1.5.2	Second generation LST camera	16
1.6	Conclusion	18

1.1 Introduction

Gamma rays emission was first detected in 1967 by the OSO III satellite. Precious information about energetic phenomena in the universe is carried by the very high-energy (VHE) electromagnetic radiations. Some of these radiations reach the earth, they are detected by nowadays telescopes. These instruments have demonstrated that VHE phenomena exist and come from everywhere in the cosmos. They have raised lots of questions whose answers demand more better data for deeper understanding of these phenomena. This is the reason why a more developed observatory *Cerenkov Telescope Array (CTA)* is needed and proposed for the future. Telescopes of different sizes (large, medium and small) are being studied to provide a wide dynamic range of gamma-rays energies. *Large size telescopes (LST)* of the CTA are planned to detect the lower energy gamma rays ever detected by a ground based instrument.

Silicon Photomultiplier (SiPM) is a new technology in photosensors that is being investigated to equip a new generation camera for CTA telescopes. The main motivation for this work is to prove the merit of exploiting SiPM detectors in the second generation camera or the LSTs. SiPMs should enable increasing the sensitivity of these telescopes to as low as possible energy ($\sim 10 \text{ GeV}$).

Here in this chapter is a very short introduction to gamma rays astronomy. More detailed information about the CTA project and the LST in particular is also presented.

1.2 Cosmic ray

Cosmic rays are particles that bombard our earth from beyond its atmosphere. The origin of these rays is still a dynamic field of research. Decades of research have shown that cosmic rays are charged particles composed of majority of atomic nuclei (drawn in Fig.1.1: 87% protons, 12% of heavy nuclei (Helium and other nuclei) and about 1% of very energetic leptons (i.e. electrons).

These particles are accelerated to extremely high energies up to 10^{20} eV . They propagate and interact with the different components of the universe and are detected either by space-satellites (AGILE and Fermi) or ground-based telescopes (HESS, VERITAS, MAGIC, etc...). Fig.1.2 is an illustration of the cosmic ray journey, including generation, propagation and detection. Astronomical instruments are trying to understand the production and acceleration mechanisms of these particles and to trace back important information about their sources.

The detection and study of the cosmic ray include *classical astronomy* and *astroparticle physics*. The classical astronomy made use of the visible light till 1945 when new wavebands have joined to optical astronomy (radio, millimeter, infrared, ultraviolet, X and gamma rays astronomies). This has led to the growth of many new areas of astrophysics[12]. Astroparticle physics studies information carried by three types of particles. These *messenger particles* are either charged particles:(protons p and heavy nuclei), photons γ or even neutrinos ν [13] and may be the gravitational waves in the future.

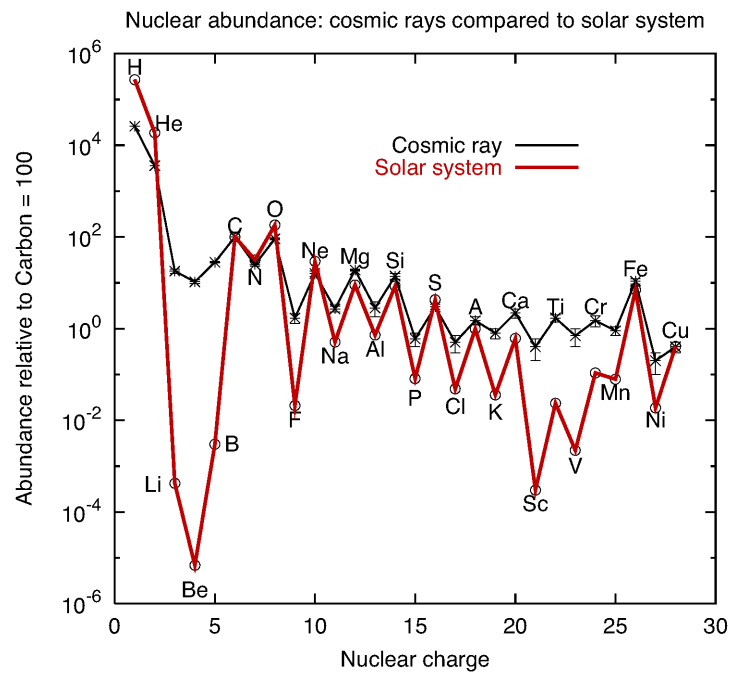


Figure 1.1: Nuclear abundance: cosmic rays compared to the solar system. Source: <http://w3.ihe.ac.be/~aguilar/PHYS-467/PA3.html>.

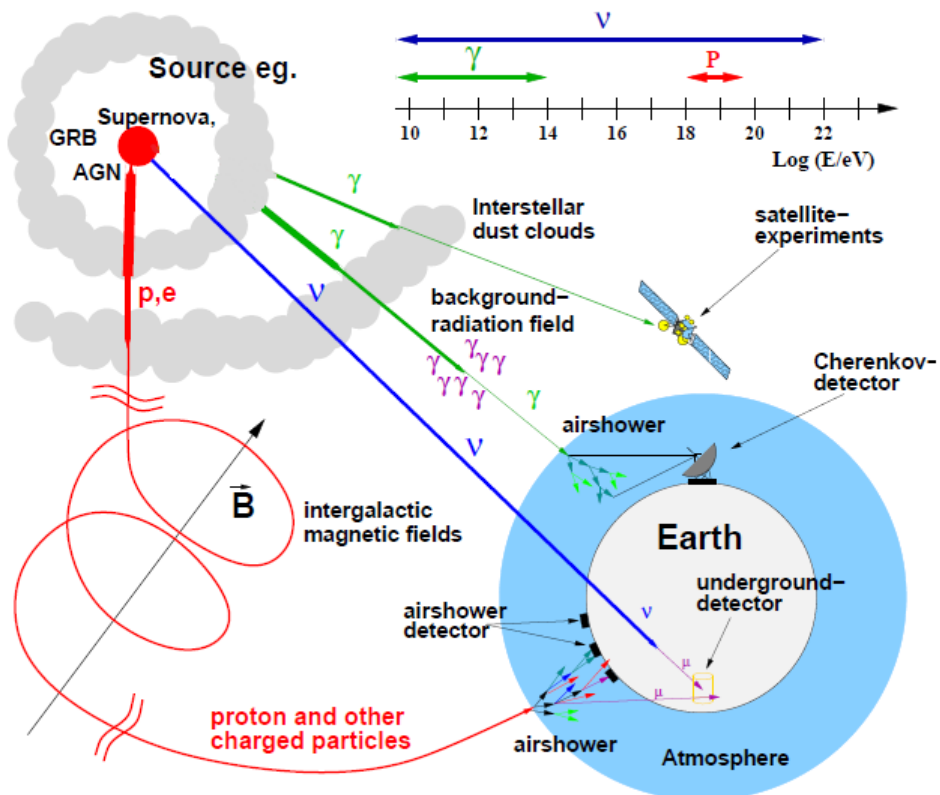


Figure 1.2: The journey of the cosmic rays from their source to their detection[13].

1.2.1 Energy spectrum

The plot of particle flux as a function of the energy is called *the energy spectrum*. It was found to follow a power-law given in Eq.1.1 and Fig.1.3, where Γ is the power law index and it is defined by the slope of the log-log plot of the power law.

$$\Phi(E) = \frac{dN}{dE} \propto E^{-\Gamma} \quad (1.1)$$

This spectrum covers a wide range in both energy (12 orders of magnitude) and flux (32 orders of magnitude). It can be divided into three regions of energy: intermediate, high and very high energies. These regions are defined by different indexes.

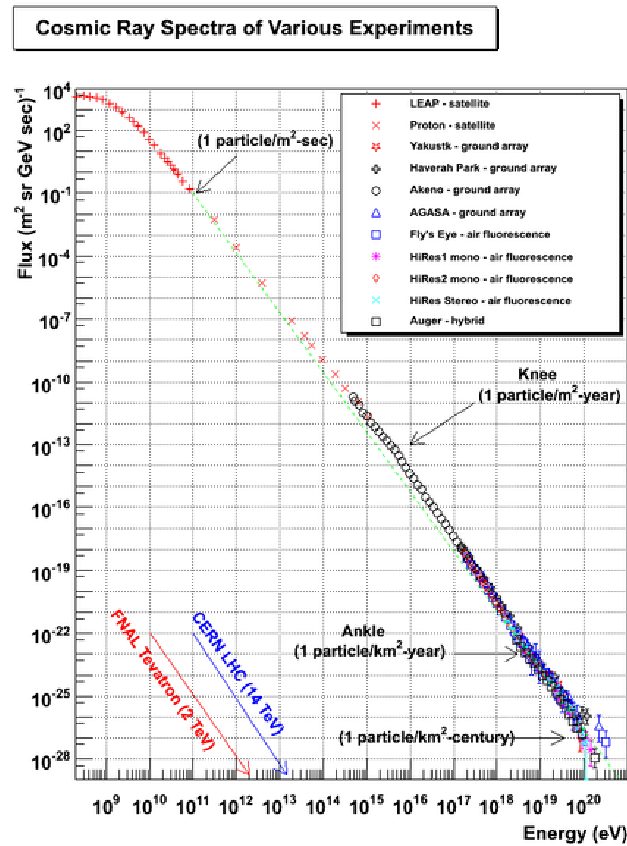


Figure 1.3: Energy spectrum of cosmic rays. Source of the figure:<http://www.physics.utah.edu/~whanlon/spectrum.html>.

Cosmic rays spectrum shows a very good regularity except in two points where the power-law index changes. The first is known as *the knee* and is situated at $10^{15.4} eV$. The second occurs at $10^{18.5} eV$ and is called *the ankle*.

These changes in the power-law have been explained by the transition between the galactic and extra-galactic origins of the cosmic rays.

Information about cosmic rays sources, acceleration mechanisms and propagation could be extracted by studying this spectrum and the composition of the cosmic rays at each energy. The fact that cosmic rays are charged particles makes it difficult to trace

them back to their sources. Charged particles are deflected in the magnetic fields (galactic and extragalactic) and their energy is uncertainly determined¹[14]. They isotropically reach the ground. Thus, neutral particles stemming from the same sources (photons in particular²) are the most useful messengers for studying sources of cosmic rays.

1.3 Gamma rays

Gamma rays are thought to be of the same sources as the cosmic rays but not only. They could also be produced by the decay of heavy particles, from collisions between relativistic particles and the ambient gas or also from the interaction of relativistic particles with their propagation medium.

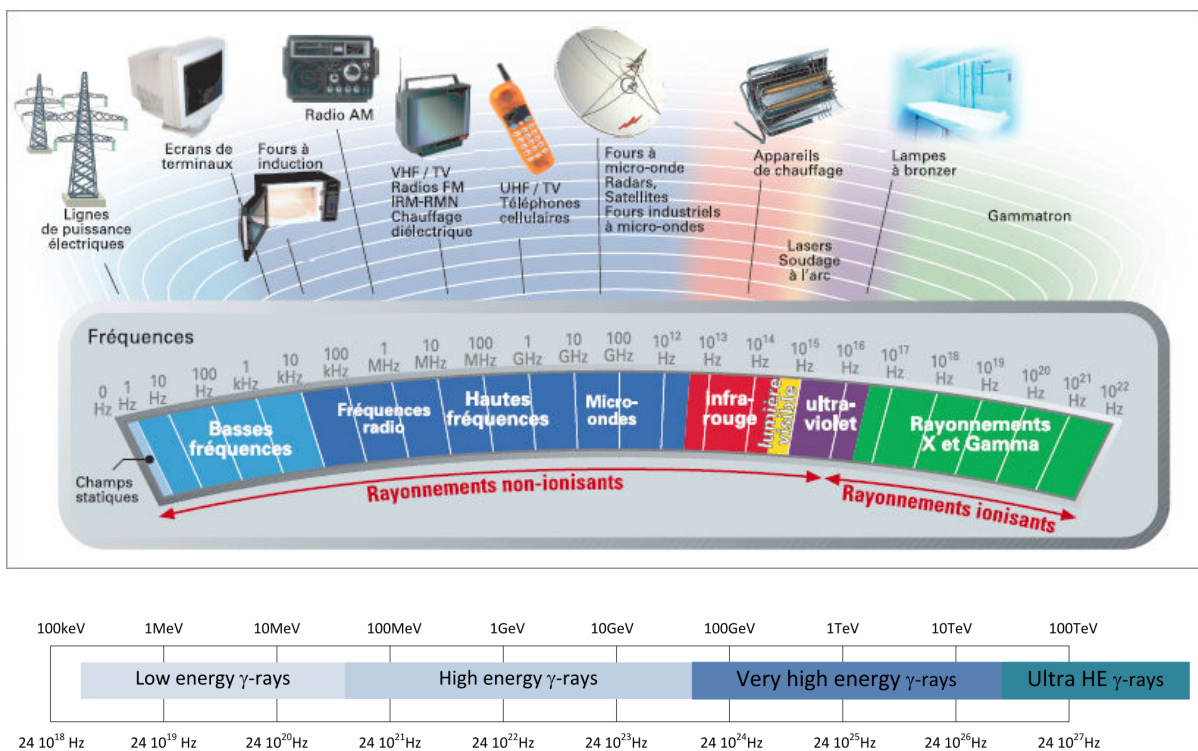


Figure 1.4: On top: Different components of the electromagnetic spectrum where gamma rays occupy the upper part. Bottom: Energy range of gamma rays.

Gamma rays are the most energetic part (highest frequency or smallest wavelength) of the electromagnetic spectrum as illustrated in Fig.1.4. They are composed of photons having an energy between $\sim 100keV$ and some hundreds of TeV . Photons having energies above some tens of MeV are referred to as high energy gamma rays. This range of energy reflects the non-thermal radiation.

Being of galactic and extragalactic sources, high energy and very high energy gamma rays astronomy is used in exploring cosmic rays sources far away in the universe, to

¹Except for the very highest energies but their origins form a large correlated areas in the sky.

²Neutrinos, are difficult to detect because of their weak interactions. Other neutral particles (like kaon k^0 and pion π^0) have short life time insufficient to travel over large cosmic distances.

enforce the knowledge of fundamental physics and also to give a glance on the nature and constituents of the dark matter.

1.3.1 Production mechanisms

High energy gamma photons are produced, by charged cosmic rays, according to two main mechanisms: leptonic and hadronic[14][15].

- In the **leptonic processes**, gamma photons are emitted through one of three scenarios[12][16].
 - Synchrotron radiation of relativistic electrons gyrating in a magnetic field.
 - The inverse Compton scattering of low energy photons by relativistic electrons.
 - Bremsstrahlung radiation emitted by accelerated electrons in the electrostatic field of nucleus.
- The **hadronic process** is based on the decay of neutral pions π^0 . These neutral pions are produced through nuclear interactions between high energy protons or heavier nuclei with ambient protons, nucleons or photons in dense regions of interstellar medium.

Other mechanisms of gamma photons production are the annihilation of dark matter particles (Weakly Interacting Massive Particles WIMP)[16][17] and the primordial black hole evaporation.

1.3.2 Detection mechanisms

It is possible to *directly* detect gamma rays in space but at high energies above 10^{10} eV, large detection area is required. This is because of the low flux estimated by some events per year per m^2 [16]. Besides, at these energies it is impossible to focus these photons of wavelengths shorter than interatomic distances. Hence, wide detection area is needed and this can not be afforded by the relatively small space-based detectors (e.g, FERMI-LAT $\sim 1m^2$ and AMS). For the very high energy gamma rays, the solution is then to *indirectly* measure them on the ground.

Considering the opacity of the atmosphere, when high energy gamma rays enter the atmosphere, they interact with its nuclei and produce cascade of secondary particles (electrons, positrons, photons) called extended air shower (EAS)³. The number of these secondary particles increases while their energy decreases. It depends on the nature and energy of the primary particle whether this air shower can reach the ground or die out earlier at high altitude.

Ground based detectors measure gamma-ray induced particle-cascades in the atmosphere by detecting those particles that reach the ground (air shower detectors), by detecting the fluorescence photons emitted from the shower during its development through the

³So do hadrons and leptons as well. In contrast to electromagnetic air shower, hadronic cascade is generally irregular and grows asymmetrically around the direction of the incident particle[18].

atmosphere⁴ (fluorescence detector in the Pierre Auger observatory) or by their Cherenkov light (Cherenkov telescopes). Fig.1.5 shows the indirect detection of $VHE - \gamma - ray$ on ground according to these two scenarios.

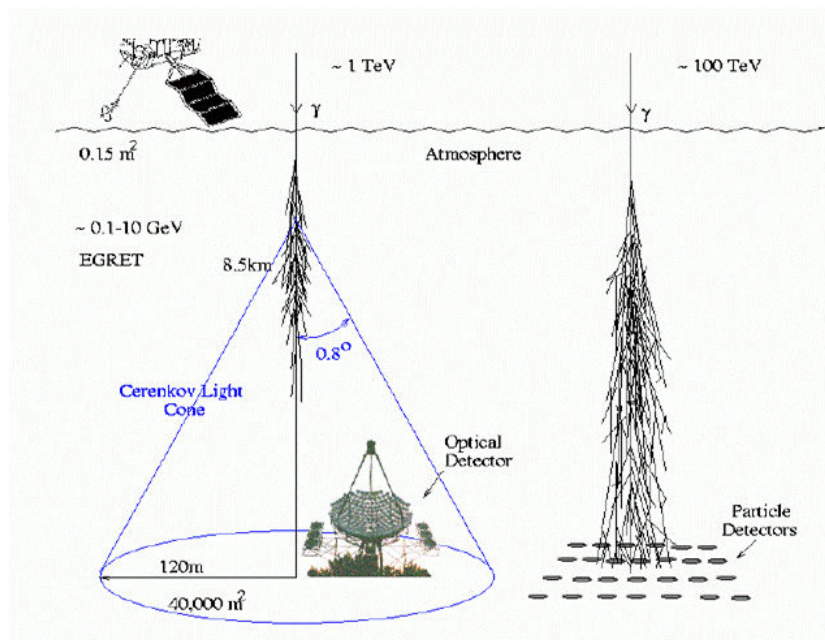


Figure 1.5: Indirect $\gamma - ray$ detection scenarios. Right: air shower particle detector (detects cascade particles that can reach the ground). Left: Cherenkov telescope (images Cherenkov light emitted by secondary gamma-ray induced particles that do not reach the ground).<http://astronomy.nmsu.edu/tharriso/ast536/ast536lecture3.html>

Here are some examples of gamma rays detectors in space. OSO-3 (third Orbiting Solar Observatory), SAS-2 (the second Small Astronomy Satellite), COS-B, EGRET (Energetic Gamma-Ray Experiment Telescope), AGILE (Astro-rivelatore Gamma Immagini LEggero) and Fermi-LAT (Fermi Large Area telescope) are telescopes that were (are still for some of them) landed on satellites.

CANGAROO (Collaboration of Australia and Nippon (Japan) for a Gamma Ray Observatory in the Outback), HESS (High Energy Stereoscopic System), MAGIC (Major Atmospheric Gamma Imaging Cherenkov Telescopes), VERITAS (Very Energetic Radiation Imaging Telescope Array System), and HAWC (High-Altitude Water Cherenkov Observatory) are examples of on-ground very high energy gamma rays ($30 GeV - 100 TeV$).

⁴Atmospheric nitrogen molecules being excited by shower particles (electrons and positrons) emit isotropically fluorescence photons with wavelengths between $300 - 400 nm$ [19][20]. The fluorescence light emitted is proportional to the energy deposited in the atmosphere by charged particles in the shower. Light observed on the ground, after some corrections related to the varying attenuation of the atmosphere and to the signal contamination by Cherenkov light, can give a measurement of the energy of the primary particle[21].

1.3.3 Cherenkov light

When secondary charged particle in gamma induced cascade move in the atmosphere with a speed greater than the speed of light ($v > c/n$), it will asymmetrically polarize the medium in front of and behind it causing an electromagnetic shock wave. Consequently, it will emit light near the ultra-violet⁵ called Cherenkov light. Cherenkov light is emitted in a cone around the direction of the original particle. It makes on the ground a circle of about 250 m diameter (for near vertical showers) called Cherenkov pool[22].

Many on-ground very high energy gamma ray telescopes were built to detect photons by the Cherenkov light. Some examples are HESS, MAGIC, and VERITAS. Fig.1.6 shows the energy range covered by some of these telescopes besides that aimed to be covered by the future CTA.

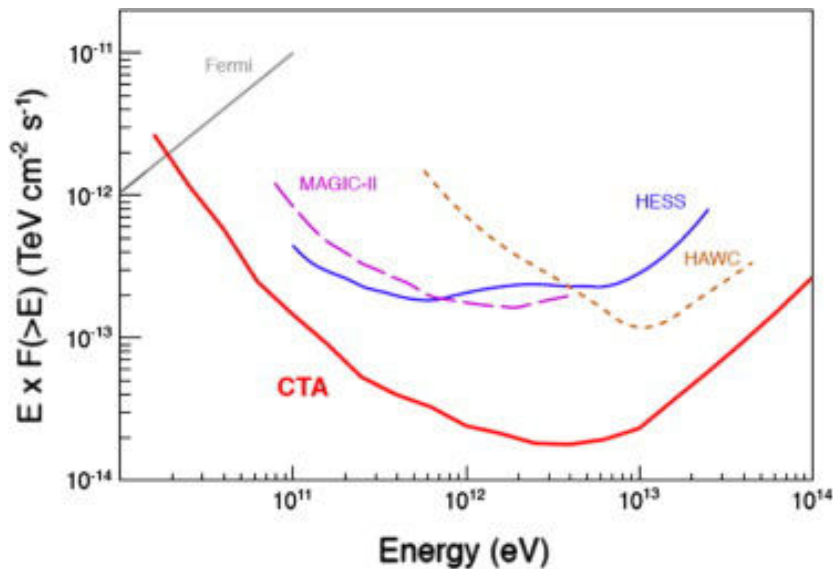


Figure 1.6: Integral sensitivity for CTA from MC simulations, together with the sensitivities in comparable conditions (50 h for IACTs, 1 year for Fermi-LAT and HAWC) for some gamma-ray observatories[3].

1.4 Cherenkov Telescope Array (CTA)

CTA is a future gamma-ray observatory that aims to achieve full-sky coverage with considerable improvements over the existing instruments (Fig.1.6). Two sites in the two hemispheres are programmed for this purpose. The northern site will be situated in La Palma in Spain while the southern site will be in Paranal in Chile⁶.

Each site will be equipped by an array of telescopes of different sizes: Large, medium, and small size telescopes. That is how a wider energy coverage is possible between some tens of GeV (20 GeV) up to some hundreds of TeV. Fig.1.7 illustrates the energy range of each telescope of the CTA.

⁵Actually Cherenkov light has a flat spectrum but due to absorption in the atmosphere, it shows a maximum around the ultra-violet.

⁶Decision was made in 2015 <https://portal.cta-observatory.org/Pages/News.aspx>.

The northern site will be dedicated to extragalactic physics (will not require coverage of the highest energies). While the southern site, will be optimized for galactic and extragalactic physics (hence it needs to be sensitive over the full energy dynamic range)[2].

Analyzing signals from an array of telescopes provides a stereoscopic view at large energies. This improves the angular and the energy resolutions (improve the quality of the data) besides allowing a better background rejection (better gamma-hadron separation)[2].

Thus CTA project will deliver better sensitivity thanks to the wider effective area covered by the array (an order of magnitude improvement with respect to the current minimum energy 30 GeV detected by HESS), wider energy coverage (span about 4 decades between 20 GeV and 300 TeV), better energy and angular resolution, besides, a wider field of view ($6 - 8\text{ degrees}$).

The technical improvements that are needed to realize such performance are being studied in the institutes member of the CTA collaboration all over the world. This includes, among many others, the choice of the photodetectors. Two main candidates are photomultiplier tubes (PMT) and the silicon photomultipliers (SiPM). SiPM-based camera will equip the dual mirror Schwarzschild-couder (SCT) MSTs and most of the SSTs. The use of SiPM in the camera of the LST is under study.

Large Size Telescope (LST): It can also be called the low energy instrument in whose context lays the question of this thesis. It will be discussed in the next section.

Medium Size Telescope (MST): It is a 12 m diameter telescope of one mirror Davis-Cotton design. Another design is also under study. That is Schwarzschild-couder dual mirror design (SCT) of smaller diameter that allows for a wider FoV and whose camera is based on SiPM detectors[23].

MST array covers an energy range from 100 GeV up to 10 TeV . These energies are well covered by other current instruments. The particularity of the CTA is the use of larger number of MSTs which will improve the sensitivity due to the increased covered area and the better quality of shower construction. An additional advantage of extended MST-grid (operating in two telescope trigger condition) is the possibility of lower triggering threshold since there are always telescopes sufficiently close to the shower core[22].

Small Size Telescope (SST): This is the smallest in size telescope ($4 - 6\text{ m}$ diameter) with a field of view of around 10 degrees . It covers the upper part of energy in the range covered by the CTA ($10\text{ TeV} - 300\text{ TeV}$). Since at these high energies light yield is large, large number of this telescope will be used to cover a wide area of the southern CTA site[22]. The northern CTA site will not host any SST because it will focus on the extragalactic sources, hence it will be dedicated to lower energy range.

Several technical solutions are proposed for the SSTs: a single-mirror Davis-Cotton telescope (SST-1M) and two telescope designs with dual-mirror Schwarzschild-Couder (SST-2M). All the three designs will use SiPM-based cameras[24].

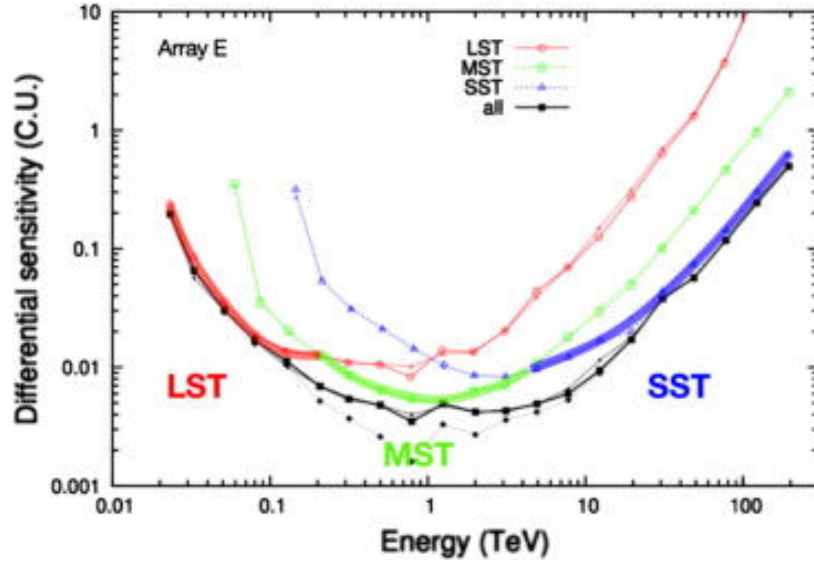


Figure 1.7: Dynamic range of CTA telescopes. Thin lines with small symbols illustrate the limited impact of a reduced dynamic range of the readout electronics (clipped at 1000 photoelectrons). The dashed black line with diamonds, shows the sensitivity if there was no electron background[3].

1.5 Large Size Telescope (LST)

It will be dedicated to the lower range of energy (down to few tens of GeV) covered by the CTA. The advantage of detecting in this energy domain by a ground-based instrument is to provide a wider effective collection area and field of view, than that in the space-based telescopes like *Fermi-LAT* whose effective area is $< 1 m^2$.

A group of 4 large size telescopes will be installed in each CTA field. These telescopes will be placed in a compact configuration with inter-telescope distances of about $100 m$. Each telescope is a $23 m$ diameter and provides a field of view of $4.5 degrees$.

The main goal of this LST grid is to achieve sensitivity in the energy domain from few tens of GeV ($10 - 20 GeV$) up to $\sim 100 - 300 GeV$ ⁷. Even if event rate is high, the uncertainty in the systematic background seems to limit sensitivity improvement (i.e, higher detection rate but lower amount of detectable light). LST allows for a higher collection efficiency and multiple LSTs allows better background suppression [2].

Detecting photons in Cherenkov light with as low as possible energy (down to $10 GeV$) requires efficient photosensors. The key feature for a better sensitivity is the photo detection efficiency (PDE: Eq.A.4) which is strongly related to the quantum efficiency (QE: Eq.A.3) of the photodetector devices in the camera[25]. For the first generation camera of the LST, photomultiplier tubes (PMTs) are planned to be adopted[26][27]. Advantages and disadvantages of such detectors will be discussed in the next chapter (Chapter.2). An emerging technology in photo detection is represented by the solid state silicon photomultiplier (SiPM). These new detectors promise to provide a rival performance in respect to that of the PMT, particularly in their quantum efficiency. SiPM structure and performance will also be presented in the next chapter(Chapter.2).

⁷In order to get an intersection with the upper part covered by the MST.

1.5.1 First generation camera of the LST

LST reflector is a parabolic dish of 23 m diameter that consists of 198 segmented mirrors. Each mirror is a hexagonal-shape of the size 1.5 m flat to flat which makes a unit of $\sim 2 m^2$. The total area of the LST reflector is then $\sim 400 m^2$ [27].

The camera is situated in the focal plane of the mirror and is conceptually divided into three parts: focal plane instrumentation, cluster electronics and the global camera elements. These three parts will be put inside a sealed structure with temperature control[26]. One can understand the motivation for such a structure since the camera of the first generation LST is planned to use PMTs. A motorized shutter will be used to protect the PMTs and to allow for a day-light operation with high voltage switched on. Electronics inside the camera dissipate power ($\sim 5 kW$) which produce a considerable amount of heat that needs to be evacuated. In order to stabilize temperature inside the camera body, two scenarios are being studied: Air flow cooling system and water cooling system based on cold plates[26].

The first generation of the LST camera will be based on Hamamatsu R11920-100 PMT photodetectors (Table.1.1 lists the main characteristics of these PMTs). 1855 PMTs will be organized in 265 clusters of 7 modules each. Fig.1.8 shows a group of three clusters, while Fig.1.9 lists the different components of one cluster.

number of dynodes	8
Window diameter	$D = 40 mm$
Sensitive area of the PMT cathode	a circular area of $D = 30 mm$
Super Bialkali Cathode	$R_{curvature} = 21 mm$
QE	35% at $\lambda = 350 nm$
Nominal gain	4×10^4
After pulse	< 0.02% above 4 pe
The Cockcroft-Walton power supply range	850 – 1500 V

Table 1.1: Main characteristics of the Hamamatsu R11920-100-20 developed for CTA project[26].

A photodetector module is composed of a light guide[28], a PMT with its Cockcroft-Walton high voltage power supply (provided by Hamamatsu) and its own preamplifier. Each photodetector module works as a pixel of the camera. While there is a preamplifier per PMT module, There is one readout board based on DRS4 ASIC per cluster as depicted in Fig.1.10.

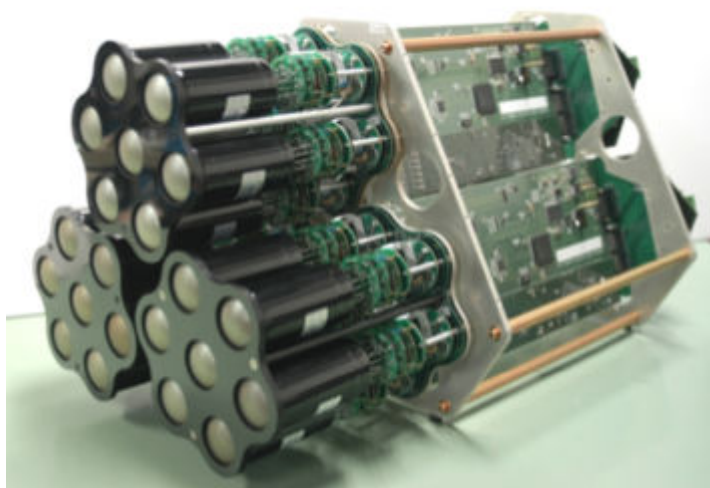


Figure 1.8: Three clusters of the first generation camera of the LST. Each cluster is composed of 7 PMT modules and the cluster electronics[26].

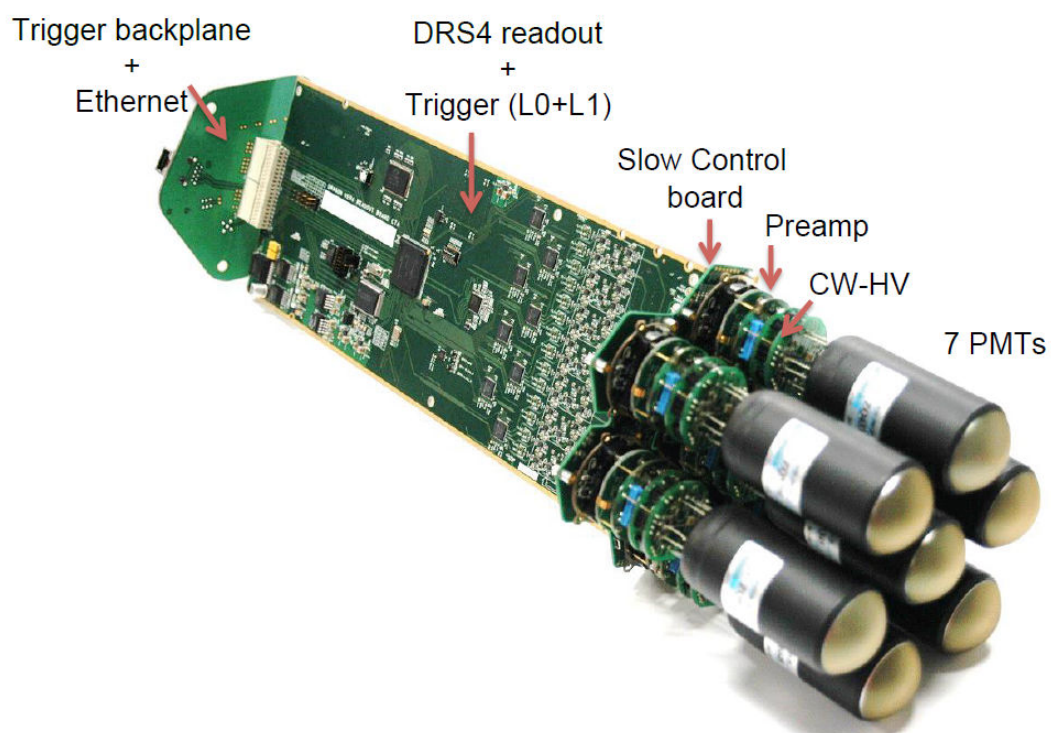


Figure 1.9: Photograph of one cluster to be installed in the camera of the first LST. 7 PMT modules in the cluster share the same readout board. The core of the readout system is based on the Domino Ring Sampler chip (DRS4), which is based on switched capacitor arrays (SCAs)[29][30].

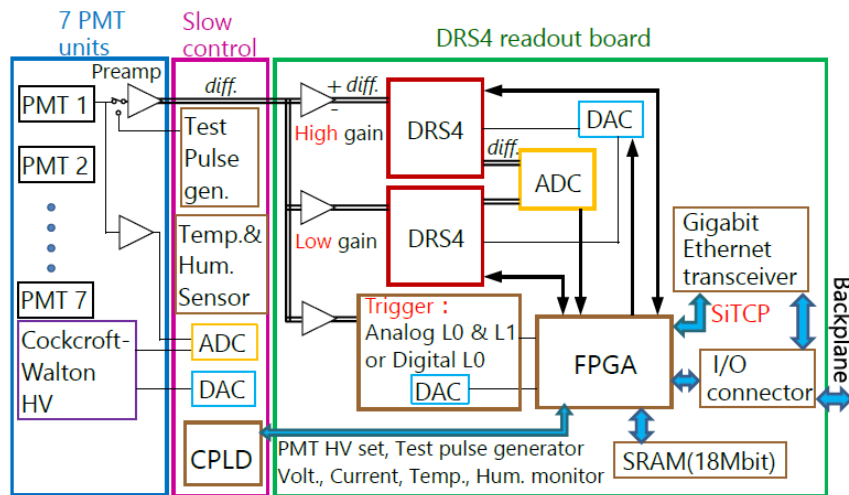


Figure 1.10: Bloc diagram of one cluster of the first LST camera[29].

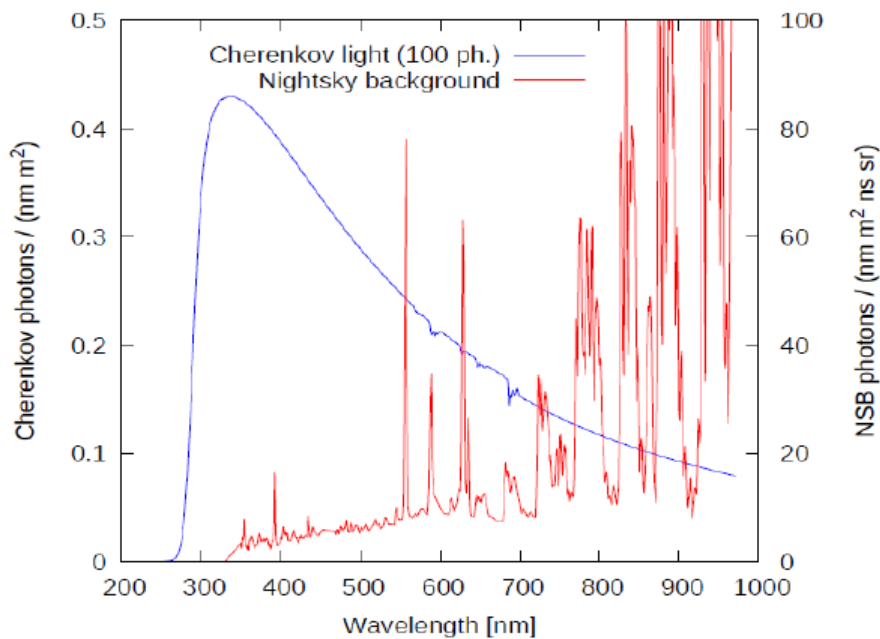


Figure 1.11: Spectrum of Cherenkov light in blue, night sky background (NSB) spectrum in red.

1.5.2 Second generation LST camera

Silicon photomultiplier (SiPM) is a new technology in the photodetector industry. These devices are being developed in an accelerated rhythm and are showing lots of advantages over the PMT devices. They are being used in wide range of applications like in the medical instrumentation field. SiPM photodetectors are becoming day after day serious candidates to replace PMTs in the Cherenkov Telescopes for their moderate operating conditions (i.e, low voltages), their high detection efficiency and fast pulse rising time.

Even though small in size and weight, SiPMs suffers from several drawbacks: small effective area, high crosstalk (section.A) and high dark current rate (section.A). These drawbacks, however, are being restricted with new improvements in the technology and building structure.

The average Cherenkov light density is given by Eq.1.2:

$$\rho_{Cher}(E) \approx 219. \left(\frac{E}{1TeV}\right)^{5/4} \quad (1.2)$$

The effective quantum efficiency of the photodetector in respect to the detected signal spectrum is described as in Eq.1.3:

$$QE_{eff} = \frac{\int QE(PDE)(\lambda) \cdot signal\ spectrum(\lambda) d\lambda}{\int QE(PDE) d\lambda} \quad (1.3)$$

Considering the Cherenkov light spectrum and that of the night sky background (NSB) presented in Fig.1.11, Table.1.2 lists the effective quantum efficiency obtained by the PMT and SiPM respectively for the Cherenkov light and the NSB.

QE_{eff}	PMT	SiPM
Cherenkov light	0.81	0.292
NSB	0.026	0.115

Table 1.2: Effective quantum efficiency of the PMT and that of the SiPM for both the Cherenkov light and the night sky background (NSB) respectively. SiPM effectively collects 1.6 times more Cherenkov photons and 4.4 times more NSB photons than that collected by the PMT[31].

Now taking into account the minimum number of photo electrons needed to reconstruct an event $N_{min} = 100 pe$, the system reflectivity $R_t \approx 0.85$ (mirrors reflectivity and losses in light guides, etc) and the reflective area lost $\eta_R \approx 0.9$ (due to shadowing by the mast of the camera); the required Cherenkov light density is then calculated from Eq.1.4:

$$\rho_{Cher}^{min} = \frac{N_{min}}{M \cdot \eta_R \cdot R_t \cdot QE_{eff}} \quad (1.4)$$

Where $M = 407 m^2$ is the total mirror dish area. This means that from Eq.1.2, one can conclude the energy threshold that can be obtained as:

$$E_{th}[TeV] = \left(\frac{\rho_{Cher}^{min}}{219}\right)^{0.8} \quad (1.5)$$

From Eq.1.4 and Eq.1.5, one can see that $E_{th} \propto QE_{eff}^{-0.8}$ and hence:

$$\frac{E_{th}^{SiPM}}{E_{th}^{PMT}} = \left(\frac{QE_{eff}^{SiPM}}{QE_{eff}^{PMT}}\right)^{-0.8} = 0.69 \quad (1.6)$$

The use of SiPM devices in the LST may reduce the energy threshold to less than 15 GeV in respect to the threshold of about 21 GeV attained with PMT detector operating

in its nominal conditions[31]. SiPM is then favorable for the LST in terms of reducing the energy threshold. At the same time, using SiPMs collects 4.4 times more night sky background (NSB) photons than those collected by PMTs. The solution to this problem may be through using optical filters with a cut-off frequency at 555 nm . The NSB could thus be reduced by 70%[31]. The number of pixels n_p needed in the camera is given by Eq.1.7.

$$n_p = \frac{f \cdot FoV \cdot \pi}{d \cdot 180^\circ} \quad (1.7)$$

Where f is the focal length of the telescope, FoV is its total field of view, and d is the physical pixel size. In order to cover the effective area of the LST, more than 10000 SiPM devices are needed. This may be solved with the new wider effective area SiPMs being developed together with the use of efficient light guides like the Winstone cones that lead to extended physical pixel size⁸[31]. i.e, the effective area of the LST camera is a circle of 2.2 m diameter which means ~ 48000 pixels each pixel is a $3 \times 3\text{ mm}^2$ SiPM with a light guide that extends its effective area to a 10 mm flat-to-flat hexagonal shape.

Light density inside the Cherenkov pool is $\rho_{Cher}(100\text{ GeV}) \approx 12.3\text{ photons/m}^2$. Due to the mirror reflectivity, effective quantum efficiency of the photosensor, to other losses this number is reduced to $\sim 2.7\text{ photons/m}^2$. Considering the total mirror area of the LST $M \approx 407\text{ m}^2$, 100 GeV corresponds to 1098.90 pe and hence 10 GeV corresponds to $\sim 61.8\text{ pe}$.

For the MSTs and the SSTs, SiPM devices may be of great advantage thanks to their extended dynamic range and their robustness to high light flux among all other moderate operating conditions.

In this thesis, a new camera based on the SiPM technology with its adapted front-end electronics is proposed. Characterization tests on the SiPM detector, front-end electronic design, and performance check-up results are successively presented in chapters that follow.

1.6 Conclusion

Gamma rays astronomy reflects the non-thermal universe. Since of neutral charge (photons), information about their direction and sources can be extracted from detecting gamma rays over wide energy spectrum extended between 100 keV and some hundreds of TeV . They can be used as a rich source of information about cosmic rays, dark matter, and to answer lot of questions related to fundamental physics.

Photons having an energy above 20 MeV are called **High Energy** γ rays, while above some hundreds of GeV are referred to as **Very High Energy** γ rays. The flux of gamma rays, like that of cosmic rays, follows a power law that decreases radically with energy, thus detecting high and very high energy gamma rays needs a wide detector area. That is the reason why indirect detection via on-ground instruments is mandatory. The propagation of gamma rays in the medium induces cascade of secondary particles. A relativistic charged particle traveling in the atmosphere emits Cherenkov light. On-ground telescopes detect photons from this light and hence, they allow a complementary research to the space-based ones.

⁸FACT uses $3 \times 3\text{ mm}^2$ pixels with light guides that enlarge them to 9.6 mm flat-to-flat hexagonal-shape.

Cherenkov Telescope Array (CTA) is a project of building a wide grid of telescopes in the two hemispheres. La Palma in the Canary Island (Spain) will host the northern grid while the southern one will be situated in Paranal in Chile. The northern site focus on extragalactic sources so sub grids of LSTs and MSTs will be built (i.e, no SST). The southern site will look for wider range including galactic and extragalactic sources. Hence in the southern site, sub grids of telescopes of different sizes (small, medium and large size telescopes) will be used to provide a full-sky coverage over a wide energy dynamic range between 10 GeV and 100 TeV . Even if some ranges of energy are covered by the current instruments, CTA promises enhancements in the sensitivity to gamma ray sources. CTA will enlarge the covered energy band and improve angular and energy resolutions with better gamma-hadron separation.

An array of four **Large Size Telescopes** will be deployed at the center of both CTA sites. These LSTs will provide low energy threshold and a wide field of view. This last point makes the advantage of such telescopes over space-based instruments like FERMI-LAT.

For the first version of the LST camera, photomultiplier tubes (PMTs) will be used as photo detectors. An emerging technology in photodetectors is the silicon photomultiplier (SiPM) which provide a better photodetection efficiency. This thesis aims to underline the merit and feasibility of a second-generation camera using this new SiPM technology. A demonstrator based on SiPM photodetector with its compatible readout electronics is discussed in this manuscript.

Chapter 2

SiPM based camera

Contents

2.1	Introduction	23
2.2	Photo detection principle	23
2.3	Photomultiplier tube (PMT)	25
2.4	Semiconductor photodetectors	28
2.4.1	PN junction	29
2.4.2	PIN junction	29
2.4.3	Avalanche Photodiode (APD)	30
2.4.4	Geiger-Mode Avalanche Photodiode (G-APD)	31
2.5	Silicon Photo-Multiplier (SiPM)	33
2.5.1	SiPM industrial variety	36
2.5.2	Multi-pixel Silicon photo multiplier (SiPM matrix)	36
2.5.3	SiPM in astrophysics instruments	37
2.6	4 × 4 SiPM matrix characterization	38
2.6.1	Test bench	39
2.6.2	Temperature Measurement	43
2.6.3	Pedestals	44
2.6.4	Gain variation with over voltage	47
2.6.5	Optimum operating point	48
2.6.6	Gain dispersion among the 16 pixels	49
2.6.7	Noise in SiPM	59
2.7	SiPM Modeling	60
2.8	Conclusion	63

2.1 Introduction

Cherenkov light detection with the large size telescope aims to work for the lowest energies covered by the future CTA. LST project is foreseen to measure showers from 10–20 GeV up to 100 – 300 GeV . This requires a very sensible camera of new and advanced technology. LST camera including light detectors and their following front-end electronics should enable more observation time, lower energy threshold and hence, more data acquisition.

This chapter shows the photo detection principle with a brief review of detection techniques and the evolution of the photodetectors up to the Silicon Photo-Multipliers (SiPM). Some results from the first experience that makes use of SiPM detectors in a high energy gamma-rays dedicated telescope (FACT), at La Palma, will be presented.

Characterisation tests were done in order to evaluate this new geometry of photodetectors. The results unveil the reason that makes of SiPM a promising candidate for the new LST camera and defines the primordial specifications of the following front-end electronics.

2.2 Photo detection principle

Photoelectric effect consists of electron emission when a material (metal or semiconductor) is illuminated. This principle is exploited in all photo-sensors. In these devices, electrons are excited by light and they may (in case they get enough energy from light) leave their atoms creating holes. The combination electron/hole forms the raw material for the outer circuit to drive these charge-carriers and pass an electric current[32][33][34].

Light is an electromagnetic radiation that was proved to have wave nature as well as corpuscular nature at the same time. The first nature is considered when discussing the interaction radiation-radiation (interference, diffraction, etc...) while the second is more helpful to understand the interaction radiation-matter[33].

In optoelectronic devices like photodetectors, the interaction light-matter goes with energy exchange. Light is then considered as particles called *photons*. A photon has an energy E_ν given by Eq.2.1, where h is planck constant¹, $\hbar = h / 2\pi$, $\omega = 2\pi\nu$.

$$E_\nu = h\nu = \hbar\omega \quad (2.1)$$

Considering the energy band structure of the material (metal or semiconductor), semiconductor in particular², the gap nature³ influences the interaction electron-photon. There are three scenarios when the interaction light-semiconductor takes place. This interaction could be: *Fundamental absorption*, *spontaneous emission* and *stimulated emission* (Fig.2.1)[33]. In photodetectors, the fundamental absorption is the interesting scenario. An incident photon with an energy E_ν greater than the energy of the bandgap (examples: E_g ($E_{g, Si} = 1.11 eV$, $E_{g, Ge} = 0.67 eV$, $E_{g, GaAs} = 1.43 eV$)) of the semiconductor material, can cause an electron to jump from the valence band to the conductance band.

This process is governed by conservation condition of both energy E and momentum

¹Planck constant: $h = 6.6262010^{-34} Js$

²In some modern PMTs, the photoemissive materials of the photocathode and dynodes are semiconductors instead of metals.

³There are semiconductors with a direct gap and others of indirect gap.

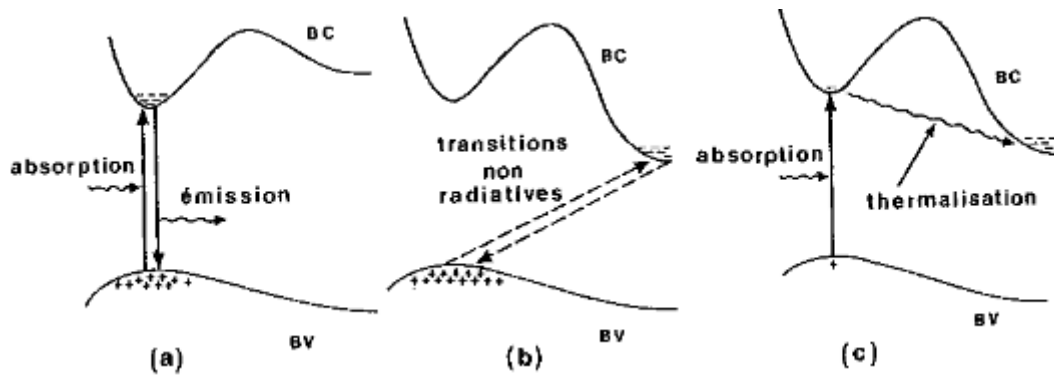


Figure 2.1: Left: Transitions between energy band extremes. a) Semiconductor with a direct gap, vertical transitions with photon absorption/emission (radiative). b) Semiconductor with indirect gap, oblique transition (non radiative). c) Semiconductor with indirect gap, stimulated vertical-transition then transition to the minimum of the conduction band: direct absorption of the photon[33].

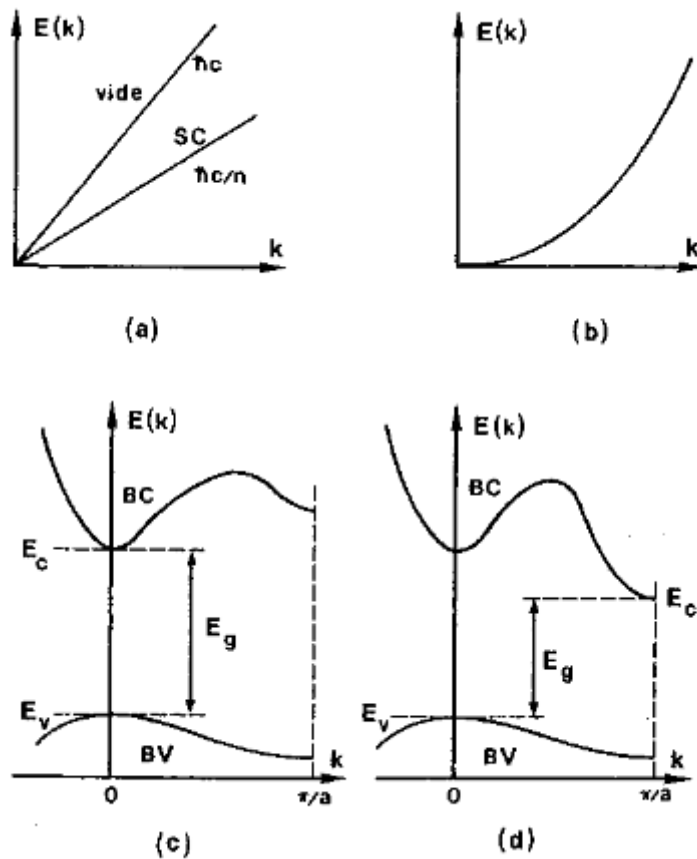


Figure 2.2: Dispersion curves: a) photon in the space and inside a semiconductor. b) Electron in the space. c) Electrons in a semiconductor with a direct gap. d) Electrons in a semiconductor with an indirect gap[33].

($\vec{P} = \hbar \vec{k}$ where \vec{k} is the wave vector)⁴. This condition is described in Eq.2.2 and Eq.2.3 where the indexes i , f and p refer to the initial state, final state of the electron and the incident photon, respectively. The + sign refers to the absorption of the incident photon.

$$E_f - E_i = +E_p \quad (2.2)$$

$$\vec{k}_f - \vec{k}_i = +\vec{k}_p \quad (2.3)$$

From these equations, and considering the reflection and absorption coefficients of the illuminated area of the semiconductor (the detector), it is concluded that the rate of absorbed photons is equal to that of the electron/hole pair generation. i.e, the number of created pairs e/h is equal to the number of converted photons. Detector's output current is then proportional to the incident light intensity.

Absorption coefficient is a very important factor that limits the quantum efficiency (appendix.A) of the detector, it determines the distance in the material that the photon passes through before being absorbed. Materials with low absorption coefficient are transparent for photons with long wavelengths[33][34].

Development in photodetectors starts with the photomultiplier tubes (PMTs) and continues with the solid state devices that make use of the emerging technologies in the semiconductor materials that doesn't stop with the invention of the silicon photomultipliers.

2.3 Photomultiplier tube (PMT)

Nowadays cameras of all gamma rays telescopes use this kind of detectors. Its structure and principle are demonstrated in Fig.2.3, [32][35]. It consists of a *window* whose inner surface is covered with a thin layer of photo emissive material forming a *photo cathode*. This input stage absorbs incident photons and emits electrons (also called photo electrons) inside the tube. A system of several electrodes will then *accelerate and focus* the photo electron beam onto the first dynode in the tube. A dynode is an electrode covered with a layer of secondary emissive material and connected to a high voltage⁵. The *electron multiplier* is formed of a series of subsequent dynodes along the tube. The beam will be electrostatically⁶ accelerated and curved/focused from one dynode to another. Each time photoelectron beam hits a dynode (with an energy of hundreds of electron volts), it liberates secondary electrons that in turn join the beam. Secondary electrons from the last dynode will be collected at the *anode* that delivers a proportional electric current to the outer circuit.

⁴photon-electron interaction is considered as an elastic chock between two particles (electron and photon).

⁵PMTs demand high voltage source of the order of kilo volts. A volt divider circuit is then used to distribute an optimum voltage to each dynode[35].

⁶Due to potential difference between the dynodes along the tube.

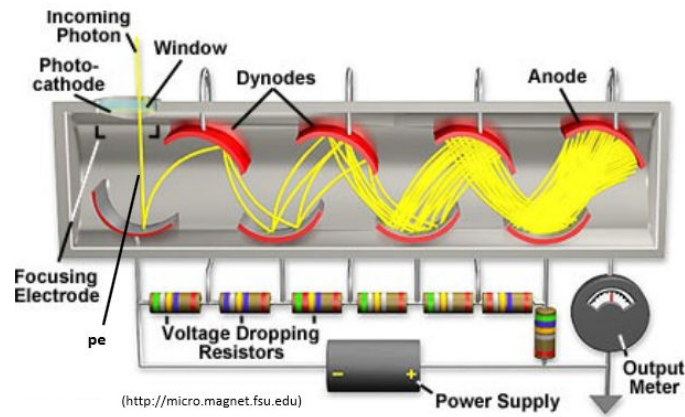


Figure 2.3: Photomultiplier tube.

Each stage of the PMT system is described by its own parameters. The photocathode is defined by its quantum efficiency, cathode radiant sensitivity and its spectral response. Other parameter which is very important is the *collection efficiency* defined as the ratio between the number of the electrons incident to the first dynode to the number of electrons emitted by the cathode. In addition, each dynode in the multiplier system has its collection efficiency as well.

The gain of the PMT is the ratio of the number of anode output current to the photoelectric current from the photocathode or it is the ratio of the number of secondary electrons to the number of primary electrons. i.e, $G_{PMT} = I_{anode}/I_{photocathode}$. It depends on the primary incident energy, dynode material and geometry, number of dynodes in the electron-multiplier and the applied voltage. This gain is controlled by varying the high voltage supplied to the dynode system.

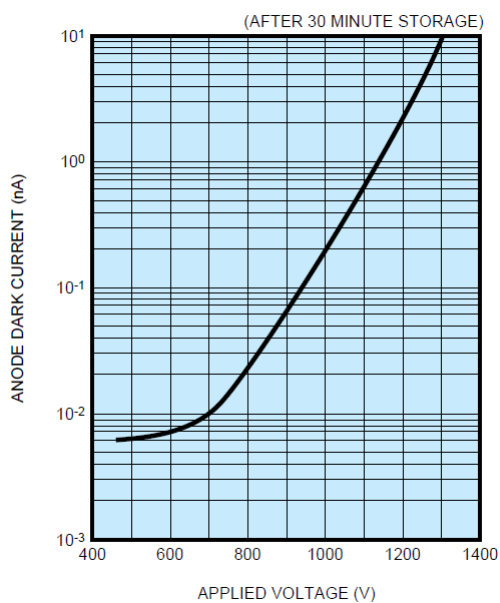
If δ is the secondary emission ratio per stage, n is the number of dynode stages (usually 8 to 12), E is the interstage voltage, α is a coefficient related to the dynodes' material and geometric structure (0.7 to 0.8) then gain per stage can be written as $\delta = AE^\alpha$ where A is a constant. And the overall gain of the PMT is $G_{PMT} = \delta^n$.

PMTs have a very high gain which makes them very sensible to high voltage fluctuations. As an example, one need to hold the power supply stability within 0.1% in order to maintain that of the output within 1%.

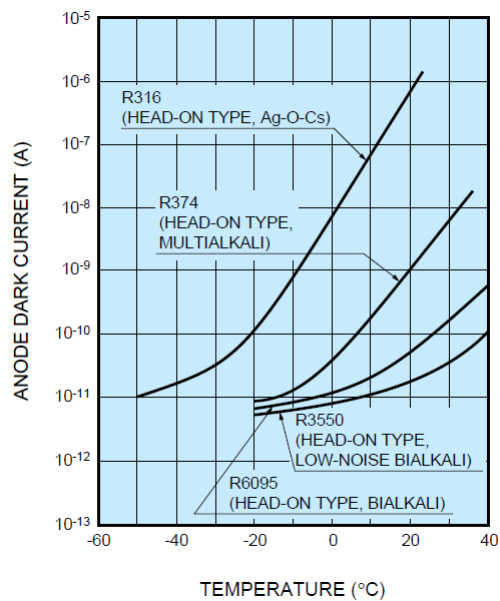
PMTs show a very good performance in terms of gain. PMTs gain is estimated by the order of some 10^6 with a reasonable amount of noise of the order of $10^{-15} - 10^{-16}$ Watts. However, they are relatively big detectors (their size is of the order of *cm*) and they need a stabilized, very high voltage power supplies of the order of some hundreds of volts (500 – 1000 V). Dark current of the PMTs strongly depends on the supply voltages and temperature as shown in Fig.2.4a and 2.4b. This may demand cooling techniques to stabilize and reduce noise levels in these tubes.

A main drawback of PMTs is also their sensibility to magnetic field depicted in Fig.2.4d. An external magnetic field can deflect the trajectory of the electron beam inside the tube causing a loss of gain.

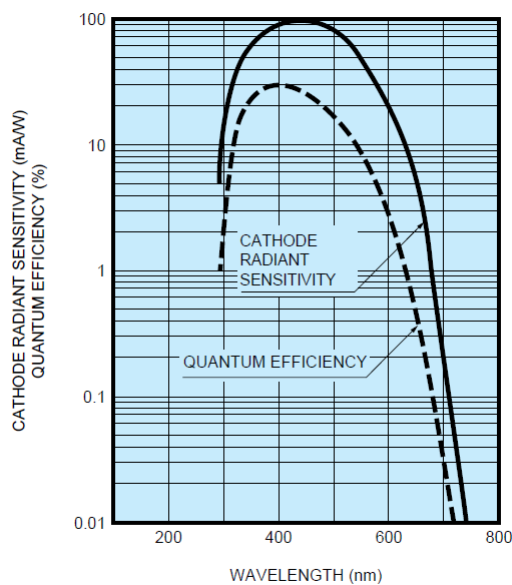
Moreover, PMTs are easily damaged when exposed to high light levels. Protection from day light and night moon light adds more expenses to the already expensive production techniques. PMTs operate at lower gain in order to be compatible with moon time.



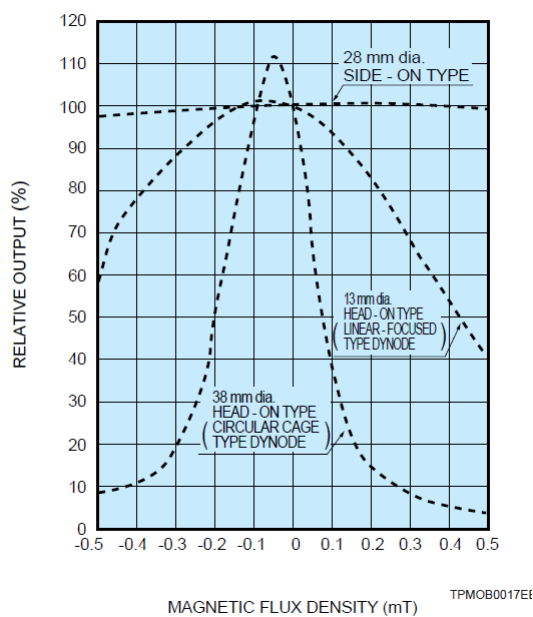
(a) Typical dark current vs. supply voltage



(b) Temperature characteristics of dark current



(c) Typical spectral response of head-on Bialkali photocathode



(d) Typical effects by magnetic fields perpendicular to tube axis.

Figure 2.4: Typical drawbacks of PMT. Source: <http://www.hamamatsu.com/us/en/support/>.

2.4 Semiconductor photodetectors

The technology of Photodetectors based on semiconductor materials has been in development along with the semiconductor industry and the market needs. Their popularity is due to their compact size, robustness and performance. They are insensitive to magnetic field, they tolerate higher light levels than that for the PMTs and they are cheaper. These aspects have opened a wide range of application for these devices especially in medical imaging (e.g, positron emission tomography (PET) and single-photon emission computed tomography (SPECT)), and analytical and medical diagnostic instruments.

Used materials vary from simple semiconductors like silicon *Si* and Germanium *Ge* to the III-V compound semiconductors and their alloys like Gallium-Arsenide *GaAs*, Indium Gallium Arsenide *InGaAs*, Galium Phosphide *GaP* and Galium Arsenide Phosphide *GaAsP*, to mention some.

In these solid state photodetectors the minimum energy that the incident photon should have in order to create a pair electron/hole depends on the type of the detector. It is the energy of the gap for the simple detectors built with one material or it can also most of the time be the barrier height as in hetero-junctions (like metal- semiconductor or semiconductor -semiconductor) devices or even homo-junction devices composed of two regions of the same semiconductor but with different types P and N. It should be mentioned that the materials and the structure of the solid state photodetectors are carefully optimized for the wavelength (or the range of wavelengths) of interest. Si and Ge have indirect gap and hence their absorption coefficient is low in respect to the III-V compound semiconductors which have a direct gap and hence high absorption coefficient. For materials with indirect gap, like Si, in order to create a pair electron/hole, there will be vibrations in the crystal lattice called *phonons*⁷ which are slow phenomenon[33][34]. However, silicon stays the major semiconductor in modern photodetector industry due to its good electrical properties, less generated noise (thanks to its relatively high gap $E_g = 1.12 eV$), and above all its flexible characteristics and compatibility with the ongoing improvement in electronic circuits manufacturing. In particular, because of the easy formation of one of the best insulators with excellent transmission of light, the silicon di-oxide *SiO₂*[36][37].

The principle of these detectors is the simple *PN junction* and all other more sophisticated detectors are its descent: PIN, avalanche photodiode (APD), Geiger-APD. The main motivation for developments in structure and mechanism of solid state photodetectors is the improvement of the quantum efficiency, gain and consequently the device sensibility.

Gain in advanced solid state photodetectors is obtained by electron multiplication process. This process was observed long time ago in broad junctions of silicon (and germanium)[38][39]. The multiplication rate increases rapidly as the breakdown voltage is approached. Hence, avalanche multiplication of photo-generated electrons and holes can be triggered by applying high reverse voltage through a PN junction. This scenario imposes more complicated structure than the simple PN photodiode.

The development of these semi conductor photosensors from the simple PN junction to the silicon photomultiplier is discussed in the sections that follow.

⁷A phonon is a quantum of the lattice vibrations that results from the thermal vibrations of the atoms in the material[32].

2.4.1 PN junction

A PN photodiode is a junction of two semiconductor materials, one of the type-P (*the active surface or photosensitive layer*) and the other is of the type-N (*substrate*). Putting two inversely doped materials side by side will give birth to an intermediate region called *depletion layer*. The structure and charge carrier movement in the diode are illustrated in Fig.2.5.

Incident light creates electron/hole pairs in the three regions P, N and depletion. In the vicinity of depletion region, photo generated minority charge carriers (electrons in the P-layer and holes in the N-layer) will diffuse toward the depletion layer. While those generated far from depletion region in P/N layers will recombine quickly[32].

Charge carriers generated in the depletion layer together with those reaching it from its vicinity of other layers will be pushed to the layer where they become dominant (electrons to N-layer and holes to P-layer) because of the internal electric field.

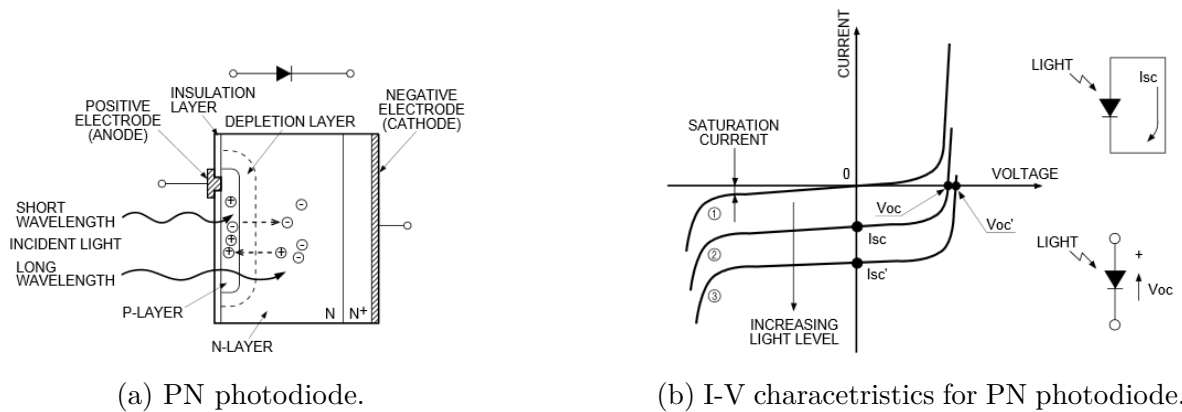


Figure 2.5: PN operation principle[40].

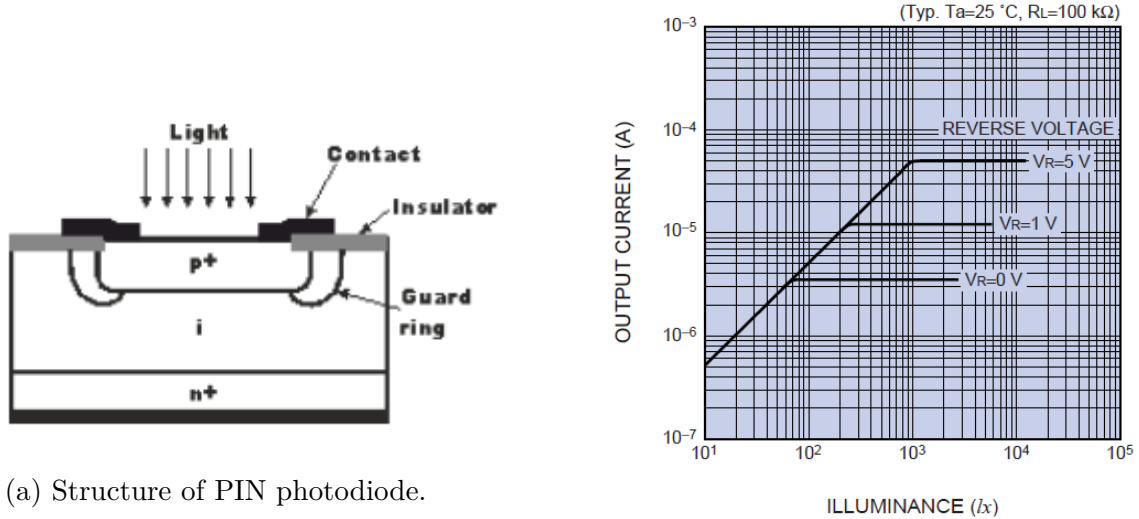
The photo current has double origin: generation and diffusion. Generation current is the current due to charges generated in the depletion layer. Diffusion current is due to charges generated in the depletion neighborhood and that diffuse into the depletion layer. The diffusion mechanism is slow. It has a time constant of the order from 10^{-8} to 10^{-9} second [33] and affects the response speed of the diode.

Under reverse bias (positive tied to N-type part and negative to P-type), the external electric field will reinforce that of the local internal one in the depletion layer. Thus, limiting time needed by charge carriers to reach their final destination. Nevertheless, PN junctions shows no multiplication mechanism of the number of photo-generated charge carriers and its gain is then unity.

2.4.2 PIN junction

PIN detector is a PN photodiode with an additional intrinsic layer (*I*) inserted between the P-layer and N-layer. This new layer will widen the depletion region. The probability that the incident light is absorbed in this layer is then higher. As a consequence, the diffusion part of the photocurrent will be negligible in favor of the generation current.

Applying a reverse bias to the PIN photodiode, a high electric field in the depletion layer increases the speed of the photo generated charge carriers. These photodiodes are fast (response time in the tens of pico seconds) and very sensitive.



(a) Structure of PIN photodiode.

(b) PIN output current vs. illuminance for different reverse voltages[41].

Figure 2.6: PIN photodiode: structure and linearity limits for different bias voltages.

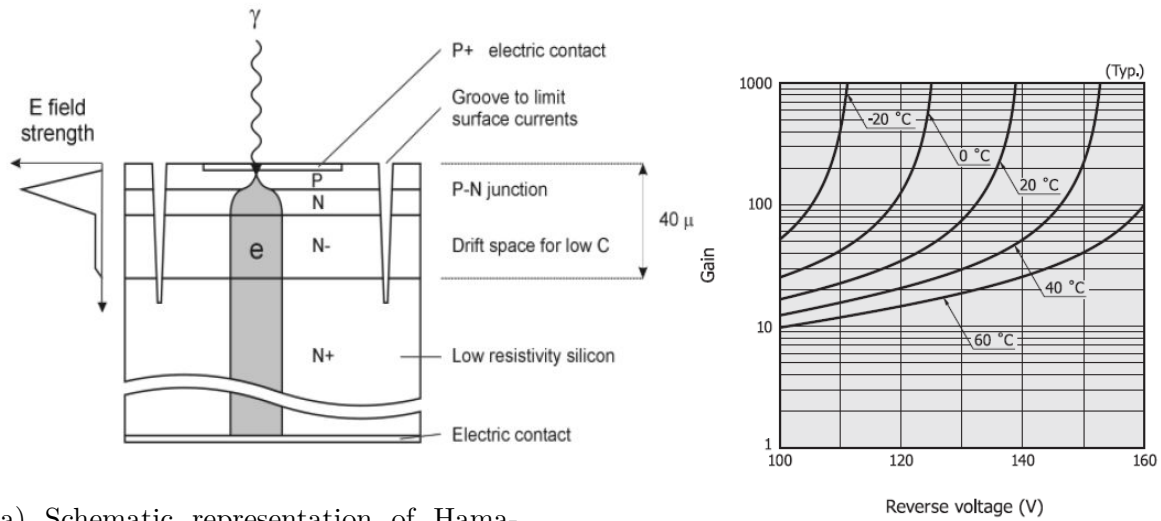
Applying a reverse voltage also helps to improve frequency response and linearity but it has several disadvantages like increasing the dark current and noise levels[41]. Reverse voltage should not exceed certain limits not to damage the device. Same as in the PN junction, in PIN photodiodes the ideal quantum efficiency is unity⁸ and there is no internal gain in the material i.e, its gain is unity.

2.4.3 Avalanche Photodiode (APD)

In contrast with the PN and PIN photodiodes, avalanche photodiodes (APDs) are designed to handle high reverse voltages close to the breakdown value. They provide a gain ranging from *dozen* to *several hundred* for some hundreds of volts as bias voltage. Having certain gain improves the sensibility of the device to lower light levels with respect to that detected by the normal PIN diodes.

If incident photon is absorbed in the depletion layer, it creates a pair of electron/hole exactly like in PIN diodes. However, the high electric field in the depletion region accelerates these charge carriers giving them high energy. Moving very fast, these carriers collide with crystal lattice and new electron/hole pairs are generated (by ionization). The new charge carriers generate themselves other pairs in a chain reaction process as illustrated in Fig.2.7a. The number of pairs generated by a charge carrier during the time per unit distance is defined as the *ionization rate*. Electrons are found to have an ionization rate α higher than that of holes β and the ratio $k = \frac{\beta}{\alpha}$ is a parameter that indicates the noise

⁸In practice, $QE \leq 1$ because of current loss due to reflection, incompleteness absorption (when absorption coefficient is low) and recombination[34].



(a) Schematic representation of Hamamatsu "reversed" APD structure used in CMS ECAL[37].

(b) Temperature characteristics of APD's gain vs. reverse voltage[40].

Figure 2.7: APD structure and gain.

in these APD devices. The gain in APD devices depends on the ionization rate which depends on the drift speed and hence on the strength of the electric field⁹. This requires an attention to the bias circuit in order to stabilize the APD gain. Another aspect of interest is the dependency on the temperature depicted in Fig.2.7b. At high temperatures, vibration in crystal lattice causes collisions with charge carriers not yet having enough energy to induce ionization which is translated in gain decrements. The solution is then to adjust the bias voltage with temperature.

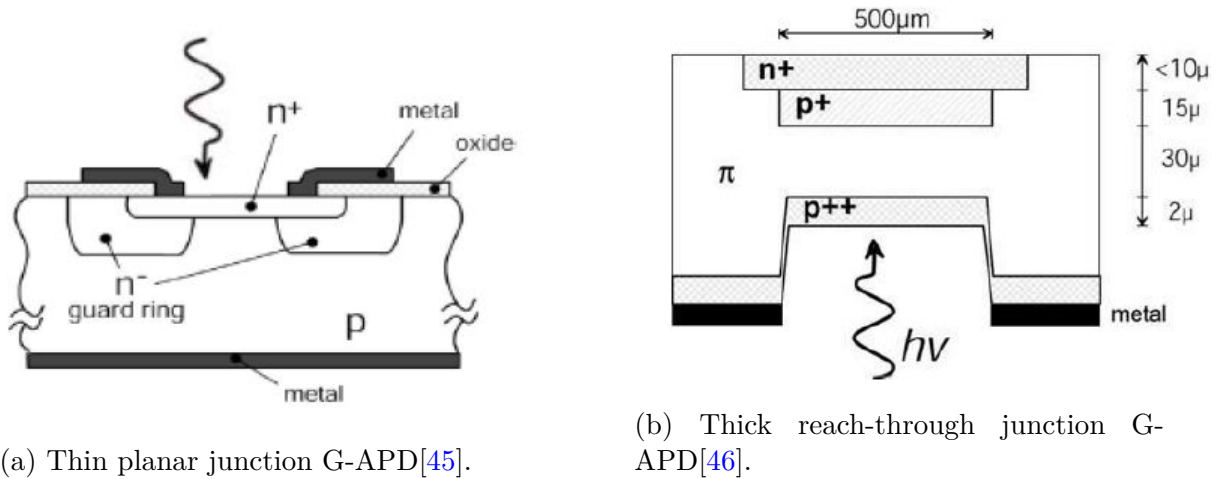
The multiplication or gain doesn't depend on the place in the depletion region where charge carriers are generated[38]. However, according to its wavelength, the incident light may be absorbed near surface or deep in the junction. The spectral response of the APD is then a function that shows a peak for certain incident wavelength[40].

2.4.4 Geiger-Mode Avalanche Photodiode (G-APD)

Applying a reverse voltage above the breakdown voltage through an APD makes it work in a mode called *Geiger*. The device is then called Geiger-mode Avalanche Photodiode (G-APD). The difference between the operating voltage V_{Bias} and the breakdown value V_{BR} is referred to as the *over voltage* $\Delta V = V_{Bias} - V_{BR}$ as described in section.A. It is worth to mention that for such type of photodiodes V_{BR} is estimated between 30V and 70V[42].

For a device to tolerate such bias voltage, special structures and geometries are exploited[43]. An example is depicted in Fig.2.8a which is based on planar arrangement. This structure offers an efficient, ultra-sensitive, low-power, low-cost and miniaturized photodetector especially when using n-well guard rings[44]. Another example of another technology is the reach-through structure shown in Fig.2.8b.

⁹Reach-through structure of the near infrared Si-APD guarantees the concentration of the electric field in the depletion layer and hence the efficiency of the ionization process.



(a) Thin planar junction G-APD[45].

(b) Thick reach-through junction G-APD[46].

Figure 2.8: Two different structures of the G-APD

In the thin junction G-APD, n^+ layer forms the optical window where the incident photons penetrate into the device. High electric field is concentrated in the $n^+ - p$ depletion region that includes the breakdown and thus the avalanche process. The n^- diffusions are guard rings used to limit and isolate the breakdown region and to avoid the premature edge breakdown (PEB phenomenon)¹⁰.

Under bias condition over the breakdown, the strong avalanche multiplies the number of photo-generated electrons and holes faster than they can be extracted on the output. This gives an exponential growth to their population before forming the output-photo current. In this operating mechanism, G-APD is high-speed detector with a gain that can reach infinity if not controlled. Hence, these devices are sensitive to very low light levels down to one single photon.

The growth of charge carrier population (i.e., photo current) lasts as long as the electric field is constant in the diode (more precisely in the avalanche layer) which blinds the detector to the newly incident photons. It is then important to stop the avalanche and recover the device to detect the next photon.

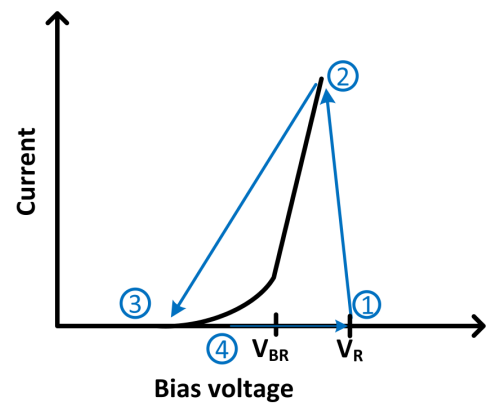
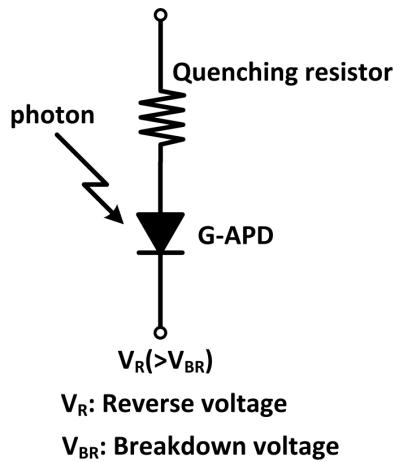
Quenching circuit is used in order to stop the Geiger discharge and make the device able to detect separate successive incident photons. It consists of an outer circuit connected in series with the detector (e.g, Fig.2.9a). Photo current flows into this circuit developing a voltage drop across it. This reduces the voltage between the device's terminals down to its breakdown voltage. The avalanche is then stopped and consequently the gain is not infinity any more (the gain of quenched G-APD is of the order of 10^6 which is a high gain value, though). The avalanche process takes a time that depends on the inner parameters of the G-APD (resistor R_d and capacitor C_d as we will see in section.2.7). After this time, the photo-current pulse vanishes and the operating voltage across the device recharges to the initial value $V_{Bias} = V_{BR} + \Delta V$. The device is then recovered and is again sensible to an incident photon. Recovery time depends on the device capacitor (hence, it depends on the size of the device¹¹ and on its structure) and on the quenching resistor R_q . If the resistance value R_q changes with temperature (the case of polysilicon

¹⁰Edge breakdown is due to high electric fields at the edges of typical planar junctions.

¹¹G-APD devices of $5 - 30 \mu m^2$ are considered small cells. Large cells are about $50 - 100 \mu m^2$ [47].

resistors), recovery time will strongly depend on temperature. It is then recommended to use metal alloy with high resistivity (like FeCr) for quenching resistors to avoid the temperature dependency[47].

There are two types of quenching, passive and active. In the passive quenching drawn in Fig.2.9a, a resistance (of the order of hundreds of $k\Omega$) is used in series with the G-APD. While in the active quenching, an active charge designed using a CMOS transistor is used[43]. Fig.2.9b resume the different steps of the detection and quenching process in a G-APD. A reach-through structure of the G-APD with the quenching mechanism was described in details in[48].



- ① Waiting for carrier generation.
- ② Avalanche multiplication is triggered by detecting carrier.
- ③ Voltage between terminals is reduced and avalanche stopped
- ④ Bias voltage is restored for next carrier.

(a) G-APD with its quenching resistor[49].

(b) Quenching principle[40].

Figure 2.9: Operation principle of a G-APD.

The active layers of silicon are thin ($2 - 4 \mu m$). Working in the Geiger mode, the avalanche process through the intrinsic resistor of the device (R_d : between few hundreds of ohms and some $k\Omega$) is fast (some hundreds of ps). The recharge process takes more time (recovery time could take some tens of ns) since it occurs through the quenching resistor which is larger than that of the diode ($R_q \gg R_d$).

Time resolution is an important parameter that also defines the device immunity to overlapping or blinding successive photons. G-APD shows a time resolution of the order of some tens of pico seconds $\sigma = 42 ps$ [47].

Thanks its internal high gain, G-APDs gives a better output signal than the PN, PIN or even APD diodes. Nevertheless, the output current pulse is the same whatever the number of simultaneously incident photons. G-APD is then a dual state device (on/off device) that can only give an information whether photons were detected or not regardless their number. Therefore, G-APD can not measure light intensity.

2.5 Silicon Photo-Multiplier (SiPM)

One SiPM is a parallel connection of large number of Geiger-mode avalanche photodiodes (G-APDs) with their series quenching circuits as illustrated in Fig.2.10. Henceforth, I will

call *micro pixel* or *micro cell* each individual G-APD inside one SiPM.

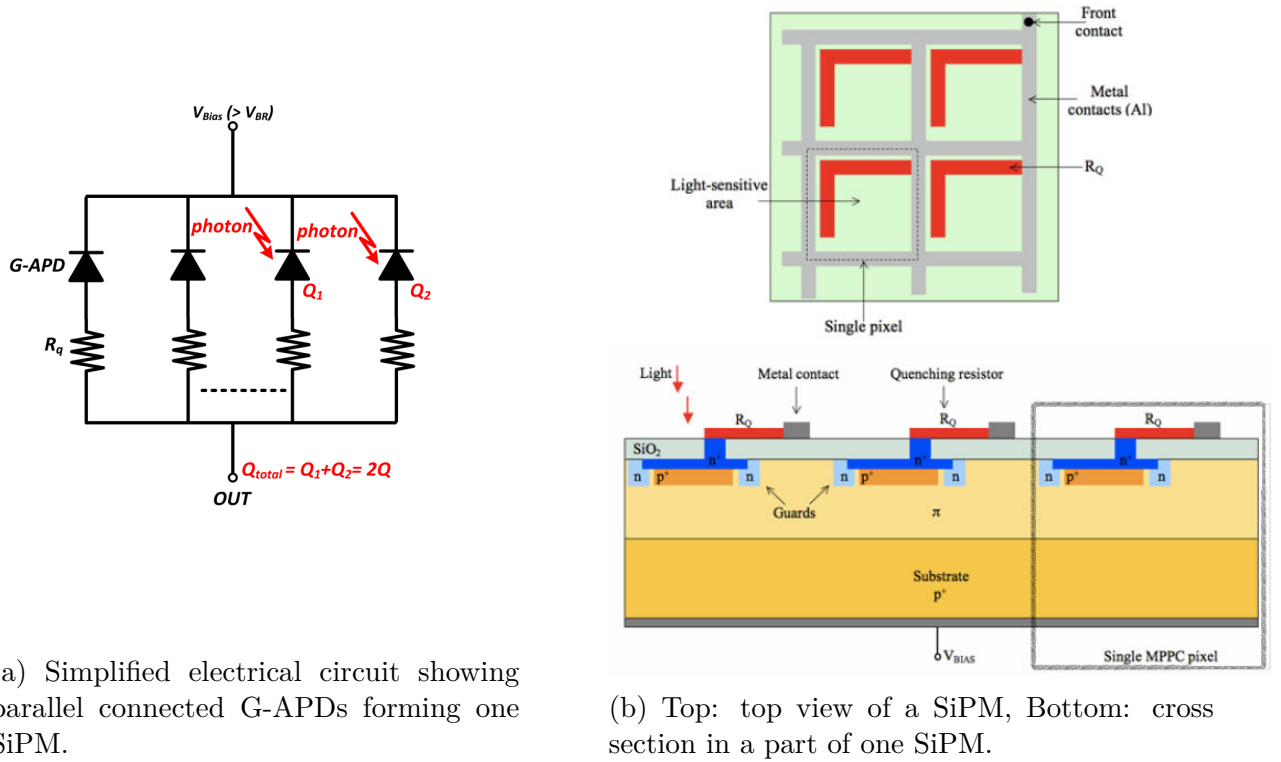


Figure 2.10: SiPM structure: Source: http://www.hamamatsu.com/us/en/community/optical_sensors/tutorials/physics_of_mppc/.

This arrangement is helpful in order to overcome the fact that the output signal is independent of the number of input photons in a single G-APD. In the SiPM and since all G-APDs (micro cells) are connected in parallel, their output pulses will superimpose on each other creating a large pulse. All micro cells produce identical pulses when receiving one photon (Fig.2.11). Measuring the height of the resulting pulse refers to the number of detected photons as illustrated in Fig.2.12a. Another method is the charge measurement that uses the relation between the number of photons and the number of fired cells as described by Eq.2.4, Eq.2.5 and Fig.2.12b.

$$Q_{out} = C * \Delta V * N_{fired} \quad (2.4)$$

$$N_{fired} = N_{total} * \left[1 - \exp\left(\frac{-N_{photon} * PDE}{N_{total}}\right) \right] \quad [49] \quad (2.5)$$

Where, C is the capacitance of one individual micro cell, N_{fired} is the number of the G-APDs that detect photons. Very essential issue should be in mind here. Number of incident photons must be smaller than the total number of micro cells. Otherwise, more than one photon could enter individual micro cells and the linearity of the PDE will be damaged. By this SiPM photodetector makes an analogue device from an array of digital devices.

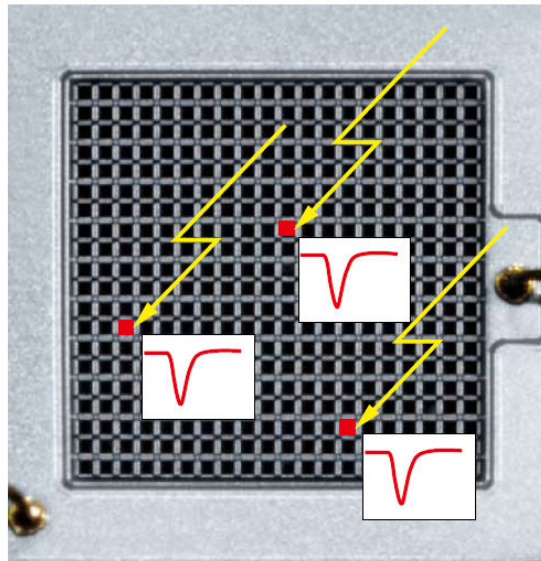
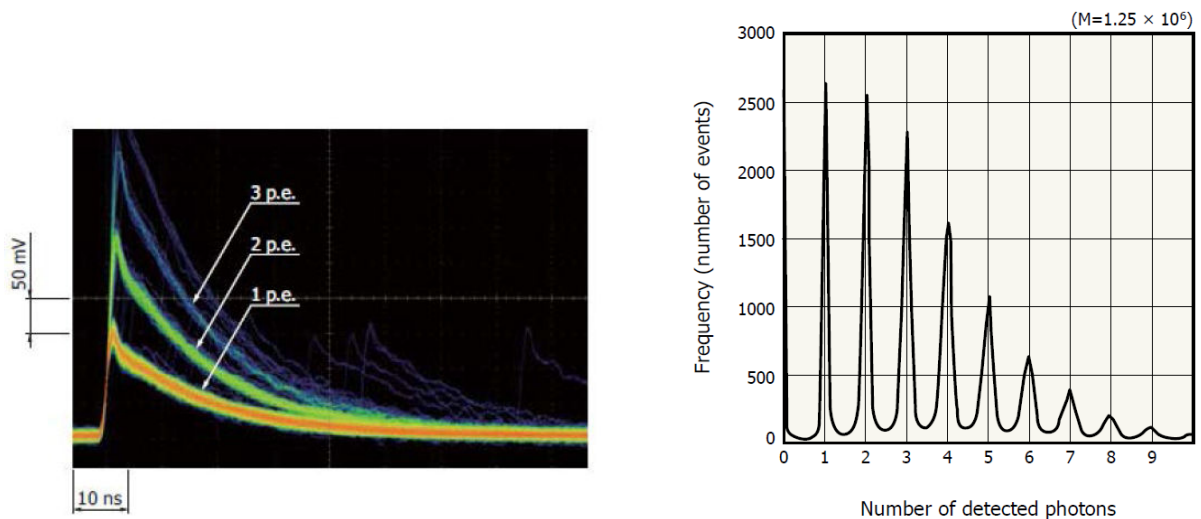


Figure 2.11: Photon counting with a SiPM[50].



(a) Photon counting by measuring pulse height. (b) Photon counting by measuring the charge.

Figure 2.12: Methods for estimating number of detected Photon by a SiPM[50].

SiPM was found to have a fast response (some hundreds of pico seconds). And the average time resolution was found to be some hundreds of pico seconds for one photoelectron signal (Hamamatsu MPPC has $\sigma \simeq 260 ps$, while in [51], they found $\sigma_{1pe} \simeq 600 ps$ for a SiPM of 3600 micro-cells).

Another aim of making one SiPM as the combination of several G-APDs is to fabricate a wider photodetector. It is well known that thermal noise increases exponentially with surface[52]. The DCR is the most important noise factor in the SiPM. Thermally generated electron or hole can trigger an avalanche[48]. This means that one single detector of large surface suffers from noise. In this case, the background noise count (i.e, the dark count rate) may not allow the detection of single photon events.

Connecting small diodes in parallel to form a wide one device avoids noise increment. Nevertheless, its active detection area still depends on the form and size of individual diodes. Active area¹² of the SiPM varies between 30% and 80% and its improvement is still an important field of research. One SiPM has a surface of about 1mm^2 optimized for the limitation of the dark current[48], and even recently SiPM can also be of $3 \times 3\text{mm}^2$ or $6 \times 6\text{mm}^2$ while an individual photodiode (micro cell) could be of different sizes (e.g, $10 \times 10\ \mu\text{m}^2$, $25 \times 25\ \mu\text{m}^2$, $50 \times 50\ \mu\text{m}^2$, $100 \times 100\ \mu\text{m}^2$). Dead spaces between photodetectors in a Cherenkov telescope camera can be reduced by using light concentrators (as mentioned in section.1.5.2). Light concentrators (e.g, Winston cones) increase the effective photon collection area of the detectors and hence they help to obtain a lower energy threshold.

2.5.1 SiPM industrial variety

Since its invention in the 1990s in Russia, SiPM photodetectors are being fabricated and developed world wide by different companies and laboratories. Some are MePhi/Pulsar in Russia, Hamamatsu in Japan, Sensl in Ireland, RMD in USA, Excelitas USA, FBK-Advanced SiD in Italy, ST microelectronics in Italy, Philips in Germany.

Each foundry produce several forms (linear, square)and sizes of the SiPM photodetectors. They use different technologies and structures, different number of micro cells and different fill factors. Thus the performance of the same size SiPM differs according to its fabricator.

The most heavy in the market is the Japanese company Hamamatsu that covers almost 70% of the market need in both PMTs and Solid state photodetectors.

2.5.2 Multi-pixel Silicon photo multiplier (SiPM matrix)

In order to widen further the photodetection area, an array of several detectors of the type SiPM was built. These individual SiPMs will be connected on one electrode cathode or anode while the other electrode forms the individual output terminal. The array geometry may provide position information that could not be obtained from single SiPM. There exist two types of such arrays discrete and monolithic.

Discrete SiPM matrix is formed by putting several independent SiPMs together in some form. While in monolithic matrix, all individual SiPMs share the same Si substrate. The main advantage of the monolithic array with respect to the discrete one is the effective detection area. Building a discrete array is easy and the uniformity of voltage parameters (bias voltage and breakdown voltage) is better controlled. However, it suffers from a significant dead space dedicated to wire bonding pads between adjacent active areas. This problem is solved in monolithic arrays since the wire bonding pads are built at the edge of the chip. Trace lines become longer (i.e, output current signals follow longer paths to propagate between the pixels and the output) and their impedance is hence greater (more recovery time). As a consequence, time resolution of monolithic array is damaged¹³. In monolithic array, wafer quality and process conditions play an important role in the

¹²The ratio of the active area size of a pixel to the pixel size including circuits is called *the fill factor*[49]. It is also known as *the geometrical efficiency*.

¹³In 2014, Hamamatsu announced an effective photosensitive area of up to $3 \times 3\text{mm}^2$ for its 4×4 SiPM array. This was achieved by using the through-silicon vias TSV to minimize non sensitive portion around the sensitive area.

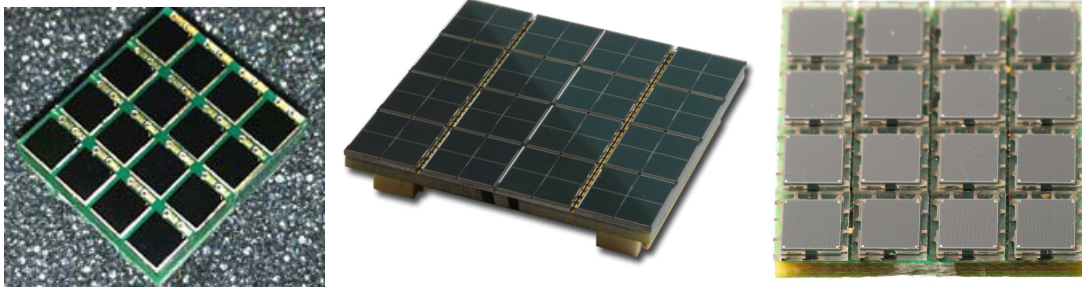


Figure 2.13: Discrete SiPM arrays (fabricated by from left to right: Hamamatsu, FBK, Sensl). Pixels are assembled on a printed circuit.

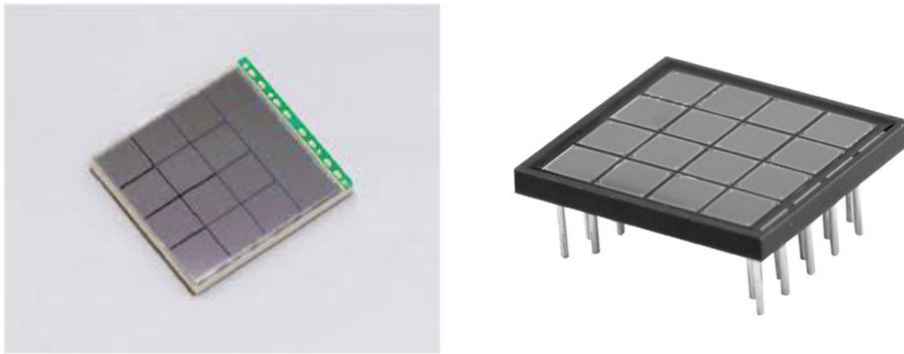


Figure 2.14: Monolithic SiPM arrays (left form Hamamatsu, right from Sensl). Pixels are integrated on the same substrate.

voltage (breakdown and bias) uniformity. All these constraints could be improved by ameliorating the characteristics uniformity within individual pixels as explained in [53].

Such multi pixel arrays of SiPM have very wide applications in various domains where wide detection area is an important aspect (e.g, in medical imaging and astrophysical instruments). Even if the SiPM array form is already exploited in some scientific fields, it is still a premature technology that needs further development in what concerns its crosstalk, dark count rate (DCR), and performance dependency on temperature. The resulting image is promised to have high quality as the independence of each pixel ameliorates.

2.5.3 SiPM in astrophysics instruments

Even though of high gain and high photo detection efficiency (PDE), PMTs actually used in high energy gamma-ray telescopes show a group of drawbacks: Their need for a stable high voltage power supply, their sensitivity to even weak magnetic fields, being easily damaged by high light levels, their limited QE (limited possibilities to further increase QE) and their expensive production techniques. This made them in competition with the emerging solid state detectors that provide higher PDE, operate at lower voltages, show robustness toward both high light levels and magnetic fields. A complete review of the advances in solide state photodetectors was published in 2009[36]. Since then, industry continued to develop new techniques and solutions for enhanced performance.

The first G-APD Cherenkov telescope (FACT) project was born in the aim of exploring the feasibility of replacing PMTs by using G-APDs in Imaging Air Cherenkov Telescope

(IACT). A prototype camera was built. The prototype was based on a camera composed of 144 G-APD in groups of four that makes 36 pixels. This prototype camera has managed the strong dependency of the G-APDs on temperature by using a feedback system that continuously tracks temperature changes and compensates with adapted bias voltage. The first observation of air showers with this prototype was reported in 2009[25][54][55].

As a consequence, the full camera of FACT was constructed with a hexagonal array (Fig.2.15) of 1440 SiPMs (characteristics in Table.2.1), with a feedback system that stabilizes the over-voltage against the effects of both temperature and background light changes[56].

After the preamplifier stage, signals are buffered in the switched capacitor array of the Domino Ring Sampling chip (DRS4). The trigger decision is made upon a signal over threshold logic. This first level of triggering is done over sum signals of nine-pixel patches each. Then a global OR operation is applied to these trigger signals in order to generate the final trigger signal of the telescope FACT[56]. A trigger signal will stop writing to the ring buffers and data will then be digitized by an external ADC.

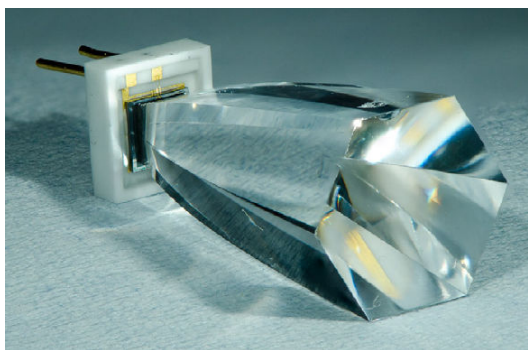


Figure 2.15: [56]

Parameter	Value
Sensitive area	$3 \times 3 \text{ mm}^2$
Number of cells	3600
Cell size	$50 \times 50 \mu\text{m}^2$
Dark count rate	5-8 MHz
Crosstalk probability	$\sim 10\%$
Photon detection probability	$\sim 33\%$
Operation voltage	70-72 V

Table 2.1: [56]

Table 2.2: Left: One pixel of the FACT camera. We can see a hexagonal entrance window of the light guide that concentrates light onto the square sensor. Right:Parameters of the SiPMs chosen for the FACT project: Hamamatsu S10362-33-050C[56].

Since October 2011, FACT operates at the Observatorio del Roque de los Muchachos. Datataking continues during dark nights up to full moon nights without any problems or modification to the datataking routine[4].FACT camera makes proof of the merit of G-APDs as a great option for the future CTA project since they have shown easy handling and stable operation. They essentially afford continuous (full observation time 24/7) monitoring of even brightest sources on long term[5].

2.6 4×4 SiPM matrix characterization

In order to verify the commercial performance of the multi-pixel SiPM and to decide whether it can be useful for the camera of the large telescope of CTA, we have been holding characterization tests on a sample composed of an array of 16 macro pixels (SiPMs). These tests are the first step in the project of this thesis. Their main purpose is to study the effect of bias voltage on gain and to define gain characteristics of the SiPM array. It will

lead to extract the specifications and priorities that our new front end electronics must respect.

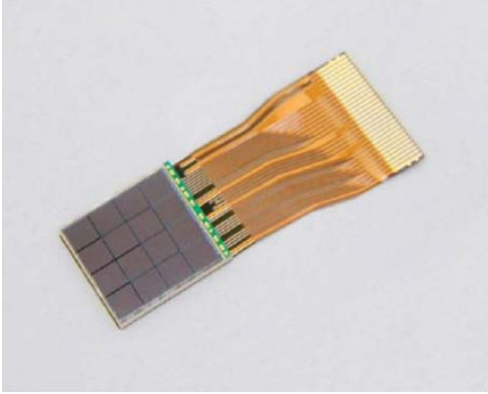


Figure 2.16: SiPM array under test.

Parameter	Value
Number of elements	16 (4×4)
Effective active area/channel	$3 \times 3mm$
Pixel pitch	$50 \mu m$
Number of pixels/channel	3600
Number of pixels/device	57600
Fill factor	61.5%
PDE for $\lambda = 440 nm$	50%
Dark current/channel	$3 \mu A$
Terminal capacitance/channel	$320 pF$
Gain	$7.5 \cdot 10^5$

Table 2.3: Specifications of the tested array.

Table 2.4: Source: Product information of *Monolithic MPPC array with FPC (S11829-3344MF, S11830-3344MF)*.

The matrix under test is a monolithic 4×4 square-form matrix from Hamamatsu depicted in Fig.2.16 whose specifications are listed in Table.2.3. Product reference: *S11830-3344MF* with FPC¹⁴ of $5cm$ large. It consists of 16 pixels that we call macro pixels. Each macro pixel is a SiPM that has an effective area of $3 \times 3mm$ and is formed by 3600 G-APDs connected in parallel. Each G-APD is a 50μ pitch and hence called micro pixel.

The sixteen macro pixels are connected to power supply by their common cathode, while each individual anode drives each macro pixel's signal to the external circuit represented by the front end electronics.

We consider for our application a dynamic range about 2000 photoelectrons over the whole matrix. *This means 125 pe per one macro pixel.* According to the large number of micro cells inside one macro pixel (3600 cells per macro pixel) and considering the proportionality condition between the number of incident photons N_{photon} and the number of cells N_{total} ($N_{photon} \ll N_{total}$), each SiPM could linearly achieve the required dynamic range. The front end electronics should then be able to cover signals due to number of incident photons ranging from one photon up to such wide dynamic range. It will be also necessary to pay attention to the big capacitance ($320 pF/macro\ pixel$) of the device when tailoring the readout electronics.

2.6.1 Test bench

A test bench has been used to characterize this matrix. It is depicted in Fig.2.17 and Fig.2.18. This test bench was used to characterize the PMTs for HESS-I experiment[57]. SiPM output signal is positive while that of a PMT is negative. The test bench was then modified to meet the needs of SiPM tests.

Test bench consists of a dark chamber that contains the photodetector and the electronic system. All power supplies and control instruments are outside the dark chamber.

¹⁴FPC stands for Flexible Printed Circuit which is the connector type.

The SiPM matrix is included in a box that is shown in Fig.2.17a. FPC connector passes through the box leading power supply to the matrix and driving the 16 output signals to an electronic interface. In this first discrete electronic circuit, amplification and inversion stages are included. Signals are amplified by $G_{interface} = -4$ ¹⁵. The circuit scheme is drawn in Fig.2.17b). The purpose of this stage is to reshape signals so they have an adequate form compatible to HESS-I acquisition system.

Shown in Fig.2.18a, two identical acquisition electronic boards digitize the 16 signals (8 channel/board) and send them to a Labview program outside the dark chamber. A light emitting diode (LED) that gives light around blue ($\lambda = 450nm$) is used to simulate Cherenkov light. The LED is controlled by a pulse series of $300Hz$ and $5ns$ wide in order to synchronize it with the measurement window. A fiber optic is used to guide light to the SiPM box inside the dark chamber.

Data acquisition Considering one acquisition channel, input signal is sent to two sub channels of different gains ($G_{HG} = 72.7$, $G_{LG} = 5.3$)[57]. This gain duality helps to measure small signals as well as large signals and thus to manage a wide dynamic range. Plus, signal on the high gain is also derived to a discriminator of programmable threshold in order to contribute (if it passes the threshold) in the generation of a trigger signal.

Signal processing includes sampling at $1GHz$, storing samples in the analog memory, reading analog memories, digitizing (12-bit analog to digital conversion) and then ADC outputs are stored in a *first in, first out (FIFO)* register. Data are then transferred to Labview computer that forms data files before analyzing them with C++ codes via ROOT platform.

Reading Analog Memories Analog Ring Sampler (ARS) is a front end ASIC that was designed for PMT signal processing for the ANTARES detector¹⁶. It contains 4-channel, 128-memory-cells, $1GHz$ sampler (i.e, sample duration is $1ns$). Samples are written at the place of those from the precedent cycle[58]. It was used for HESS-I telescopes[57]. When a trigger signal arrives, the storage into analog memories is stopped after some time equivalent to stopping at the cell of the order $(128 - N_d)$. This means that only N_d previous samples will be kept from the precedent sampling cycle. N_d was adjusted so that the signal is at the center of the reading window in order to avoid loss[57]. And only samples in the N_L cells are read at $1MHz$. N_L is defined as the time window during which we read analog memories and this time should be superior to FWHM of the signal. It shouldn't be that much to avoid integrating noise in the signal¹⁷. N_L value is set to 16 as pointed out in [57].

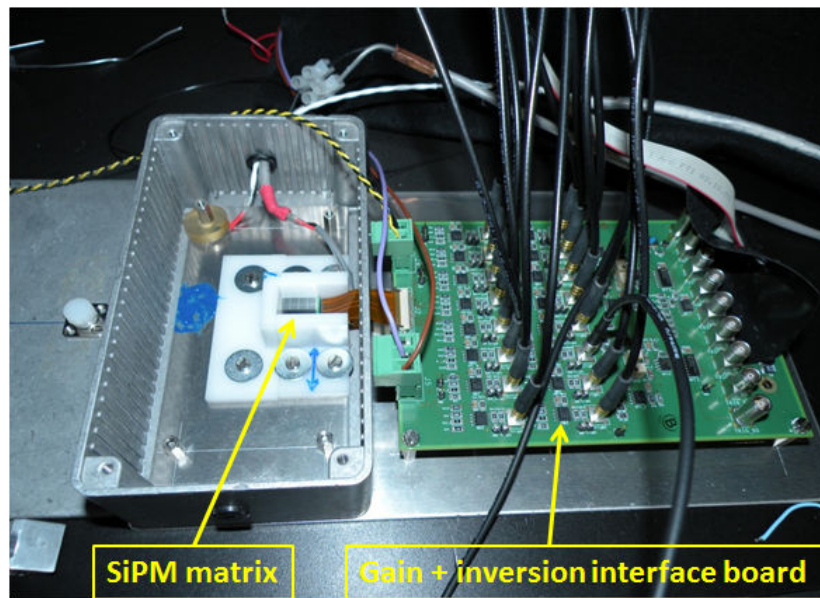
For sixteen macro pixels of two channels each (high gain and low gain), we need 32 channels of analog memory. Each analog memory has $N_{ch/AM} = 4$ channels[58]. So we need 8 analog memories, this means $N_{AM/board} = 4$ analog memories per acquisition board.

Reading analog memory channels in one board is done in parallel and that can be accomplished in two modes. Either summing N_L samples per channel and thus reading

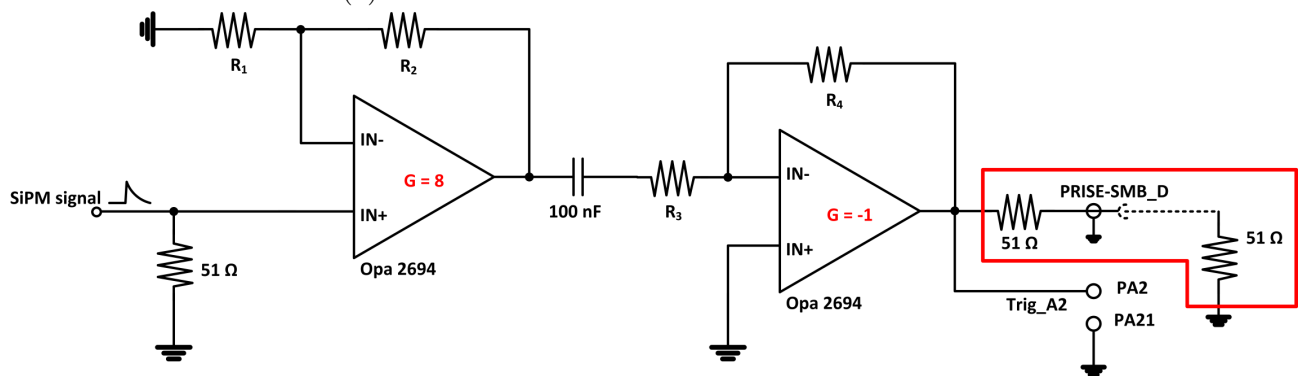
¹⁵In theory, this interface circuit has a gain of about -10 , however, gain measurement has shown a gain of -8 . The signal divider formed by the two 51Ω resistors gives half the signal at the output. Which makes a total gain of -4 .

¹⁶ANTARES used a developed version of the chip: ARS1.

¹⁷ N_L should be of suitable value so that to insure having the interesting signal in the cells we read.

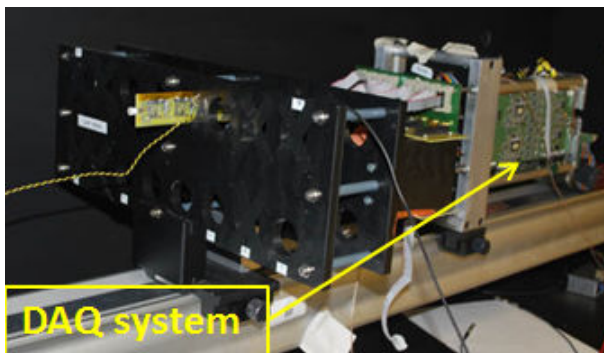


(a) SiPM box with the electronic interface.

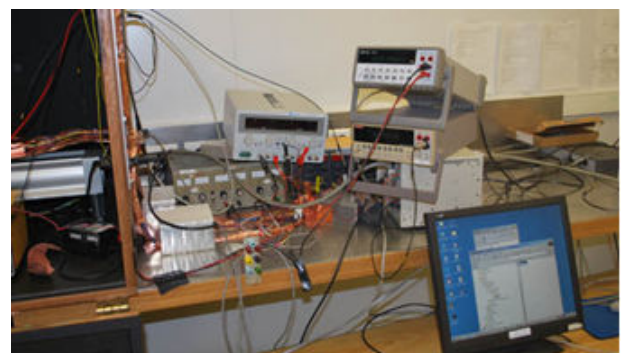


(b) Electronic scheme of the interface circuit. We recognize the measured gain with the potential divider on the output.

Figure 2.17: SiPM characterization test bench (I).



(a) The acquisition system of HESS-II.



(b) Power supply and Labview control.

Figure 2.18: SiPM characterization test bench(II).

the charge per channel, or reading the whole N_L samples of each channel. The second mode is slower than the first one since each reading cycle we read $N_{AM/board} * N_{ch/AM} * N_L$ samples. If one sample time is $1ns$ this means $16 N_L = 256 ns$. While in the first mode we need only $N_{AM/board} * N_{ch/AM} = 16 ns$.

Digitization As for the analog to digital conversion, the full dynamic range of the ADC is $5V$ with $12 - bit$ resolution. This means that an ADC channel (or also called ADC count) corresponds to what we call *ADC conversion factor*:

$$V_{ADC} = LSB = \frac{5}{2^{12}} = 1.22 mV \quad (2.6)$$

Slow Control (SC) Fig.2.19 shows Labview program interface where we choose the test to hold (over voltage variation, temperature variation, light flux variation) and where we control test's parameters (initial, final values and the step). Fig.2.19 shows the interface of the Labview program. Test type and all its parameters are controlled via this interface.

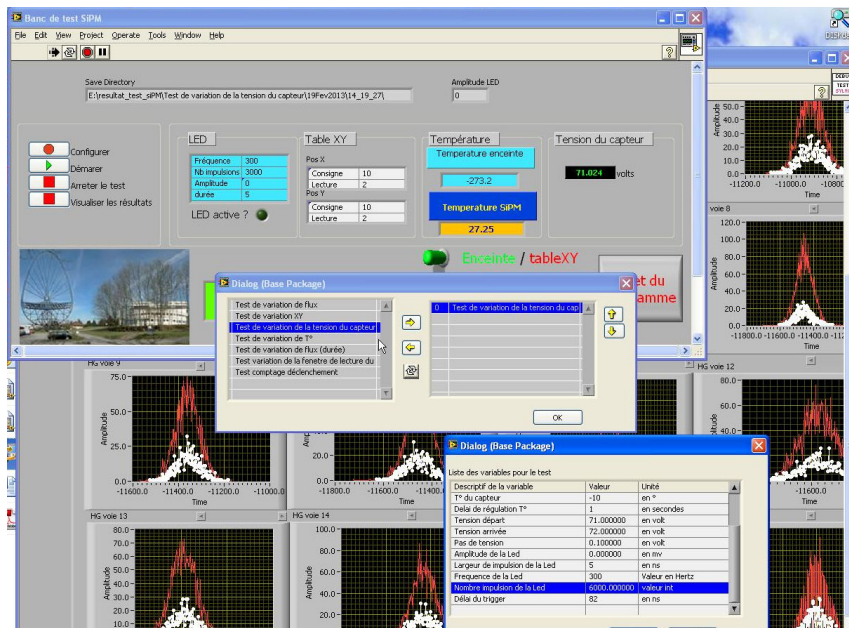
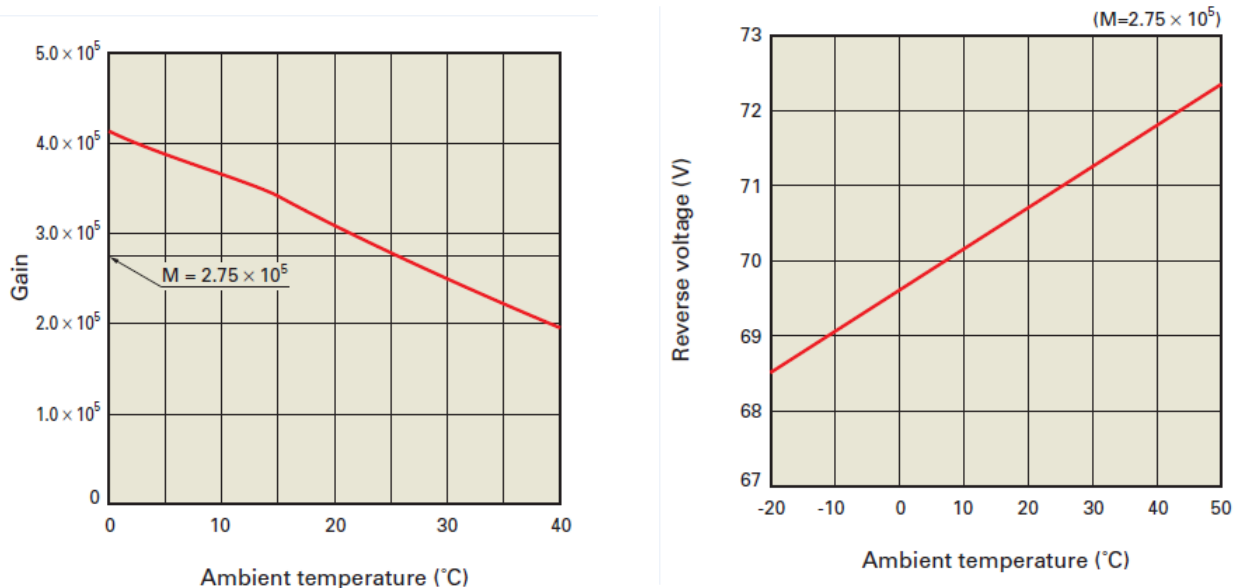


Figure 2.19: Example of test configuration via labview interface.

This program communicates with a FPGA on each acquisition board and thus organize the acquisition process. All tests that follow have the same purpose of studying the gain in a monolithic array of SiPM. The elements that can affect gain stability or uniformity are also investigated.

2.6.2 Temperature Measurement

G-APD characteristics (gain, photodetection efficiency PDE, dark count rate DCR, crosstalk, ...) depends on the applied over voltage that depends on the breakdown voltage which is in turn relative to temperature. Hence, SiPM photodetectors is found to be sensitive to temperature as depicted in Fig.2.20b and Fig.2.20a. Adjusting bias voltage could compensate gain dependency on temperature. It is then trivial to define an optimal over voltage compatible with the operating conditions including temperature so that a sufficient gain is obtained.



(a) Gain vs temperature at constant voltage.

(b) Reverse voltage vs. ambient temperature at constant gain ($G = 2.75 \times 10^5$).

Figure 2.20: Temperature characteristics of one SiPM[49].

Temperature sensor is inserted inside the SiPM box so that temperature measurements are recorded during the tests. As seen in Fig.2.21 temperature rises of about 1°C at most during these tests.

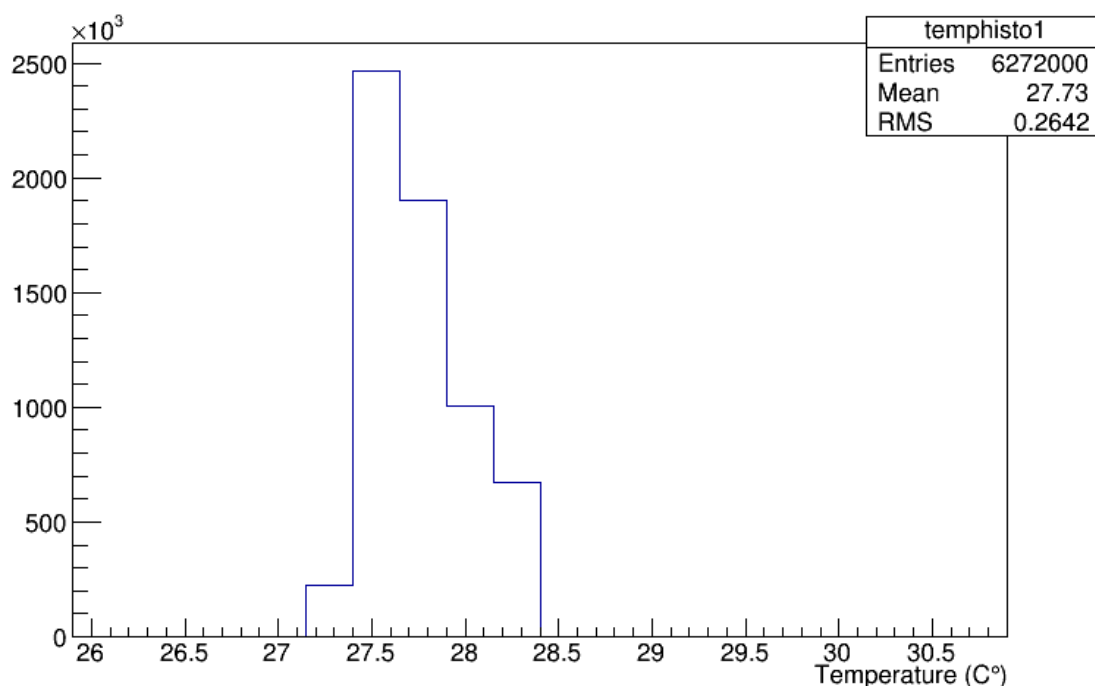


Figure 2.21: Temperature variation measurement during tests.

In general, temperature affects the breakdown voltage of the SiPM leading to gain fluctuations. Usually, cooling techniques are used to compensate this effect. From this viewpoint, cooling dispenses could be put away simply through controlling bias voltage so that to keep a stable over voltage and hence a constant gain.

2.6.3 Pedestals

The first test was done in dark, Fig.2.22 and Fig.2.23, show the distribution of the total charge measured respectively on high gain and low gain when SiPM array is in dark with no incident light. These signals, called pedestals, are due to noise.

Taking the distribution of the pedestal of one SiPM, the mean value is the position of the pedestal that represents the electronic bias (i.e, base line). The width of the distribution is due to fluctuations in the base line because of noise, i.e, pedestal RMS depends on the read out electronics. In general, two main actors contribute to noise in such systems that are: the readout electronic circuit noise and the background noise (from night sky background) detected by the SiPM. These two types of noise are not correlated. However in our case, electronic noise is permanent and dominant since the SiPM array is put in the dark room (the background noise is negligible). Pedestals here are due to the electronic noise.

Spectra of Fig.2.22 and Fig.2.23 also show a very good performance of the SiPM in terms of dark count rate since no distinguished peaks exist after the pedestal.

Pedestals can be recognized in tests with light as the first peak of events in the spectrum as shown in Fig.2.24.

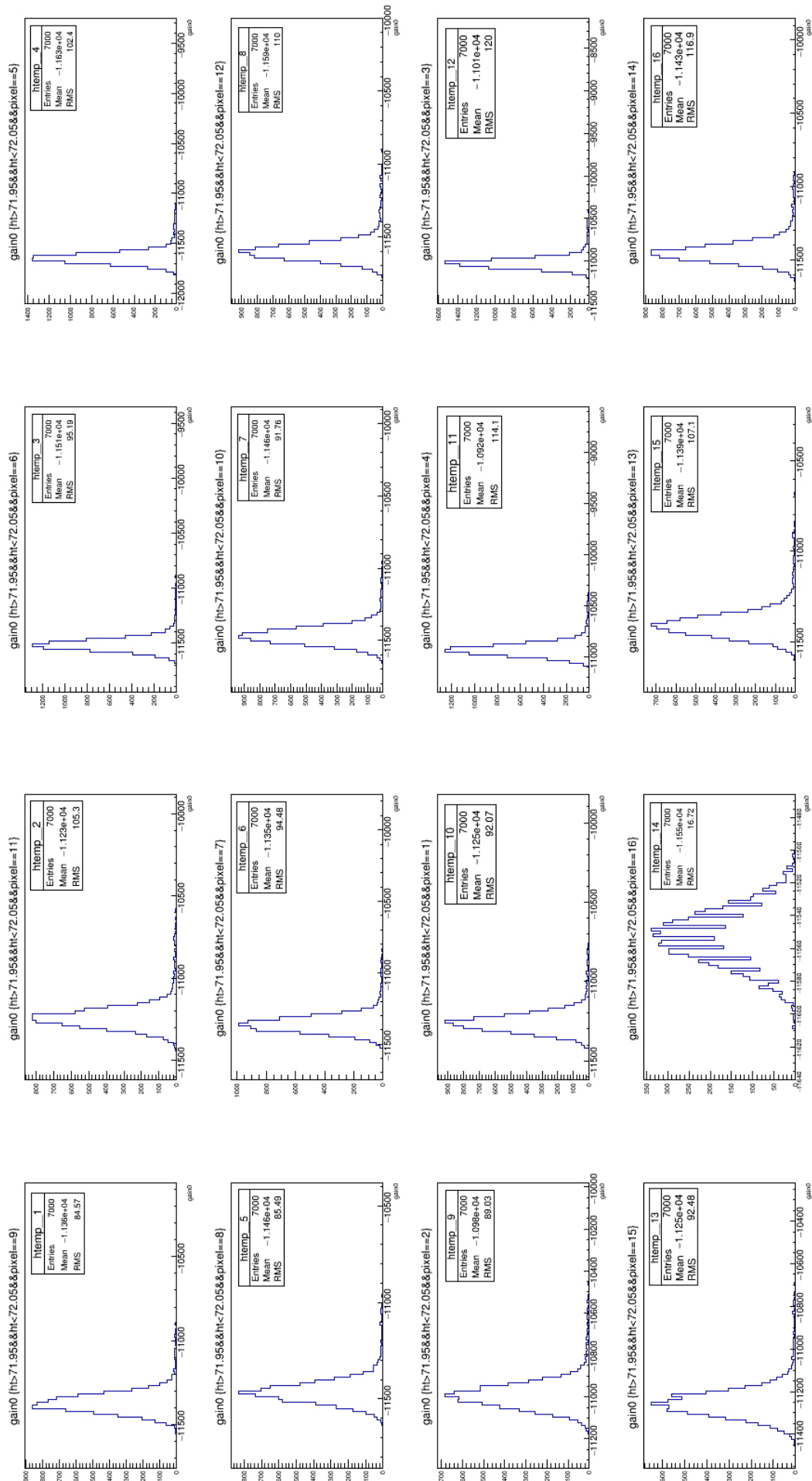


Figure 2.22: Pedestals measured on the high gain of each SiPM of the array (for 15 macro pixels). Pixel number 16 was connected to the oscilloscope which explains its distribution.

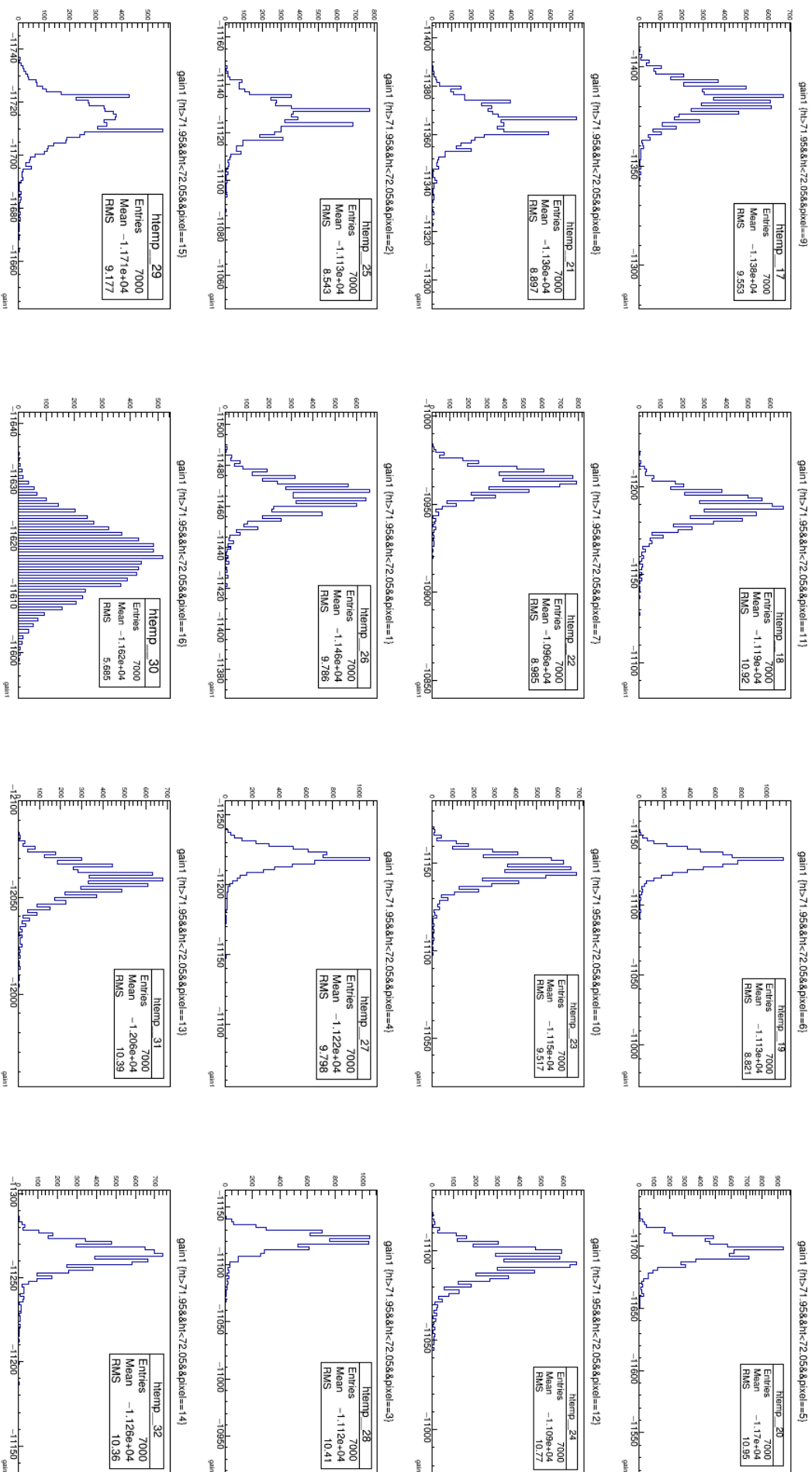


Figure 2.23: Pedestals measured on the low gain of each SiPM of the array (for 15 macro pixels). Pixel number 16 was connected to the oscilloscope which explains its distribution

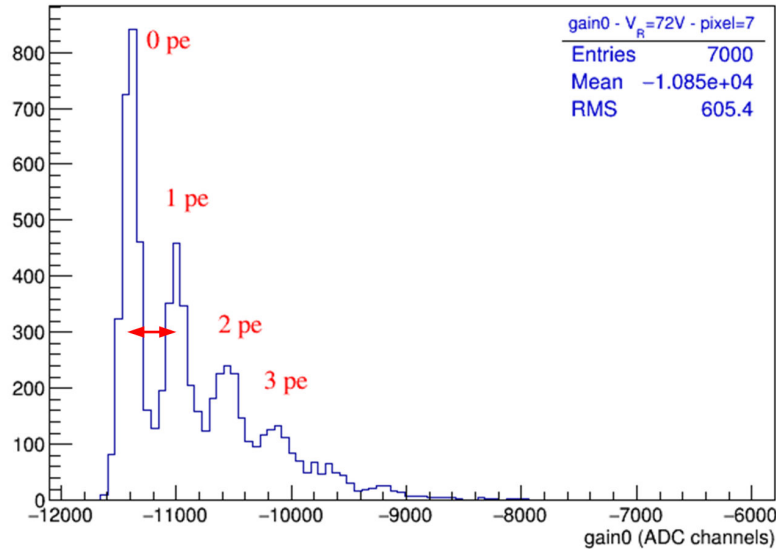


Figure 2.24: Charge spectrum of one pixel biased with 72V measured on the high gain: LED was controlled by a pulse of 2.35 V amplitude, 5 ns width with repetition of 300 Hz. We can see the pedestal represented by the 0 pe peak, the peaks of the single photo electron, two photo electrons, three photo electrons, respectively. The red arrow points out the position of the single photo electron in respect to the pedestal.

Signal of the SiPM under light In addition to the electronic base line and noise, other information can be extracted from the spectrum of one pixel (Fig.2.24). The distance between the pedestal position and that of the first peak represents the amplitude of the signal due to one photo electron. The signal to noise ratio (S/N) is the ratio of this amplitude to half the width of the pedestal (σ_{ped}). Fig.2.24 shows $S/N \sim 5$ ¹⁸.

The amplitude of the one photo electron signal refers to the system gain including SiPM gain and readout electronic gain. Now the question is how does this amplitude change with over voltage?

2.6.4 Gain variation with over voltage

One SiPM is a dense matrix of parallel connected G-APD. The Geiger mode is triggered when applied reverse voltage passes the breakdown voltage. Geiger gain is a function of the applied voltage. As a consequence, SiPM gain depends on the operating voltage. More precisely, the gain of the SiPM is a function to the so called over voltage (section.2.4.4, section.2.5 and Eq.A.7).

Analyzing output charge spectrum of one SiPM in the previous section (section.2.6.3), we found that information about gain is implicit in the position of the one photo electron peak ($P_{1,pe}$) in respect to that of the pedestal (P_{ped}). Gain dependency on over voltage can be concluded from the shift in the photo electron position as the applied voltage changes.

¹⁸The Fit of this spectrum and the parameters used to find this value of signal to noise ratio can be seen in Fig.2.32.

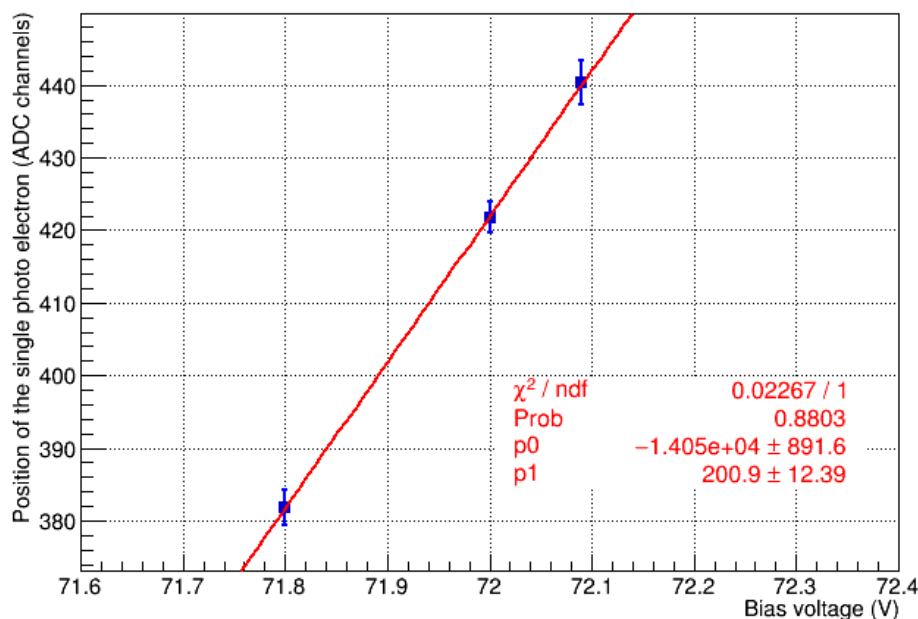


Figure 2.25: Shift of the photo electron peak position as a function of bias voltage for one pixel.

The position of the single photo electron (P_{1pe}) is measured on the high gain for three different bias voltages (71.8V, 72V, and 72.09). The peak is found to move linearly as a function of bias voltage. Break down voltage value is constant during the test since the temperature was constant ($V_{BR} = 70V$ at $T = 27C^\circ$). Photo electron position varies linearly with over voltage by about 40 ADC channel per 200mV as shows Fig.2.25. So one can control SiPM gain by adjusting the applied high voltage.

2.6.5 Optimum operating point

The overall performance of the SiPM depends on its over voltage (section.A, section.2.4.4, and section.2.5). The importance of bias voltage comes from its direct effect on gain as we see in the previous section (section.2.6.4).

One of the power supplies that feed the matrix is fixed to produce 50V and the second in series completes the potential to the value defined by a parameter that is set via Labview.

We are looking for the smallest possible bias voltage that guarantees enough gain to separate signal due to photoelectron from noise.

In these tests we are scanning the bias voltage from $V_{Bias} = 71V$ to $V_{Bias} = 72V$ with a step of $\Delta V = 100mV$ and with test iterations of 7000 events. Tests were hold at room temperature whose average is $\sim 27C^\circ$. Output charge during the reading window is measured for each macro pixel (SiPM) at each bias voltage.

The criterion that will define the optimal operating voltage is the peaks separation. A uniform distance (in ADC counts) between each two successive peaks refers to gain. The distance between the first photo electron peak and the pedestal leads to signal to noise ratio as well.

As an example, Fig.2.26 and Fig.2.27 show the quality of peak separation on both high and low gains for fifteen pixels of the matrix when it is biased with $V_{Bias} = 71.3 V$. The conclusion to consider is that reverse voltage should be higher for the sake of enough gain.

At several bias values, we can distinct several peaks of events at well different amplitudes. $V_R = 72V$ was found to offer good results, according to the conditions above, like illustrated in Fig.2.28 and in Fig.2.29. $V_R = 72 V$ was thus adopted as the optimal operating voltage for the tests that follow. The complete spectra of the array measured respectively on high gain and low gain acquisition outputs for $V_{Bias} = 72 V$ is shown in Fig.2.30.

2.6.6 Gain dispersion among the 16 pixels

The reliability of multi-pixel SiPM array is defined by its homogeneous characteristics. Especially in monolithic array and since we focus on the gain, it is essential to investigate gain uniformity of the array elements (SiPMs).

At $V_{Bias} = 72V$, we are drawing the distribution of the charge generated by each macro pixel. Spectra on the high gain are shown in Fig.2.28, and on the low gain in Fig.2.29 with the absence of one macro pixel which was connected to the oscilloscope. Signal form of the macro pixel sixteen is shown in Fig.2.39. The complete spectra of a 16-SiPM matrix illuminated with less light intensity (LED control pulse is of less amplitude 2V) can be seen in Fig.2.30 at the same reverse voltage $V_{Bias} = 72V$.

We can notice that each spectrum consists of at least two peaks. The first is the *pedestal* that represents the electronic noise (section.2.6.3). The second is the response to the first photoelectron, and the photon counting continues in order (second photoelectron, third, etc...). In this test the whole matrix is illuminated, that is why all pixels have signals. Those whose spectra show more peaks are in the center of spot light emitted by the fiber optic into the matrix box and hence they receive more light intensity.

The position of the first photoelectron peak in respect to the pedestal peak represents SiPM gain measured in number of ADC channels (γ_{1pe}^{ADC}). The gain of an individual macro pixel can be calculated from Eq.2.15 and can be written as.

$$G_{SiPM} = 1713.5 \gamma_{1pe}^{ADC} \quad (2.7)$$

γ_{1pe}^{ADC} can be extracted from fitting the spectrum to a suitable function (Eq.2.8). Each spectrum can be approximated by a combination of a Gaussian distribution (pedestal) and several Poisson distributions (photo electron events). Fig.2.31 shows a fitted spectrum of one SiPM of the matrix with fit parameters.

$$f(x) = \frac{N e^{-\ell} e^{-0.5 \left(\frac{x - \mu_{ped}}{\sigma_{ped}} \right)^2}}{\sigma_{ped}} + \sum_{i=1}^{20} \frac{N_1 N e^{-\ell} \ell^i e^{-0.5 \left(\frac{x - (\mu_{ped} + i\delta)}{\sigma_{pe}} \right)^2}}{i! \sqrt{i} \sigma_{pe}} \quad [57] \quad (2.8)$$

$mu = \ell$ is the height of the first photoelectron peak in respect to the first minimum, it depends on the luminosity.

pedestal = μ_{ped} is the position of the pedestal.

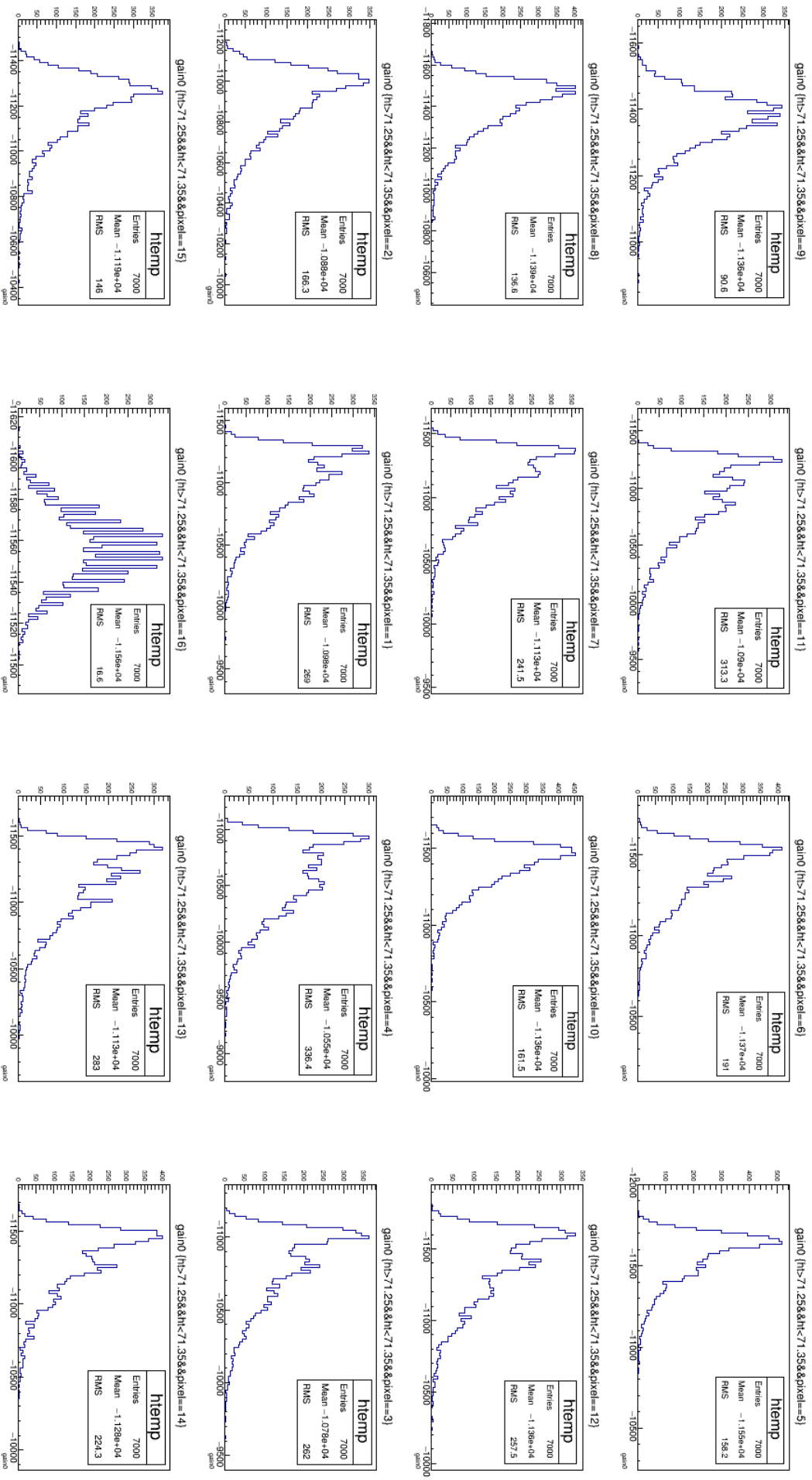


Figure 2.26: Charge distribution measured on the high gain for each pixel. SiPM array was biased at 71.3V and received light from a LED controlled by a pulse of 2.35 V amplitude, 5 ns width with repetition of 300 Hz.

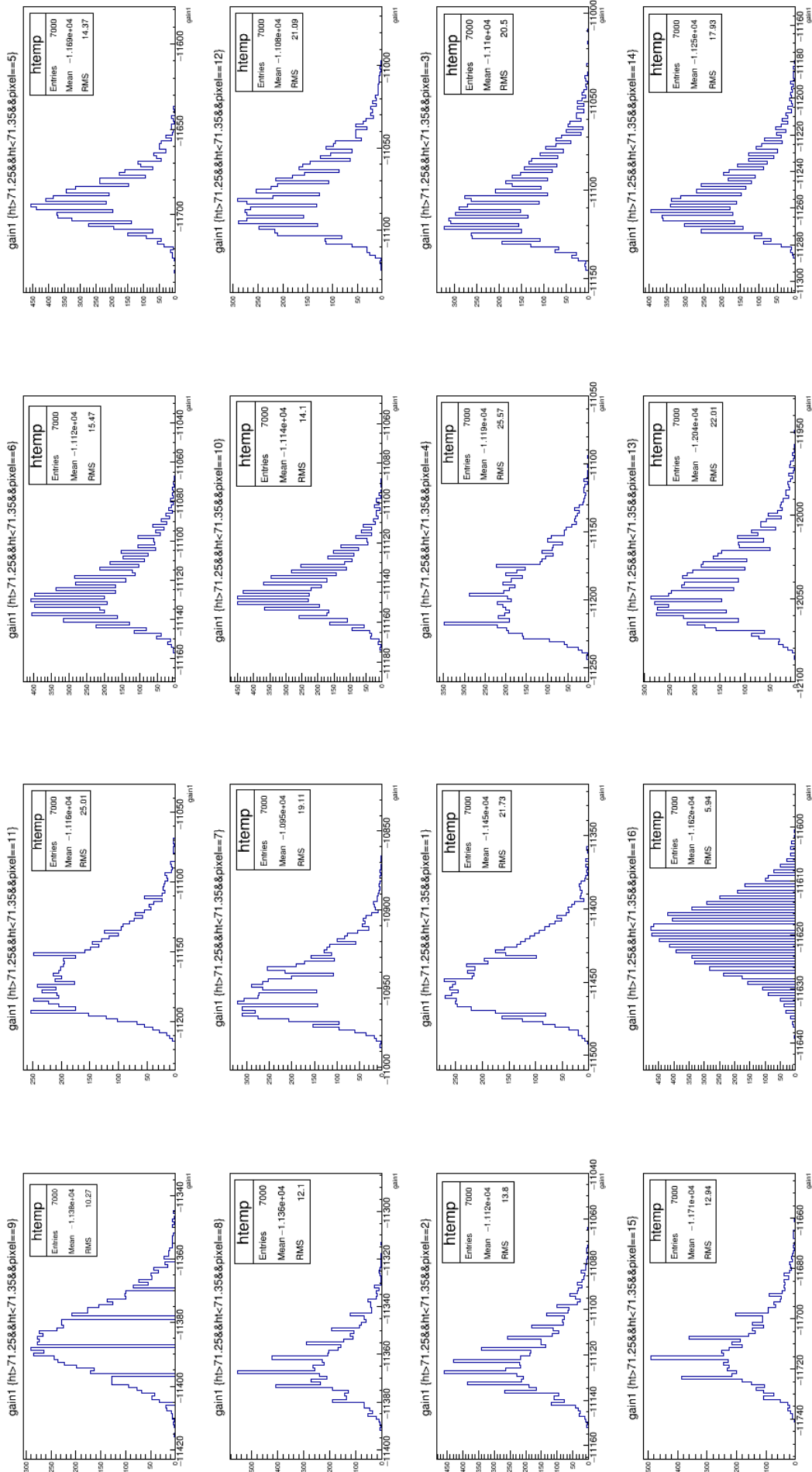


Figure 2.27: Charge distribution measured on the low gain for each pixel. SiPM array was biased at 71.3V and received light from a LED controlled by a pulse of 2.35 V amplitude, 5 ns width with repetition of 300 Hz.

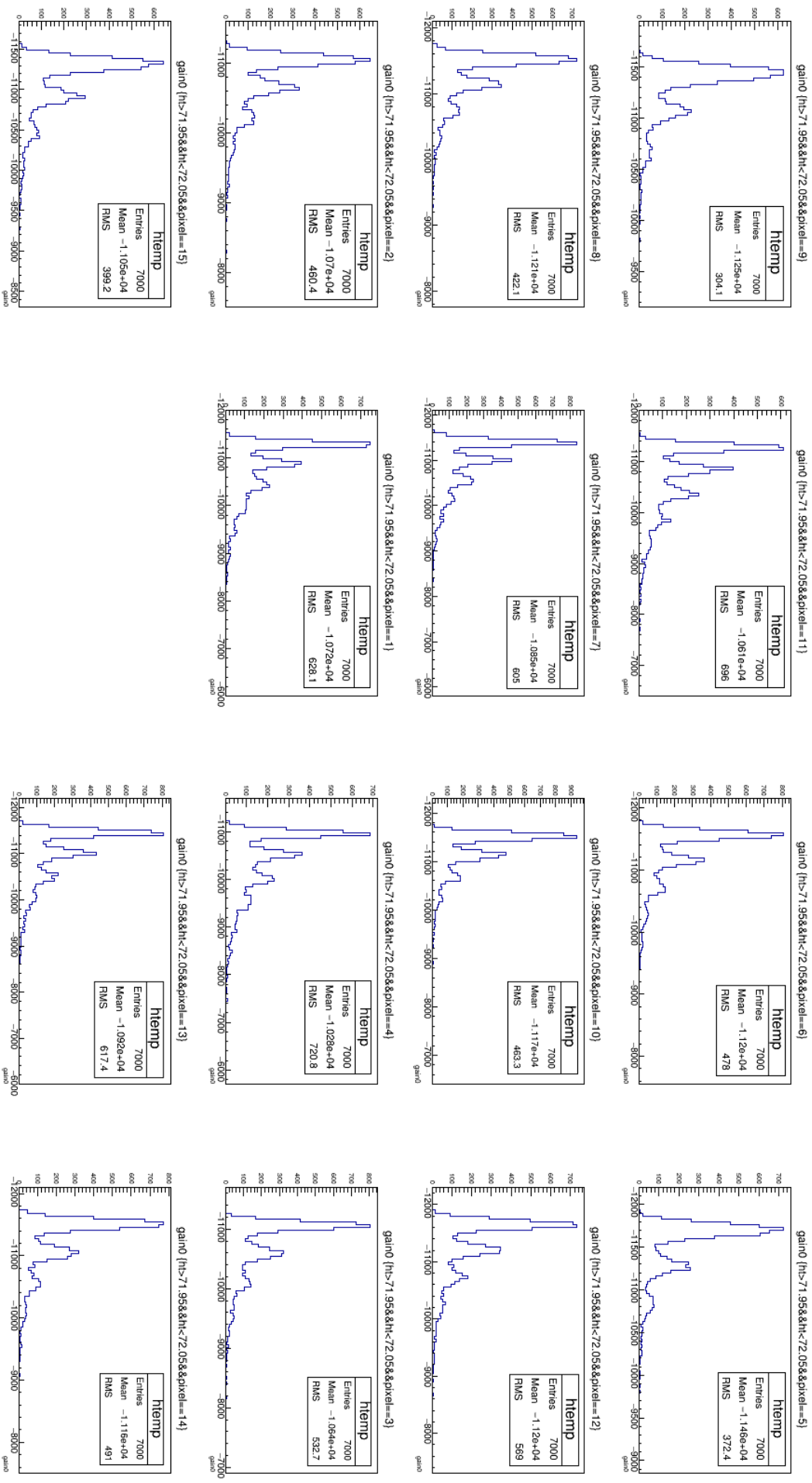


Figure 2.28: Charge distribution, measured on the high gain, of 15 macro pixels of the SiPM array. The matrix was biased at 72V and received light from a LED controlled by a pulse of 2.35 V amplitude, 5 ns width with repetition of 300 Hz. Plots are organized in the same connection order of array elements and readout channels.

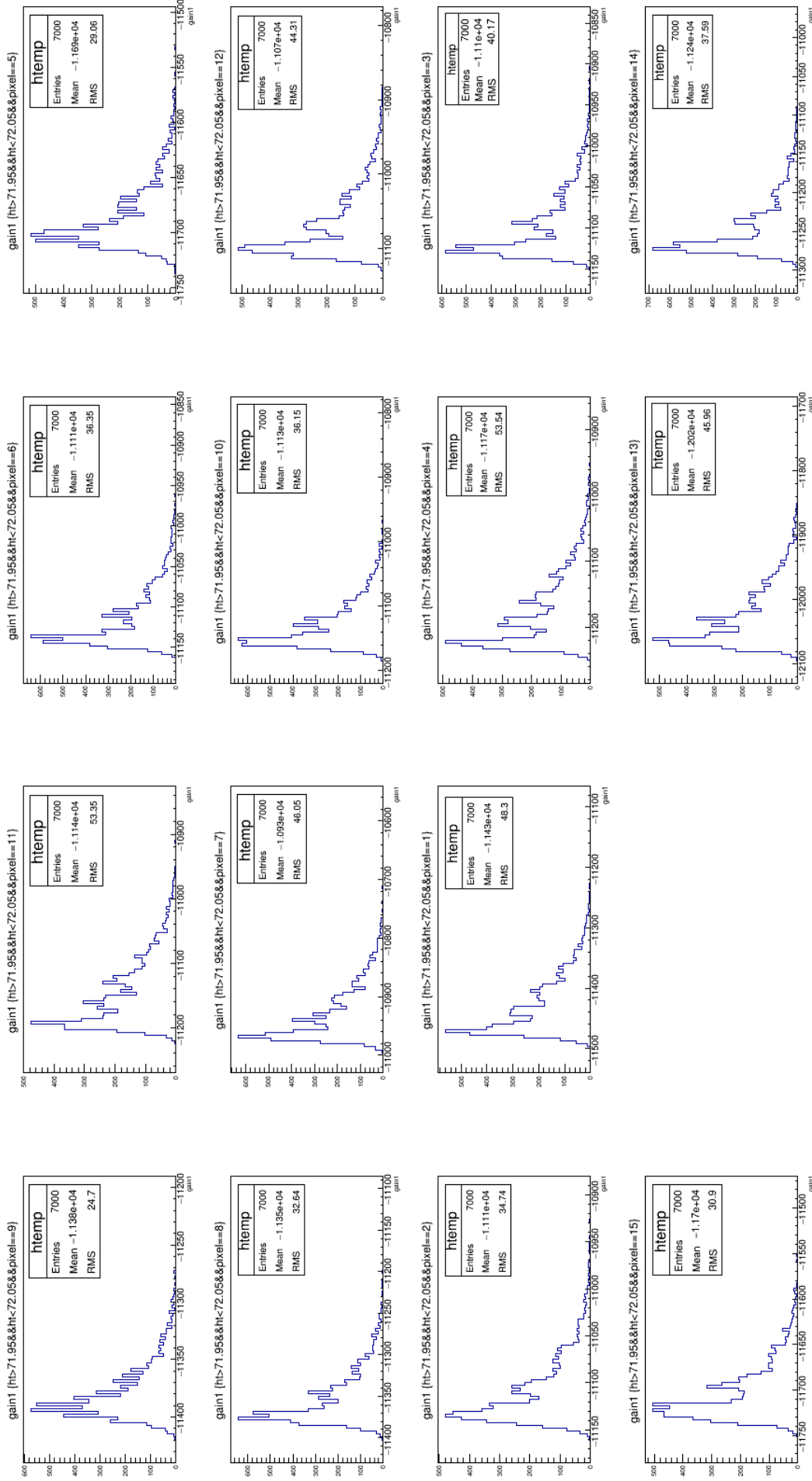


Figure 2.29: Charge distribution, measured on the low gain, of 15 macro pixels of the SiPM array. The matrix was biased at 72V and received light from a LED controlled by a pulse of 2.35 V amplitude, 5 ns width with repetition of 300 Hz. Plots are organized in the same connection order of array elements and readout channels.

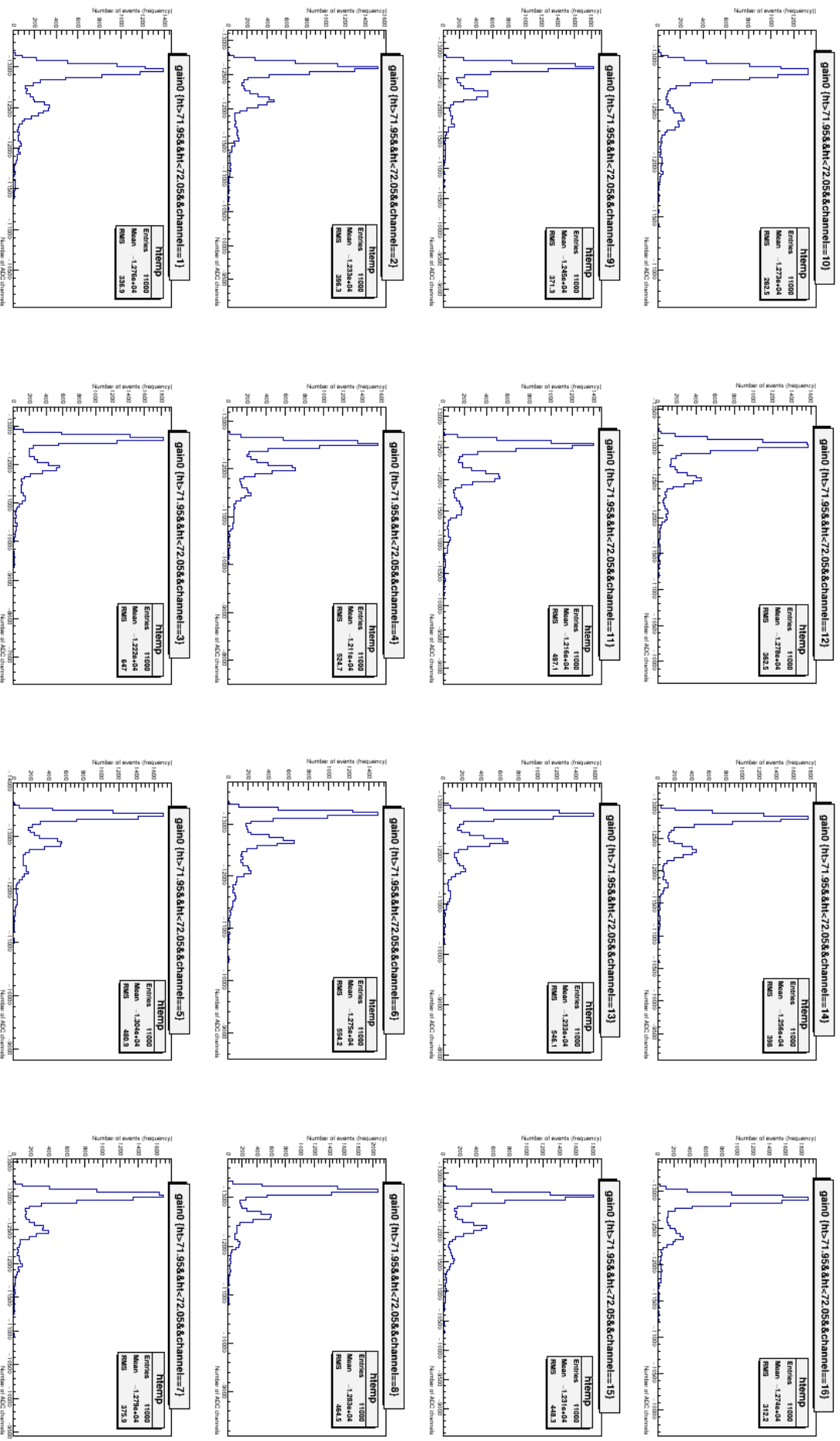


Figure 2.30: Charge distribution of 16 macro pixel of the SiPM array. The matrix was biased at 72V and received light from a LED controlled by a pulse of 2V amplitude, 5ms width with repetition of 300 Hz. Plots are organized in the same mapping of the SiPM array. Less luminosity was applied here that can be noticed from short spectra containing one or two photoelectron peaks at most. Test iterated with 11000 events.

$single_pe = \gamma_{1pe}^{ADC}$ that shows the gain (the distance between the first photoelectron and the pedestal or the amplitude of the output signal in response to one photo electron).

$sigma_ped = \sigma_{pedestal}$ is the standard deviation of pedestal distribution and it represents the electronic noise.

$sigma_gamma = \sigma_{pe}$ is the half width of first photoelectron distribution.

N, N_1 are fit normalization constants. The index i refers to the number of detected photons.

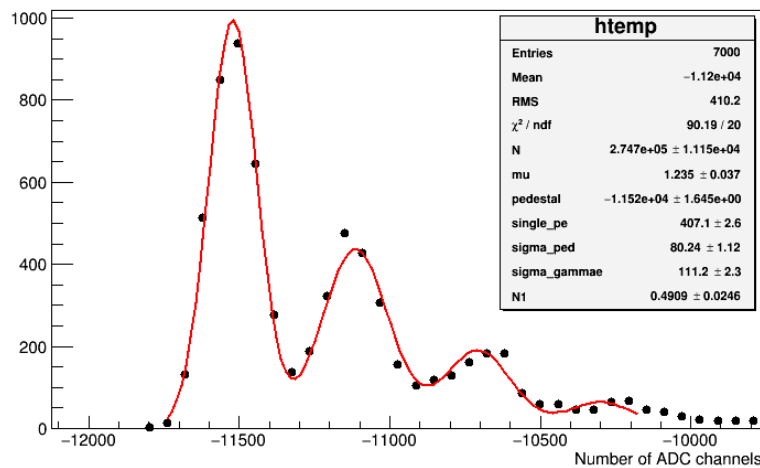


Figure 2.31: Spectrum of one macro pixel approximated to a fit function. Dots are measured data points, continued red line is the fit function.

This same function is used to fit spectra of Fig.2.28 and the result is shown in Fig.2.32.

A main question when talking about an array of SiPM, monolithic in particular, is whether all its macro pixels show the same gain under same environmental conditions (bias, temperature, noise, etc...). To verify gain uniformity among array elements, the distribution of the gain in the array is drawn in Fig.2.33.

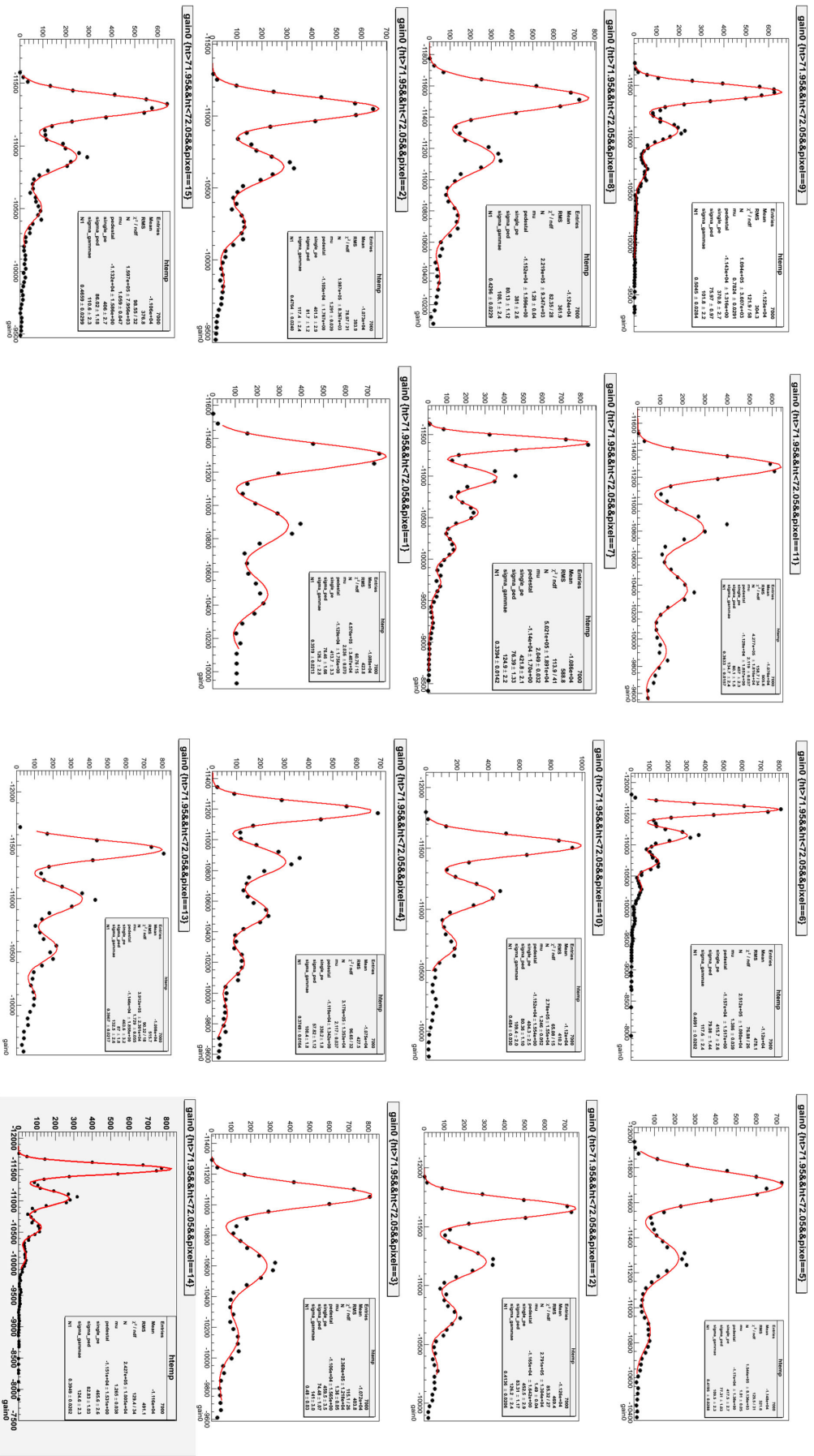


Figure 2.32: Spectra of 15 elements of SIPM array illuminated by blue LED controlled with a 300Hz pulse of 2.3V amplitude and 5ms wide.

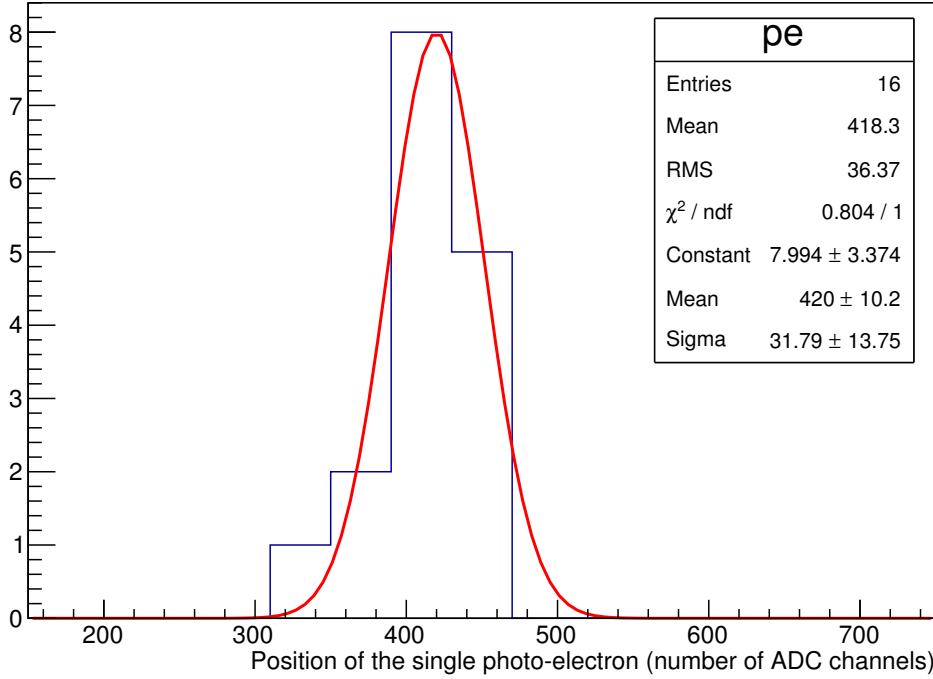


Figure 2.33: Single photo-electron position distribution among the 16 macro pixel of the SiPM array fed by $V_{Bias} = 72V$. Position parameter is extracted from fitted spectra in Fig.2.32.

We can define the system gain γ_{1pe}^{ADC} as the number of ADC counts when one photon is detected. γ_{1pe}^{ADC} includes SiPM gain, readout electronic gain G_i , the sum of $N_L = 16$ samples and the ADC conversion factor. One photon detected by a SiPM gives at its anode an electrical charge equals to $Q_{SiPM,1pe} = q G_{SiPM}$. where q is the charge of an electron and G_{SiPM} is the gain of the SiPM. This signal reaches now the electronic system where it will be amplified, on the high gain channel by $G_i = G_{HG} * |G_{interface}| = 72.7 * 4 = 290.8$ and on the low gain channel by $G_i = G_{LG} * |G_{interface}| = 5.3 * 4 = 21.2$, before getting to the ADC. Considering the ADC conversion factor previously mentioned as V_{ADC} (Eq.2.6) and assuming a number of ADC channels γ_{1pe}^{ADC} we can conclude the output voltage of the SiPM for one photoelectron as a function to the number of ADC channels as follows:

$$V_{out,SiPM,1pe} = \frac{\gamma_{1pe}^{ADC} \cdot V_{ADC}}{G_i} \quad (2.9)$$

The mean value of the SiPM gain in the 16-element array is extracted from Fig.2.33. It is found to be $\bar{G} = \bar{\gamma}_{1pe}^{ADC} = 420$ ADC counts. Substituting in Eq.2.9, we can predict the SiPM output for 1 photo electron as a $V_{out,SiPM}^{1pe} = 1.76 \text{ mV} \simeq 2 \text{ mV}$ at 51Ω load. This amount reveals a charge concentrated in a rectangular pulse of 1 ns width whose amplitude is $V_{out,SiPM,1pe}$ being developed on a load R .

$$Q_{out,SiPM,1pe} = \frac{V_{out,SiPM,1pe} \cdot 10^{-9}}{R} = \frac{\gamma_{1pe}^{ADC} \cdot V_{ADC} \cdot 10^{-9}}{R G_i} \quad (2.10)$$

Average gain of the SiPM array - consideration SiPM output signal is asymmetric, its shape is different from that of the PMT output. It has a fast rising edge but a slow falling edge because of the huge capacitance of the SiPM (terminal capacitance of the SiPM is of the order of some tens of pico Farad). This output signal can be approximated by an exponential function to time:

$$V(t) = V_0 e^{-\frac{t}{\tau}} \quad (2.11)$$

Where τ is the falling edge time constant and it is found for 1 photo electron signal as the time it takes for the signal to reach $1/e$ of its maximum V_0 . For $V(t) = V_0/e$, falling edge time constant, $\tau = 45 \text{ ns}$ was concluded from simulating the SiPM model for an input that corresponds to one detected photo electron (SiPM modeling will be discussed in section.2.7 and simulation was done with Cadence).

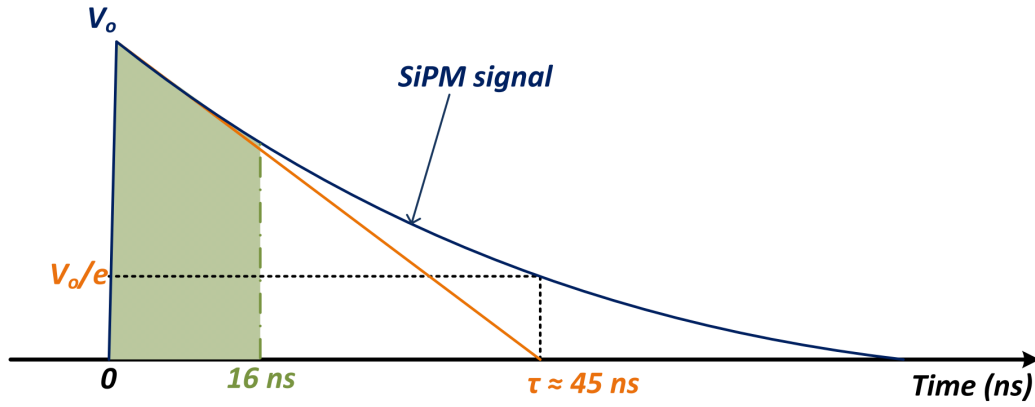


Figure 2.34: SiPM output signal (blue line). At $t = \tau = 45 \text{ ns}$, $V(\tau) = V_0/e$. The green part is the sum of the $N_L = 16$ samples being read in charge reading mode (i.e, $Q_{16 \text{ samples}}$).

In charge reading mode, acquisition system measures the sum of 16 samples of 1 ns each. Hence, reading window is then 16 ns long and is situated at the beginning of the signal (Fig.2.34 illustrates charge calculation). Considering signal shape given by Eq.2.11, SiPM output charge for one photo electron developing in a load R can be written as:

$$Q_{out, SiPM, 1pe} = \frac{1}{R} V_0 \int_0^{16 \text{ ns}} e^{-\frac{t}{\tau}} dt \quad (2.12)$$

For $t = 16 \text{ ns}$ and $\tau = 45 \text{ ns}$ we can write:

$$Q_{out, SiPM, 1pe} = \frac{0.3 \tau V_0}{R} \quad (2.13)$$

From Eq.2.10 (expression of SiPM output charge concentrated in a 1 ns pulse for one detected photo electron) and Eq.2.13 (expression of SiPM output charge concentrated in a 16 ns pulse for one detected photo electron), we can write:

$$\tau V_0 = \frac{\gamma_{1pe}^{ADC} V_{ADC} 10^{-9}}{0.3 G_i} = 1.4 \cdot 10^{-14} \gamma_{1pe}^{ADC} = 5.88 \cdot 10^{-12} [\text{V.s}] \quad (2.14)$$

The average gain of the SiPM array is then:

$$G_{SiPM} = \frac{\tau V_0}{q R} = \frac{14 \cdot 10^{-15} \gamma_{1pe}^{ADC}}{q R} = 7.2 \cdot 10^5 \quad (2.15)$$

Where the resistance at the photo detector output is $R = 51\Omega$, the charge of the electron $q = 1.6 \cdot 10^{-19}$. For the $\gamma_{1pe}^{ADC} = 420$ ADC channel, this means an average gain of $G_{SiPM} \simeq 7.2 \cdot 10^5$ close to the gain of a PMT. This gain is very close to that announced in the SiPM array data-sheet. However, we will under estimate this gain to $5 \cdot 10^5$ for a security margin.

A dispersion of about 10% is noticed in Fig.2.33 among SiPMs in the array. This dispersion can be minimized by controlling the overvoltage of each SiPM (i.e, macro pixel) individually. This function should be integrated in the front-end electronics.

Gain is found to increase linearly with bias voltage. This makes it easier to adjust gain to compensate temperature variation and to balance gain homogeneity among array components. This feature should be studied carefully. Individual pixel gain control function should then be one of the most important priorities of the front end electronics. And this will be studied in the next chapter (section.3.6.2 and section.3.6.1).

2.6.7 Noise in SiPM

Noise origins in the APD were investigated by Roland H. Haitz in [45]. Noise pulse rate was found to be determined by two aspects.

- Minority carrier diffusion from substrate to the breakdown region. Which can be suppressed using a suitable geometry.
- Carrier generation in the space charge layer of the breakdown region. Three mechanisms are responsible of this phenomenon that are:
 - Thermal generation from generation centers.
 - Re-emission of carriers trapped during preceding periods of avalanche breakdown.
 - carrier generation by internal field emission (i.e, band-to-band tunneling)

The first two mechanisms depends on the junction and material quality. The density of the generation centers and traps within the breakdown region could be reduced by localized heat treatment[45].

The dark noise rate depends on temperature, overvoltage, pixel size, and the quality of the semiconductor material[59][60]. The last two factors are fabrication aspects while temperature and overvoltage are related to operation conditions.

In 2011, noise measurements were held at LAPP by R. Kossakowski. A the dark current rate (DCR) of about $360 kHz$ was found for one SiPM of $1 \times 1 mm^2$ size at the ambient temperature $25^\circ C$. Fig.2.35 shows that DCR doubles when temperature increases by $10^\circ C$.

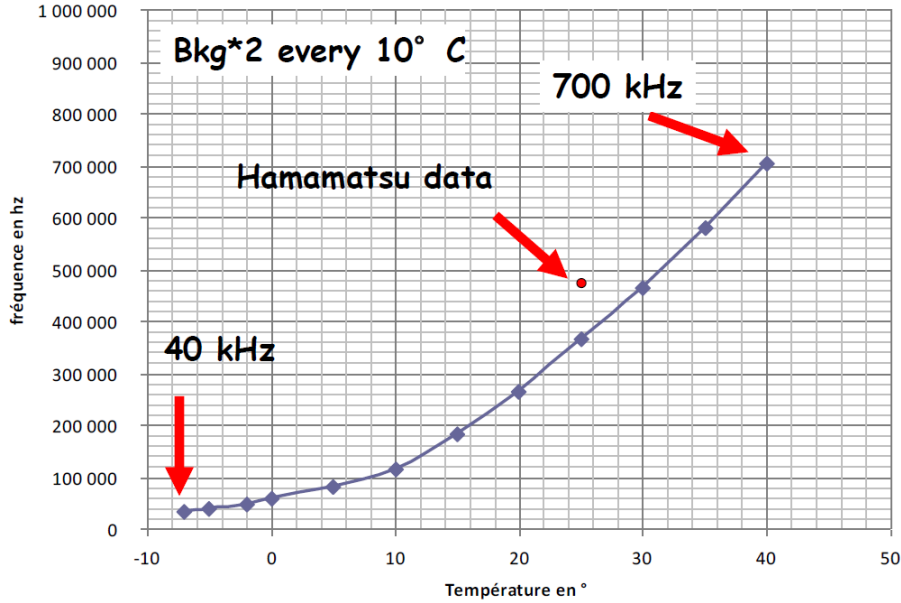


Figure 2.35: Dark current rate measurement with temperature for $1 \times 1 \text{ mm}^2$ SiPM. Source: *La photo-détection avec les SiPM dans le cadre du CTA*, R. Kossakowski - presentation CL, LAPP 2011.

For a SiPM of $1 \times 1 \text{ mm}^2$, a DCR of about 360 kHz was found at 25°C . The LST camera is about 1600 mm^2 which gives a total DCR of about 576 MHz more than the night sky background (NSB) estimated by 150 MHz .

These results confirm the need for temperature control to minimize the DCR to less than NSB. Cooling techniques will be considered in the LST.

This kind of tests have to be held on the 16-pixel SiPM array which is used since 2011 and even on a new one possibly having better noise performance.

2.7 SiPM Modeling

Understanding the electrical characteristics of the SiPM is an essential step towards a proper design of its front-end electronics. An electrical model will represent the device when designing and simulating the front-end system.

Since one SiPM is composed of large number of G-APDs (micro cells) connected in parallel (3600 micro cells in each SiPM of the tested matrix), its model is a parallel replica of the electrical model of one micro cell. This electrical model consists of the diode capacitance C_d , a current source that provides the total charge delivered by the micro cell due to an incident photon (an event). As for the series quenching resistor, it is represented by a resistor R_q in parallel with a very small parasitic capacitance C_q [61].

The presence of a current source indicates an event being detected in the micro cell and so, its absence indicates a passive micro cell that doesn't detect any event. According to this convention and assuming that only one photon is being detected in one micro cell, only one branche in the SiPM model contains the current source while all the others are grouped in an equivalent passive circuit of $(3600 - 1)$ micro cells in parallel. Fig.2.36 illustrates the model that we used for one SiPM composed of 3600 parallel connected

G-APDs.

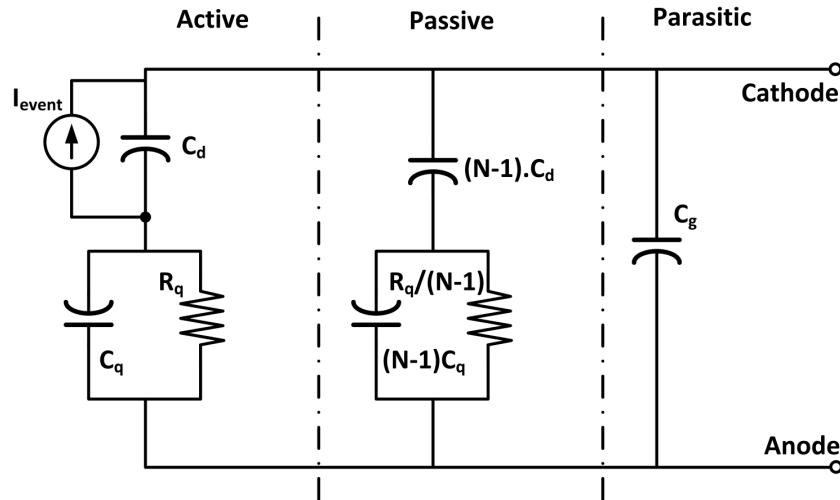


Figure 2.36: Electrical model of one SiPM. This model of photodetector is used in the design and simulation of the front-end electronics in the next chapter.

An accurate model of the SiPM should integrate the grid parasitic capacitance C_g between its terminals. This capacitance is due to the metal routing (metal grid) used to connect in parallel all the micro-cells that form each macro-cell (i.e, macro pixel or SiPM). It is the contribution of two types of parasitics. The first contributes in a small part which is the metal-substrate capacitance of the order of 11pF (considering 35% of the total surface of one SiPM ($1mm^2$) is covered by the metal grid with a capacitance of the order of $0.03fF/\mu m^2$). The second is the fringe capacitor of the metal lines, bonding pad, etc[61][62].

parameter	Value
C_d	97.22 fF
R_q	252 k Ω
C_q	2 fF
C_g	5 pF

Table 2.5: Used model parameters for one micro cell in a SiPM.

Model parameters are listed in table.2.5. These values were extrapolated and optimized for a correct signal shape desired at the output of the SiPM.

Before the avalanche, C_d charges to the value of V_{Bias} and no current exists in the circuit. When a charge carrier is photo-generated, it initiates an avalanche while passing the breakdown region. C_d starts to discharge and a current peak quickly reaches $(V_{bias} - V_{BR})/R_d$; where R_d is the diode resistance. As the current outside the diode increases, a voltage drop on the quenching resistor increases pulling down the potential across the diode to a minimum value equal the breakdown voltage. As a consequence, the current also decreases to a value estimated by $(V_{Bias} - V_{BR})/(R_q + R_d)$. The avalanche is then stopped and the sensor starts to recover for a new event. C_d recharges again to V_{Bias} . The time it takes for C_d to reach V_{Bias} is the recovery time $\tau = R_q C_d$.

R_q should be high enough to quench the avalanche, but not very high. A very high R_q degrades detector sensitivity since it makes the recovery time slow and leads to a long dead time. Typically, R_q is of the order of some hundreds of $k\Omega$ [37].

The form of the output current signal consists of three time constants, depicted in Fig.2.38, depending on the current path in the model. Rising time depends on the avalanche development in the SiPM. Recovery time, as seen above, depends on the diode charge through R_q . The third part is a fast spike on the signal leading edge due to the parasitic capacitance[63].



Figure 2.37: Output signal form of a SiPM ($3.5 \times 3.5 \text{ mm}^2$, 3600 cells, N-on-P structure)[63].

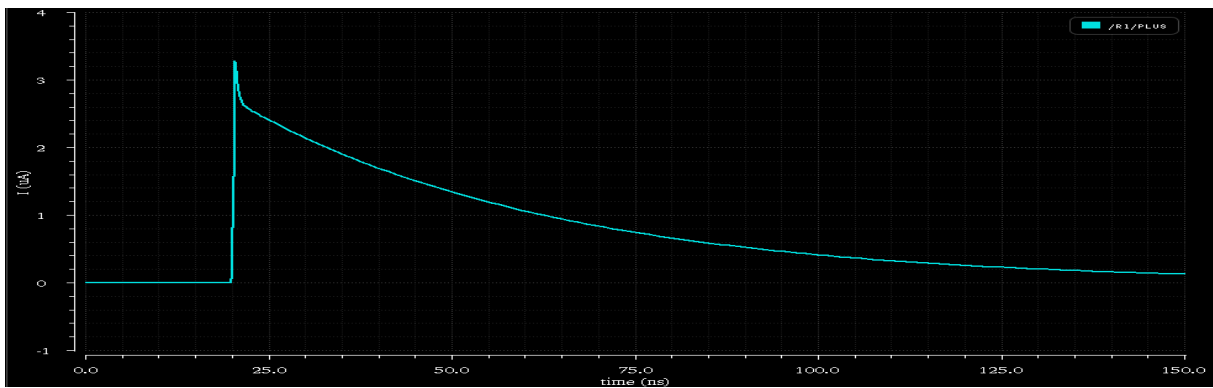


Figure 2.38: SiPM signal shape. Result from simulating the model shown in Fig.2.36 with a current pulse I_{event} of: Amplitude= $231.15\mu A$, rise time = $1ns$ = fall time, $499ps$ pulse width at FWHM.

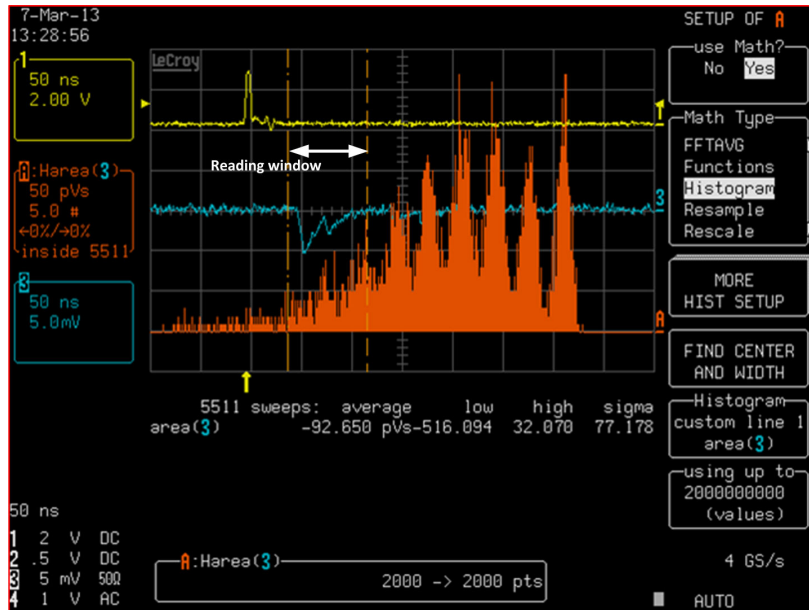


Figure 2.39: Output signal of the SiPM sixteen measured on the oscilloscope (yellow signal). Output pulse integration during the reading window, gives the charge distribution spectrum that represents the photon counting and that is shown in orange.

The shape of the SiPM output pulse is also affected by the front-end electronic characteristics, especially by the input impedance of the electronics. For the electronic signal to be proportional to the number of fired cells, the preamplifier input impedance should be zero[64].

A very influential parameter, that we did not consider here, is the coupling inductance of the wiring between the SiPM and electronics. This parasitic inductance affects the slope of the rising edge of the output current pulse and can be compensated by adding a series inductance of few nH[64][65].

2.8 Conclusion

In this chapter, we discussed the photodetection principle with a review on the development of the different types of the nowadays photodetectors.

Photomultiplier tubes (PMTs) are widely used in astrophysical instruments (e.g HESS telescopes) and they have been showing good performance till now. However, they are sensitive to magnetic field and to high light intensities and voluminous in size. Their operating conditions are somehow demanding: stable high voltages up to hundreds of kilo volts and cooling. Moreover, they have reached a limit in their quantum efficiency.

Solid state detectors are proved to be of great advantage being compared to the photomultiplier tubes. They are robust towards even high magnetic fields, light intensities and small in size. They operate with only small voltages of the order of 70V. They show very good performance in quantum efficiency, photodetection efficiency and even a high gain (of the order of that of the PMTs) in the emerging technology of Silicon photomultipliers (SiPMs). SiPM shows a very good time resolution and we can separate pulse of 1 photoelectron from that of the pedestal and from the pulse due to two photoelectrons

and so on, which makes the photon counting process very efficient. SiPM output signal is characterized by a short rise time. A new form of these detectors is an array of several SiPMs built on the same substrate (monolithic) is investigated as the base element toward a large area detector.

Results of our tests on a monolithic array of 16 macro pixel were presented. Each SiPM is able to detect number of incident photons ranging from single photoelectron up to 2000 photoelectrons. For an optimum bias voltage of 72V, we found a mean value of gain of about 10^5 with a small dispersion among the array elements $\sim 10\%$. A correction procedure will be considered in the front-end electronics that we will develop in the next chapter in order to improve gain homogeneity of the SiPMs in the array. Moreover, the specifications of our proposed FE-electronics should consider the high capacitance of the SiPM and their input impedance should approach zero not to influence the timing performance of each SiPM and to keep its proportionality.

Table.2.6 resumes a comparison between one PMT and an array of 16 SiPMs. SiPM is a serious candidate to replace PMTs in the future Cherenkov telescopes that will be constructed for the CTA project. The encouraged experience of the FACT camera is a reference example. SiPM applications go beyond high energy gamma-rays astronomy to biology domain and medical instruments.

	PMT	SiPM array
Sensitivity to magnetic field	Yes	No
Sensitivity to high light intensities	Yes (destroyed)	No
Size	bulky	compact
Polarization	\sim hundreds of kV	$\sim 70 V$
Quantum efficiency	20 – 30% ($\lambda : 300 - 450 nm$)	30 – 40% (visible light)
Gain	$10^6 - 10^8$	at the order of $7 \cdot 10^5$ ¹⁹
Noise (dark current)	low	$\sim 3 \mu A / SiPM$
Crosstalk	No	Yes

Table 2.6: Comparison of the critical characteristics of photo-multiplier tubes and the tested array of SiPM.

¹⁹Tests have shown an average gain of $7.2 \cdot 10^5$, while SiPM gain about $7.5 \cdot 10^5$ announced by Hamamatsu.

Chapter 3

ALPS Design

Contents

3.1	Introduction	67
3.2	State of the art in readout-electronics	67
3.3	Readout chip, block diagram development	70
3.4	The preamplifier	73
3.4.1	Interface with the detector - Input stage	74
3.4.2	Gain stage	79
3.4.3	Current mirror choice	80
3.5	Proposed preamplifier and simulation results	85
3.5.1	Symmetric currents (transimpedance gain)	87
3.5.2	Symmetric loads (current gain)	89
3.5.3	Combination of transimpedance and current adjustment	91
3.5.4	Response speed	91
3.5.5	Dynamic range, Linearity	93
3.5.6	Signal to noise ratio	95
3.5.7	Power consumption	98
3.6	Slow control	98
3.6.1	8-bit DAC for per-pixel over-voltage control	99
3.6.2	Preamplifier gain correction	100
3.6.3	Noisy channel elimination function	101
3.7	Analog sum function	103
3.8	Trigger	104
3.9	Overall chip and layout	104
3.10	Single-ended to differential converter	107
3.11	Conclusion	107

3.1 Introduction

In order to benefit from the new emerging technology in photo detection industry, that is presented by SiPM and its matrix form detectors; a parallel development should be driven on the readout electronics and data acquisition systems as well.

Presented in the previous chapter, section.2.6 and 2.7, a detector of the type SiPM has special electronic characteristics; in particular: its high capacitance and the dependency of its output impedance on the number of fired cells. These characteristics make it difficult to use the same readout electronics for the SiPM as its PMT counterpart. A new approach is being studied for the front-end electronics in order to take full advantage of the SiPM potential (fast response and high gain).

For the astrophysical application in the LST of CTA, in case of a possible upgrade of the LST camera, SiPM characterization in the previous chapter raises a group of specifications for the readout electronics to adapt: Large dynamic range of about 2000 photo electrons (for an SiPM array of 16 macro pixels that is proposed to replace one PMT, this means a dynamic range of $125 pe$ per macro pixel of the array), with a special care and study of the single photo electron signal (localizing the single-photon peak provides the possibility to control the gain of the electronic chain[11]), high speed within $3 ns$ and a group of functionalities for gain control and noise minimization. The more these specifications are fulfilled the better translation of the detector signals and so, the more accurate and precise data are gathered.

This chapter is the second part of the practical work of this thesis. It is dedicated to the full-custom circuit design of a readout ASIC to be attached to the SiPM in the new camera of the large size telescope (*LST*) of the Cherenkov telescope array *CTA*.

The chip is labeled ALPS, that stands for "*ASIC de Lecture Pour SiPM*". It consists of 16 channels each of which reads the output of one macro pixel of Hamamatsu 4×4 SiPM array previously characterized in section.2.6.

In this chapter, the design process is presented. The chip is designed in *Austria Micro Systems (AMS)* $0.35 \mu m$ *SiGe* technology. Simulation results that represent the theoretical performance of the main blocks of the chip (ALPS) will be shown. A special attention is dedicated to the design of the preamplifier considering its major role and impact on the overall performance of the chip as a unity.

3.2 State of the art in readout-electronics

Front-end readout electronics vary according to their application and requested performance. Their concept depends, among others, on the physical amount to measure whether it is the charge, time, position, speed, trace of the detected particle.

Lots of readout ASICs were designed to read signals from photomultipliers, they can be found in LHC calorimeter, in medical and biological devices and instruments using positron emission tomography *PET*. They are used in space based detectors *AMS* and in the gamma ray telescopes.

Table.3.1 is a short introduction to some readout chips that were used in the last decade. Some details of each chip follow in separated paragraphs.

chip name	photodetector	PA type	measurement	channels	DR	power
FLC	SiPM	charge	energy	18	11 bits (1 mV – 2 V)	200 mW
MAROC2	MAPMT	current	energy	64	10 pe	> 220 mW
MAROC3	MAPMT, SiPM	current	energy	64	30 pe	220 mW
SPIROC	SiPM	charge	energy, time	36	1-2000 pe	25 μ W/channel
EASIROC	SiPM	charge	energy, time	32	1-2000 pe	155 mW
PARISROC	16 PMT	voltage	energy, time	16	0.3 – 300 pe	-
PACTA	PMT	current	energy	1	15.9 bits	160 mW

Table 3.1: Some examples of the readout electronic chips that read different types of photo detectors.

FLC-SiPM A charge sensitive front end chip that consists of 18 channels. It was designed in $0.8 \mu\text{m}$ CMOS technology in 2004 for the ILC analog hadronic calorimeter. Each channel is a series of a shaper (first derivation by a high voltage decoupling capacitance and a resistor), a variable gain charge preamplifier (4 bits control the feed back capacitance that varies the gain between $0.7 - 10 [V/pC]$), a $CRRC^2$ shaper with a variable shaping time ($12 - 180 \text{ ns}$), and a track and hold buffer that gives one multiplexed output. In parallel, an input DAC allows to tune the detector gain by varying the operating voltage by up to 5 V excursion. The chip provides a dynamic range of 11 – bit (1 mV to 2 V) and consumes $\sim 200 \text{ mW}$ with 5 V supply voltage[66].

MAROC readout chip series The name stands for Multi-Anode ReadOut Chip. MAROC series is a development of the MAROC chip including version-2 and version-3. It consists of 64 channels designed in $0.35 \mu\text{m}$ *SiGe AMS* technology between 2005 and 2006. It is a generic readout chip dedicated to read multi anode PMT and similar detectors. The main feature is the individual variable gain preamplifiers that could correct gain dispersion among the detector channels. Each preamplifier is a current mode, low noise, low input tunable impedance ($50 - 100 \Omega$) that minimizes crosstalk. Currents are then delivered to two paths (slow and fast shapers). A $CRRC^2$ slow shaper followed by two sample and hold buffers. One buffer allows charge storage in a 2 pF and then analog and digital multiplexed charge output. The other buffer measures the base line and the maximum of the signal. Beside, a CRRC fast shaper path followed by discriminator with 10-bit DAC that generates the trigger output. MAROC chip operates with 3.5 V power supply and consumes $3.5 \text{ mW/channel} \simeq 220 \text{ mV}$ for the 64 channels[67] [68].

MAROC3 was used to test the feasibility of a SiPM-based cameras for Fluorescence and Cherenkov Telescopes[69].

SPIROC Stands for Second Generation SiPM Read-Out Chip is the evolution of the FLC chip. SiPM Integrated Read-Out Chip is a 36-channel ASIC dedicated for a prototype that uses the SiPM in the ILC hadronic calorimeter. The circuit was built in $0.35 \mu\text{m}$ *Si-Ge AMS* technology in 2007. An 8-bit DAC was inserted at the input of each channel in order to adjust individual SiPM gain within $0.5 - 4.5 \text{ V}$. Input charge is taken from each detector anode and is sent to two preamplifiers of different gains (low and high gains). Each preamplifier is followed by a $RCCR^2$ slow shaper ($25 - 175 \text{ ns}$) and an analog voltage memory (16-bit depth switched capacitor array). In parallel, high gain preampli-

fier output is sent to a fast shaper (15 ns shaping time). This fast signal is compared to a threshold by the following discriminator to produce trigger signal. The trigger threshold is generated by a common 10-bit DAC. Four additional bits are used to finely tune this threshold inside each channel. Trigger output is sent to the digital part of the chip that in turn manages the switched capacitor arrays. A voltage ramp of 300 ns (generated by each clock edge of the ILC and stopped by the trigger signal from the discriminator) is used to give analog time measurement. Time and voltage outputs can be digitized using a common 12-bit Wilkinson ADC. SPIROC is a system on chip whose digital part was integrated in the ASIC. It was designed to match the beam structure of the ILC (2 ms of acquisition, conversion and readout data for 198 ms of dead time) and hence a precious power saving was possible (in power pulsing mode the chip consumes 25 $\mu\text{W}/\text{channel}$). It covers the complete sensor output range (1 to 2000 photo electrons)[70][71].

EASIROC Extended Analog SiPM Integrated Read-Out Chip is based on the previous SPIROC circuit and was designed in the same technology. It consists of 32 fully analog readout channels each with a 8-bit DAC for SiPM gain control within 4.5 V. It measures charge ranging between 160 fC up to 320 pC (1 up to 2000 photo electrons) thanks to its two gain paths (low and high gains). Each gain path is a series of tunable gain charge preamplifier (4 bits are used to adjust the low gain preamplifier between 1 – 15, and other 4 bits are used for the high gain between 10 – 150), a slow shaper (seven shaping times between 25 – 175 ns defined by the slow control facility), track and hold analog memory (switched capacitance array). The output of the high gain preamplifier is also treated by a fast shaper (15 ns) and is then compared to a threshold in order to generate a trigger signal. A unique threshold is generated by a 10-bit DAC (DAC resolution is 1.3 mV allows threshold tuning between 1.1 – 2.4 V) and is then sent to 32 discriminators inside each channel. This gives 32 trigger analog outputs of the ASIC (can be used for timing measurements) beside a digital trigger output (a trigger multiplexed output) and the logic OR of these 32 signals. EASIROC chip consumes about 4.8 mW/channel which means a chip consumption of 155 mW and unused features could be disabled to reduce power consumption[72].

PARISROC Stands for Photomultiplier ARray Integrated in SiGe Read Out Chip, it was designed in 0.35 μm AMS SiGe technology. It was proposed as the readout electronic for the square meter photodetector project for neutrino experiments. The idea is to segment the large surface of the detector into arrays with a single front-end electronics. Only useful data will be sent in surface to be stored and analyzed. There are 16 independent and self triggered channels that measure charge and time. Each channel has dual gain paths. A gain path is composed of a voltage preamplifier (of adjustable gain by variable feedback capacitance), a slow shaper ($CRRC^2$ with a variable shaping time up to 200 ns), and then the shaped signal is stored in an analog memory (depth of 2). Only the correct signal (of the high gain path or the low gain one) will be digitized by an internal ADC. The trigger path takes its signal from the high gain preamplifier. It consists of a fast shaper (5 ns) followed by a discriminator. Two time values are measured: time stamp by a 24-bit counter at 10 MHz and a fine time by Time to Digital Converter that converts amplitude into time. Time signal will also be stocked in an analog memory before being digitized by another ADC. A common digital part for all the chip manages all these op-

eration in all channels. PARISROC measures input signals ranging from 1 *photo electron* up to 600 *photo electrons* with a signal to noise ratio of 12 for the minimal signal with a gain of 12. It is triggered at 50 *fC* and measures time with 1 *ns* resolution[73][74].

PACTA Acronym for PreAmplifier for CTA, is a current mode preamplifier that was designed for CTA project considering a PMT based camera. The design uses AMS 0.35 μm BiCMOS technology and reads output signal of one pixel in the camera (one PMT). Preamplifier is attached to the Camera pixel and its output is transmitted to the FE -signal conditioning electronics by a cable. Input current is split into two scaled currents by factor n before being copied to the corresponding gain stage. Each gain stage consists of a current mirror with a saturation control mechanism on the high gain direction.

PACTA covers high dynamic range with low noise and low input impedance. However, the power consumption of its input stage is about 10 *mW*. In order to drive the transmission line (cable) while conserving the wide band width (500 *MHz*), it uses an AB output stage after the transimpedance amplifier. This adds about 150 *mW* for dual high and low gains differential outputs[75].

From PACTA, a new prototype was designed for SiPM readout electronics. It includes 3 channels each of which consists of a preamplifier with high gain, high speed timing path and a lower gain, lower speed energy measurement path, besides a fast current discriminator with digital output. In this new prototype, they have also integrated a saturation control circuitry that prevents any effect of the high gain saturation on the linearity of the low gain path. This new prototype provide a 400 *MHz* band width on the high gain and 218 *MHz* on the low gain. It consumes about 7 *mW/channel*[76].

Discrete electronic approaches In parallel to the development of a readout ASIC (ALPS), two other discrete electronic approaches were built. Both of them are adder circuits that consider demonstrating the feasibility of SiPM solutions for large Imaging Atmospheric Cherenkov Telescopes (IACT) cameras.

The first scheme, developed at the Max Plank Institute for Physics - Munich, is based on a common base amplifier for each SiPM. The amplified currents of 7 SiPMs are then summed. The total current pulse gives a voltage signal on the output capacitor proportional to the number of detected photons. Using this scenario, the single photon peak is separated with a signal to noise ratio ~ 4 . The pulse width is ~ 4 *ns* and the circuit consumes ~ 300 *mW*[11].

The second scheme, developed at INFN - Padova, is based on two sum stages built with fast, low noise operational amplifiers. An additional gain stage can be used to implement two-gain output design. Two prototypes were tested. With the first prototype, of 16 (3×3 mm^2) SiPMs, the single-photon peak could be separated with a signal to noise ratio ~ 3 . For the second prototype, of 32 SiPMs, the power consumption is ~ 300 *mW*, while the pulse width is ~ 3 *ns*[11].

3.3 Readout chip, block diagram development

Towards a new Cherenkov telescope, the camera will be subject to development and upgrade. Readout electronics should adopt the choice of the new photo detector which may

most probably be based on SiPM arrays. The motivation for this choice is to reduce the minimum energy detected by this telescope to $\sim 10 \text{ GeV}$ about half the energy considered today (20 GeV) as mentioned in section.1.5.2.

In order to develop this front end part of the camera, we propose a demonstrator composed of a readout ASIC for a 16-SiPM array detector. The ASIC could be interfaced with the current acquisition system¹. This last point determines types of signals to be delivered by the readout electronics to data acquisition part.

The first readout diagram we proposed for this purpose is shown in Fig.3.1. It is a dual gain chip able to cover as wide dynamic range of 2000 *photo electrons*. High gain (*H.G.*) is responsible for detecting the smallest signal (including the single pe) while low gain (*L.G.*) tolerates the higher range of signals.

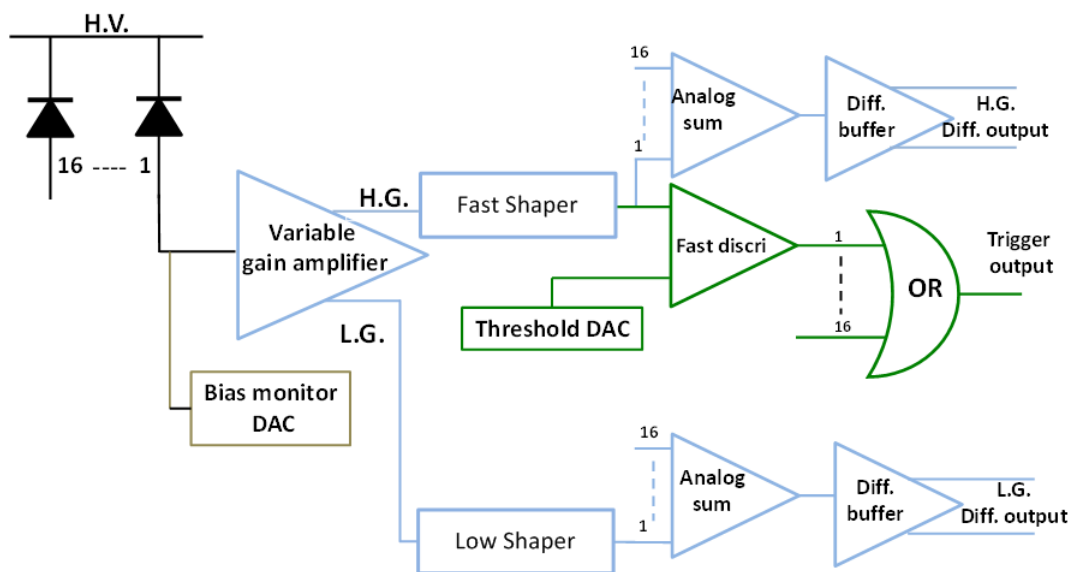


Figure 3.1: Preliminary block diagram of ALPS (presented in the SiPM advanced workshop - July 2013).

A productive brain-storming with the Italian partners² has led to modify our proposal. The aim is to replace every PMT in the first generation camera by an array of SiPM photo sensors. In practice, there is no physical interest in reading individual macro-pixels' signals so far. Since the acquisition system accepts only the outputs of the photo detector and the trigger signal, a need rises to group outputs from all SiPMs of the array in only two output signals, one for each gain besides the pixel-level trigger output.

As for the LST trigger strategy, Monte Carlo simulations showed that the Sum-Trigger have the best performance in terms of triggering showers at the lowest energies. In this strategy, analog signals of the trigger region are analogically added. The LST is aiming to reduce the energy threshold as much as possible. This explains the choice of Sum-Trigger configuration for the LST camera[77].

¹Examples of nowadays used data acquisition systems are NECTAR and DRAGON. At this stage of CTA design, these systems will probably be reused.

²During the 1st SiPM advanced workshop at Munich-Germany on July, 2013. <https://www.cta-observatory.org/indico/conferenceDisplay.py?confId=487>

On the one hand, huge detector capacitance makes it useless to sum signals directly at the detector level. Summing that way means connecting the SiPMs in parallel which implies a huge capacitance (proportional to the detector area: $\sim 50 \text{ pF}/\text{mm}^2$). At the input of the readout electronics, this is translated into high levels of electronic noise[11] and probably an early saturation as well. On the other hand, temperature sensitivity and gain dispersion among detector³ macro pixels concluded from SiPM characterization in section.2.6.2 and section.2.6.6 showed an advantage in treating signals from every macro pixel individually. Therefore, our ASIC reads SiPM macro pixels separately one by one and it contains a sum function that gives both one high gain and one low gain signals besides the trigger signal. These three signals will be delivered to the acquisition system behind ALPS (NECTAR[7][78] and Dragon[8]). Fig.3.2 depicts the final bloc-diagram of a 16-channel readout chip.

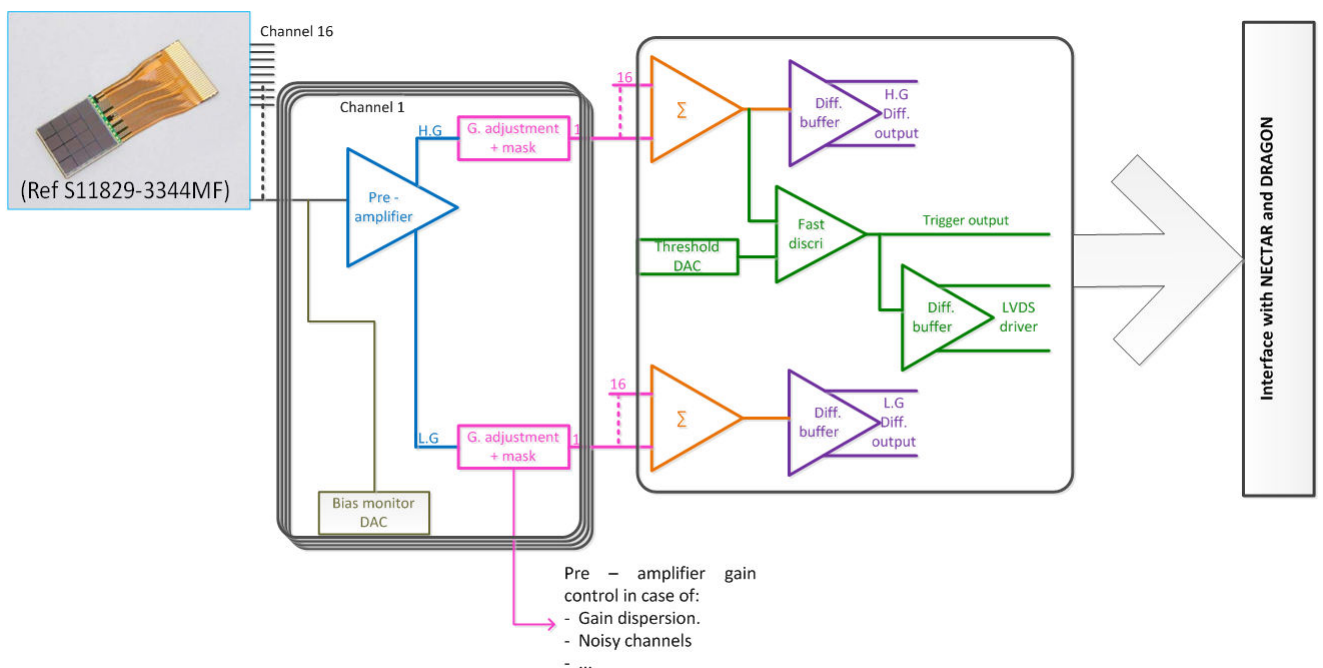


Figure 3.2: Block diagram of ALPS

ALPS consists of 16 channels compatible with a 4×4 SiPM array. Each channel reads one macro pixel (one SiPM), therefore it includes a preamplifier of two gain paths (high and low gains) to cover the largest possible range of input signals. One requirement was to unify the gain among all channels which is the role of the gain control block that makes it possible to even eliminate (mask) the channel if it is found to be noisy. A DAC of 8 bits resolution will adjust the over-voltage of each SiPM so that to reduce the gain dispersion among the 16 SiPMs (section.2.6.4, section.2.6.6) and to neutralize temperature-sensitivity of the gain.

Signals out of the 16 individual preamplifiers will then be summed on both: low and high gain paths. Resulted sum signals are converted into differential form. This last

³From here on, *the detector* is used to mention the array of 4×4 SiPMs. One element of the array is a *macro pixel*.

step is necessary for ALPS to be interfaced with the acquisition boards like *NECTAR* or *Dragon* since only two signals in addition to the trigger signal are available. Gain will be treated on two levels. First, gain dispersion among array elements (SiPMs) will be reduced by means of an 8-bit DAC. Sixteen DAC channels are available for this purpose (one DAC per macro pixel is inserted at the beginning of each channel of the sixteen readout channels). The role of these DACs is to adjust the applied voltage of each SiPM enabling gain unification and temperature effect compensation at the same time. Second, gain control after the preamplifier stage. To assure identical weight of signals in the sum, a control bloc is inserted between the preamplifier of each channel and the sum bloc. This bloc is programmable by the slow control routine (the rose block labeled "G. adjustment + mask" in Fig.3.2) that will be loaded in a FPGA situated on the mother board.

A trigger signal is generated from the high gain sum through a fast discriminator of programmable threshold. Trigger signal will also be delivered in differential form as well as single-ended mode.

Design process was realized using AMS BiCMOS $0.35\mu\text{m}$ technology. It may not be the today's most fine technology but it was more reliable for the purpose and time of this work. It provides high performance bipolar NPN transistors, better performance for a given power budget for analog electronics, relatively high power supply (3.3V used in our design which is good in order to achieve the high dynamic range desired and which may be difficult with newer technologies of 1V supply voltage). In addition, for short-term research project like this thesis it is easier and cheaper to carry-out thanks to the multi-project runs.

3.4 The preamplifier

The preamplifier is considered as the core of the readout chip, it plays a crucial role in determining the performance of the overall chip in what concerns the speed, linearity and the covered dynamic range. There exist three types of preamplifiers according to how to deal with the input signal: current mode, voltage mode or charge sensitive preamplifiers. Each of these three preamplifier types has its advantages and disadvantages.

Current mode preamplifiers are pulse-shape conservators thanks to their low input impedance. This will shorten the time constant formed by the equivalent capacitance of the detector itself with the input impedance of the preamplifier. It is a benefit for a fast response since the rising edge is kept with minimum distortion.

In voltage mode preamplifiers, high input impedance is needed as current-voltage converter. This will be useful for amplitude measurement but its time response is slow. The most important shortcoming here is that using high resistance for current-voltage conversion provokes variation in the detector bias under signal.

Charge sensitive preamplifiers (*CSA*) are integrators where a special attention should be paid to the saturation (i.e, the dynamic range), and the bandwidth of the amplifier. To guarantee that most charge produced in the detector is transmitted into the amplifier, *CSA* should have high feedback capacitance, high gain, and hence high input capacitance[79]. Such large feedback capacitance occupies large area when integrated in the silicon. Moreover, a heavy capacitance (formed by the detector capacitance in series with the feedback one) requires an additional output stage able to drive it. A suitable output stage can ameliorate speed performance but it entails a significant increase in

power consumption[62].

Timing is one of the targeted aspects in the desired performance of our ASIC (section 2.5). This makes current mode preamplifier the best fit for the astrophysical application to take advantage from the timing characteristics of the SiPM detectors.

As mentioned in the previous chapter (section 2.6), SiPM matrix has common cathode tied to the power supply. Output signals from individual macro pixels can then be read from each anode. Positive current pulses result from this arrangement as photo generated electrons are derived to the common cathode. These signals are uni-polar ones, which means that it is possible to push the operating point of the pre-amplifier so that it covers as much as possible dynamic range without being saturated (without distorting or clipping signals)

Pre-amplifier is made of two stages, the first one is the input stage that will transfer the input current into the second stage whose role is to provide the gain and to send the signal to the next part of the readout circuit (gain correction and sum circuits).

3.4.1 Interface with the detector - Input stage

Input stage is the very first interface with the detector. From the detector side, SiPM proportionality tightly depends on the input impedance of the front-end electronics[64] (section 2.7). The varying output impedance of the SiPM combined to the input impedance of the following electronics causes nonlinear behavior[80]. The high capacitance of the SiPM causes slowness in the overall system response, it could degrade system performance in terms of both bandwidth and noise[81]. In order to improve the system linearity and to speed up its response, the preamplifier input impedance should approach zero[64].

From the electronic side, as signals generated by the detector are currents, this first stage should ideally provide a zero input impedance. Low input impedance is also important not to disturb the operation mechanism of the detector (the discharge and the quenching process). Reducing the input resistance will also boost the bandwidth of the system.

Two types of amplifiers could achieve this aim. Drawn in Fig. 3.3 both transimpedance amplifiers and current amplifiers are possible candidates as they both have small input impedance. The difference between them is that the first have a zero output impedance, it then provides voltage output; while the second have an infinite output impedance and delivers a current output. In what follows, each possibility discussed in order to make the appropriate choice between both of them.

3.4.1.1 Transimpedance amplifier

An example of transimpedance amplifier is shown in Fig. 3.4. In this example, the circuit consists of two stages tied in cascade. That is a common gate (common base for bipolar transistor) of a small input impedance, and source follower (an emitter follower for bipolar transistor) which insures a small output impedance. Input impedance can be described as $Z_{in} = 1/g_{m1}$ and output impedance is $Z_{out} = 1/g_{m2}$. The function of this configuration is said to be current to voltage conversion as it senses current and generates voltages. The following gain stage of the pre-amplifier is then fed by voltages.

At high input current levels, high output voltages are predicted. Unless voltage dividers (converters) are considered, gain stage will be soon saturated and only poor dy-

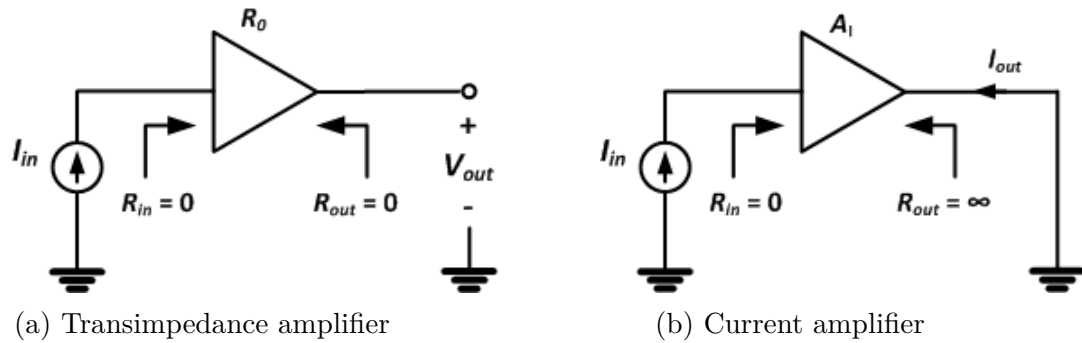


Figure 3.3: Input stage candidates

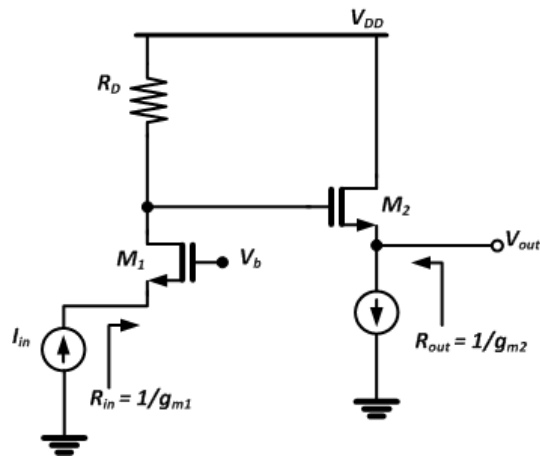


Figure 3.4: Example of transimpedance amplifier

dynamic range could be covered. Several techniques may be implemented to improve this dynamic range, e.g, output signal limiting, input current steering or variable transimpedance gain. A complex circuit with much bias and feedback control results[82]. These techniques are not that simple to edit for a correct operation.

As for bandwidth extension, there are several techniques like for example: series inductive peaking and regulated cascode architecture (*RGC*)[81][83][84][85][86] including reducing the input resistance. The used technique ought to avoid additional noise and power consumption.

The disadvantage of this kind of circuits is that it compromises dynamic range, low voltage, low detection threshold. Not forgetting the response speed, since working with voltages makes the circuit slower as parasitic capacities will charge and discharge to the full voltage swing. This causes more dynamic power consumption[87].

3.4.1.2 Current amplifier (current conveyor)

It is simpler than the transimpedance amplifier according to the fact that one transistor tied in common gate (common base for bipolar transistors) can represent the concept[88]. According to this topology, transistor shows a small input impedance at the source (or emitter for bipolar transistors) and ideally an infinite output impedance at the drain (at the collector for bipolar transistors). It senses current and provides current with a unity

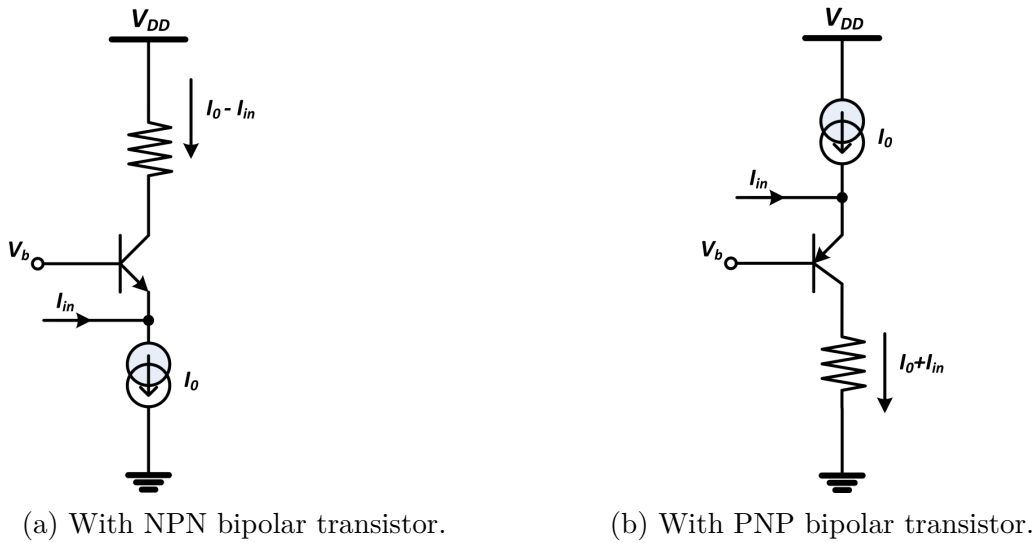


Figure 3.5: Building the input common base current conveyor with bipolar transistor.

gain as the same input current flows to the output.

For the next stage (gain stage), it is more flexible to deal with currents as they can simply be replicated into other parts of the circuit using few transistors that forms a current mirror. Using current mirror structure makes it easy and efficient to design multi-gain stages. Saturation can be controlled by managing an appropriate copy ratio (scaling factors). The solution of multi-gain stages is an easy feasible matter. As a consequence, desired dynamic range can then be easily looked after.

Common base bipolar transistor biased to work in its active region has an input impedance of $1/g_m = V_T/I_c$ which is smaller than that for its MOS counterparts (in its saturation region) for the same bias current. Moreover, bipolar transistors could be faster and more immune to noise.

Using NPN transistor for this stage (Fig.3.5a) means that the positive input current pulse will be subtracted from the bias current. In order to detect large signals, bias current should be as large as possible which means more power consumption and that increases the minimum detectable signal.

Instead, using PNP transistor (Fig.3.5b) input current will be added to bias current. This latter could be chosen as small as possible to sense the minimum input signal (1 *photo electron*) and to detect large signals at the same time.

AMS technology does not support vertical PNP bipolar transistors. Besides that circuit may induce a large bias current that could be avoided using common gate PMOS. According to these constraints the only solution is to build a common gate PMOS input.

Fig.3.6a shows common-gate stage whose input impedance can be written as:

$$Z_{in} = \frac{1}{g_m + g_{mb}} \simeq \frac{1}{g_m} \quad (3.1)$$

where,

$$g_m = \sqrt{2\mu C_{ox} \left(\frac{W}{L}\right) I_D} \quad (3.2)$$

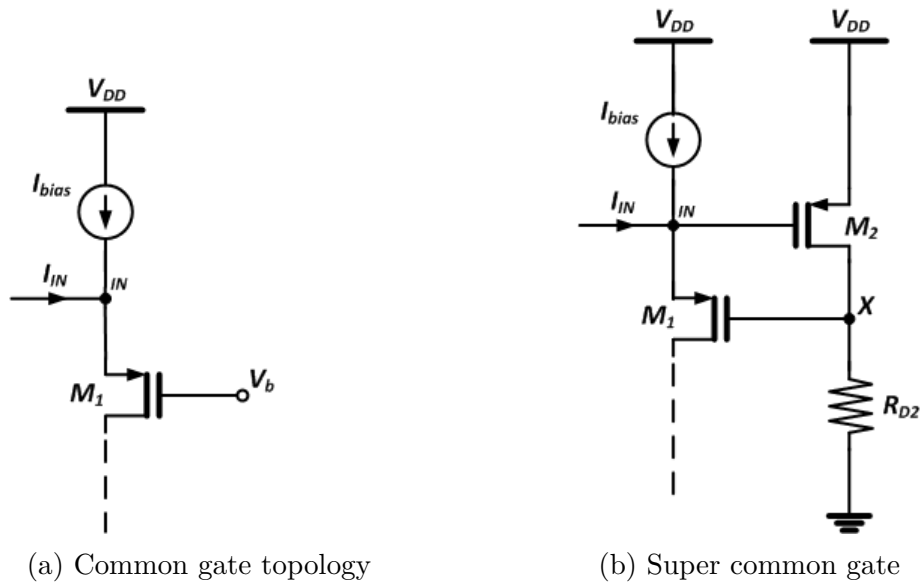


Figure 3.6: PMOS input stage.

Where, C_{ox} is the gate oxide capacitance per unite area. W and L are MOS dimensions that refers respectively to the width and length of its channel (neglecting channel length modulation effect, $\lambda = 0$).

Now the question is how to scale back this impedance and keep a stable operating point of this input stage? The normal expression of g_m reveals that input impedance depends on the current flowing through the circuit. At the upper limit of the dynamic range this could degrade the performance since large currents are expected. One further, voltage disturbance at node IN affects the operating region of the transistor M_1 if V_b stays constant. To solve these problems super common gate topology could be efficient.

Shown in Fig.3.6b, another PMOS M_2 , tied in common source topology, is inserted around the input common gate M_1 in order to control its gate voltage. As the voltage at node IN rises, V_{GS,M_2} increases the current flowing through R_{D2} . The voltage at node X will be scaled up counteracting the change at the input voltage (like negative feedback principle) and keeping the operating point of M_1 constant.

Moreover, input impedance is now much smaller than $1/g_{m1}$. New Z_{in} expression in Eq.(3.3) can be found from small signal model depicted in Fig.3.7.

Component	W/L ($\mu m/\mu m$)
M_1	700/0.35
M_2	300/0.35
R_{D2}	10 k Ω

Table 3.2: Device parameters of the input stage as drawn in Fig.3.6b.

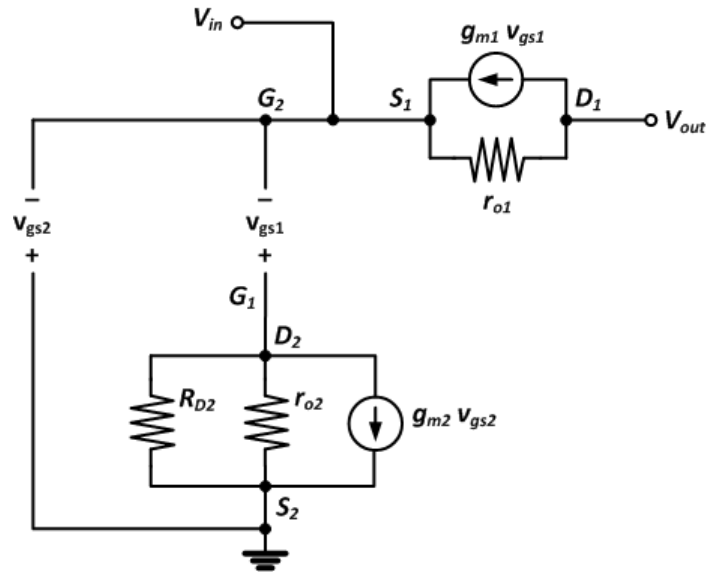


Figure 3.7: Small signal model of the super common gate input stage. Where V_{in} is an input voltage applied at the node IN of Fig.3.6b, V_{out} is the voltage at the drain of the transistor M_1 of the same figure. Z_{in} formula is found by analyzing the circuit to find the relation V_{in}/I_{in} .

$$Z_{in} = \frac{1}{g_{m1} \left(1 + g_{m2} \frac{r_{o2} R_{D2}}{r_{o2} + R_{D2}} \right)} \quad (3.3)$$

Simulation shows a low input impedance of about 20Ω depicted in Fig.3.8. The rising part of the plot is due to inductive effect that become obvious at high frequencies out of our domain of interest. Now having current out of this stage it is easy to introduce this current to next steps by using the concept of current mirroring.

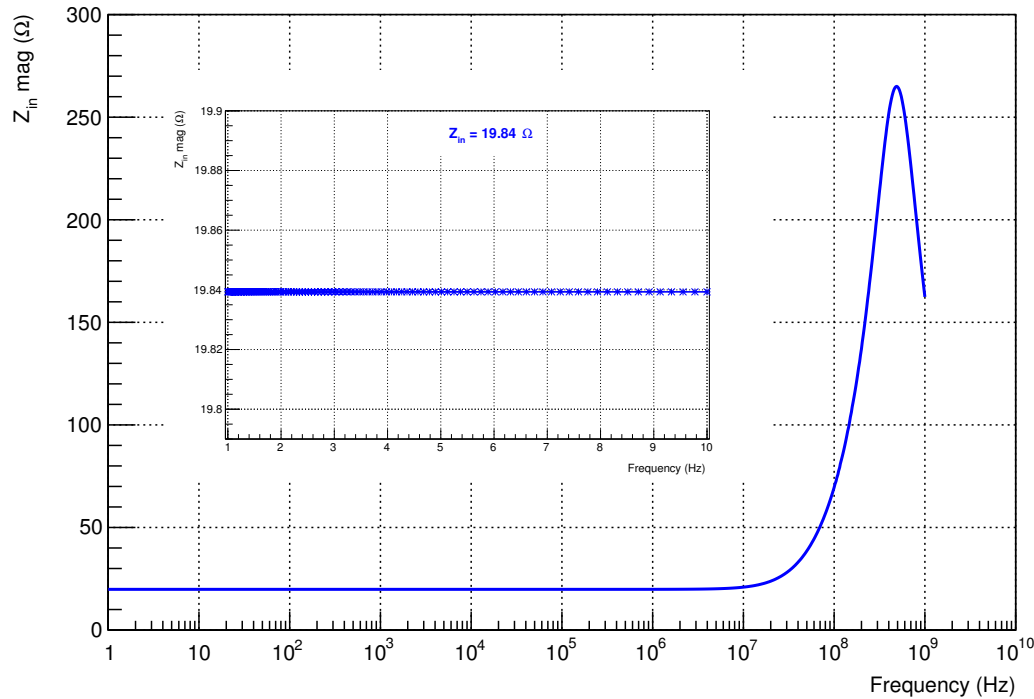


Figure 3.8: Simulation plot (by Cadence) of the input impedance of the input stage built with a super common gate current conveyor.

3.4.2 Gain stage

After copying input current-signal into the pre-amplifier, current mirrors are used to transmit this current into "gain" stages. For precision issue, MOS transistors are preferable to bipolar counterparts for building current mirrors. The reason behind this is the error due to non zero base current in bipolar transistors that makes them more affected by process variation. However, this does not mean that MOS current mirrors are the best solution. As a matter of fact, device mismatch is the main source of errors in MOS circuits in general. Many challenges rise in order to decrease this error and to meet the best possible linearity over the demanded dynamic range.

Input signals are spread over a wide range starting with one photo electron signal up to current corresponding to 2000 photo electrons and maybe even more. According to the desired dynamic range laying between one and 2000 photo electrons, current expected out of the SiPM model varies according to incident light flux between $2.7 \mu A$ and $5.5 mA$ at the pre-amplifier input⁴. One can then say that dynamic range starts with small signals and reaches even large signals. This paradoxical reality makes it necessary to build two gain lines one for small signals (high gain), the other is dedicated to large signals (low gain).

The choice made in the previous section.3.4.1.2 helps along the work. Fortunately, current mirrors can copy different ratios of the original current into several branches.

⁴In order to simulate the response of the SiPM model to one photo electron, a current pulse is used as was explained in section.2.7.

Building two gain paths is now possible without increasing the complexity of the circuit or its consumption. As a consequence an extended dynamic range is expected. Attention to linearity will be necessary as transistor mismatch limits the precision of the current copy process.

High gain This part is needed in order to measure the small signals including that issue of an incident single photo electron. This signal being small should first of all be above the noise level of the circuit. CMOS circuits are affected by random noise whose source varies from thermal noise, noise generated by the current in the channel, flicker noise caused by the imperfect interface between gate oxide and silicon substrate[88]. Design considers short-channel MOSs in order to assure minimum noise in respect to the smallest interesting signal expected.

Low gain As the light flux becomes higher, increased number of photo electrons induces stronger signals out of the detector. If we need to cover a wide dynamic range, the previous high gain path will not be enough. High gain can not compromise between the minimum and maximum of the desired dynamic range since it will be soon saturated. Here comes the role of the low gain path. In this branch, current mirror copies a fraction (tenth) of the original current so that to postpone saturation as far as possible. This means that the low gain path will not be sensitive to small quantities of photo electrons whose signals mostly lay below the circuit's noise level.

3.4.3 Current mirror choice

The principle is resumed in Fig.3.9a and Eq.3.4. It says that a current passing through the master diode-connected transistor will be copied in the slave transistor with a gain equal to the ratio between aspect ratios of the two transistors:

$$\frac{I_{copy}}{I_{ref}} = \frac{(W/L)_{slave}}{(W/L)_{master}} \quad (3.4)$$

The concept of "Mirroring" was inspired as the simplest solution to make current sources avoiding current dependency on supply, process and temperature[88]. Many different current mirror schemes have already been proofed in analog integrated circuit design literature[87][88][89]. Current-voltage relationship in transistors is non linear, as a consequence compressed output voltage swing (square root of current) goes well with the reduced supply voltage. However, a slight mismatch in devices' parameters results in a considerable deviation from the aimed linearity. Therefore, several circuit schemes should be checked for better linearity over an optimal output swing. Fig.3.9b shows an example of a current mirror scheme that can be used for this purpose.

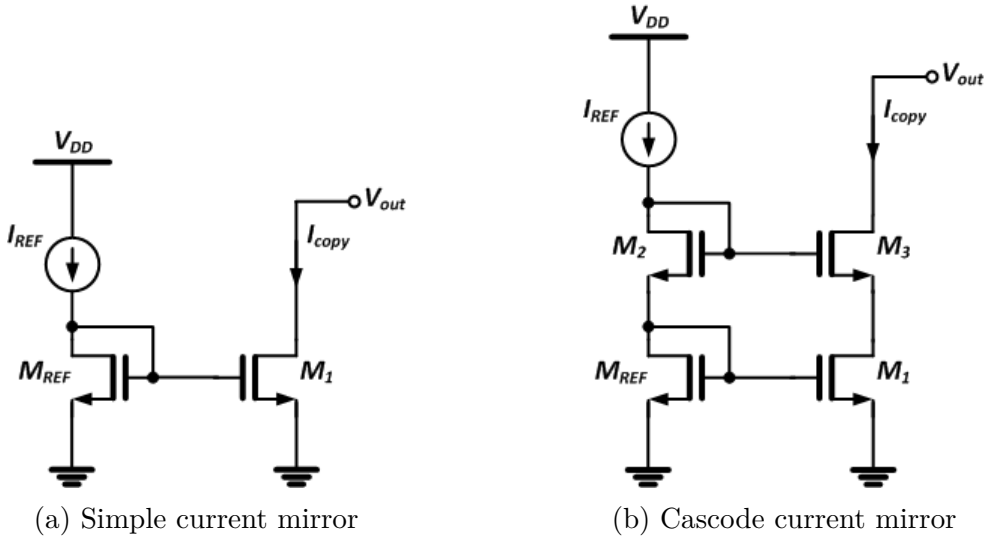


Figure 3.9: Gain stage, current mirror choice

3.4.3.1 Simple current mirror

The first simple scheme drawn in Fig.3.9a is a demonstrator of current mirroring principle. Now a simple current mirror like exemplified in Fig.3.9a should have at least V_{Dsat} at the output. This condition is necessary to drive the slave device (M_1) in saturation region. It is still a low voltage headroom, or let's say the lowest possible; which leads to high output swing.

The main drawback of this scheme is that nothing guarantees the same V_{DS} across both master and slave devices (M_{REF} and M_1 respectively). If short channel transistors are used, channel length modulation plays a crucial role that limits the output impedance and thus impacts the output characteristics[90]. MOS transistor is not anymore an ideal current source with an infinite output resistance and $I_D - V_{DS}$ characteristic plot shows a slight slope in the best cases as depicted in Fig.3.10.

Ideally, output impedance is that of the load. In practice, channel length modulation should be taken into account and output impedance is then:

$$Z_{out} = R_{load} || r_{o1} = r_{o1} \quad (3.5)$$

Where in general,

$$r_o = \left(\frac{\partial I_D}{\partial V_{DS}} \right)^{-1} \quad (3.6)$$

If R_{load} is large, $Z_{out} = r_o$ is however low,

$$Z_{out} = \frac{1}{\lambda I_D} \quad (3.7)$$

Therefore, I_D becomes dependent on the V_{DS} value. Drain current in a device affected by channel length modulation ($I_{D,\lambda}$) is formulated in Eq.3.8, and hence the current ratio formula for a simple current mirror becomes that of Eq.3.9.

$$I_{D,\lambda} = \frac{1}{2} \mu C_{ox} \left(\frac{W}{L} \right) (V_{GS} - V_{th})^2 (1 + \lambda V_{DS}) \quad (3.8)$$

$$\frac{I_{copy}}{I_{ref}} = \frac{(W/L)_{slave}}{(W/L)_{master}} \cdot \frac{1 + \lambda V_{DS,slave}}{1 + \lambda V_{DS,master}} \quad (3.9)$$

The hidden circuit driven by this slave defines the potential across it. So if $V_{DS,slave} \neq V_{DS,master}$ a copying error is generated, i.e. linearity (precision) is in risque.

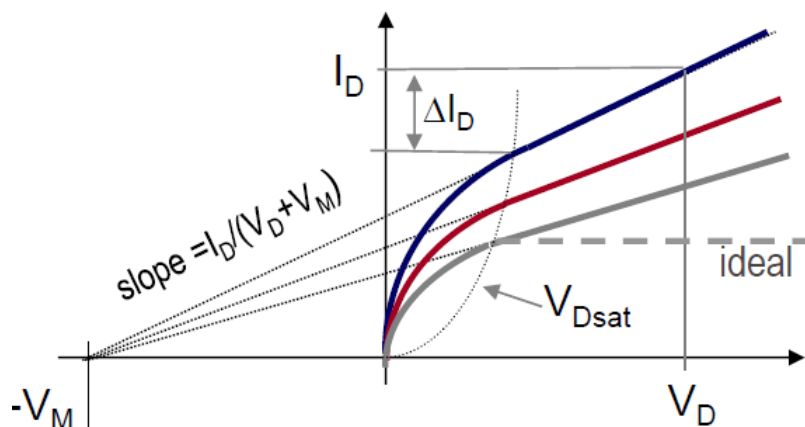


Figure 3.10: Output characteristics of a simple current mirror and an ideal current mirror. *Source: Design analogique en technologies fines, lecture by Marc Pastre from EPFL, IN2P3 summer school 2013. <http://www.in2p3.fr/actions/formation/microelectronique13/Pastre.pdf>.*

This basic current mirror was used with the previously approved current follower input stage. Devices of the current mirror were used with dimensions that are listed in table 3.3. Output swing and linearity on both gains were investigated. Then after, output voltage was checked for one photo electron equivalent signal to test both noise tolerance and response speed on the high gain path.

Component	W/L ($\mu m/\mu m$)
MN_{REF}	100/0.35
$MN_{1,HG}$	100/0.35
$MN_{1,LG}$	10/0.35
R_{HG}	5 k Ω
R_{LG}	500 Ω

Table 3.3: List of simple current mirror parameters for a gain ratio $HG/LG = 100$. R_{HG} and R_{LG} are respectively the high gain load and the low gain load.

Input signals To simulate an incident photo electron detected by the SiPM, we used SiPM model that was discussed in section 2.7. Considering a gain of $5 \cdot 10^5$ for the SiPM, that makes a charge that is equal to 80 fC at the SiPM output for one detected photon. Now to simulate that event, the current source in the model generates a pulse of $FWHM = 499 ps$ width with identical rising and falling time of 1 ps, which makes an amplitude of 160 μA per photo electron.

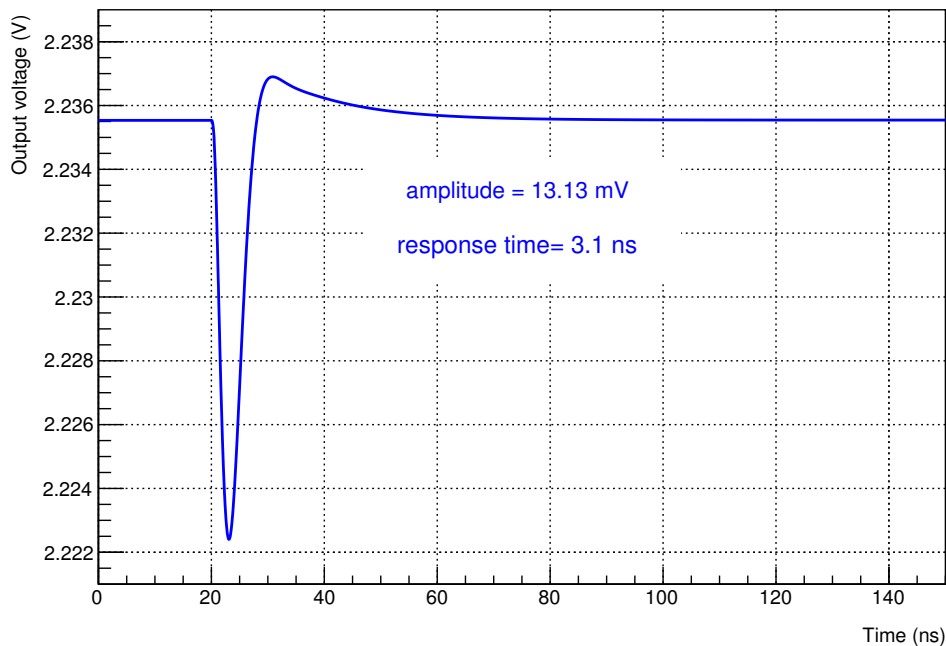


Figure 3.11: Simulated response to 1 photo electron (pe) signal measured at simple current mirror high gain output. Response time represents the rising time of this output signal calculated between the base line and the maximum of the front edge.

Output signal corresponding to one photo electron is depicted in Fig.3.11. Noise level and the covered dynamic range are shown in 3.12. The response to one photo electron shows enough level (13 mV) to be separated from noise with a limited rise time about 3 ns .

Linearity degradation may not be obvious when looking separately at high gain and low gain. Actually, we can say both gains are well linear over $200\text{ photo electrons}$ for the high gain and over $\sim 1000\text{ photo electrons}$ for the low gain. However, it can be easily distinguished that gain ratio plot (rose plot in Fig.3.12) does not show any stable constant part. Over the whole range, gain ratio shows a nonlinear decreasing that turns sharper at high rate inputs. The two gains are not of the same quality. High gain is superior to low gain, and this latter shows more clear damaged linearity at the limit of the range.

Designing MOS with longer channel decreases its speed since the speed of a MOS transistor scales down with L^2 for a constant V_{GS} and it scales down with L when I is constant. Scheme improvement may be needed to compromise both precision (linearity with a stable gain ratio) and speed (output capacitance).

3.4.3.2 Cascode current mirror

The first approach normally thought about in order to boost the output impedance is the cascode current mirror [88] shown in Fig.3.9b. Cascoding is normally used to increasing the voltage gain in amplifiers. It has another advantage here. That is to insure the same V_{DS} across both master and slave transistors of the current mirror. Therefore, desensitizing

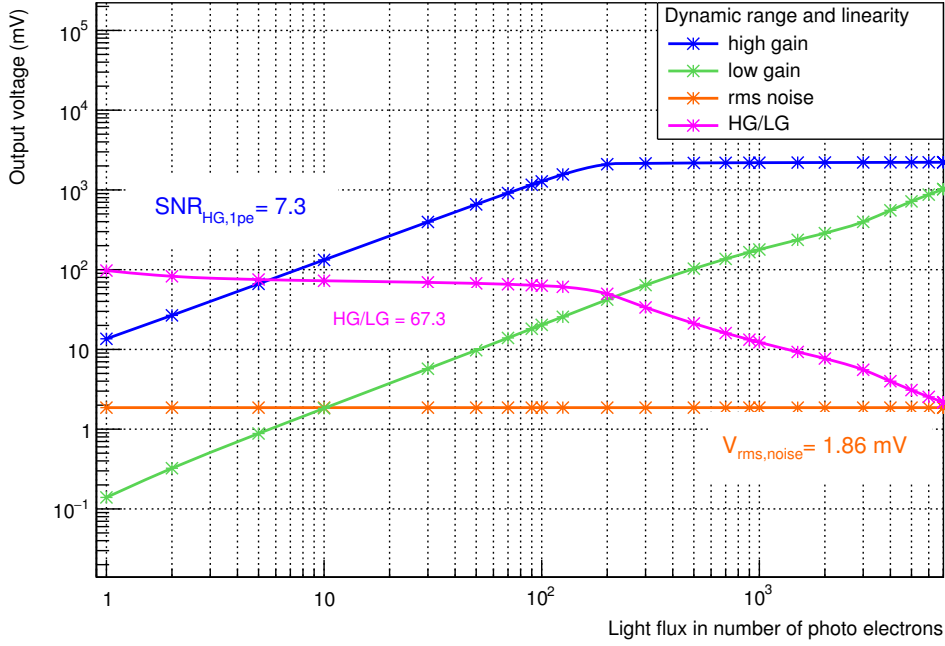


Figure 3.12: Simulated response of the preamplifier built with a simple current mirror preamplifier.

the copied current to channel length modulation and doing so minimizing the copy error by approaching an ideal current source (Fig.3.10 depicts the difference between output characteristics for both simple and ideal current mirror schemes.).

The enhanced output impedance of the cascode current mirror is given in Eq.(3.10). It can be deduced from the small signal model of the circuit depicted in Fig.3.13.

$$Z_{out} = \frac{g_{m3}}{g_{o3}g_{o1}} \quad (3.10)$$

Now, M_2 and M_3 are chosen in a way they have the same V_{GS} . Looking at Fig.3.9b, we can write that:

$$\left. \begin{aligned} V_{G,M_2} &= V_{GS2} + V_{D,M_{REF}}, \\ V_{G,M_2} &= V_{GS3} + V_{D,M_1}, \\ V_{GS2} &= V_{GS3}, \end{aligned} \right\} \Rightarrow V_{D,M_{REF}} = V_{D,M_1} \quad (3.11)$$

This technique unifies potential across both sides of the mirror. It shields the slave device from voltage variation due to load circuit and suppresses the effect of channel length modulation.

We should keep in mind that $V_{out,min} = V_{GS,3} - V_{th} + V_{GS,1}$, i.e. the added circuit above the slave must guarantee a minimum output voltage of:

$$V_{out,min} = 2V_{Dsat} + V_{TH} \quad (3.12)$$

Voltage base line has increased by $V_{Dsat} + V_{th}$. i.e, we obtain a lower output swing than that given by the basic scheme of the simple current mirror. Which will damage large

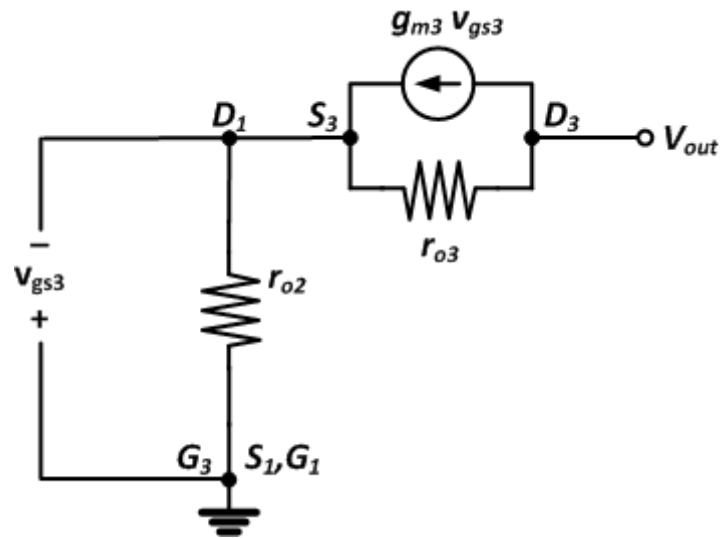


Figure 3.13: Cascode current mirror - small signal model

signals by the fact that output transistors will soon be saturated. And by consequence, this scheme covers smaller dynamic range than the basic one. The question at this step is how to improve Z_{out} without wasting on output swing? Solution is presented in Fig.3.14.

3.5 Proposed preamplifier and simulation results

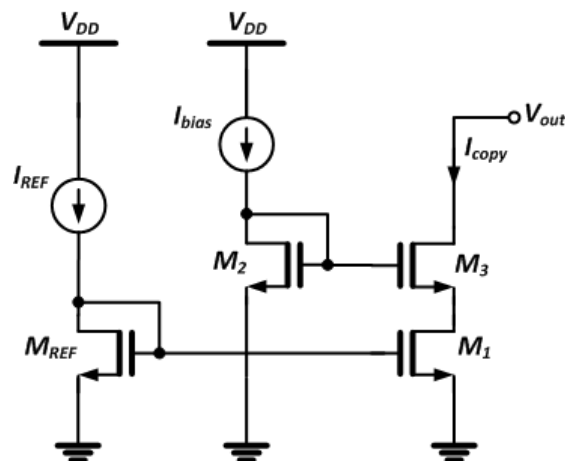


Figure 3.14: Improved current mirror

Fig.3.14 shows another scheme whose output impedance is the same as for cascode current mirror ($Z_{out} = g_{m3}/(g_{o1}g_{o3})$). However, it decreases the voltage headroom a little bit in respect to the cascode scheme. The slave part is composed of two cascaded transistors: M_1 and M_3 . The difference from the cascode current mirror is that M_1 and M_3 are biased separately. An additional device M_2 is used to correctly bias M_3 to saturation.

Now if all is biased correctly, M_1 is in saturation so its drain potential is at least $V_{D,M_1,min} = V_{Dsat}$. In addition, M_3 should also be in saturation, but its gate voltage should at least provide $V_{TH} + V_{Dsat,M_1}$ not to disturb the operation of M_1 . Eq.3.13 develops output analysis.

$$\left. \begin{array}{l} V_{GS,MREF} = V_{TH}, \\ V_{DS,M_1} = V_{Dsat}, \\ V_{GS,M_2} = V_{TH} + V_{Dsat}, \\ V_{DS,M_3} = V_{Dsat}, \end{array} \right\} \Rightarrow V_{out,min} = 2V_{Dsat} \quad (3.13)$$

As a consequence, lower voltage is lost on the output. Load circuit should maintain not less than $2V_{Dsat}$ which is lower than that of the cascode current mirror by an amount of V_{TH} . A larger output swing is then allowed. From the output swing point of view this scheme seems appropriate (the best so far) for our needs.

The final scheme of the pre-amplifier including the super common gate as its input stage, bias circuit and both high gain and low gain; is drawn in Fig.3.15. Although a new bias circuit is involved, the same bias current is reused to bias the extra transistor in this slave path M_3 .

A major advantage of this choice is that even when high gain path gets saturated, it doesn't affect the low gain performance. From the current point of view, we can say that high gain and low gain are isolated one from the other.

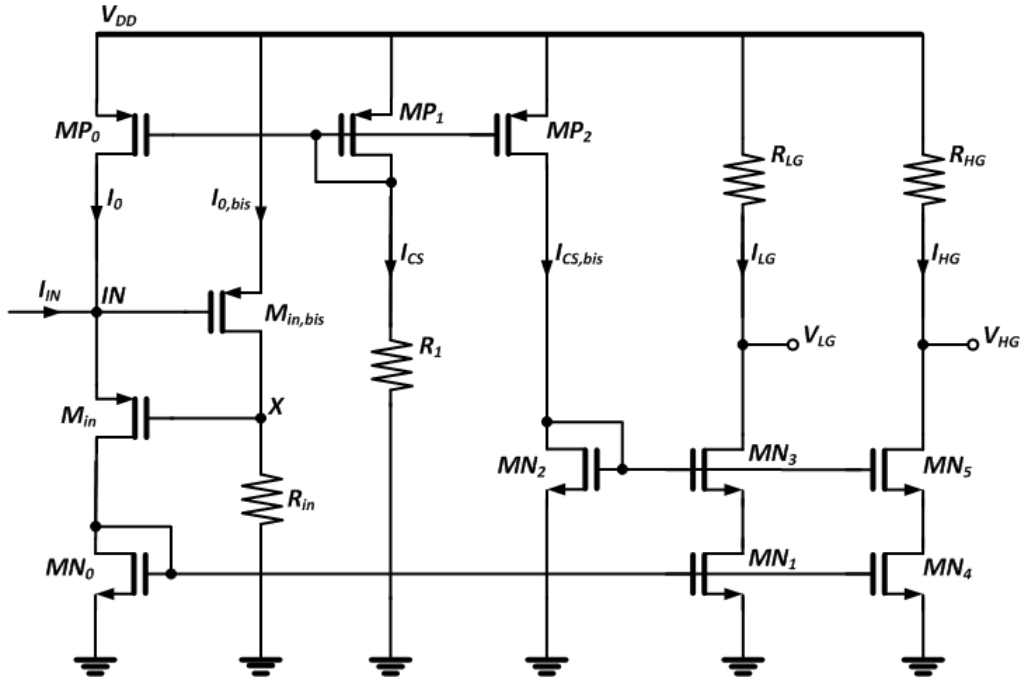


Figure 3.15: Pre-amplifier, final scheme. MP_1 , R_1 , MP_2 , MN_2 forms the general polarization circuit that is common for all the sixteen preamplifiers.

In simulation, pre-amplifier takes its input signals from the output of the SiPM model explained in section.2.7, and input signals consider the argument mentioned in section.3.4.3.1 (input signals paragraph). The main criteria to judge its performance are

response speed, linearity, dynamic range, gain ratio stability, as well as the signal to noise ratio for the smallest input signal (i.e, the single photo electron signal).

Attributing suitable dimensions to each of $MN1$, R_{LG} , $MN4$, and R_{HG} defines how we deal with signals. Here we have two scenarios: making gain by a transimpedance amplification or by current adjustment. Keeping in mind that we need both gain branches to provide the best performance without affecting each other, while different scenarios could show benefits for one but not the other gain path.

3.5.1 Symmetric currents (transimpedance gain)

Fig.3.16 and Fig.3.17 shows the results when devices' sizes are chosen so that current is copied into both high and low gains with no adjustment, i.e, with a gain of unity. Load resistors are sized to get different voltages on both sides. Table.3.4 is a list of the used dimensions for high and low gain branches.

Component	W/L ($\mu/m\mu m$)	$i_d(\mu A)$
MP_0	43.96/1	-150.7
MP_1	41.20/1	144
MP_2	28/1	99.6
MN_2	10/9	99.6
M_{in}	700/0.35	-150.7
$M_{in,bis}$	300/0.35	-172.5
MN_0	500/0.35	150.7
MN_1	500/0.35	158.9
MN_3	12.58/0.35	158.9
MN_4	500/0.35	158.2
MN_5	12.58/0.35	158.2

R_{in}	10 $k\Omega$
R_1	10 $k\Omega$
R_{LG}	1 $k\Omega$
R_{HG}	5 $k\Omega$

Table 3.4: List of devices' dimensions for the transimpedance gain scenario.

In spite of the very good measurement of the single photo electron signal on the high gain, rising time is more than $3ns$ which is good. Besides, low gain can not cover much more signals than the high gain. On the low gain saturation is quickly reached and it is hopeless to achieve the demanded 2000 *photoelectrons*. Low gain hardly covers 400 photo electrons. Consumption will be higher in this case due to the same current level as in high gain that passes in the low gain branch. Considering a total number of sixteen preamplifiers having in common the polarization part mentioned in Fig.3.15 we can find a total consumption of $\sim 34.6mW$.

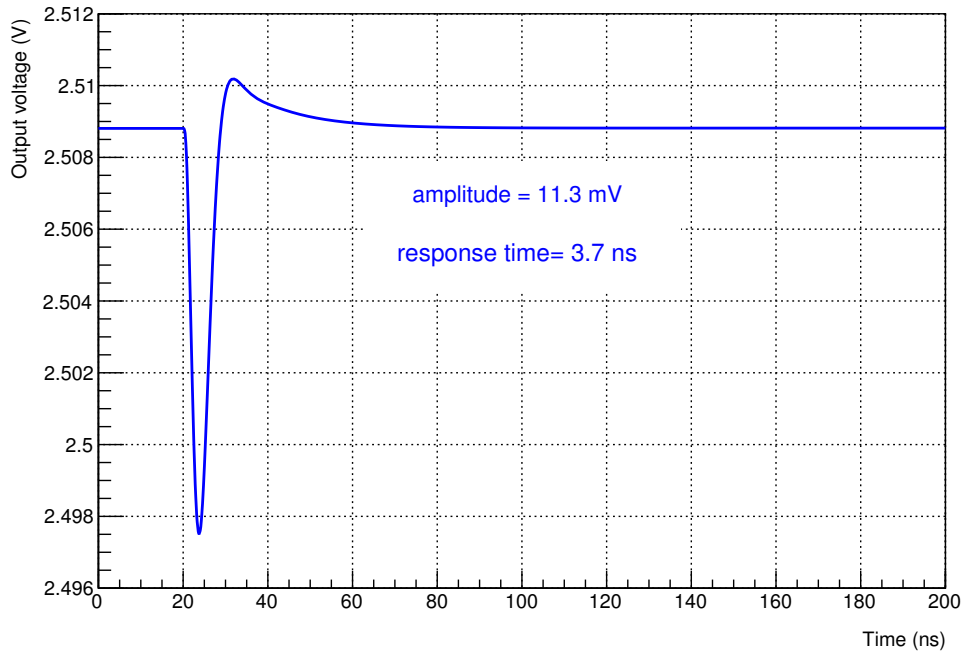


Figure 3.16: Simulation of high gain response to one photo electron signal according to the symmetric currents scenario.

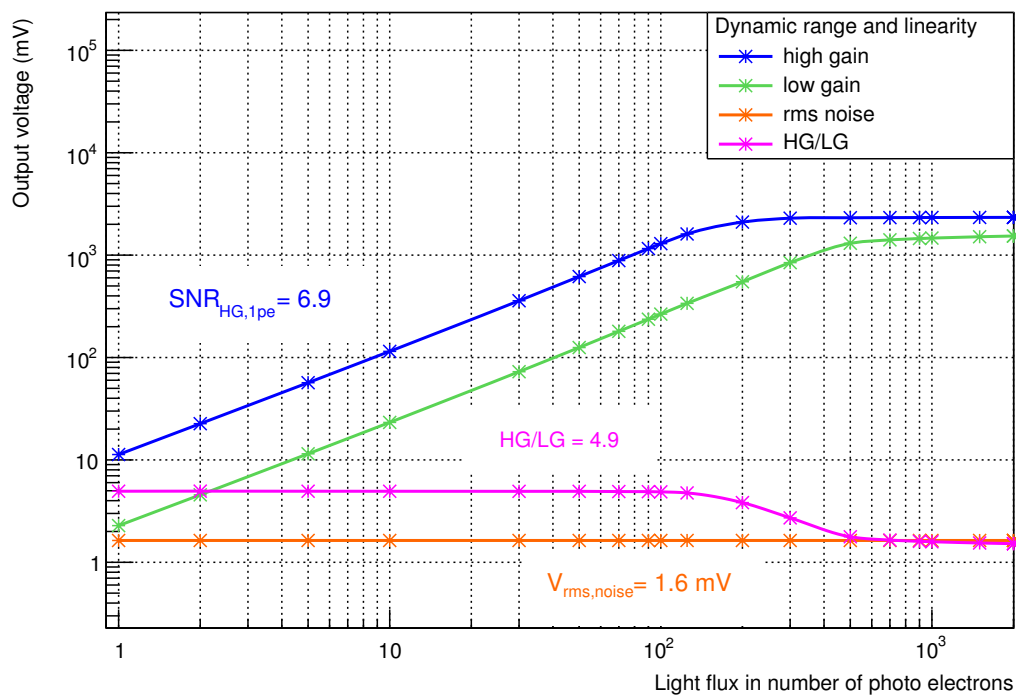


Figure 3.17: Symmetric currents (transimpedance gain) scenario, preamplifier simulated results of the high gain response (blue), low gain response (green) to input signals ranging from 1 to 7000 photo electrons.

3.5.2 Symmetric loads (current gain)

In this scenario, devices are sized to copy current in the high gain path with no gain, while on the low gain side, only a fraction of this current is copied. Symmetric loads are used on both sides. Table.3.5 is a list of used devices that shows a current gain of unity on the high gain while on the low gain we copy a fraction 1/5 of the current.

Component	W/L ($\mu/m\mu m$)	$i_d(\mu A)$
MP_0	43.96/1	-150.7
MP_1	41.20/1	144
MP_2	28/1	99.6
MN_2	10/9	99.6
M_{in}	700/0.35	-150.7
$M_{in,bis}$	300/0.35	-172.5
MN_0	500/0.35	150.7
MN_1	100/0.35	32.8
MN_3	12.58/0.35	32.8
MN_4	500/0.35	158.2
MN_5	12.58/0.35	158.2

R_{in}	10 k Ω
R_1	10 k Ω
R_{LG}	5 k Ω
R_{HG}	5 k Ω

Table 3.5: List of devices' dimensions for the current gain scenario.

Depicted in Fig.3.18, high gain responds slowly (rising time more than the standard 3ns) to the one photo electron signal, even if it shows good signal level. Fig.3.19 shows simulated performance of the pre-amplifier working in this scenario. Low gain hardly reaches the limit of 700 photo electrons before getting saturated. Power consumption was found about $\sim 28 mW$ less than that of the previous scenario.

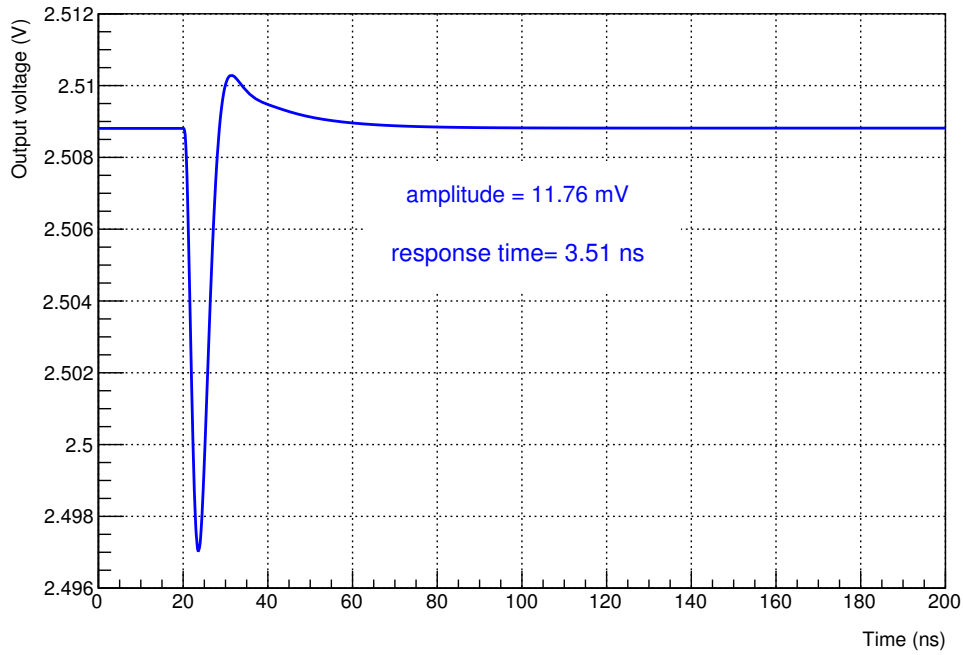


Figure 3.18: High gain response to one photo electron signal according to Symmetric loads scenario.

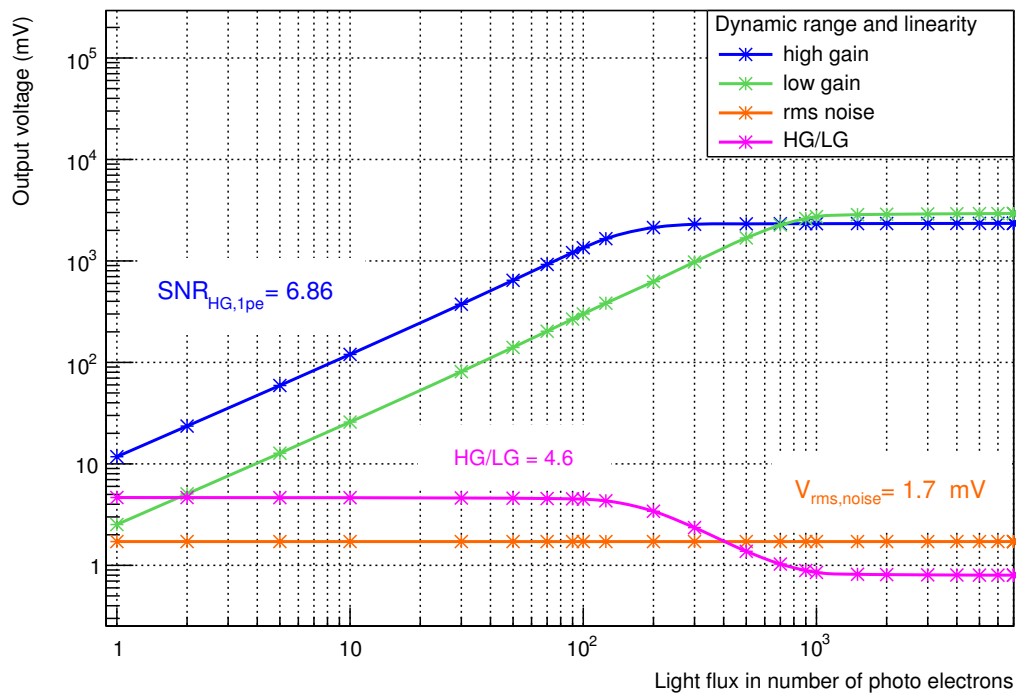


Figure 3.19: Symmetric loads (current adjustment) scenario, preamplifier simulated results: (blue) on high gain, (green) on low gain. Input signals range from 1 to 7000 photo electrons.

3.5.3 Combination of transimpedance and current adjustment

In this scenario current signal is copied to high gain path with a gain of unity. It was found enough to measure the signal of the single photo electron with good signal to noise ratio (section.3.5.1 and section.3.5.2). In order to respect the high level of current signal at the limit of the desired dynamic range a fraction of input current is copied into the low gain path. Low gain load is also lowered in order to boost the maximum measured signal as far as possible. Design devices and dimensions are listed in Table.3.6. Here after are simulation results of this new configuration.

Component	W/L ($\mu m\mu m$)	$i_d(\mu A)$	$g_m(\mu A/V)$	$g_{ds}(\mu A/V)$
MP_0	45/1	-160	746	10.41
MP_1	40/1	-144.4	675.8	7.35
MP_2	45/1	-164.3	767	7.9
MN_2	10/9	164.3	195.1	0.62
M_{in}	700/0.35	-160	3129	85.7
$M_{in,bis}$	300/0.35	-170.4	2744	78.2
MN_0	100/0.35	160	3632	33.3
MN_1	10/0.35	18.72	295.5	3.32
MN_3	10/0.35	18.73	301.1	5.1
MN_4	100/0.35	172.2	2796	32.2
MN_5	10/0.35	172.2	963.9	20.5

R_1	15 k Ω
R_{in}	10 k Ω
R_{LG}	500 Ω
R_{HG}	5 k Ω

Table 3.6: List of preamplifier component parameters and DC operating point.

3.5.4 Response speed

This characteristic is tightly related to the effective detectable dynamic range. It defines the time it takes for the readout electronic channel to output a maximum signal level in response to a given input. Output pulse width also affects the system's time resolution since the readout electronics should recover fast in order to minimize the dead time and the pile up phenomenon.

High gain can measure one photo electron with a good level 14mV that guarantees a good signal to noise ratio. It also responses in 2.5ns (within the standard 3ns) which is very important for trigger system strategy. Fig.3.20 shows a pulse corresponding to 1 photo electron simulated at the output of SiPM model (section.2.7). This pulse represents the input of one readout channel. Since low gain is insensitive to such input because of the noise level and its gain of current fraction, observation is made on the high gain output. The resulting pulse as depicted in Fig.3.21 is narrow that reduces the dead time needed by the channel before recovering and being able to measure another successive signal. This fact alleviates the risk of piling up several successive signals produced by different successive photo electron packets detected by one SiPM macro pixel and delivered to the corresponding readout channel.

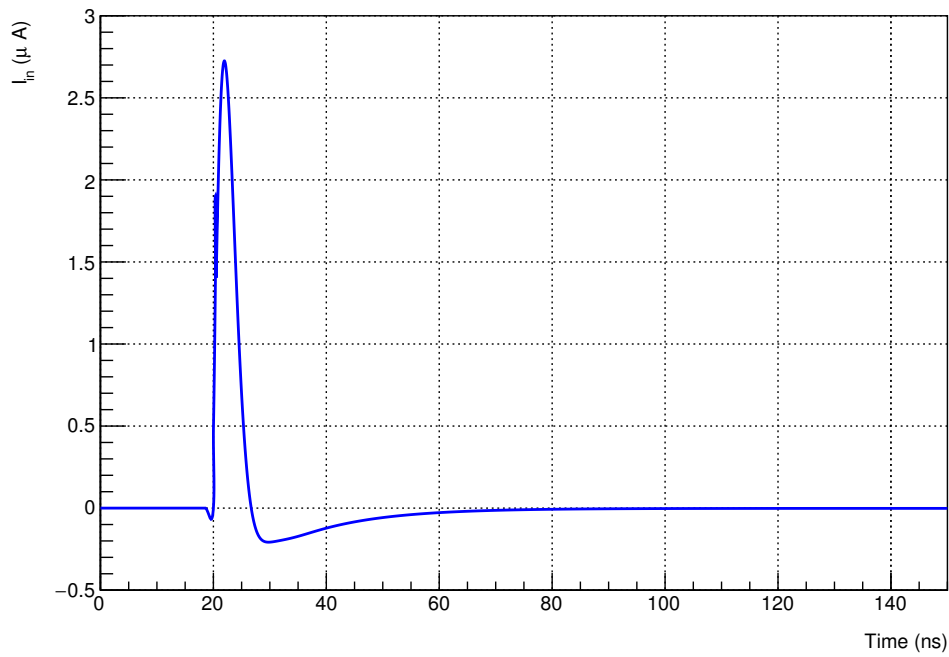


Figure 3.20: Current pulse *simulated* at the output of the SiPM-model for one photo electron equivalent input pulse.

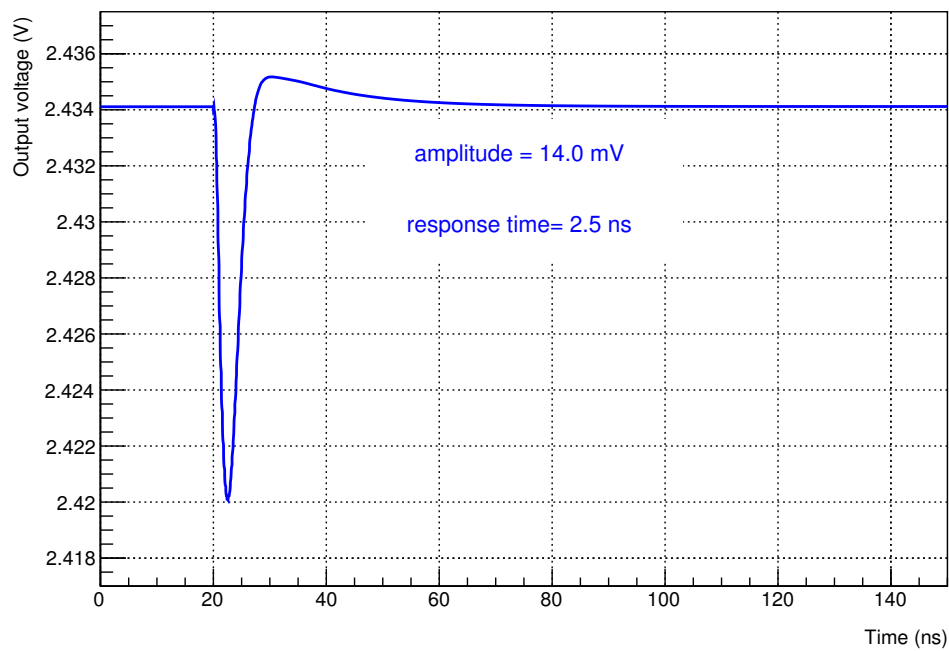


Figure 3.21: Voltage signal *simulated* at high gain output as a response to one photo electron response of the SiPM model.

3.5.5 Dynamic range, Linearity

Simulation results in Fig.3.22 show good linearity especially on the high gain. On the one hand, high gain effectively measures low signal level due to low light flux. We can clearly see in Fig.3.22 that the single photo electron signal is about 14 mV a very good level that could sustain for next stages. The whole plot lays above the noise. Linearity error on the HG is depicted in Fig.3.23. Linearity error passes the desired 3% for small signals ($1 - 20\text{ pe}$) but it lays beneath $\pm 3\%$ for the rest of the dynamic range. High gain covers a good range with a good linearity before reaching its saturation limit at 125 photo electrons per macro pixel.

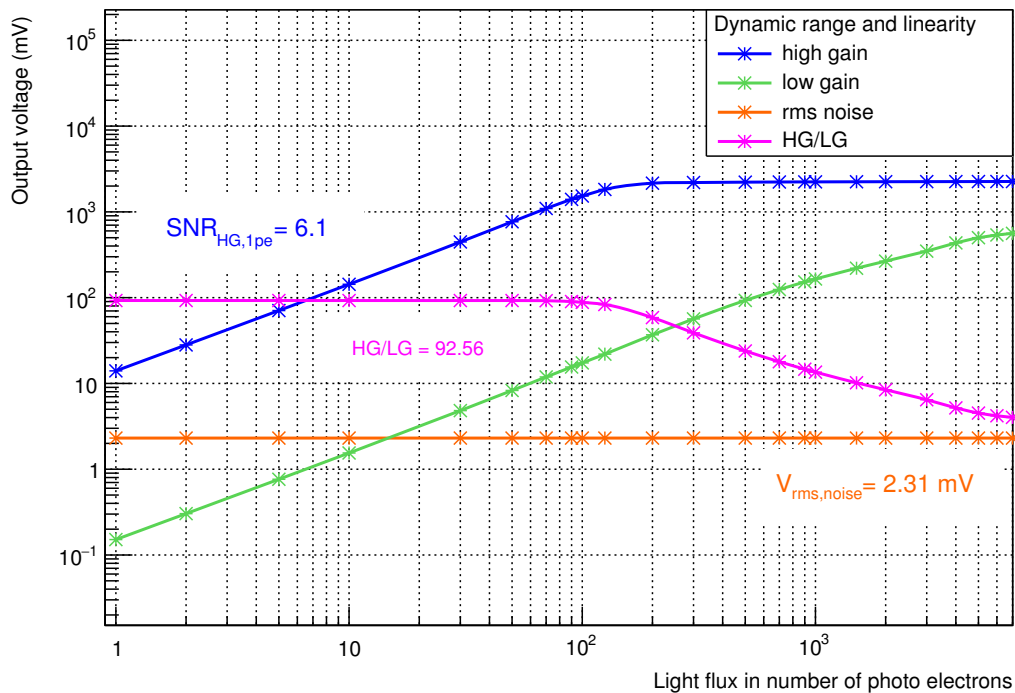


Figure 3.22: Preamplifier simulated results on dynamic range for the transimpedance and current adjustment scenario.

On the other hand, low gain covers a wider range between $\sim 15\text{ pe}$ and 2000 photo electrons as depicted in Fig. 3.22. As predicted in section.3.4.2 the first part of low gain response goes beneath noise. Low gain is useful for signals higher than 15 photo electrons and till more than 2000 photo electrons. However, it shows a deviation from the straight line. The linearity error on the low gain is shown in Fig.3.24 where it is found to be in a band between 3% and 10% for input levels between $125 - 1000\text{ pe}$.

For both gains, linearity correction and calibration may be necessary for analyzing signals lower than 20 pe and over 1000 photo electrons. Above all these, the two gains intersect over about one decade with a constant stable ratio shown in Fig.3.22 (the rose plot points out a gain ratio of ~ 92). This area will be helpful for system adjustment and calibration.

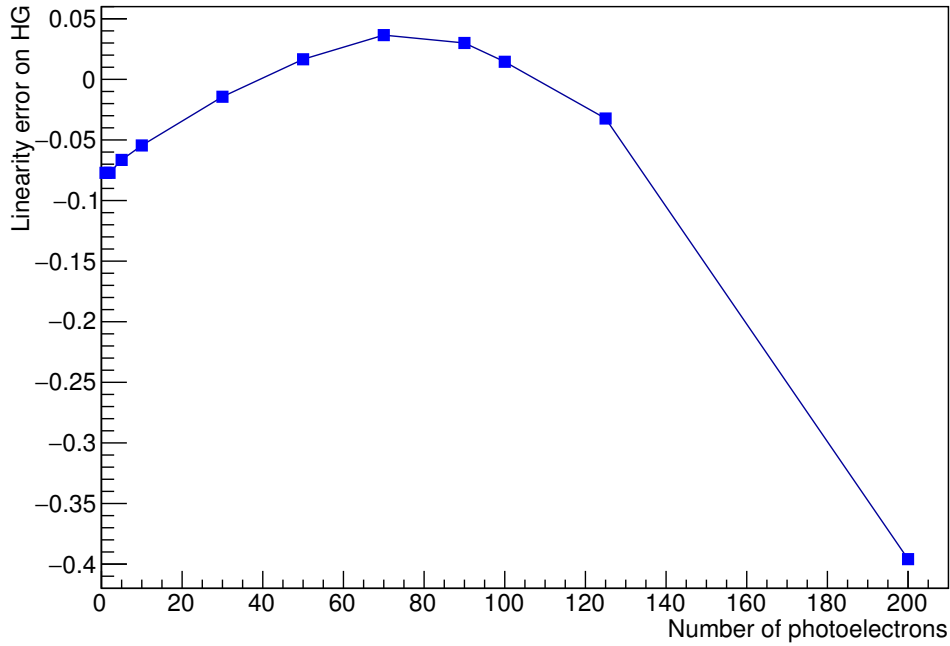


Figure 3.23: Linearity error on the high gain can be seen about 8% at the beginning of the covered range. The error stays in the range of 3% for inputs between 20 pe and 125 pe which is the maximum covered by the HG before it gets saturated.

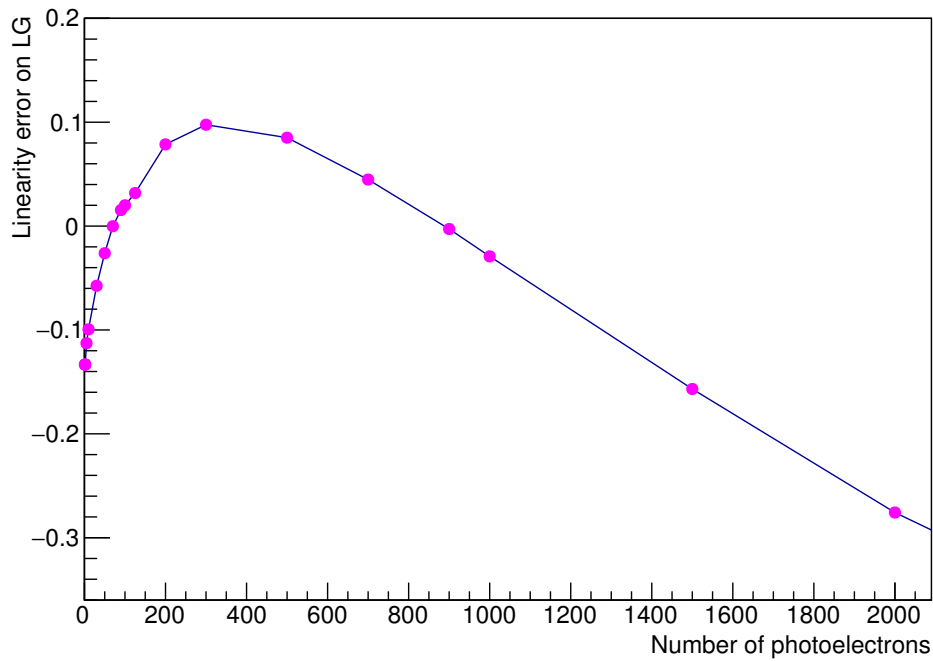


Figure 3.24: Linearity error on the low gain is about 3% for an input of 125 pe , it increases to 10% before drawing back to 3% for an input of 1000 pe .

3.5.6 Signal to noise ratio

From readout-electronics perspective, and after putting aside the distortion in signal form caused by a bad choice of operating point (i.e, if the operating point is perfectly chosen so that preventing signals from being clipped), noise is the main disturbance that signal may suffer from. Noise can limit the performance of the electronic circuit.

Preamplifier performance toward noise should be heeded in order to achieve the promised minimum detectable signal of the dynamic range with least or no compromises and also to produce reliable signal level that can sustain the rest of the readout and signal processing circuit.

Eliminating the environmental noise sources, noise is mainly produced in MOS circuits according to two mechanisms⁵⁶, thermally (thermal noise also known as Johnson noise or Nyquist noise) and industrially-physically (flicker noise also known as low frequency noise or $1/f$ noise).

Noise is a random phenomenon whose value can not be predicted at any time. It is then presented by the probability density function *PDF* of its amplitude in the time domain. It can also be presented by its power spectral density *PSD* in the frequency domain.

Thermal noise is due to the random motion of charge carriers in a conductor. This random motion is induced by the thermal energy and could be found in resistors as well as in transistors since the channel material of MOS transistors is resistive.

The current spectral density of thermal noise in a resistor is expressed in Eq.3.14 and in a MOS transistor by Eq.3.15. Where $K = 1.38 \cdot 10^{(-23)} [m^2 kg s^{-2} K^{-1}]$ is Boltzmann constant, γ depends on the channel length. It is found to be $2/3$ for long channel MOS, whereas it takes larger values ($2 - 3$) for short channel MOS[91][92][93][94]. It is then measured in I^2/Hz .

$$S_{ith-R}(f) = \overline{I_{n,th}^2} = \frac{4kT}{R} \quad (3.14)$$

$$S_{ith-MOS}(f) = \overline{I_{n,th}^2} = 4kT(\gamma g_m) \quad (3.15)$$

Thermal noise owing to resistive nature of gate material in the preamplifier can be reduced while drawing the layout by folding the used transistors or connecting the gate on both sides of each transistor[88].

The origin of flicker noise was the subject of several theories e.g. [95][96][97]. However, two theories seem to dominate among them[98].

The first one says that flicker noise is produced by the imperfect implementation of gate-oxide over the silicon surface. Traps will catch and release charge carriers in the channel causing a disturbance in the surface potential and hence a fluctuation in the number of charge carrier in the channel[99][100].

⁵Other sources of noise is shot noise which is usually generated at a junction between two materials where exist an electric field. Charge carriers may flow across the potential barrier. The probability that one carrier crosses the barrier is independent of the other carriers. So charge movement has a discrete nature and it is uncorrelated. The result is the so called shot noise given by $S_{ishot} = 2qI(I^2/Hz)$.

⁶In MOS transistors, shot noise is due to gate leakage current into the channel, and the ac gate current due to the gate-channel capacitance that becomes important in RF amplifiers for example[90].

The other theory attributes the origin of flicker noise to fluctuations in the charge carrier mobility because of their interaction with the lattice fluctuations[101]. It is worth mentioned that both theories may reunion to explain flicker noise in one device[102].

In NMOS devices dominates the theory of carrier number fluctuations[103], whereas in PMOS counterparts⁷ it is the theory of mobility fluctuations[107].

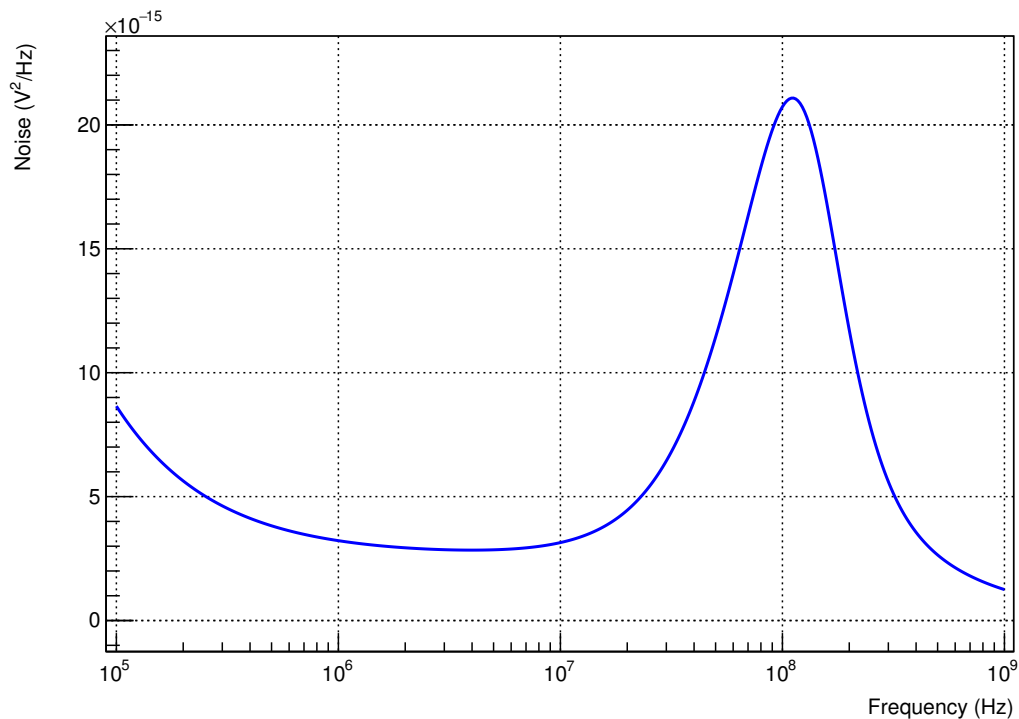


Figure 3.25: Noise simulated on the high gain output of the preamplifier. RMS noise is the square root of the integration of this plot over the same frequency range. RMS noise is found to be 2.3 mV .

Noise in the proposed preamplifier (for a combination of transimpedance and current adjustment) was verified and is shown in Fig.3.25. Flicker noise dominates at low frequencies which is totally expected as its spectral density can be described by Eq.(3.16)[91].

$$S_{if}(f) = \overline{I_{n,1/f}^2} = g_m^2 S_{vf}(f) \quad (3.16)$$

Where according to the first theory:

$$S_{vf}(f) = \overline{V_{n,1/f}^2} = \frac{K}{C_{ox}} \frac{1}{WL} \frac{1}{f^\gamma} \quad (3.17)$$

And according to the second theory:

$$S_{vf}(f) = \overline{V_{n,1/f}^2} = \frac{K(V_{GS})}{C_{ox}} \frac{1}{WL} \frac{1}{f} \quad (3.18)$$

⁷Buried-channel PMOS keeps charge carriers farther away from the $Si - SiO_2$ surface and thus they are less affected by the interface traps[104][105][106].

Where K is called flicker noise coefficient, f is the frequency of the trap-release process of the charge carriers. While supporters of the first theory on the origin of flicker noise says that K depends on fabrication details and that it is independent of the bias conditions[108][109]. Moreover, noise spectral density is proportional to $1/f^{\dot{\gamma}}$ instead of $1/f$ (Eq.3.17) where $0.8 < \dot{\gamma} < 1.2$ because the spatial distribution of the traps in the oxide is not uniform[108]. Those who support the second theory show the dependency of K on V_{GS} and noise spectral density is proportional to $1/f$ (Eq.3.18). K is in the order of $10^{-25}(V^2F)$ in CMOS processes[88][110]. \dot{C}_{ox} is the oxide capacitance and it is of the order of $(fF/\mu m^2)$.

The spectral density of the total noise in MOS transistor can then be summarized in Eq.3.19 as thermal noise sources and flicker noise sources are uncorrelated.

$$S_i(f) = S_{ith}(f) + S_{if}(f) \quad (3.19)$$

Since the bias current source is built with relatively low transconductance PMOSs and a big resistor ($R_1 = 15K\Omega$), its flicker noise effect on the output signal is low and can be neglected. The same argument is applied to the input stage formed of two wide PMOSs and a big resistor R_{in} . However, the transimpedance amplifier built of NMOS current mirror of big transconductance and relatively narrow channels for the high gain path makes its flicker noise contribution dominant to those of the other components. For the low gain path, the slave NMOS has narrower channel but smaller transconductance making its flicker noise negligible.

For one preamplifier, Table.3.7 lists the contribution of each component in the total noise over a frequency bandwidth between 100 kHz and 1 GHz.

Component	noise type	Noise contribution	% of total
$M_{in,bis}$	id	$2.75e - 06$	51.6
MN_4	id	$8.1e - 07$	15.22
M_{in}	id	$5.53e - 07$	10.39
MN_0	id	$4.83e - 07$	9.07
R_{HG}	rn	$3.81e - 07$	7.16
R_{in}	thermal	$1.19e - 07$	2.23
R_{HG}	thermal	$8e - 08$	1.5
MP_0	id	$5.67e - 08$	1.07
MP_1	id	$4.8e - 08$	0.9
MN_5	id	$1.83e - 08$	0.34
MP_2	id	$5.93e - 09$	0.11
R_1	thermal	$5.57e - 09$	0.1
$M_{in,bis}$	rs	$2.98e - 09$	0.06
MN_4	fn	$2.78e - 09$	0.05
Integrated noise summary (in V^2) sorted by noise contributors.			
Total summarized noise = 5.32e-06.			
Total input referred noise = 4.62e-08.			

Table 3.7: Noise summary showing the contribution of each device in the preamplifier. **id** is the drain-source resistance thermal noise, **rn** is the noise due to the physical resistor (i.e, thermal noise), **rs** is the source parasitic thermal noise, **fn** is the flicker noise.

Three dominant devices are responsible of output noise in the circuit. These are, $M_{in,bis}$, MN_4 and M_{in} . All of which contribute in the drain-source resistance thermal noise (pointed out by *id*) as they are the largest devices in the circuit and hence they show the highest values of transconductances. However, the preamplifier shows good performance towards noise as seen in Fig.3.22. RMS noise is the square root of the total summarized noise shown in Table.3.7. It is calculated over the same band width (100 kHz – 1 GHz) and it is found to be about 2.307 mV (the value was shown and used to calculate signal noise ratio in Fig.3.22). As depicted in Fig.3.22, this level still doesn't affect the measurement of the single photo electron at the high gain path.

The preamplifier can then be said to cover a real dynamic range between 1 to 2000 photo electrons thanks to its two gains. It is still sensitive to low signals down to one photo electron with good signal to noise ratio Fig.3.21 and Fig.3.22.

3.5.7 Power consumption

A major criterion in all systems and so as for the preamplifier is its power consumption. Table.3.8 details the calculation of the static power being consumed in the preamplifier. Voltage source used for the design is 3.3V. Calculation is done for the whole block consisting of 16 channels.

Branch	$I(\mu A)$	$Power/channel(mW)$	$Power/16channel(mW)$
I_0	160	0.528	8.448
$I_{0,bis}$	170.4	0.56232	8.99712
I_{cs}^*	144.4	0.47652	0.47652
$I_{cs,bis}^*$	164.3	0.54219	0.54219
I_{LG}	18.72	0.061776	0.98842
I_{HG}	172.2	0.56826	9.09216
total power consumption		2.73907	28.54441

*These values are common for the 16 channels.

Table 3.8: Power consumption calculation

About 30mW is consumed in the entire pre-amplifier. simulation shows good power saving at this stage in respect to current mode preamplifiers readout chips existing so far[111]. The preamplifier built with both current and transimpedance adjustment shows to full fill the specifications defined at the beginning of this chapter. It covers wit good linearity the demanded dynamic range (1 up to 2000 photo electrons) thanks to its dual gain design. Its high gain path response within 3ns to the single photo electron signal with a signal to noise ratio of about 6. As a consequence, this scenario will be adapted for the readout chip ALPS. The added gain control facilities are described in the following.

3.6 Slow control

A gain dispersion of about 10% among the 16 macro pixels was found from SiPM matrix characterization in section.2.6.6 (Fig.2.33). The 16 output signals being summed together, they should respect a uniform standard of gain. This gain dispersion will be controlled

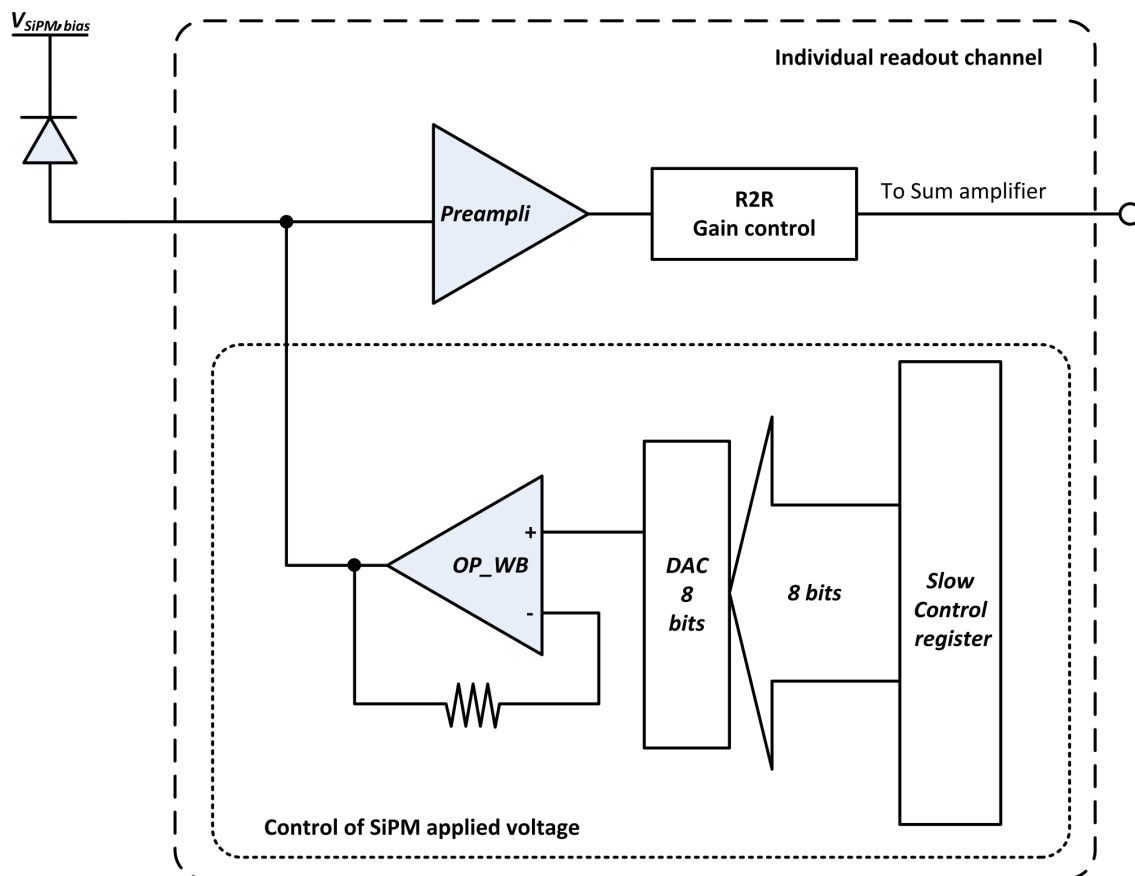


Figure 3.26: Controlling the applied voltage at the anode of one macro pixel (SiPM).

and minimized on two levels: at the detector level (optical gain adjustment) and at preamplifier level (electronic gain adjustment).

3.6.1 8-bit DAC for per-pixel over-voltage control

Since photo-detector gain is proportional to the applied over voltage, it can be adjusted via controlling the over voltage of each macro pixel individually. This is the role of the DAC included in each readout channel preceding to the preamplifier input. The optimal operating point for a well biased pixel lays between $70V$ and $72V$ (i.e. $2V$ of margin). The optimal gain is then defined by tuning the over voltage of every macro pixel between these two values. Considering the limited voltage supply of the chosen technology $3.3V$, $2V$ full scale sounds suitable. AMS kit provides DAC blocs of several resolutions and that were found reliable in previous experiences[112] and POLAR chip. DAC of 8-bit resolution can largely attempt this $2V$ full scale range with an adequate precision defined as the least significant bit (LSB) of $7.8mV$. A higher resolution makes small gain variations (given the smaller LSB). Gain gets less sensitive to over voltage variation at each step (LSB). 8-bit resolution is then enough and a standard AMS 8-bit DAC is then used. The block diagram of the over voltage control is drawn in Fig.3.26.

DAC8 cell followed by an op-amp *OP_WB* from the *A_CELLS* library of the AMS technology is used. The architecture is a dual resistor divider each of which consists of 16 resistors. This DAC has a high output impedance that depends on the received code.

Because of code dependency, this DAC requires a low-offset operational amplifier whose common mode range includes both the negative and positive reference voltages of the DAC (according to AMS DataSheet).

The code used to control the over voltage is set in a Labview program that masters the slow control process. It will be written in an in-chip register that feed the DAC 8 bits.

3.6.2 Preamplifier gain correction

The second gain adjustment step is via controlling the electronic gain of each preamplifier in every channel. There exist many solutions inspired from DAC's known structures. Binary weighted-resistor or weighted-capacitor network are just examples[113]. The main drawback of many of these structures is that for long control word (more than 4 bits), accuracy in resistors' or capacitors' values is not guaranteed because of the large spread in the smallest and largest components[114](exponentially increasing capacitance spread). For some other structures like potentiometric DACs, the main drawback is the impractical large number of required resistors (2^n) and switches ($2^{n+1} - 2$). For these reasons R-2R architecture is preferred.

The principle of the so called R-2R ladder is shown in Fig.3.27. It can be looked at as a high speed current divider.

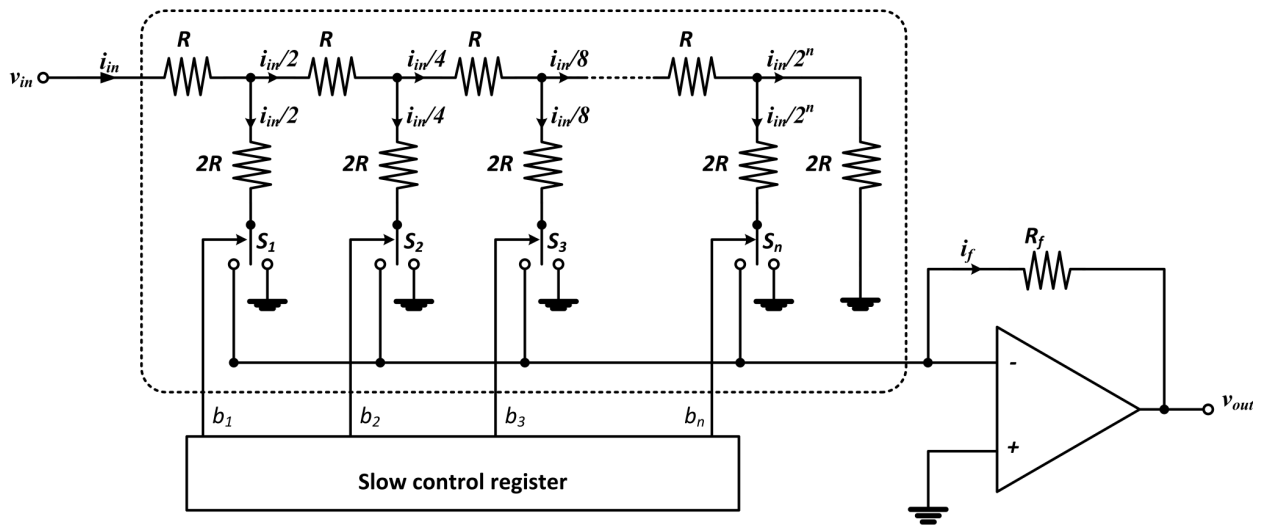


Figure 3.27: Adjusting a channel's gain by R-2R ladder

Accuracy, precision and stability are assured by limiting the used resistances to two values $R, 2R$. Where the last $2R$ resistor has only a terminating function. Adapting this arrangement, preamplifier will always be loaded by the same charge $2R$ regardless the position of the digitally controlled switches.

At each node, currents and voltages are binary-weighted:

$$i_{j+1} = \frac{1}{2}i_j \quad \text{hence,} \quad v_{j+1} = \frac{1}{2}v_j \quad (3.20)$$

Since the precedent circuit always sees $2R$ resistance, the pulled current into the structure is:

$$i_{in} = \frac{V_{in}}{2R} \quad (3.21)$$

According to the control word, ladder currents are diverted to the ground or to the virtual ground of the following operational amplifier (op-amp). The total current flowing out of the R-2R ladder can be written as:

$$i_{out} = \frac{i_{in}}{2}b_1 + \frac{i_{in}}{4}b_2 + \frac{i_{in}}{8}b_3 + \dots + \frac{i_{in}}{2^n}b_n \quad i.e. \quad i_{out} = i_{in} \sum_{k=1}^n \frac{b_k}{2^k} \quad (3.22)$$

And since $i_f = i_{out}$ the consequent output voltage is then:

$$v_{out} = -R_f i_{out} = -R_f \cdot i_{in} \sum_{k=1}^n \frac{b_k}{2^k} \quad (3.23)$$

For $R_f = 2R$, substituting Eq.3.21 in Eq.3.23 the weighted output voltage is expressed in Eq.3.24. Output voltage is proportional to the control word.

$$v_{out} = -v_{in} \sum_{k=1}^n \frac{b_k}{2^k} \quad (3.24)$$

Now how to define the length of the control word? Like the over voltage DAC, for a full scale potential of $2V$, 8-bit resolution means $LSB = 7.8mV$ and the output will vary among 2^8 values which is enough for this purpose. A higher resolution would not be more effective. The control word will be generated by the slow control system from outside the chip (Labview program). The 8 bits are stored in a register included in the gain control bloc inside the chip.

In order to properly polarize the operational amplifier (op-amp), its non-inverting input is attached to a reference voltage $V_{ref} = 1V$. A minimum offset in the op-amp is desired so that limiting errors. However, error in currents is produced because of the asymmetric directions of the current at the end of each branch (In case the switch is off: current flows to a point whose potential is V_{ref} . In the case the switch is on current flows to the ground). To keep the symmetry of this structure and to reduce this error, each switch will connect to V_{ref} (instead ground) in case the corresponding branch is on.

This structure can be exploited in voltage mode as well as current mode. However, current mode was found to have lower power dissipation than the voltage one[115]. Especially when high value of R is used (order of some $k\Omega$, and low noise levels is an advantage also), smaller currents passes through the activated branches. Besides, remembering that after gain adjustment of each channel individually, signals of the 16 outputs of the preamplifier will be summed together. This sum process boosts the interest of the current version of R-2R ladder for simplicity.

In the case when gain meets the standard uniform value and no need for gain control, the preamplifier signal could be turned directly to the sum input bypassing the R2R network. This decision is taken at the input of the R-2R block. This is possible via attributing a high logic level to an additional bit (labeled *gain_fix*) that will drive current directly to op-amp input.

3.6.3 Noisy channel elimination function

If a macro pixel (SiPM) in the detector matrix is found more noisy than predicted, out of service or if a fabrication defect makes a readout channel noisy to the extent of affecting

the data gathering, in these cases it is possible to eliminate the output signal of this channel. It will not be summed with the other signals of the rest of the chip.

A channel is said to be noisy when high trigger rate occurs. If high noise level is detected, the decision of elimination is then taken. This is decided after the calibration tests on the chip and during the SiPM matrix characterization. Or it could be found necessary after data analysis in late stages of the entire readout system, in this case a re-calibration process may be needed as the external slow control is done in series for the whole chip.

For this aim, an additional bit is added to the R2R network to alter the signal of this channel away from the sum direction. It is done by giving a high logic level to the corresponding bit of the slow control word. This bit is named *no_CB* on the Labview interface that communicates with a FPGA on the mother board holding the chip.

Fig.3.28a shows a scheme of the used switches. The principle consists of a combination of PMOS and NMOS transistors called a pair of complementary transistors put in parallel.

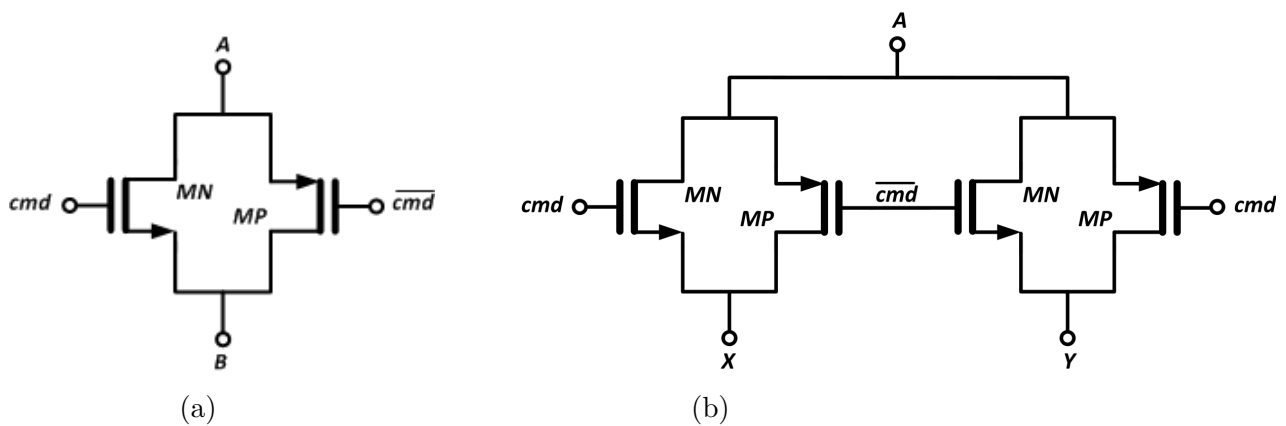


Figure 3.28: (a) Analog switch, (b) 1 to 2 Multiplexer

The advantage of this switch is its ability to perfectly connect both low and high voltage levels to the output. The switch being in series with the signal path should not degrade signal level. For this last point large devices are required in order to keep the on resistance of the switch as small as possible. So as minimum as possible voltage headroom is consumed by this on resistance. Devices' dimensions were chosen to compromise a small on-resistance with the response speed of the switch keeping in mind that larger devices have greater gate capacitance and hence are slower.

It could be used as a building bloc for the two-output switch (i.e. multiplexer) needed in order to drive currents between sum direction and the elimination direction. The command signal *cmd* is generated from a *NOR* operation between the *no_CB* bit and the inverted bit of slow control that corresponds to the branch as depicted in Fig.3.29.



Figure 3.29: The generation of the command bit *cmd* for one multiplexer.

Table. 3.9 summarizes all considered cases of gain control function and the noisy channel suppression.

gain_fix bit	R2R control-word of 9 bits									switch direction	Comments
	b1	b2	b3	b4	b5	b6	b7	b8	no_CB		
1	regardless									to sum amplifier	bypassing R2R bloc
0	regardless								1	to false out	channel is suppressed
	1	0	1	0	1	1	1	0	0	1 => to sum 0 => false out	$I_{out} \propto code$

Table 3.9: Gain control and noisy channel suppression function, in short.

3.7 Analog sum function

Inverting input of the operational amplifier in Fig.3.27 actually receives currents from the sixteen channels that are reading signals from the sixteen SiPMs of the array. Fig.3.30 illustrates this idea, we can then write:

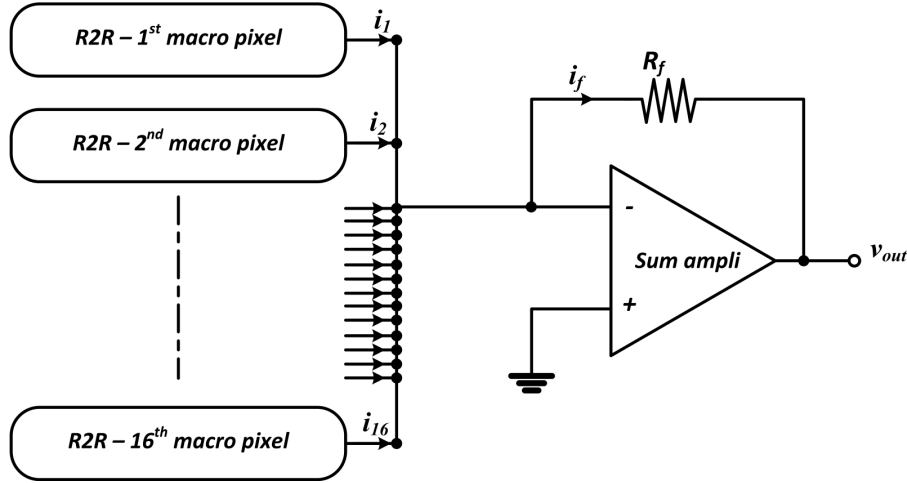


Figure 3.30: Summing the sixteen controlled signals after the preamplifier gain correction.

$$i_f = \sum_{j=1}^{16} \left(i_{in,j} \cdot \sum_{k=1}^8 \frac{b_{j,k}}{2^k} \right) \quad (3.25)$$

The output voltage of summed signals can be written as:

$$v_{out} = -R_f \cdot \sum_{j=1}^{16} \left(i_{in,j} \cdot \sum_{k=1}^8 \frac{b_{j,k}}{2^k} \right) \quad (3.26)$$

Substituting Eq.3.21 and the value of $R_f = 2R$ gives:

$$v_{out} = - \sum_{j=1}^{16} \left(v_{in,j} \sum_{k=1}^8 \frac{b_{j,k}}{2^k} \right) \quad (3.27)$$

Which is the sum of weighted outputs of the sixteen preamplifiers. The performance of this block will be verified and test results will be shown in the next chapter.

3.8 Trigger

Trigger is a very important function in astrophysical telescopes. The purpose of this system is to select and focus on data corresponding to the targeted events (Cherenkov light produced by gamma-ray photons) excluding data due to night sky background (NSB⁸). Each camera is divided into clusters (group of adjacent pixels). And trigger system (for a group of at least two telescopes) is divided into two levels: local and central.

Trigger strategy lays on the fact that photons due to Cherenkov light are detected by several close pixels in a narrow time window (few nanoseconds) while photons due to night sky background follow a Poissonian distribution and rarely form compact images. Hence, the local trigger gives a signal only if there is a time coincidence among signals detected by different pixels in one cluster. This step makes it possible to differentiate between NSB-induced events and gamma-like events. On the central level, signals are registered if several cameras (several telescopes) show a time coincidence among their trigger signals. This helps to reject the NSB more effectively.

In the previous experience HESS, there are three parameters that control the trigger process. Threshold per pixel, it is the minimum number of detected photo electrons that decide whether the pixel will contribute or not in the cluster trigger process. Threshold per cluster, which is the minimum number of pixels in the cluster whose signals passes the first threshold. When this condition is verified, a trigger signal is sent to the central trigger level. Threshold per telescope, minimum number of cameras (telescopes) whose trigger signals show a time coincidence.

Trigger function that is integrated in the front-end electronic belongs to the local trigger system. It is used to perform a first evaluation of signals per pixel. It should be noticed that a pixel here is one array composed of sixteen SiPMs since this array is considered the alternative of one PMT. That is why this first step of trigger system is performed on the sum of the sixteen SiPMs' signals.

As mentioned before, LST trigger strategy will be based on the Sum-trigger scenario. Since Monte Carlo simulations found it to be the most effective strategy in terms of lowering the energy threshold[77].

Fig.3.31 shows the main blocks that compose the trigger function inside the chip (pixel-level trigger). Trigger in ALPS consists of a discriminator that compares the sum of the sixteen readout channels on the high gain path to certain threshold. A programmable user-defined threshold is produced by a 10-bit DAC (*DAC10* cell) of the AMS library (*A_CELLS*) that receives its 10-bit word from labview interface. As for the 8-bit DAC that controls the over voltage (section.3.6.1), this DAC is followed by a low offset, high input impedance op-amp (*OP_WB* from the same library) as recommended by AMS to minimize errors. Besides that the discriminator uses an input stage of dual bipolar transistors in order to minimize the offset.

3.9 Overall chip and layout

ALPS chip design respects the rules of BiCMOS AMS $0.35\mu m$. The mask draw (layout) is shown in Fig. 3.33. It makes a die of about $3.673 \times 3.298 mm^2$. It has 96 pins in all, some

⁸NSB is light emitted by different sources i.g, stars or the moon itself. It could be due to star-light scattered in the atmosphere or scattered light from the rising or dawning moon, to mention some.

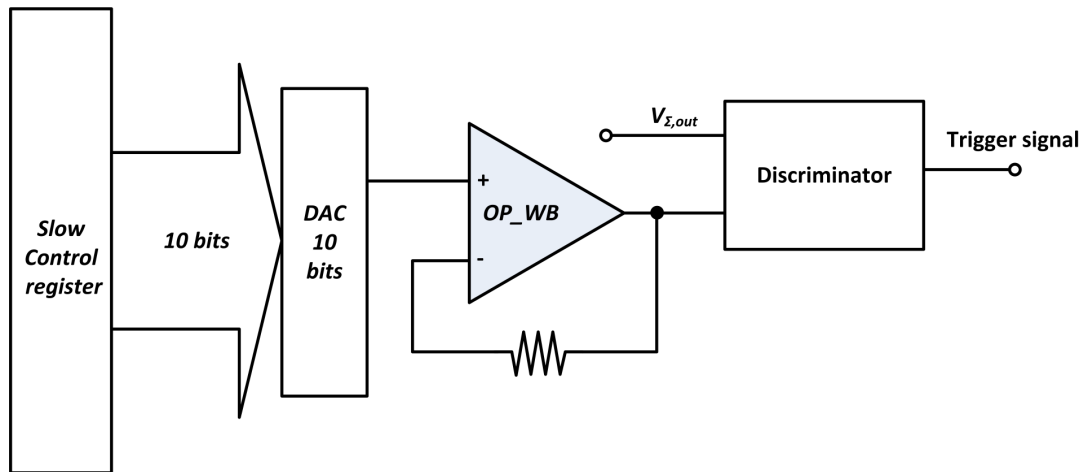


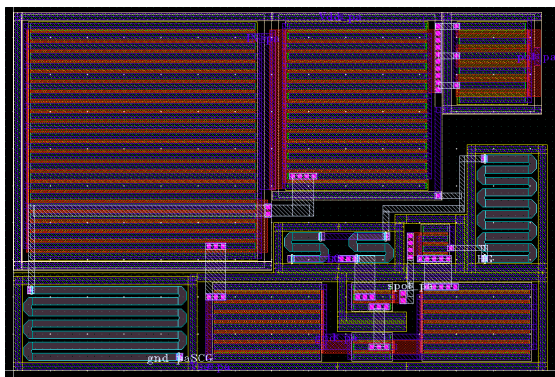
Figure 3.31: A block diagram of the trigger function integrated inside ALPS.

of which will be used in order to probe signal at some critical points of the circuit and to test the functionality of certain blocks, in particular the preamplifier. Some other pins will be used to force some points in the circuit to different potentials in case of unwanted deviation from the design and in case of errors.

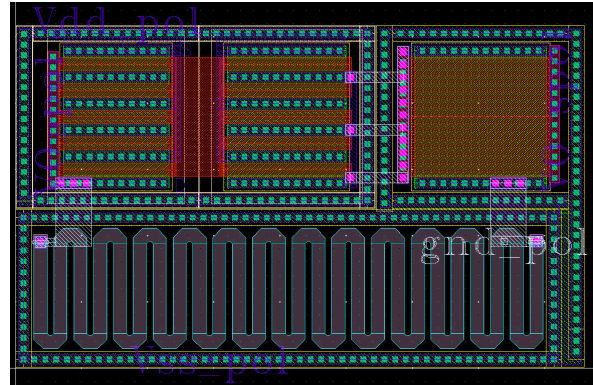
Multiple power pins were preferred to a general unique one. Blocs inside circuit will then be isolated in terms of power supply. The benefit of this arrangement is to avoid power supply degradation and its undesired impact on the performance of the different blocs of the circuit. Power supplies are grouped into two categories, one for the analog part and the other is dedicated to slow control registers. The second should be permanent not to loose the control in case of stop while the first one can be turned off if not used to save power.

In the preamplifier layout, polarization part was extracted as an independent block since it is common for the 16 channels. One channel layout is shown in Fig.3.32a side by side with that of the common polarization part Fig.3.32b.

Besides measurements of SiPM array performance with this chip, tests on the performance and functionality of the circuit itself are planned to be held. For this purpose, test points are integrated to probe some internal points of the different blocks as was said before. These test points will be activated by the slow control. Test facilities are mentioned in the next chapter. Measurements will be discussed and compared to the simulation results.



(a) One channel layout



(b) 16 channel common-polarization

Figure 3.32: Preamplifier layout parts

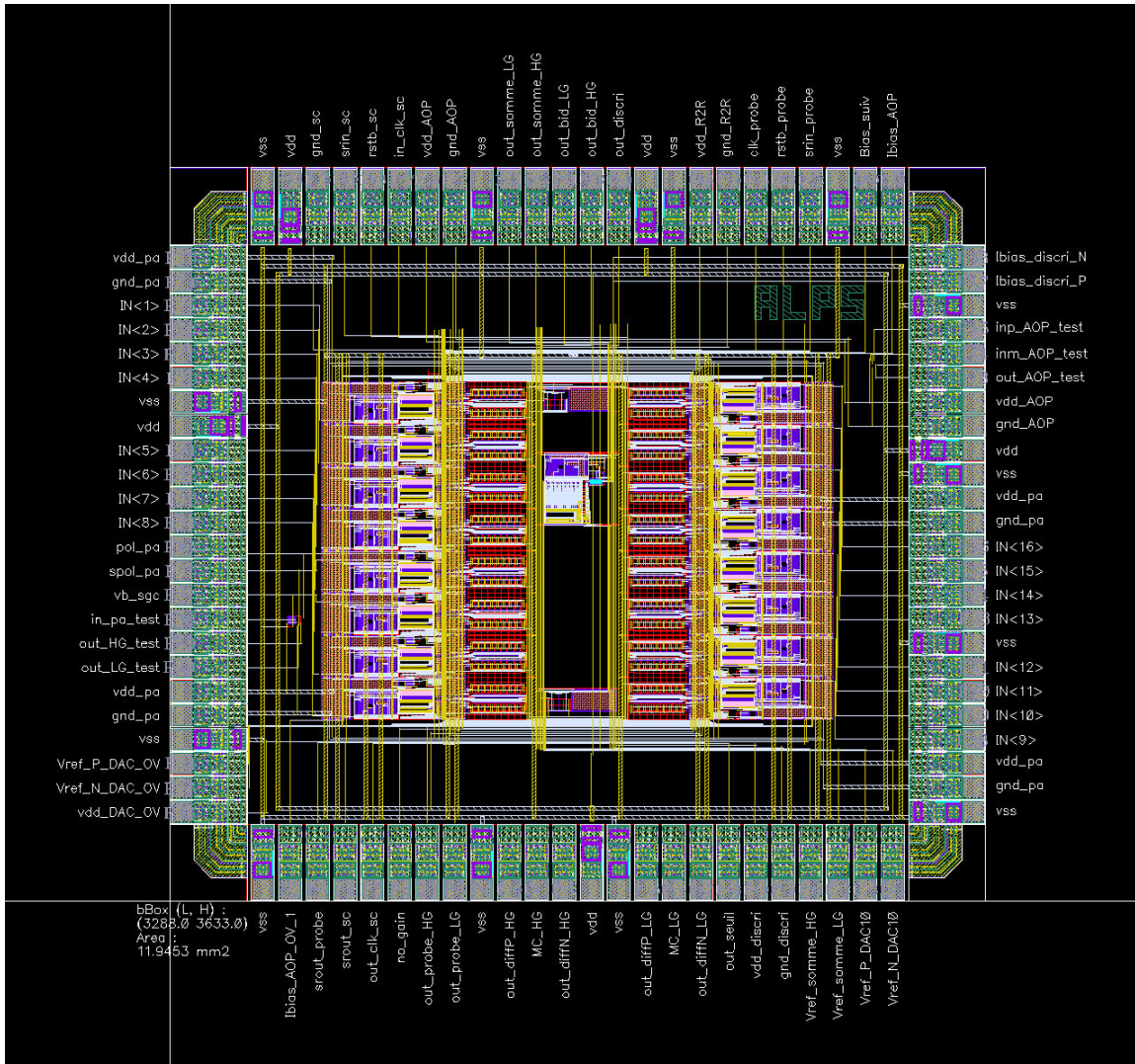


Figure 3.33: ALPS layout

test purpose. Its input and outputs are separated from the inputs and outputs of the readout channels.

Around the preamplifier, several important functions were predicted for an optimal performance. A coupling capacitance shapes the output signal of the detector before introducing it to the readout channel. Each gain path of the preamplifier is followed by a follower that connects its signal to a R-2R block. The role of this R-2R block is to adjust the preamplifier gain within $2V$ according to 8-bit word fixed by the user. An additional bit (*no_CB*) was added to enable the suppression of the channel if it is found to be noisy. Suppression of the high gain and low gain of each readout channel is also possible independently. A general bit (*gain_fix*) was added to enable bypassing all R-2R blocks for all channels. This option will be helpful in case of dysfunctional performance probably caused by hardware or software errors in these blocks.

Gain adjustment can also be done by changing the over voltage of each macro pixel separately. Changing the over voltage within $2V$ can compensate the dispersion of gain among the SiPM array elements. This is possible thanks to an 8-bit DAC that is inserted at the beginning of each readout channel. The over voltage 8-bit control word is also decided by the user.

In order to be able to interface this front end electronic circuit with the existing acquisition system (NECTAR or DRAGON), the sixteen signals will be directed to an analog sum amplifier. Sum function will be performed on high gain as well as on the low gain and hence the chip gives two output signals.

A trigger function is also integrated in the ASIC. Trigger signal (the third output signal of the chip) is produced by a discriminator that compares high gain sum signal to a programmable threshold. This dynamic threshold is generated thanks to 10-bit DAC controlled by the user.

Both 8-bit DAC and 10-bit DAC are standard cells of AMS technology library. The process of setting control bit sequence of the over voltage, R-2R gain control including the suppression bit and the R-2R bypassing bit, trigger threshold besides activating intermediate signal probing is done through a Labview interface that will be described in the next chapter. ALPS performance will be tested and checked in the next chapter.

In a forthcoming version of this ASIC, single ended to differential converters will be integrated inside the chip to directly provide differential signals.

Chapter 4

ALPS

experimental results and measurements

Contents

4.1	Introduction	111
4.2	Test board design	111
4.2.1	Labview slow control interface	113
4.3	Test bench of Electrical tests	115
4.4	Preamplifier tests	118
4.4.1	Linearity and dynamic range	119
4.4.2	Signal shape	121
4.5	Slow control tests	123
4.5.1	Residual pedestal	123
4.5.2	Gain control	124
4.5.3	Gain equalization	126
4.5.4	Noisy channel suppression	130
4.5.5	Bypassing gain control	131
4.6	Sum function	133
4.6.1	The shape of output signal	133
4.6.2	Sum as a function of the controlled gain	134
4.6.3	Sum of different signals	137
4.6.4	Sum as a function of the input level	137
4.7	Test bench for ALPS test with SiPM	139
4.8	Signal shape	141
4.9	Conclusion	143

4.1 Introduction

ALPS readout chip was submitted at the beginning of March 2014 and was received at mid July. It was realized as a part of a fabrication run gathering several chips of different projects called -in french- Circuit Multi Projet "CMP". We have received 25 dies. 5 samples were packaged in ceramic *CQFP100* type package. During fabrication time a test board with all slow control facilities was designed. Slow control consists of producing a sequence of bits that will help controlling the gain of each channel on both detector side (over voltage control) and electronic side (gain adjustment after the preamplifier) besides activating test points to probe signals or force some values to some points inside the circuit.

Tests involve two main categories. Electrical test is the experimental characterization of the chip to verify its own functionality and performance. Tests with the detector under light will follow to take a glance of the performance within more realistic conditions. In this chapter I present the test environment and will discuss test results for both test categories.

4.2 Test board design

Two test boards were designed. The first one aims to test each of the 5 packaged samples of the chip. This step is important in order to decide which sample to be soldered on the second test board. The purpose of soldering a chip on the test board has been proved to be of less noise usually captured by the socket pins and connectors.

The first test board is depicted in Fig.4.1. It can receive input signals in three ways:

- 16 analog inputs (lemo connectors) that serves as gates leading electrically-generated signals into readout channels of the ASIC.
- a spare *data link connector* to an interface board simulating the SiPM.
- a *HIROS(HRS) to FPC¹ connector* of the SiPM itself in case we need to test it with this board.

Besides, three analog inputs (lemos) for the isolated test-dedicated blocks: preamplifier block called *PA_TEST* and amplifier block called *AOP_TEST*. Chip under test will be put in a weld *yamaichi IC socket* and so every chip of the 5 packaged samples in turn.

Analog outputs are sensed from lemo connectors or test points at the preamplifier level, at the chip outputs and at the outputs of the test blocks previously mentioned.

Digital part of the chip is controlled by the FPGA firmware that communicates with a Labview program via *USB connector*. The control code installed in the FPGA is written in VHDL ².

¹Flexible Printed Circuit cable.

²Hardware Description Language.

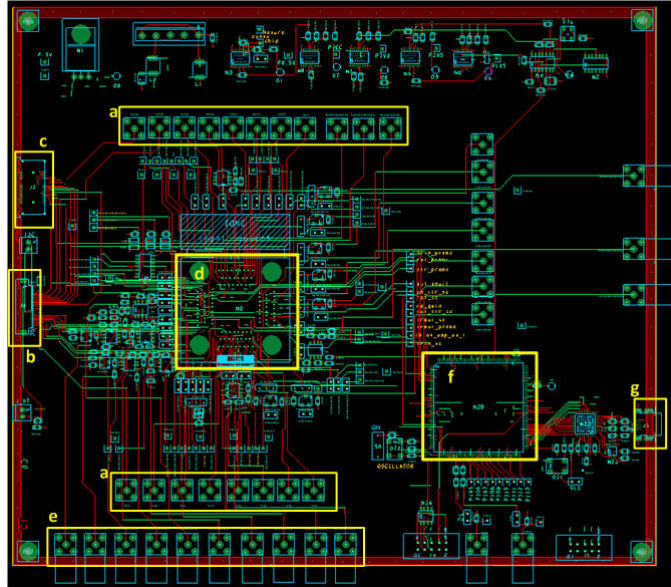


Figure 4.1: The first test board. a) analog inputs leading electrical signals into the ASIC, b) SiPM connector, c) interface connector, d) chip socket, e) analog outputs, f) FPGA, g) USB connector

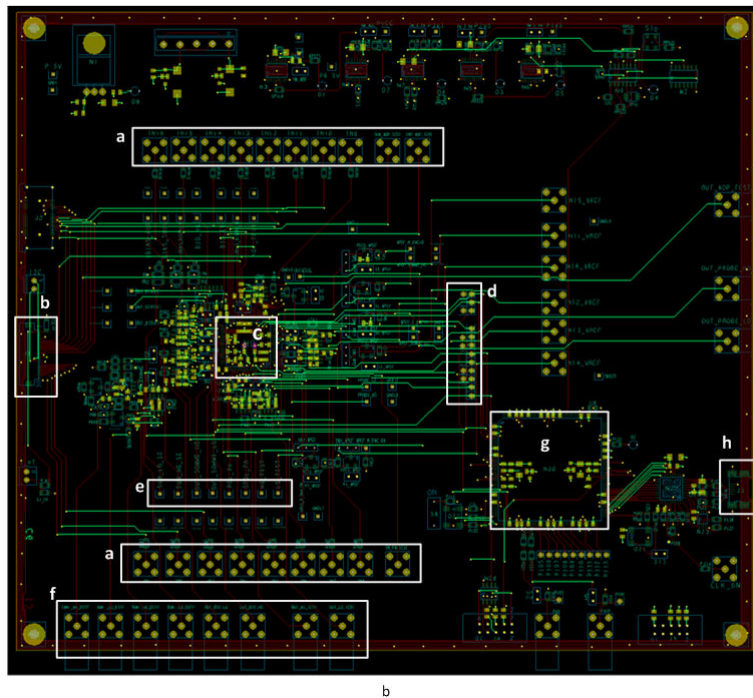


Figure 4.2: The second test board. a) analog inputs , b) SiPM connector, c) ALPS chip, d) digital slow control probes, e) analog output probes, f) analog outputs (lemos), g) FPGA, h) USB connector

The second test board is almost the same geometry but the chip will be directly welded on it. It basically has the same functionality as the first one. In addition, it involves isolation buffers to protect output signals from added noise that could be picked

in from cables or surrounding environment. Besides, single-ended to differential converters (section.3.10) with adjustable common mode were added for both high gain and low gain sum outputs in order to interface these outputs to the acquisition system represented by NECTARCAM (for the MST camera) or DRAGON. These converters could be integrated in the readout chip in the forthcoming version.

On both boards, potentiometers are used to fix reference voltages of high gain sum, low gain sum, overvoltage DAC-8 bits, discriminator DAC-10 bits ³ and discriminator threshold.

4.2.1 Labview slow control interface

ALPS contains gain control facilities, in particular, pixels' overvoltages (section.3.6.1) and channels' gains control (section.3.6.2), not forgetting the trigger threshold (section.3.8). All these facilities are controlled according to user data as entered in a Labview interface that is shown in Fig.4.3.

In this interface we can adjust the following parameters:

- The overvoltage of each macro pixel of the SiPM array within 2 V . This is done by defining an 8-bit word for each of the sixteen DACs (section.3.6.1). These digital to analog converters are inserted before each readout channel inside the ASIC.
- The gain of the R-2R block (section.3.6.2) of every channel on both high and low gain directions. 8-bit word defines the number and location of the connected switches in the R-2R block. Hence, It defines the fraction of the current transmitted from the preamplifier to the sum amplifier via the R-2R block. As a consequence, the gain of each preamplifier will be adjusted and identical signals on different channels will be identically weighted in the sum output.
- Suppression decision of noisy channels (one bit labeled *no_CB*). There are two bits per channel, one for the high gain and the other for the low gain. Activating this bit will mask the corresponding signal from the sum step.
- Discriminator threshold. A 10-bit word is the input of the DAC that will accordingly generate the threshold over which the chip output (sum output) is defined.

It is even possible to neutralize the gain control process (i.e, bypassing the preamplifier gain-control block) by activating a separated bit labeled *gain_fix* bit. This bit is unique for the sixteen channels and is allocated in the second Labview interface which is shown in Fig.4.4.

³according to AMS kit, positive and negative references for these DACs should be within the common mode range of the op-amp that follows (e.g. between 0.8V and 2.4V)



Figure 4.3: Labview interface(I). a) 8-bit words for overvoltage adjustment by per macro-pixel DAC 8-bit, b) 8-bit words for high/low gain adjustment via R-2R blocks, c) high/low gain noisy channel suppression (no_CB bits), d) 10-bit word to the DAC 10-bit for discriminator threshold adjustment.

Since preamplifier is the main part of this chip, it is important to evaluate its performance independently from the rest of the circuit. For this purpose, a part of the Labview program, which is shown in Fig.4.4; is dedicated to activating and probing the preamplifier outputs of a chosen channel. Please notice that even though essential, signal probing at a test point affects the signal level because of the added capacitive loading (test point and probe). A way to limit this effect will be to use active probes instead of the passive high-impedance resistor divider probes.

These commands are sent to the on-board FPGA by *usb protocol* connector. The VHDL program in the FPGA translates the received commands into a serial sequence of bits that will be written in a FIFO standard to the in-chip register.

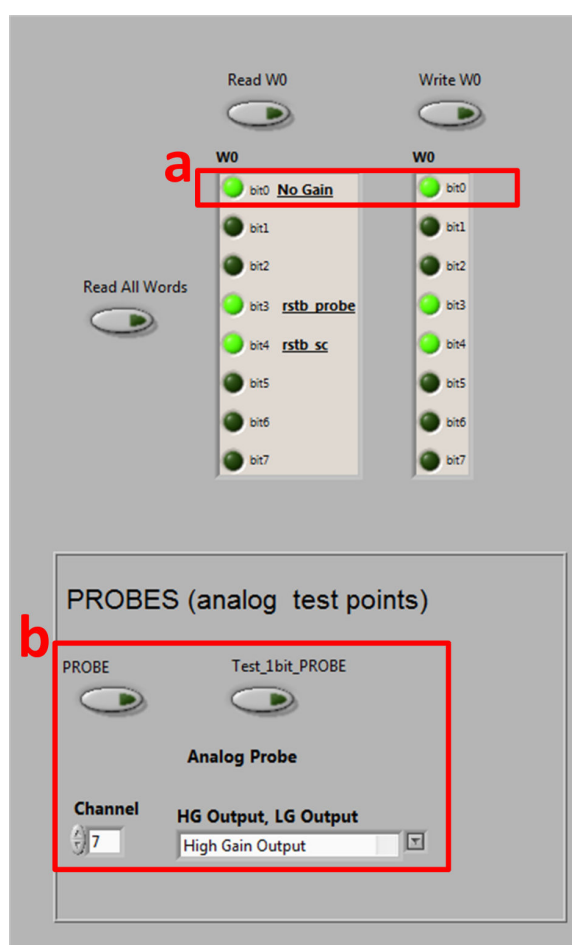


Figure 4.4: Labview interface(II). a) bypassing the gain control process with active *gain_fix* bit, b) probing a selected channel preamplifier outputs.

4.3 Test bench of Electrical tests

Electrical tests are the first set of planned tests. Electrical signals will be injected into the chip to verify its behavior and compare it with the simulation. In this section, the test bench is described. In the following sections, the purpose of each test is mentioned and followed by a discussion of its results. At the end of these tests the concept of the preamplifier and the efficiency of its facilities will be evaluated.

The test bench that was used for the electrical tests is shown in Fig.4.5.



Figure 4.5: Test bench for chip electrical tests.

It is composed of the following devices:

- *Stabilized power supply AL 936*, a DC generator for power supply. Different power supplies will be separated on the test board among the different blocks of the chip and the digital part of the board. Table.4.1 shows a list of all used voltage values on the board.
- *Agilent 81110A 165-330 MHz* pulse generator that will simulate the output of the photo detector, i.e, generate input signals to be injected in chip inputs. The generated pulse is limited to a minimum transition time of 2 ns . This pulse generator also serves as an external trigger for the oscilloscope.
- *RSA-35110D-BNC-R* attenuator that provides an attenuation between 0 and 110 dB with 1 dB step over a wide frequency range from DC to 3 GHz. This attenuator is used to change the ASIC input levels according to the adjusted attenuation.
- *LeCroy wavepro 950* oscilloscope whose band width is of 1GHz in order to visualize and measure output signals.
- *Labview program on a dedicated computer to control the digital part of the ASIC and to define the slow control values.*

Symbol	Value(V)	Purpose
V_{CC}	5	USB buffers
P-5	-5	buffers
P6.5	6.5	FPGA
P3V3	3.3	
P2V5	2.5	
P1V5	1.5	
V_{DD}	3.3	ALPS chip

Table 4.1: Power supply list

Input signals In order to simulate the current output of the SiPM, Fig.4.6a shows the arrangement which is used as the input circuit. It consists of adding a $1.1\text{ K}\Omega$ resistor between the attenuator and the channel input. A $50\ \Omega$ load is used to properly adapt the impedance between the attenuator and the impedance composed by the $1.1\text{ K}\Omega$ and the input impedance of the chip being of the order of $50\ \Omega$.

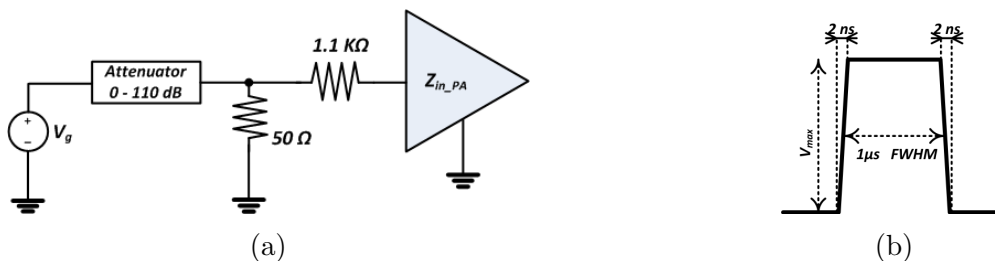


Figure 4.6: (a) Input circuit configuration, (b) Input signal form.

Using the pulse generator mentioned above limits the speed of the signal used as input to a minimum rising time of 2 ns while that of the SiPM signal is of the order of 1 ns (more precisely, some hundreds of pico seconds). Fig.4.6b illustrates the form of the generated input pulse. As a matter of fact, rising edge is the important part of the input pulse even if the falling edge is slow or that the pulse is wide. This is because rising time describes the response speed of the detector itself⁴ and that only the rising edge includes information about higher frequency components of the signal⁵. i.e, the critical anomaly in what concerns the readout electronic bandwidth comes from that rising edge. Besides, coupling capacitors were inserted before the input of each preamplifier inside the chip ALPS. These coupling capacitors will perform a shaping of the input signal.

Now to approach the input levels that were provided by the SiPM model to the chip design during simulation, another simulation was performed with a voltage source and its $50\ \Omega$ impedance as the input of the preamplifier instead of the SiPM model. Input voltage level is found to be of about $385\ \mu\text{V}$ for one photo electron signal that will give a response

⁴The response speed measures how fast a current output is formed by charge carriers generated in the detector and extracted to the external circuit.

⁵The cut-off frequency of the detector is given by $f_c = \frac{0.35}{t_r}$, where t_r is the rising time of the output signal.

at the high gain output similar to that obtained when SiPM model was used. Figure 4.7 shows the response of the high gain path of the preamplifier simulated with one macro pixel (SiPM) model and with a voltage source. One photo electron is considered in both cases and output amplitudes are almost identical.

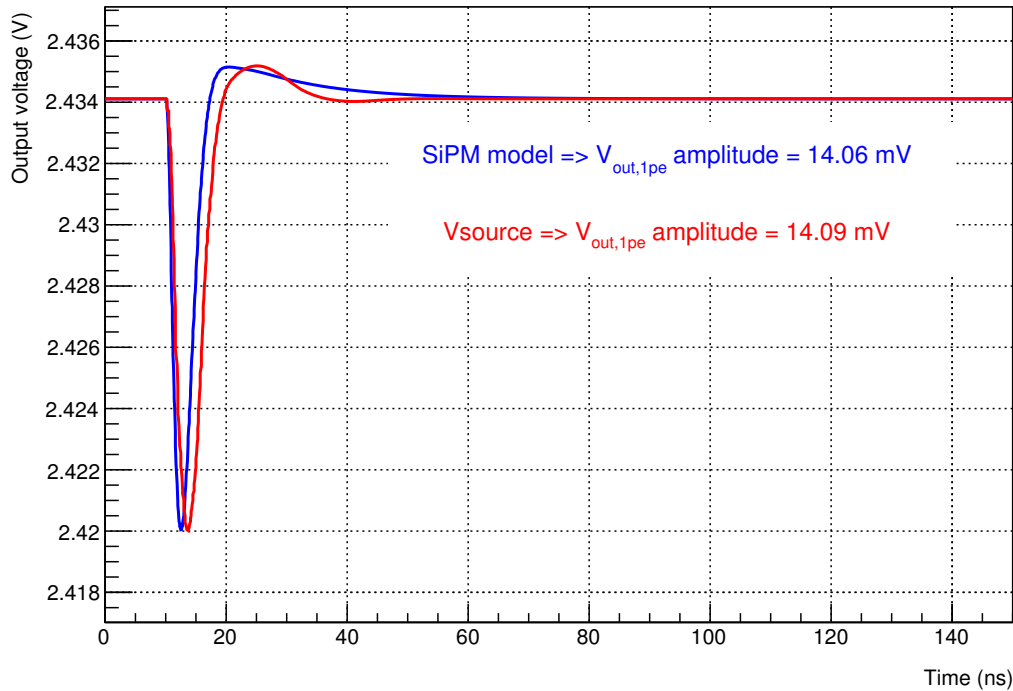


Figure 4.7: High gain output of the preamplifier for one photo electron equivalent signal. In red, when a voltage source of $385\ \mu V$ amplitude, rising time of $2\ ns$ is used as input. In blue, when SiPM model is used as input.

From here on, input voltages can be translated into number of photo electrons knowing that one photo electron is the equivalent to an input voltage of about $385\ \mu V$.

Input circuit shown in Fig 4.6a doesn't affect timing resolution of the signal at the chip input. The coupling capacitor inserted at the preamplifier input (inside the chip ALPS) together with the input impedance forms a shaper that shortens the input pulse. Input amplitude could be adjusted according to the attenuation. The output signal appears on the oscilloscope as the average of 1000 iterations. The purpose is to average the random noise picked up by cables.

4.4 Preamplifier tests

A preamplifier block was put in the chip out of the readout circuit for the purpose of individual test. In this section, the performance of this block called *PA_TEST* will be discussed.

4.4.1 Linearity and dynamic range

Input signal varies according to the attenuation of the input voltage V_g . Voltages injected in the chip inputs, via the lemo connectors, go from $50 \mu V$ up to $400 mV$. Which are the equivalent to a number of detected photo electrons that goes from $1/7.7$ up to 1038.9 photo electrons.

Outputs are measured on the *PA_test* lemo outputs called *OUT_HG_TEST* and *OUT_LG_TEST* for high gain and low gain outputs respectively. Each output is the average signal of 1000 iterated signals done by the oscilloscope, and the output potentials that we measure as the Y-axis in Fig.4.8 are the maximum amplitude of the preamplifier's output pulse at each input.

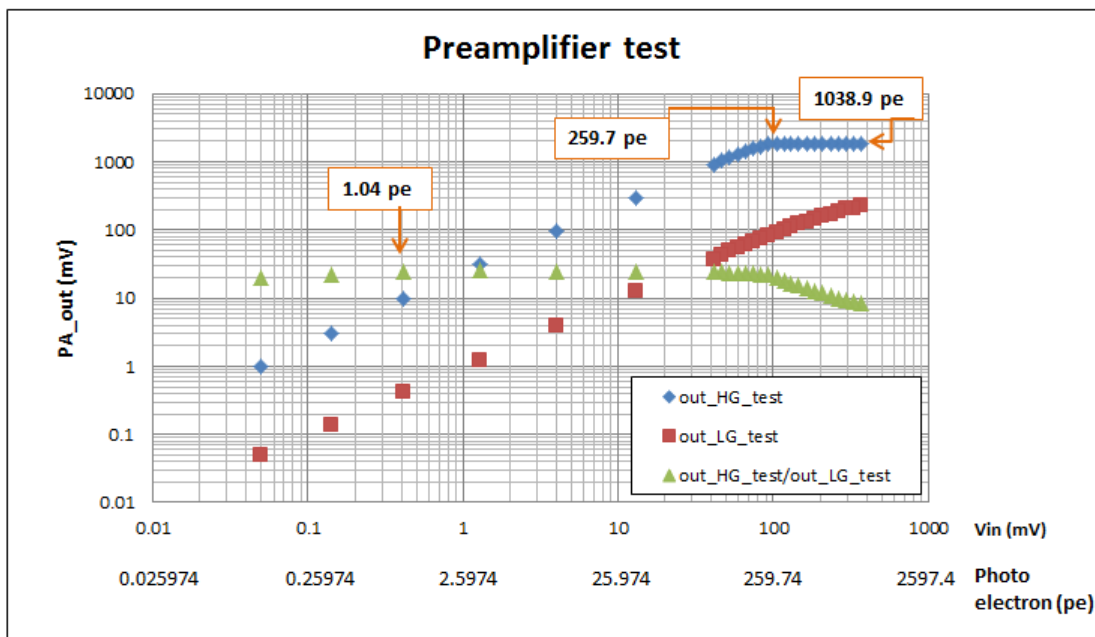


Figure 4.8: Preamplifier output on both high gain and low gain for different input signals. The high gain seems to be less than what was found by simulation while low gain is higher than predicted.

The amplitude of output signals are ranging between $1 mV$ to $\sim 2 V$ on the preamplifier high gain before it reaches saturation as depicted in Fig.4.8. These outputs correspond to input voltages between $50 \mu V$ to $100 mV$. Which is equivalent to a number of photo electrons between $1/7.7$ and 259.7 photo electrons.

While on the low gain and because of the noise it is difficult to measure small signals with good certainty. However it was possible to measure output signals up to $200 mV$ corresponding to input voltage approaching $400 mV$ i.e, 1038.9 photo electrons. It is worth to mention that at this extent, the low gain path is not yet saturated. Now what about the linearity of these preamplifier plots?

Figure.4.9 shows the linearity error on the high gain. High gain can measure signals starting by $11 pe$ up to $193 pe$ with good linearity (linearity error is less than 3% except for the second point $\equiv 34 pe$ where the error is about 4%). Linearity error on the low gain is illustrated in Fig.4.10. A maximum linearity error is 3% for a range of inputs between

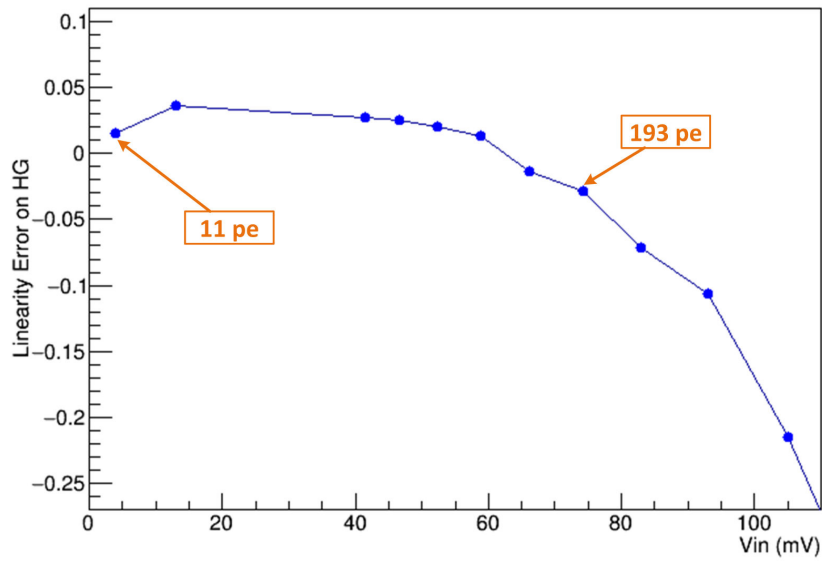


Figure 4.9: Non-linearity on the HG of the preamplifier shows a similar pattern to what was found in simulation. The error in linearity stays in the range of 3% for a dynamic range that goes between 11 pe and 193 pe excepting the second point corresponding to 34 pe where the non-linearity is about 4%.

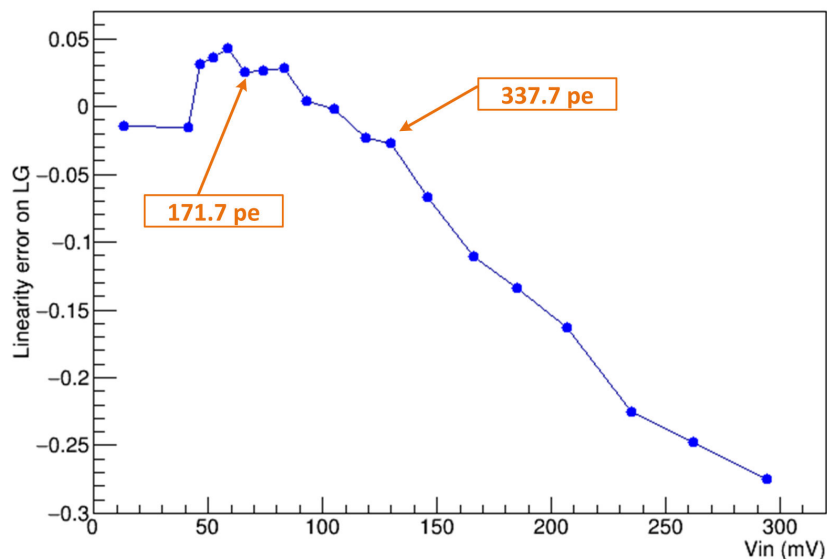


Figure 4.10: Non linearity on the LG of the preamplifier is within the desired value 3% for a dynamic range between 171.7 pe and 337.7 pe .

171.7 *pe* and 337.7 *pe*.

The gain ratio between high and low gain is less than that found in simulation. It was measured to be of about 20 while the expected ratio is ~ 90 . A possible cause of this reduction is due to the test board since a ratio of only 10 was measured using the first test board (Fig.4.1) while by using the second one (Fig.4.2) the gain ratio was doubled.

For conclusion, the preamplifier covers a wide dynamic range of 11 *pe up to more than* 300 *pe* on the combination high gain and low gain with a very good linearity that meet the need of the LST (linearity error $< 3\%$) as shown in Fig.4.8, Fig.4.9 and Fig.4.10.

4.4.2 Signal shape

As for timing, Fig.4.11 shows the shape of the output signal of the test block of preamplifier for an input of 1.28 mV. The output on the high gain is a pulse of leading edge as slow as 12.25 ns as a response to a charge equivalent to 3.3 *photo electrons* which is slow recalling that in simulation we had a 2.8 ns leading edge output pulse for 1 *photo electron* equivalent input.

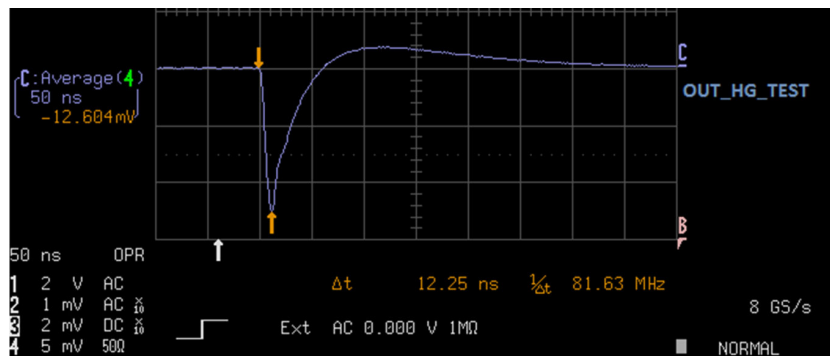


Figure 4.11: Preamplifier output signal seen on high gain for an input of $V_{in} = 1.28mV \equiv 3.3$ *photo electrons*.

Beside the slow rising edge of the input signal (limited by the voltage generator itself), possible reasons for this degradation are parasitics. From the one hand, capacitive and inductive elements added by the signal path from the lemo connector where the signal is injected till the ASIC input. These parasitics were not considered in the simulation. For proper design an inductance should be added between the input source (SiPM model or voltage source) and preamplifier input. Fig.4.12 shows the difference in input signal shape with and without this inductance.

On the other hand, there are the parasitic elements that charge the output of the preamplifier. These parasitic elements are caused by the test board and lemo connectors whose capacitance is of the order of 10 *pF*.

So to verify this assumption, it is helpful to re-simulate the preamplifier circuit taking into consideration these undesired loads and using the same input arrangement (voltage source). The results shown in Fig.4.13 support the explanation and confirm the performance of the pure preamplifier. For a long term verification, it is worth designing another test board with reduced parasitics.

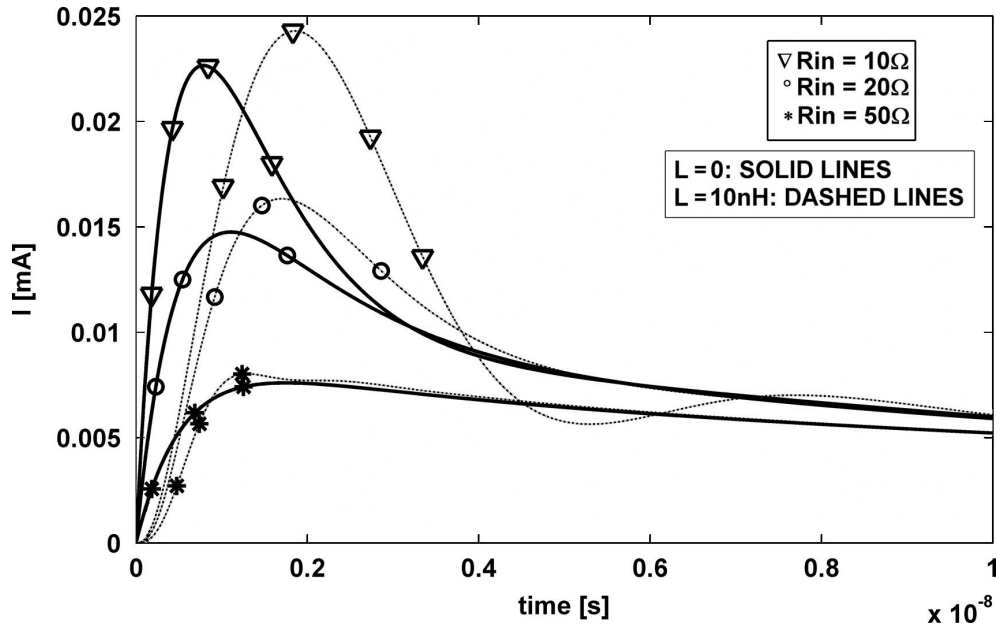


Figure 4.12: Elementary current pulses produced by the SiPM for BW=300 MHz and different values of R_{in} and L the inductive element added by the connector between the SiPM and the readout electronics[65].

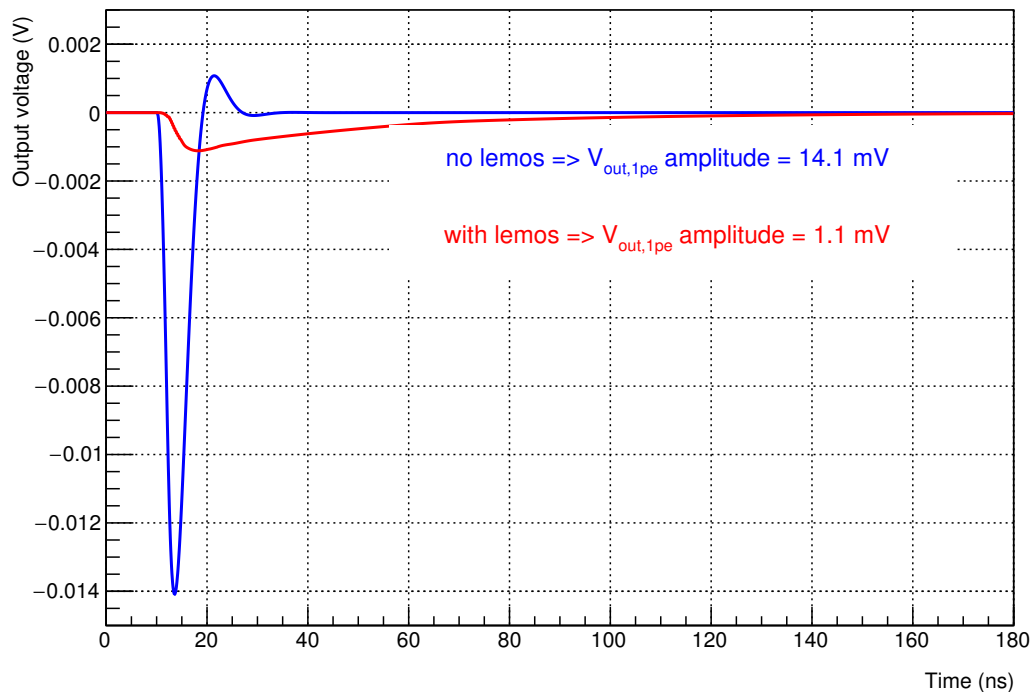


Figure 4.13: The effect of a parasitic capacitive load due to lemo connectors (estimated by 10 pF) at the input and on the preamplifier high gain output (in red). Output of the preamplifier with no capacitive loads (in blue). Input signal is the equivalent of 1 photo electron voltage being simulated as a pulse of $385\text{ }\mu\text{V}$ amplitude and 2 ns leading edge.

4.5 Slow control tests

These tests aim to verify the gain control facilities that were integrated in the chip for each readout channel (section.3.6). Since over voltage adjustment uses a DAC taken from AMS library, the following tests concentrate on the preamplifier gain control. The performance of the R-2R block (section.3.6.2) is discussed.

In order to test the performance of the sixteen readout channels, only one channel will be fed by an input signal at a time. All other channels will not be connected to any input signal. Output signals are measured at the single ended outputs of the sum amplifier. Single ended sum outputs are labeled SUM_HG_SE and SUM_LG_SE for the high gain and low gain respectively.

4.5.1 Residual pedestal

The output of the pre-amplifier passes through a control block ($R-2R$) described in section.3.6.2 before being summed with other controlled preamplifiers' outputs.

Talking about one channel fed by input signal, when its R2R code is set to zero, no signal supposed to appear on the ASIC output and the preamplifier output signal should be canalized to a false output called OUT_BID after the R2R gain control block. This case is normally supposed to be the equivalent of suppressing the channel contribution in the sum output by activating the no_CB bit. However, this is not the case. As a matter of fact, we can measure a non zero signal that we will call the *residual pedestal* even if the R2R code is set to zero or the no_CB bit is activated.

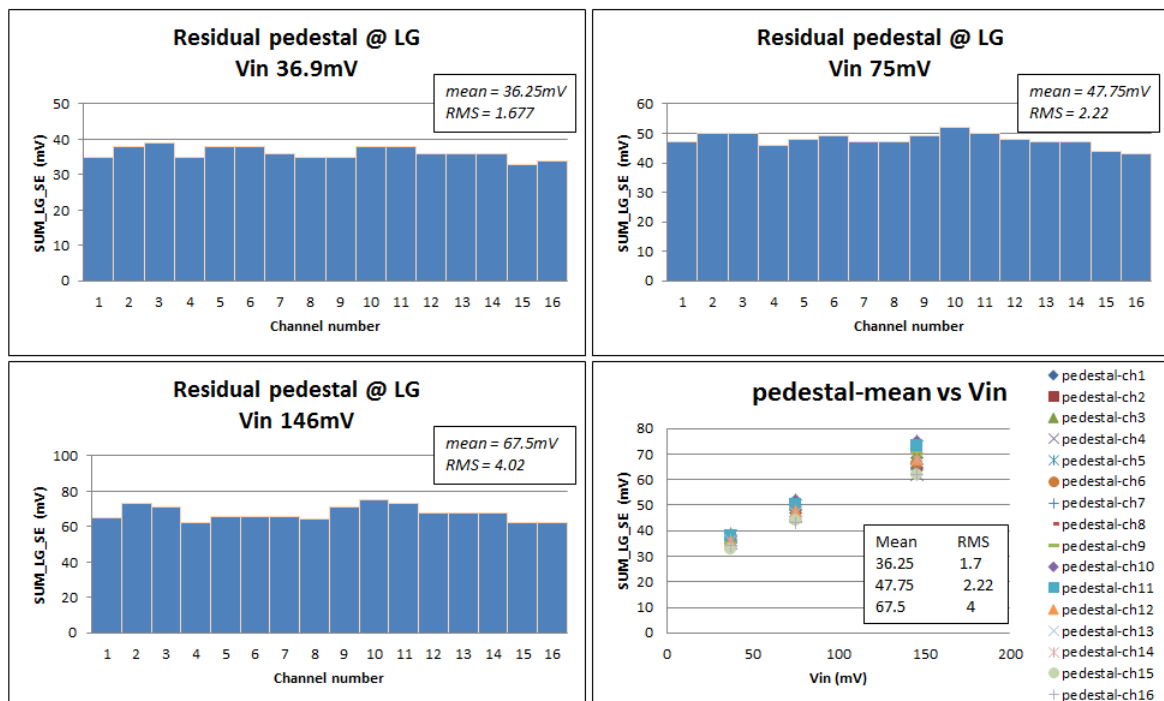


Figure 4.14: Residual pedestal measured on the SUM_LG_SE for different input levels. The dispersion found to be 4.7%, 4.6% and 6% for the used input levels of 36.9 mV, 75 mV and 146 mV (equivalent to 95.8, 194.8, and 379.22 photo electrons) respectively.

Fig.4.14 shows the distribution of the residual pedestal over the sixteen channels. It is not unique for all channels and its value shows a dispersion that, at its turn, depends also on the input signal. This residual pedestal appears on low gain output as well as on the high gain output. The residual pedestal measured on the high gain can be seen in Annex.B.1. It is then necessary to correct measured values by deleting their contents due to residual pedestal as we will see later in section.4.5.3.

When no input is applied to the channel, no signal appears on the preamplifier output. Which eliminates the preamplifier responsibility of this phenomenon. Residual pedestal could be due to current leakage through R2R switches or to an error in the slow control bit-sequence propagation.

4.5.2 Gain control

The purpose of this test is to show the concept of gain control block (section.3.6.2) and to verify its performance for each of the sixteen channels. This test passes through applying an input at one channel at a time and measuring its output for the four essential gain-control codes of the gain control block (R-2R). These are the four codes 64 , 128 , 192 , 255 that correspond to gains of 0.5 , 1 , 1.5 , 2 of the control block respectively. Normally if no gain adjustment is needed, R-2R code should be set to the mean value of 128 that means a gain of 1 .

For an input signal $V_{in} = 3.69 \text{ mV}$ ($\cong 9.6 \text{ photoelectrons}$), Fig.4.15 shows output dispersion among the sixteen channels for each gain-control code on the high gain path. This is an average dispersion of around 3.6% for the considered input pulse value 3.69 mV .

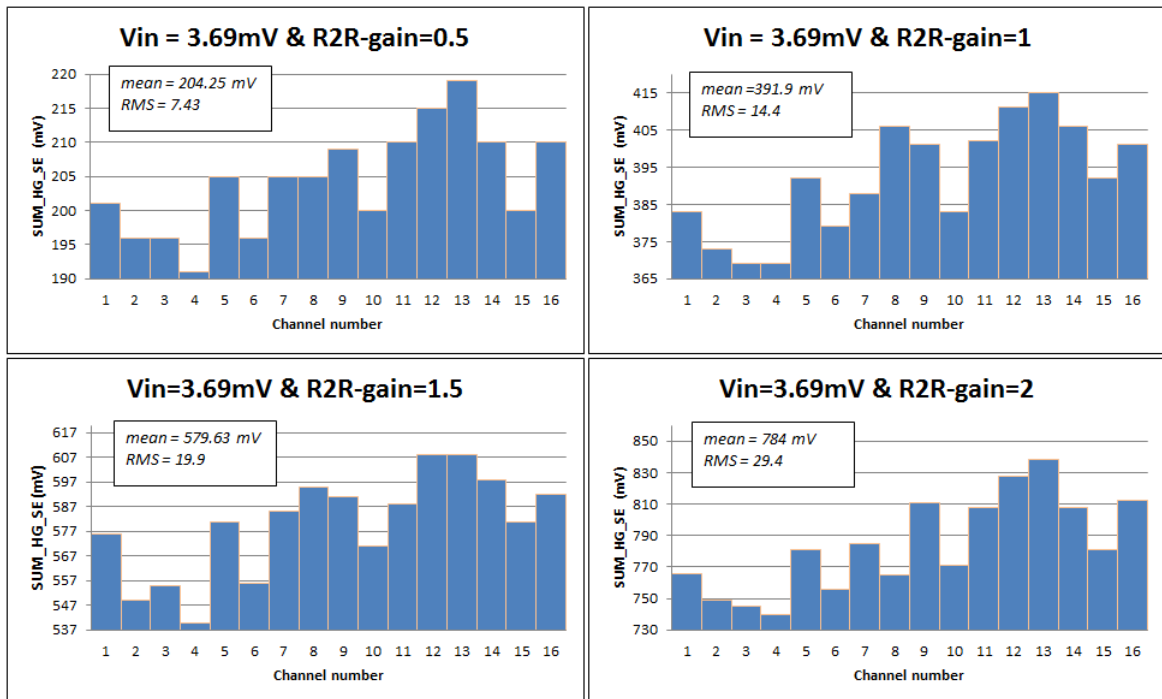


Figure 4.15: Dispersion among the sixteen channels for $V_{in} = 3.69 \text{ mV}$ is about 3.6% , 3.7% , 3.4% and 3.8% respectively for R-2R-gain 0.5 , 1 , 1.5 and 2 .

The origin of this dispersion is believed to be the residual pedestal that was discussed

in the previous section.4.5.1. It could be solved by using the gain-control block exactly for the job it was designed for, as will be shown in the next section.

More test results on high gain output and also on the low gain output for different input signals are shown in Annex.B.2.

Now considering the mean from each sub-figure of Fig.4.15 and trying to verify the linearity of the gain control block gives Fig.4.16 where we can distinguish the very good linearity on the high gain part in respect to the input signal.

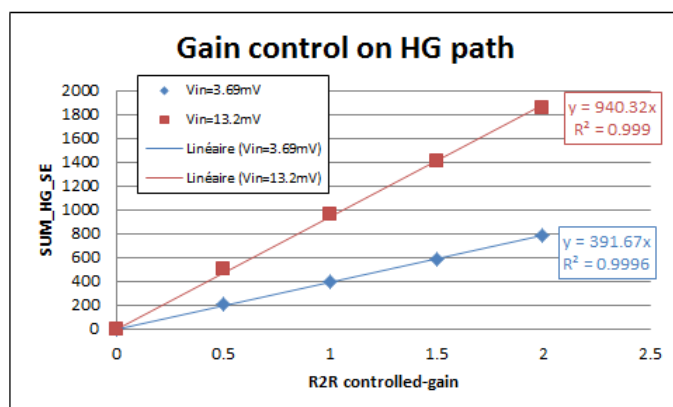


Figure 4.16: Linearity of gain control process on high gain path for two different inputs. Each point is the mean of the sixteen channels outputs for the given input and gain-control code. In blue, plot represents average outputs of the sixteen channels for $V_{in} = 3.69\text{ mV}$. In red, plot represents average outputs of the sixteen channels for $V_{in} = 13.2\text{ mV}$

Gain control process is also found well linear on low gain part of the ASIC as we can see in Fig.4.17.

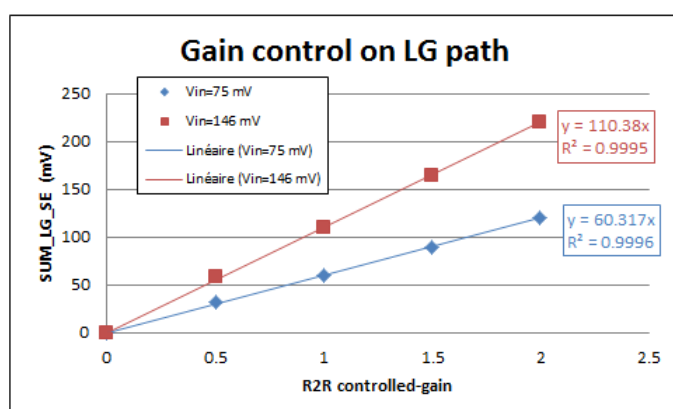


Figure 4.17: Linearity of gain control process on low gain path for two different inputs. Each point is the mean of the sixteen channels outputs for the given input and gain-control code. In blue, plot represents average outputs of the sixteen channels for $V_{in} = 75\text{ mV}$. In red, plot represents average outputs of the sixteen channels for $V_{in} = 146\text{ mV}$.

4.5.3 Gain equalization

Even if the schematic is the same for all the sixteen channels, nothing really guarantees the exact same response to the same input. The dispersion on the output could be explained by the effect of potential parasitic elements that are inserted according to the environment of each channel and its neighborhood which is not the same for all channels. The used fabrication technology also plays a role according to the precision of chip layers that it can manage during fabrication. Besides, the added residual pedestal discussed in section.4.5.1. Nevertheless, readout electronics must show a homogeneous response to a given input signal.

Here comes the role of the gain control block whose idea is based on the the R2R network (section.3.6.2) and whose performance was shown in section.4.5.2. The aim is to change the code of each channel so that unifying their response to a given input signal.

Gain equalization should then take account of this undesired residual pedestal value and its annoying characteristics. The correction procedure implies the following steps:

1. Measuring the residual pedestal ped for each channel at the given input.
2. Deciding a standard output level out .
3. Knowing the pedestal value gives the output level predicted including the pedestal.
 $out_i^6 = ped + out$.
4. Gain control code is then to be adjusted so that predicted output out_i can be measured at the output.
5. A manual correction of measurements is then to be done by rolling out the pedestal from the measured output and the result is nothing but the decided standard output which is the same for all the sixteen channels.

Fig.4.18, shows gain equalization procedure step by step on the high gain, for an input of $V_{in} = 3.69 mV \cong 9.6 photo\ electrons$. The target is to reduce output dispersion among the sixteen channels to about 1%. Gain equalization process for other inputs can be seen in Annex.B.3. Fig.4.19 shows final results of high gain equalization for other different inputs.

⁶ out_i is the intermediate output

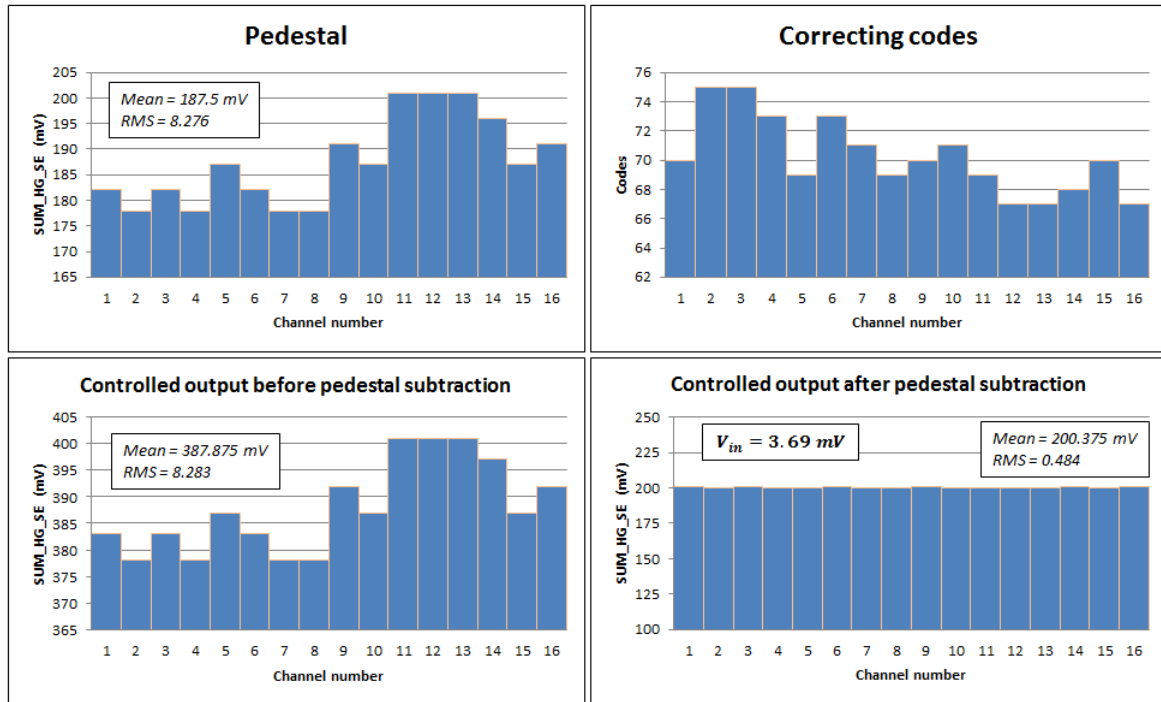


Figure 4.18: The procedure of gain correction after the HG pre-amplifier for an input signal of 3.69 mV : a) measuring the pedestal of each channel and fixing the standard output (here it was put to 200 mV), b) digitally control the gain of each channel via programming the switches of each R-2R bloc, c) measuring the output which at this step includes the pedestal and here we can notice the 2.1% dispersion of the output value, d) the sixteen outputs after residual pedestal subtraction from measured data. We can notice a dispersion of about 0.24% among the sixteen channels. The gain is now homogeneous for almost all the channels and the small dispersion (less than 1%) is better than expected.

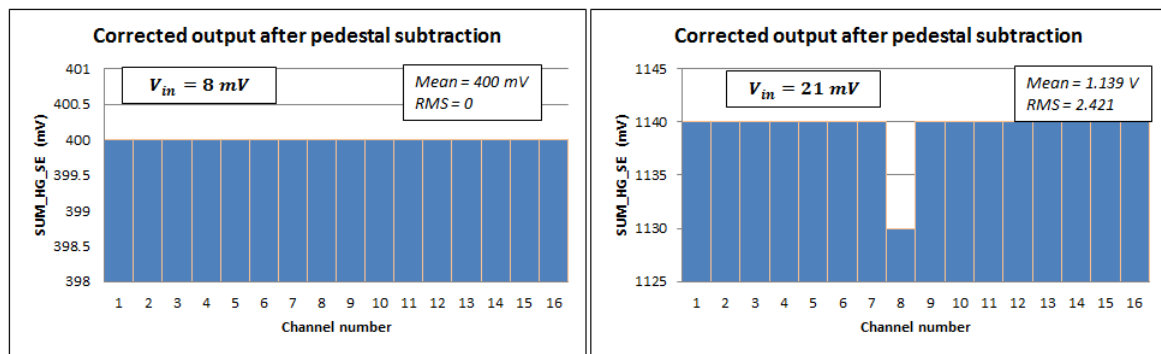


Figure 4.19: Gain equalization on high gain path for two other different input signals $V_{in} = 8\text{ mV}$ and $V_{in} = 21\text{ mV}$ (equivalent to $20.78\text{ photo electrons}$, $54.5\text{ photo electrons}$). That reduces gain dispersion in the sixteen readout channels to less than 1% (about 0%, and 0.2% respectively).

The same procedure is applied on the low gain of the sixteen readout channels for two different input levels $V_{in} = 146\text{ mV}$ and $V_{in} = 292\text{ mV}$. Process details can be seen in Annex.B.3 (Fig.B.7 and Fig.B.8).

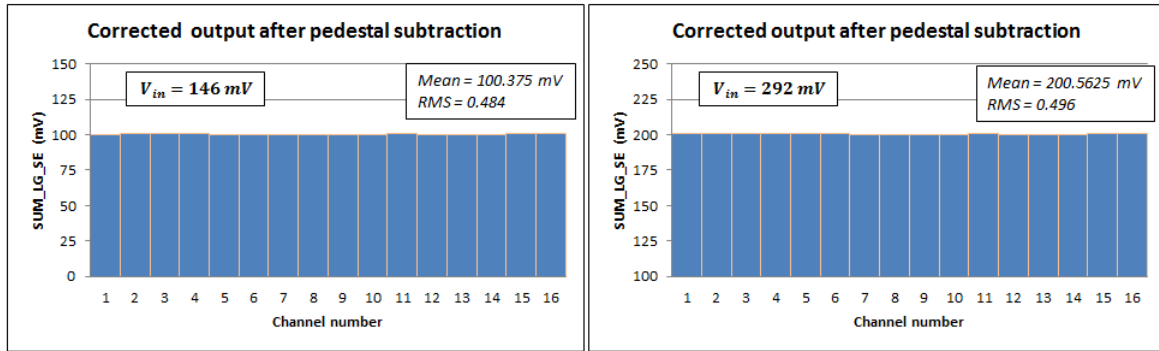


Figure 4.20: Gain equalization on low gain path for two different input signals $V_{in} = 146\text{ mV}$, and $V_{in} = 292\text{ mV}$ (equivalent to $379.2\text{ photo electrons}$, $758.4\text{ photo electrons}$). That reduces gain dispersion in the sixteen readout channels to less than 1% (about 0.48%, and 0.25% respectively).

The final results of low gain equalization for $V_{in} = 146\text{ mV}$ and $V_{in} = 292\text{ mV}$ are shown in Fig.4.20. The corresponding outputs were equalized to $\sim 100\text{ mV}$ and $\sim 200\text{ mV}$ respectively.

Standard outputs chosen above are arbitrary, a correction table should be put including all expected input levels with the corresponding standard outputs and correction codes.

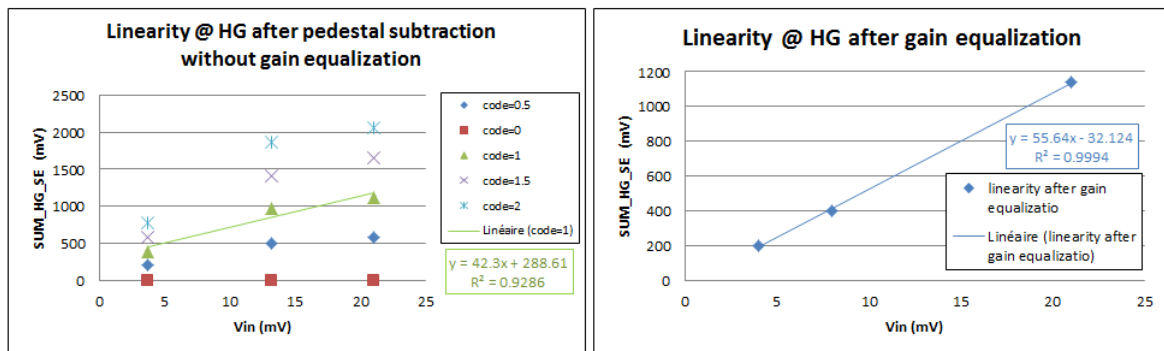


Figure 4.21: Each high gain output is the mean of the 16-channel outputs measured for only one channel fed at a time. Left: high-gain output vs V_{in} after pedestal subtraction, for different R-2R gains (i.e, for different gain control codes which are unique for the sixteen channel each time). Right: high-gain output vs V_{in} after gain equalization including pedestal subtraction.

This procedure is helpful not only for gain equalization purpose itself, but also to boost the covered dynamic range and for linearity correction if needed (Fig.4.21). For example, high gain path of one channel may get saturated at some limits of the input signal (only one pixel is saturated but not the others for example). This saturation will be translated in a deviation from linear response of the sum amplifier. Using gain equalization could force standard levels of output that optimize the linearity in such cases and hence increase the accepted range of inputs within this linear domain.

4.5.4 Noisy channel suppression

ALPS chip provides the possibility of software deleting any channel. This solution may be considered if a high noise level was measured on a given channel. This is done by giving a high logic value to the bit labeled *no_CB* that forms the ninth bit of the R-2R block control word. This process consists of driving the signal to a false output away from the sum amplifier input.

gain_fix bit	R2R control-word of 9 bits									switch direction	Comments
	b1	b2	b3	b4	b5	b6	b7	b8	no_CB		
0	1	0	0	0	0	0	0	0	1	to false output	channel is suppressed

Table 4.2: Gain control configuration with an active *no_CB* bit that leads to delete the low gain path of the corresponding channel (channel 15 here) even if the gain control was set to 128 (i.e., $G_{R2R} = 1$).

Fig.4.22 depicts channel 15 suppression on low gain path according to the configuration in table.4.2. Low gain path and high gain path of the same channel can be suppressed individually since each path has its own *no_CB* bit.

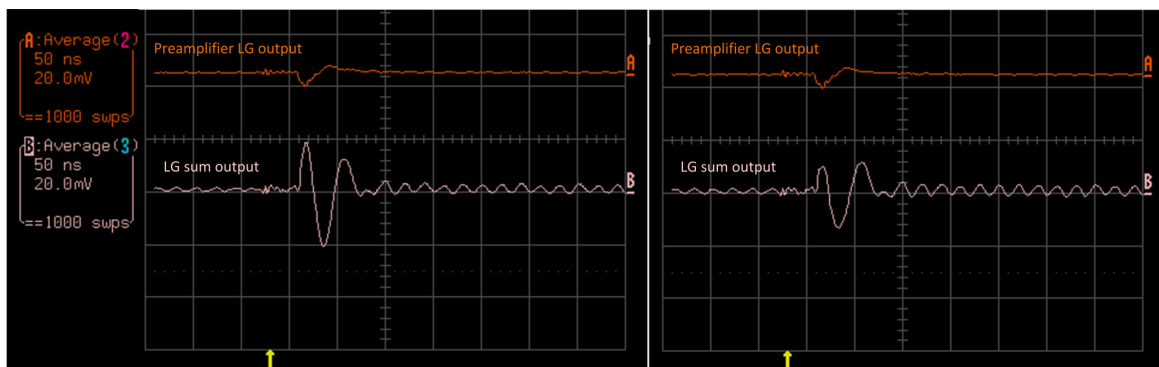


Figure 4.22: Left: low gain sum output of channel 15 when receiving an input of $V_{in} = 100 \text{ mV} \cong 259.7 \text{ photo electrons}$ and passing through R-2R block that was programmed according to the code 128. Right, the output at the same point if channel 15 was suppressed by activating the bit labeled *no_CB*. The signal that appears on the output is a residual pedestal. This result was obtained with the first test board.

The deleted channel will be suppressed from the sum output whatever its state was before activating this *no_CB* bit (i.e., regardless the 8-bit word that forms the R-2R code previously as was shown in Table.3.9).

Fig.4.23 depicts the output level when channel 15 is suppressed while its R-2R gain control code is set to 255 as depicted in table.4.3. We can notice the same output level in Fig.4.22-right.

gain_fix bit	R2R control-word of 9 bits									switch direction	Comments
	b1	b2	b3	b4	b5	b6	b7	b8	no_CB		
0	1	1	1	1	1	1	1	1	1	to false output	channel is suppressed

Table 4.3: Gain control configuration with an active *no_CB* bit that leads to delete the low gain path of the corresponding channel (channel 15 here) even if the gain control was set to 255 (i.e, $G_{R2R} = 2$).

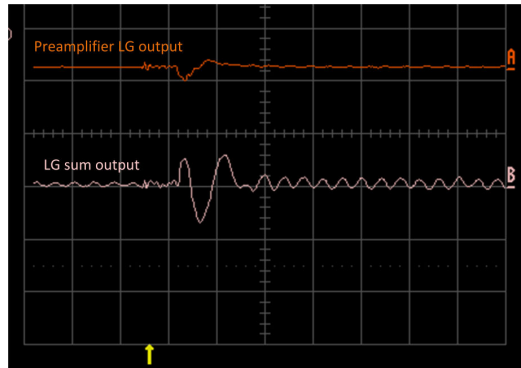


Figure 4.23: Low gain sum output when channel 15 is suppressed while receiving an input of 100 mV and gain control code of 255. The same output level is noticed as when the gain control code was set to 128 in Fig.4.22. This result was obtained with the first test board.

Channel suppression on high gain can be seen in Fig.4.24. All these results were obtained with the first test board that is the reason of the kind of oscillation on the base line.

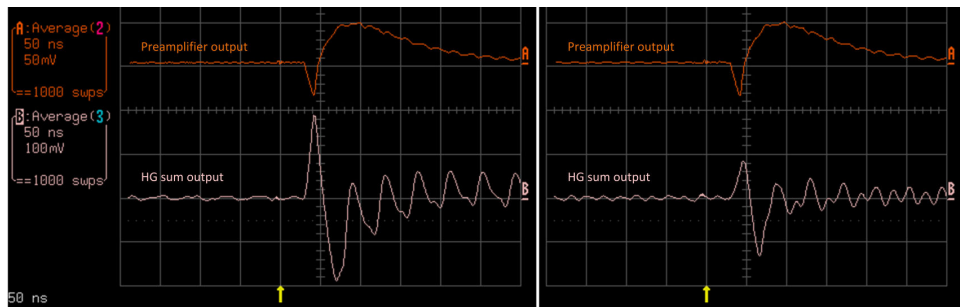


Figure 4.24: Left: high gain sum output of channel 15 when receiving an input of $V_{in} = 100\text{ mV}$ and passing through R-2R block that was programmed according to the code 255. Right, the output at the same point if channel 15 was suppressed by activating the bit labeled *no_CB*. This result was obtained with the first test board.

4.5.5 Bypassing gain control

This option may be needed in case of a dysfunction of R-2R control block. It consists of activating the *gain_fix* bit from the labview interface (Fig.4.4). An example of the gain control configuration is shown in table.4.4. The preamplifier output of all channels will bypass the R-2R block directly to the sum amplifier.

This means that the input signal will be amplified by the product of preamplifier gain and the sum amplifier, i.e, $G_{PA} * G_{sum-ampli}$.

gain_fix bit	R2R control-word of 9 bits									switch direction	Comments
	b1	b2	b3	b4	b5	b6	b7	b8	no_CB		
1	1	1	1	1	1	1	1	1	0	to sum amplifier	bypassing the R2R block

Table 4.4: Gain control configuration with an active *gain_fix* bit.

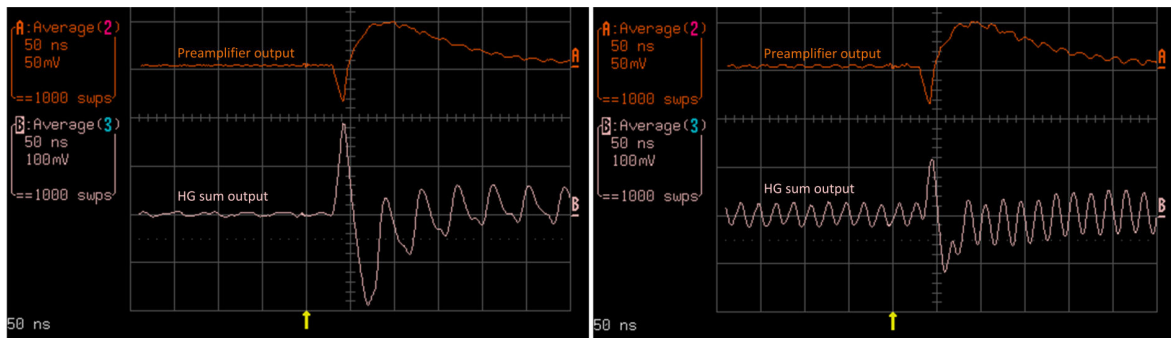


Figure 4.25: Using the first test board, for an input signal of 100 mV: Left, high gain output when signal is treated by the gain control whose code is fixed to full scale (255). Right, the same output when the signal bypasses the control step (active *gain_fix*).

For a given input of $V_{in} = 100 \text{ mV}$ applied at channel number 15, Fig.4.25 shows the sum high gain output before and after *gain_fix* bit is activated. While Fig.4.26 shows the same effect on the low gain path. These results were obtained with the first test board that is the reason of the kind of oscillation on the base line.

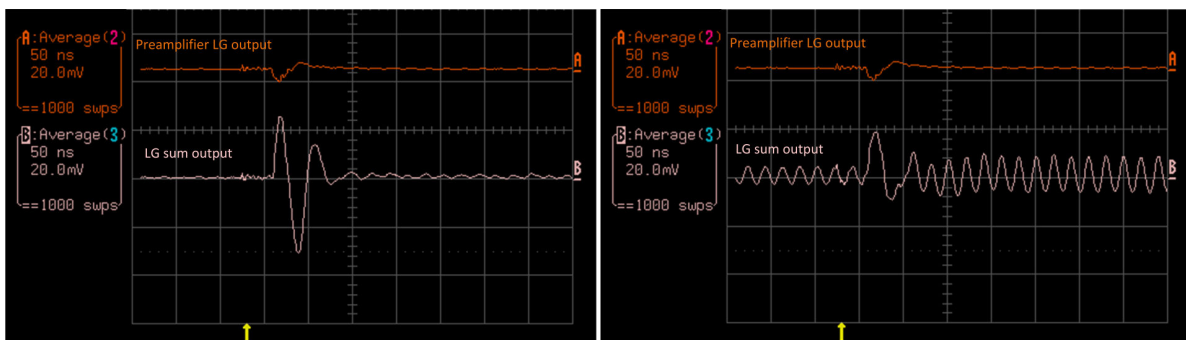


Figure 4.26: Using the first test board, for an input signal of 100 mV: Left, low gain output when signal is treated by the gain control code of 255. Right, the same output when the signal bypasses the control step (active *gain_fix*).

4.6 Sum function

The purpose of this test is to show the reliability of the output sum of several channels. The used method implies choosing two channels, applying an input on one channel at a time and measuring its own output. Then simultaneously applying the same input signal⁷ on these two channels and check whether the output of the chip is identical to the calculated sum of the two precedent measured values.

This test is divided into two sub-tests since the output signal depends on the gain of the readout circuit. It particularly depends on the programmed gain of the intermediate block (R-2R). The first sub-test verify the effect of gain control code on the reliability of the sum function whether we are summing two identical signals or two different signals. The second sub-test verify the sum as a function to the input signals.

In all these tests a pedestal correction will be done but not the equalization of the gain (for which an improvement of the performance is foreseen).

4.6.1 The shape of output signal

Observing signals on the oscilloscope gives an idea about signal form besides that we can verify the analog sum function. Fig.4.27 shows the high gain sum output of the ASIC for different gain-control codes (vertically). It shows also the output when two inputs ($V_{in} = 21 mV$) are separately applied to two different channels (*channel 5, and channel 16*) and then the measured sum output when both channels read simultaneously these two inputs(horizontally).

Table.4.5 shows the configurations set via Labview interface to control the $R2R$ gain for each case.

Each signal is the average of 1000 measurements done by the oscilloscope to eliminate the random noise.

gain_fix bit	R2R control-word of 9 bits									switch direction	Comments
	b1	b2	b3	b4	b5	b6	b7	b8	no_CB		
0	0	0	0	0	0	0	0	0	0	to sum amplifier	$G_{R2R} = 0$
0	0	1	0	0	0	0	0	0	0	to sum amplifier	$G_{R2R} = 0.5$
0	1	0	0	0	0	0	0	0	0	to sum amplifier	$G_{R2R} = 1$
0	1	1	0	0	0	0	0	0	0	to sum amplifier	$G_{R2R} = 1.5$

Table 4.5: Gain control configuration for the four cases considered in the signal shape test of the sum output.

⁷In order to generate two input signals a splitter is inserted between the pulse generator and the attenuation part. Two attenuators are then necessary to allow the selective suppression of one input on one channel while measuring the output of the other input on the other channel.

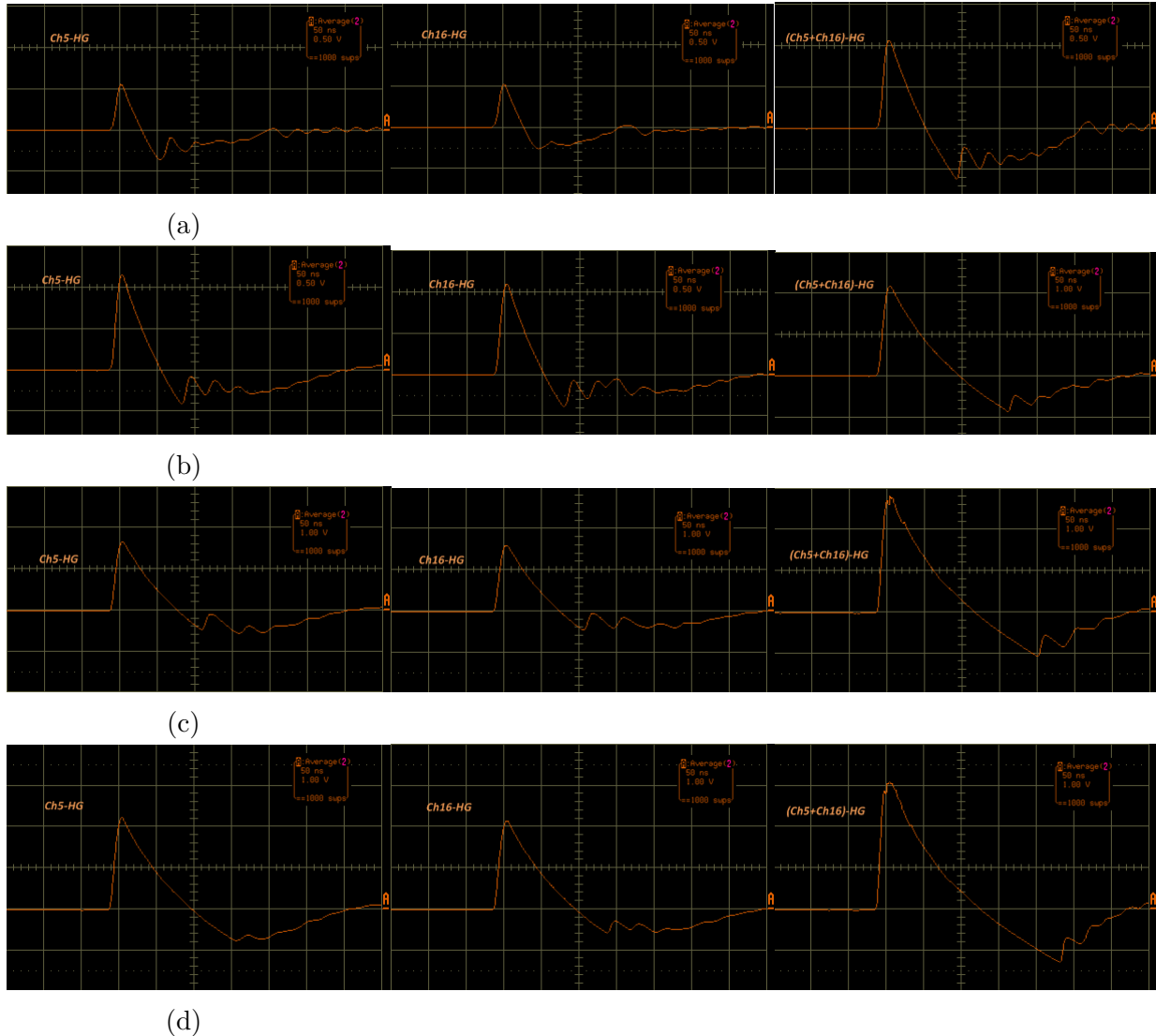


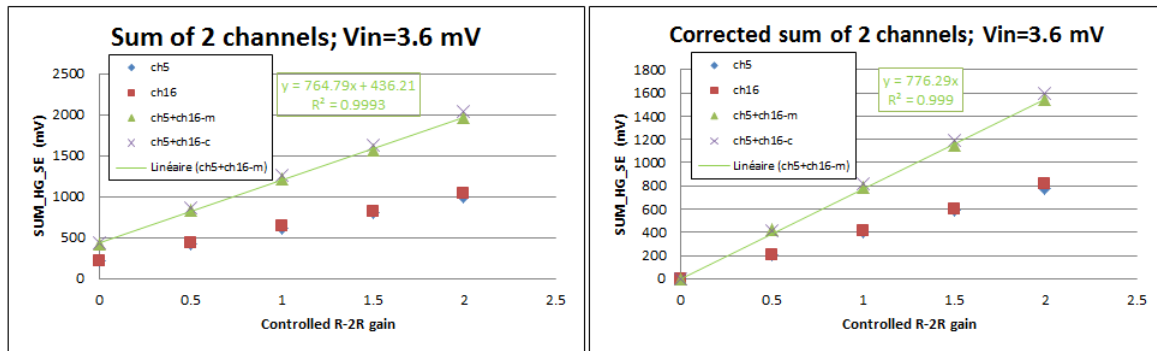
Figure 4.27: ASIC outputs (from left to right) of $ch5$, $ch16$ and $ch5+ch16$ for $V_{in} = 21mV$ when: a) R-2R gain = 0, which is also the residual pedestal discussed in section 4.5.1; b) R-2R gain = 0.5, c) R-2R gain = 1, d) R-2R gain = 1.5.

4.6.2 Sum as a function of the controlled gain

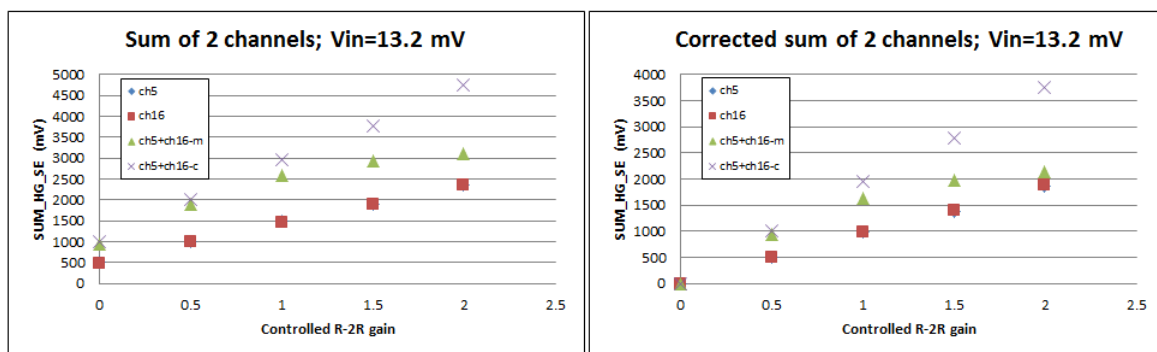
Fig. 4.28a shows the variation of the sum on the high gain path as a function of the R-2R gain. The summed output is a linear function to the R-2R code. Changing this code doesn't degenerate the expected sum value (i.e, the sum will change so we get the expected sum output for the new R2R configuration).

As the input signal gets higher the sum output stops rising at the saturation limit of the preamplifier or that of the sum amplifier which is found to be $V_{sat} = 2V$ as shown in Fig. 4.28b and Fig. 4.28c.

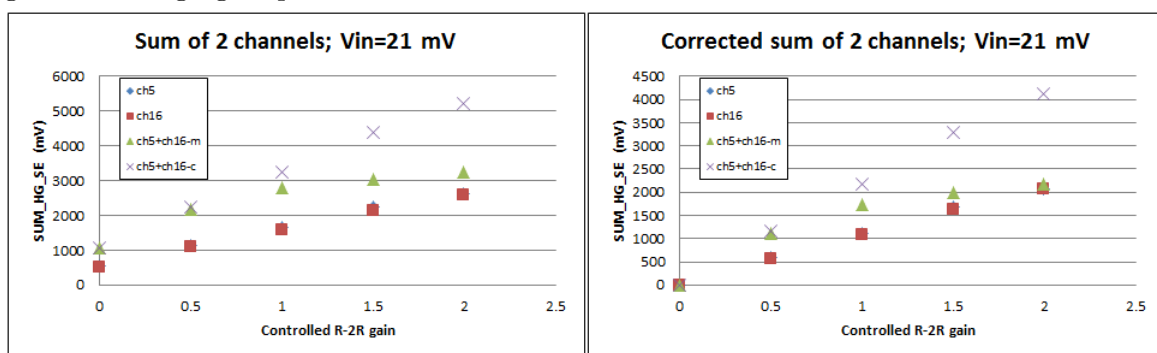
Fig. 4.29 is the result of doing the same process on the low gain path. In these tests for higher inputs a very good linearity with the controlled gain was also found on the low gain path.



(a) Left: sum of two identical inputs before pedestal subtraction. Right: the corrected sum after pedestal subtraction. In both figures, in blue is the output due to $V_{in} = 3.6\text{ mV}$ applied to $ch5$ as a function of the R-2R gain of $ch5$. In red is the output due to $V_{in} = 3.6\text{ mV}$ applied to $ch16$ as a function of the R-2R gain of $ch16$. The x plot labeled ($ch5+ch16-c$) is the manual sum of the output of the two channels fed and measured separately while the plot in green labeled ($ch5+ch16-m$) is the plot measured at the high gain sum output when both channels are simultaneously fed by two identical inputs of $V_{in} = 3.6\text{ mV}$ each. There is good agreement between both plots at each point. And sum function shows very good linearity with the R-2R gain.

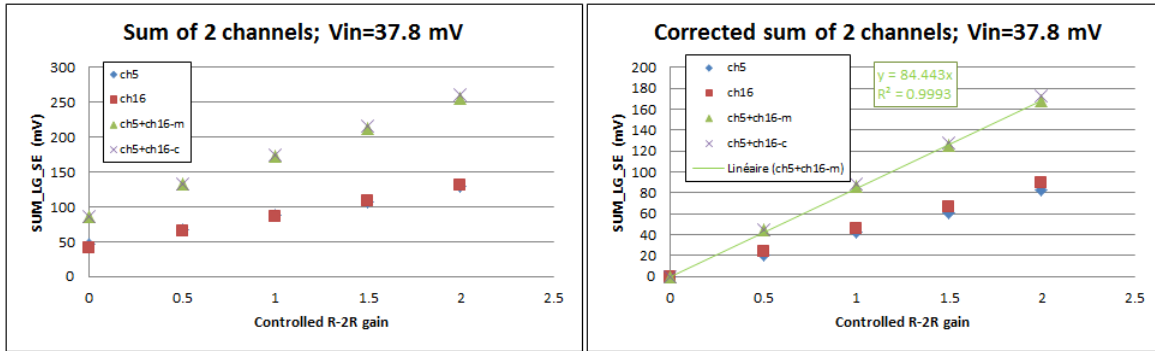


(b) Sum of two signals of the value $V_{in} = 13.2\text{ mV}$ on $ch5$ and $ch16$ for different controlled gains. The high gain path is saturated at 2 V .

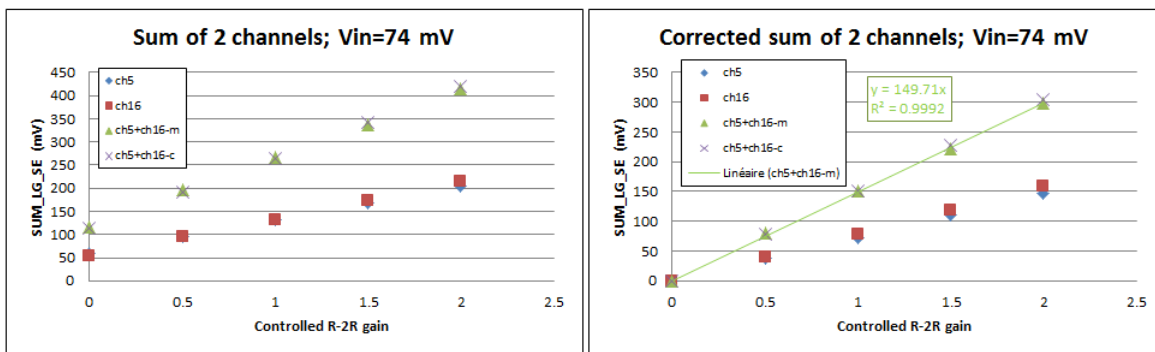


(c) Sum of two signals of the value $V_{in} = 21\text{ mV}$ on $ch5$ and $ch16$ for different controlled gains. The high gain path is saturated at 2 V .

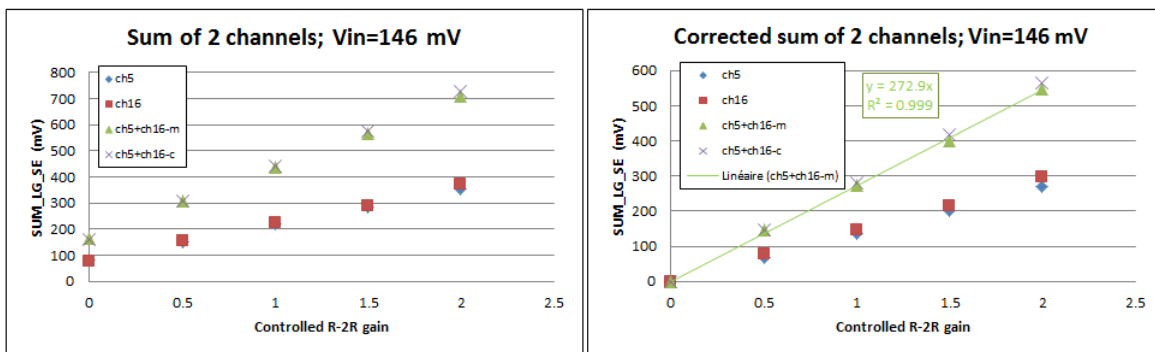
Figure 4.28: Sum measured on the single ended high gain output of the chip when two identical inputs are applied on two channels for different controlled gains.



(a) Left: sum of two identical inputs before pedestal subtraction. Right: the corrected sum after pedestal subtraction. In both figures, in blue is the output due to $V_{in} = 37.8$ mV applied to *ch5* as a function of the R-2R gain of *ch5*. In red is the output due to $V_{in} = 37.8$ mV applied to *ch16* as function of the R-2R gain of *ch16*. The x plot labeled (*ch5+ch16-c*) is the manual sum of the output of the two channels fed and measured separately while the plot in green labeled (*ch5+ch16-m*) is the plot measured when both channels are simultaneously fed by two identical inputs of $V_{in} = 37.8$ mV each. There is good agreement between both plots at each point. And sum function shows very good linearity with the R-2R gain.



(b) Low gain sum output of two signals $V_{in} = 74$ mV applied on *ch5* and *ch16* for different controlled gains.



(c) Low gain sum output of two signals $V_{in} = 146$ mV applied on *ch5* and *ch16* for different controlled gains.

Figure 4.29: Sum measured on the single ended low gain output of the chip when two identical inputs are applied on two channels for different controlled gains.

4.6.3 Sum of different signals

An example of the case where two different input signals are read by two channels at the same time is considered. Their sum measured on the single ended low gain output of the chip is depicted in Fig.4.30. It shows very good linearity with the programmable gain of the R - $2R$ block.

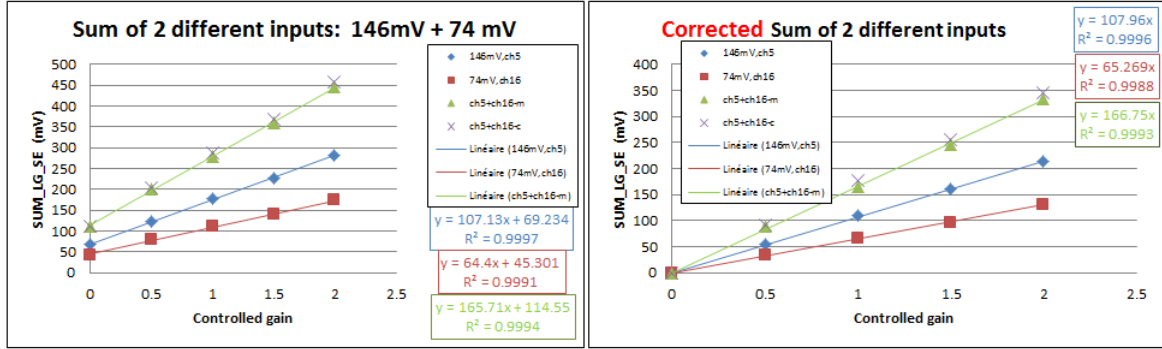


Figure 4.30: Left: sum of two different inputs where the plots include the residual pedestal. Right: corrected plots after pedestal subtraction. For both sides, in blue is the output when only $ch5$ receives an input signal of 146 mV . In red is the output when only $ch16$ receives an input signal of 74 mV . The x plot labeled $ch5+ch16-c$ is the expected sum of these two outputs in blue and in red. While the green plot labeled $ch5+ch16-m$ is the measured output when simultaneously $V_{in,ch5} = 146\text{ mV}$ and $V_{in,ch16} = 74\text{ mV}$.

This will compensate the limit of the high gain path for measuring upper limits of the covered dynamic range. An input voltage of 74 mV is the equivalent of 192 photo electrons. As for $V_{in} = 146\text{ mV}$ it corresponds to ~ 379 photo electrons. These light intensities can not be measured by the high gain readout electronics since the preamplifiers will already be saturated. While as seen above, low gain path can easily measure such quantities.

4.6.4 Sum as a function of the input level

The second part of the sum tests is to check the linearity of the sum function with the input level. For each R - $2R$ four principle gain control codes, single ended sum output is measured. Detailed results can be seen in Annex.B.4. At R - $2R$ gain of unity, this block is neutralized and its role is only to deliver preamplifier output to the sum amplifier. Considering this case, we can focus on the sum as a function to the input signal.

Here also we measure the output when one channel reads an input signal at a time before measuring the single ended output when both channels simultaneously read the two identical inputs. The different input signals are 3.6 mV , 6.6 mV , 13.2 mV , and 21 mV . Equivalent to 9.35 , 17.14 , 34.3 , and 54.5 photo electrons respectively.

Some deviation from linearity can be seen on the high gain sum output in Fig.4.31 (the point equivalent to 34 pe has already shown more nonlinearity in Fig.4.9), while the low gain sum output is very good linear as a function to the input signal as seen in Fig.4.32.

Low gain sum output as a function to input signal levels is shown in Fig.4.32. Input signals are 37.8 mV , 74 mV , and 146 mV . Equivalent to 98.18 , 192.2 , and 379.2 photo electrons respectively.

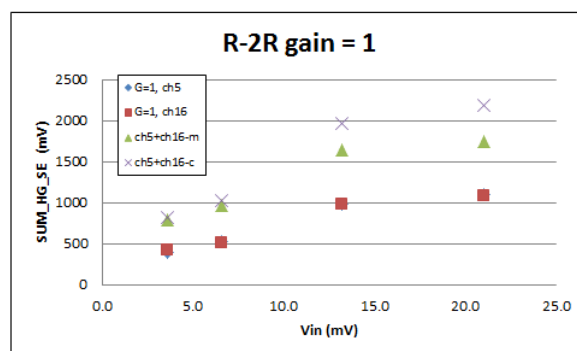


Figure 4.31: Sum on high gain path of two signals as a function of the level of these input signals. Here the R2R gain was set to 1 and in Fig.B.9, measurements are shown for different R-2R controlled gains. Results are after pedestal correction. In blue is the output when only *ch5* receives an input signal. In red, is the output when only *ch16* receives an input signal. In green, the plot labeled *ch5+ch16-m* is the measured sum output when both *ch5* and *ch16* are fed by identical inputs. The x plot labeled *ch5+ch16-c* is the arithmetic sum of the measured outputs when input signal is applied only on *ch5* and the measured output when the same input signal is applied only on *ch16*. For input signals that cause saturation on the high gain path, the output should be measured on the low gain path.

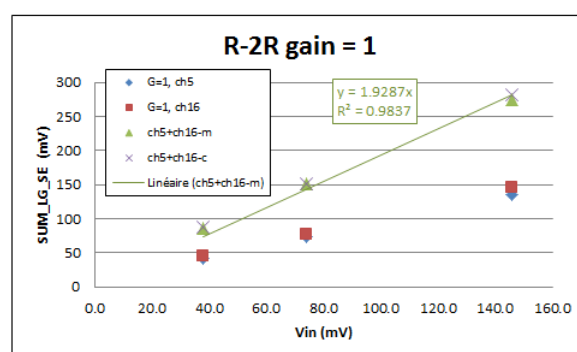


Figure 4.32: Sum on low gain path of two signals as a function of the level of these input signals. Here the R2R gain was set to 1 and in Fig.B.10, measurements are shown for different R-2R controlled gains. Results are pedestal free. *ch5+ch16-m* is the plot of the measured sum output when both *ch5* and *ch16* are fed by identical input. *ch5+ch16-c* is the plot of the manual sum of the measured output when input signal is applied only on *ch5* and the measured output when the same input signal is applied only on *ch16*.

The non ideal linearity of the high gain path is due to the saturation of one (since in this test no gain equalization is done) or both channels. It may be produced if at least one pre-amplifier is saturated or even if saturation occurs at sum amplifier.

Since high gain path is designed to detect and measure the lowest signals issue of the detector, especially the single photo electron signal; it is sufficient to be as perfectly linear over the beginning of the dynamic range and we can manage this nonlinearity for big signals that should be measured on the low gain path. Nonetheless, as was shown in section.4.5.3, gain equalization may have good influence on this performance (Fig.4.21).

4.7 Test bench for ALPS test with SiPM

The second part of tests are tests that were held with the detector SiPM connected to the test board. Fig.4.33 shows the different devices used in these tests.

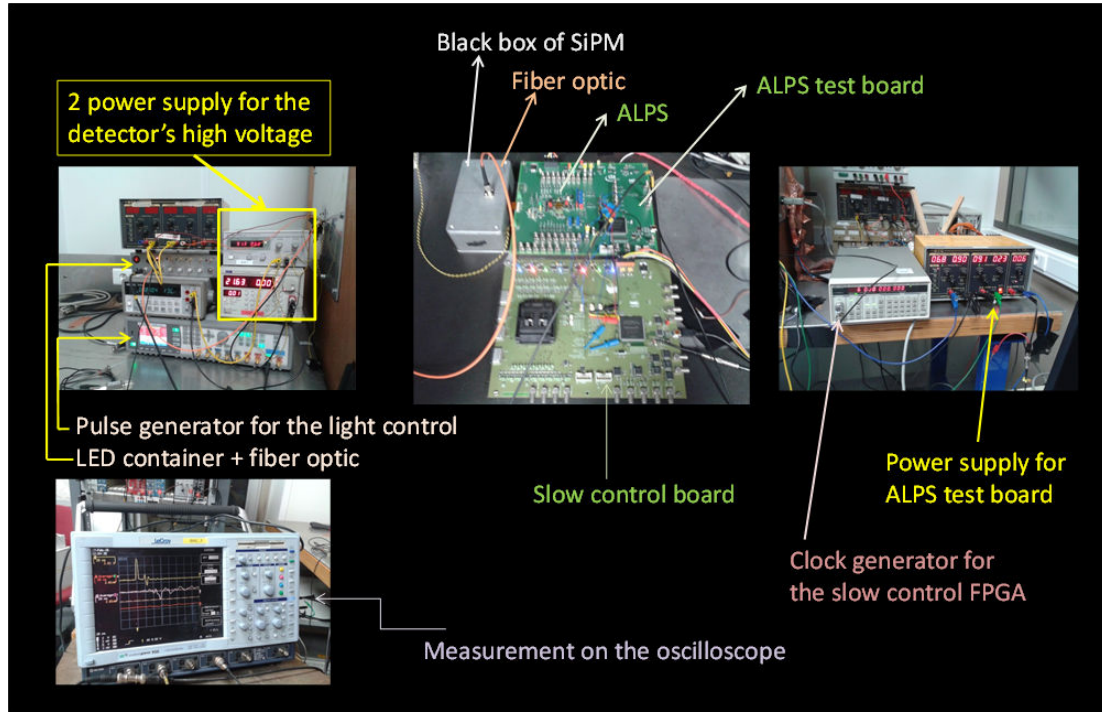


Figure 4.33: Test bench for tests with SiPM

This test bench is composed of the following devices:

- *Stabilized power supply AL 936*. A DC power supply for the test board that carries the chip ALPS and its slow control intermediate manager FPGA.
- A combination of 2 DC generators for the SiPM bias in order to be able to precisely change the detector's high voltage with a resolution of $\Delta V = 10mV$. These generators are: *Agilent E3612A DC power supply* that gives a maximum of 60V in series with *TSX35 10P programmable DC PSU* that gives the rest of the bias voltage.
- *Agilent 81150A 120MHz pulse function arbitrary generator* that provides the LED control signal. Table.4.6 shows the light control pulse characteristics.
- *LeCroy wavepro 950* oscilloscope whose band width is of 1GHz in order to measure output signals.

In order to approach the CTA telescope conditions, a blue light emitting diode (LED of 450nm wavelength) is used to simulate Cerenkov light. The relative intensity emitted by this LED (Annex.C - section.C.1) at the considered wave length is found to be 0.675 which means a transmitted intensity of $20.25 mcd^8$.

⁸cmd: millicandela the unit used to express luminous intensity that is the light flux emitted per solid angle (lumen/sr).

V_{pp}	5 V
V_{DC}	2.5 V
Load impedance	50Ω
Output impedance	50Ω
Polarity	Normal
Frequency	10 KHz
Pulse width	5 ns
Lead edge	2.5 ns
Trail edge	2.5 ns

Table 4.6: LED control pulse

This LED is controlled by a pulse generator output whose parameters are shown in Table.4.6. Light is transmitted by a fiber optic to the black box where is put the SiPM matrix. The fiber optics is a multimode type that has a relatively big diameter⁹ and a large numerical aperture¹⁰. From the fiber optic side, basic alignment technique is enough to get a good coupling with the light source¹¹. Still, SiPM matrix need to be in a horizontal position perpendicular to the Fiber optic emitting side. SiPM connector goes out of the box to the test board that carries ALPS readout chip. The chip is controlled by a LabView program and output signals are measured manually on the oscilloscope.

The second board that appears in Fig.4.33 was used to provide communication between the chip and the Labview interface because of the breakdown of the FPGA on ALPS test board. This arrangement will limit the tests that could be performed and will damage test results.

Optical filters For different light intensities, a neutral light density filters¹² are used. These filters have a flat wavelength response i.e, they are insensitive to wavelength for absorption. The optical density of a filter is given in Eq.4.1, where I_i is the intensity of the incident light and I_o is the intensity of the transmitted light through the filter. It is then the base 10 logarithm of the filter's opacity, where the opacity is the amount of light that the filter blocks.

$$D = \log \frac{I_i}{I_o} \quad (4.1)$$

An optical filter is usually marked with the percent of its optical density. The filters used in these tests have the reference $ND-D\%$ that goes from $ND-10$ to $ND-100$. The transmitted light intensity can be found knowing light intensity of the light source and the optical density of the used filter. Table.4.7 is a list of the used optical filters with their optical densities and the transmitted light intensities.

⁹There are two types of multi-mode fiber optics: gradient-index and step-index fiber optics. The first one has a bigger diameter with respect to the latter.

¹⁰Multimode fiber optics have a large acceptance cone, i.e, a large acceptance angle $\Theta_{max} = 1/2$ angle of the cone. Their numerical aperture is then bigger than that for the single-mode counterparts. $NA = n \sin \Theta_{max} = \sqrt{n_{core}^2 - n_{clad}^2}$ where n_{core} is the refraction index of the core material of the fiber and n_{clad} is that of its clad.

¹¹However, their band width is small and this is essentially due to the phase distortion and the group delay distortion.

¹²CVI Laser Optics home: <http://cvilaseroptics.com/>

Filter	D	relative intensity I_o
No filter	-	0.675
ND-10	0.1	0.536
ND-20	0.2	0.423
ND-40	0.4	0.269
ND-60	0.6	0.17
ND-80	0.8	0.11
ND-100	1	0.068

Table 4.7: Light intensities at the output of each used optical filter (losses in optical connection and fiber optic were ignored).

SiPM matrix was polarized at a reverse voltage of 72.7 V that was found to give the best results. It should be mentioned that the spot of light emitted by the fiber optic on the SiPM array is not precisely focused on the center of the matrix neither the matrix is well horizontally held inside the dark box. These damages occurs because of some treatment that was necessary to connect the SiPM array to the test board that carry the chip. For these reasons besides a damage in the FPGA that transmits slow control bit-sequence to the chip, it was difficult to redo all the essential tests on the chip as was done in the electrical tests. As a consequence, it was only possible to do basic tests to check the shape of the signal at the output of the preamplifier and at the sum output of the chip.

4.8 Signal shape

Fig.4.34 shows an example of the signal measured on the high gain output of the preamplifier. This amplitude was obtained with full light intensity of the LED (with no filter used) and with a new cover of the dark box that allows to approach the fiber optic end from the SiPM surface.

Fig.4.35 shows the sum signal shape at the single ended sum output measured on the high gain for an active *gain_fix* bit that will bypass the gain control process of the whole readout channels to avoid the slow control anomaly.

As a matter of fact, measurements at the preamplifier outputs require probe activation by slow control intervention. Instability and several anomalies were observed in this function like for example the activation of both low and high gain outputs with sometimes one bit and other times two different bits in the probe part of the Labview program. The dysfunction of probe bits for some channels were also noticed. A review of the slow control program is an essential task for future tests.

Besides, with this new arrangement (new cover of the dark box that holds the SiPM matrix), it was not possible to measure signals from all preamplifiers since we can not move the new cover precisely (the movement of the cover is limited) and the position of the SiPM matrix is not precise neither.

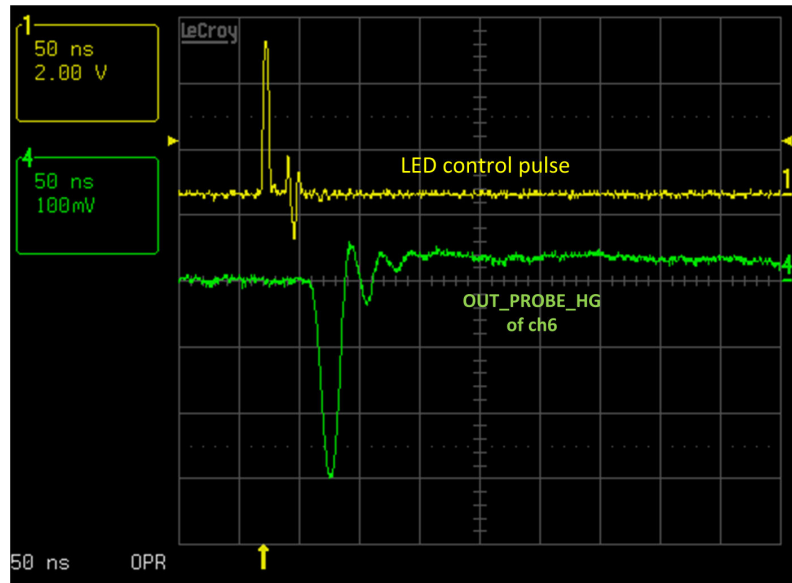


Figure 4.34: High gain preamplifier output of channel 6 reading a signal produced by the corresponding macro pixel (SiPM) when the SiPM matrix is illuminated with the full LED intensity.

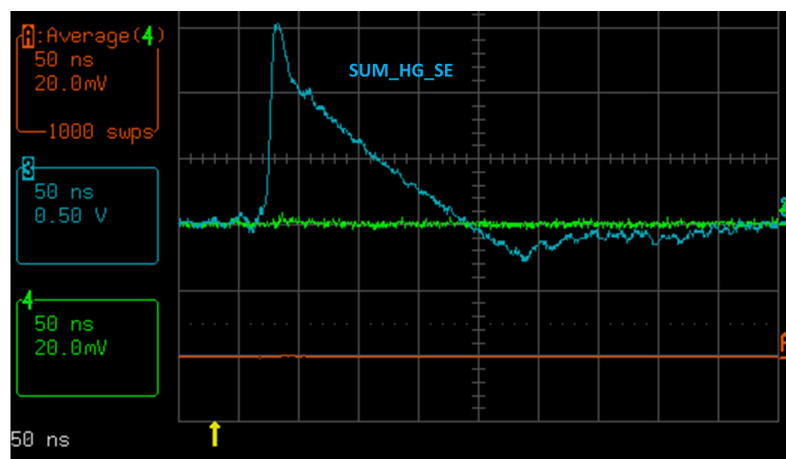


Figure 4.35: Sum signal shape measured at the single ended output of the high gain, slow rate effect can be noticed.

The try to do linearity tests on the preamplifier and on the sum amplifier can be seen in section.C.3 and section.C.4. There is no precise physical interpretation for those plots since the light intensity on X-axis could not be found because of filter mismatch. The fact that more measurements could be done on the sum output bypassing all slow control intervention while most of these measurements were not possible at the preamplifier outputs involving probe activation by slow control commands implicates errors in slow control. That is the reason why new test board should be designed. It would be of great interest to separate the chip from all digital parts. We can envisage two sub boards, a small chip holder board and FPGA holder, with the possibility to do one time charge of chip register before performing tests and then cut-off every connection between the analog and digital parts (i.e, between the chip and the FPGA).

4.9 Conclusion

A first test board was designed with a 100-pin chip socket in order to test the 5 packaged samples of ALPS readout chip. A labview interface was also programmed allowing to set codes that will form the slow control bit sequence. Slow control consists in adjusting the applied voltage (and hence, controlling the gain) of each individual macro pixel (SiPM) of the detector, the gain of each of the sixteen preamplifiers, and the discriminator threshold. Besides that, several test points could be activated to probe signals at different critical points inside the chip and to read signals directly at the preamplifiers' outputs. FPGA is welded on this test board to handle the communication between the labview interface and the chip registers.

The first tests used electrically generated signals as inputs. At the output of the preamplifier, oscillation and noise were observed to affect the measured signals. In addition, high gain to low gain ratio was measured $HG/LG = 10$ while a ratio of about 90 was obtained from simulation. These tests have raised the need for a **second test board** on which isolating buffers were added to protect signals from noise picked by cables, signal paths, and socket pins since the chip is directly welded on the second test board. Tests with the second test board have lead to the following results:

Electrical tests use a voltage pulse generator with an attenuator and an input resistor of $1.1\text{ k}\Omega$ in order to vary the input level. Input signal that corresponds to one photo electron signal was found to be $385\ \mu\text{V}$.

Preamplifier can measure signals ranging from one photo electron up to 259 photo electrons on the high gain ($50\ \mu\text{V}$ up to 100 mV). And it measures up to 1039 photo electrons on the low gain path (the maximum applied input voltage of 400 mV). It is worth mentioning that at this maximum input signal the low gain path is not yet saturated. Considering the linearity condition (linearity error below 3% for CTA), high gain measures a dynamic range between $11 - 193\text{ pe}$. While low gain respects this linearity condition for a range $171 - 337\text{ pe}$.

The high gain to low gain ratio was doubled using this new test board. The gain ratio at the output of the preamplifier was 20. Regarding the gain ratio of 10 that was found with the first test board, this enforces the theory of a test board problem.

The rising time of the minimum input signal was limited by the minimum provided by the pulse generator which is 2 ns (more than double the rising time of a SiPM signal). As a consequence, the response speed of the preamplifier could not be checked. Another reason that has prevented this test is the additional parasitic capacitive and inductive loads related to lemo connectors and test points. These elements directly affect the timing characteristics of output signals.

For what concerns **slow control facilities**, they were checked in two cases: when each individual readout channel was fed by an input signal (gain control and gain equalization). And when two channels were receiving input signals (sum function).

Testing the sixteen readout channel individually has shown a gain dispersion among them of about 5.5% in the worst case. Gain of each channel was found to change linearly according to corresponding gain control word of 8 bits that should be set in the Labview interface. High gain and low gain of each channel can be controlled independently.

Moreover, gain dispersion among the sixteen readout channels could be reduced to less than 1% fulfilling the goal. For a given input, gain unification process consists of

several steps: measuring the output of each channel when its gain control word is set to 0 (*the residual pedestal*), deciding the standard output for this given input, finding the corresponding gain control code for each channel (that will give the nearest output to the standard output), the last step is to measure outputs corresponding to the gain control codes and to subtract the corresponding residual pedestals from measurements. This facility is helpful to correct linearity and to boost the covered dynamic range even more. A correcting table should be put listing all expected levels on the input with their corresponding standard outputs and correcting gain control codes.

Noisy channel suppression (for each channel, there are two *no_CB* bits one for the high gain and the other for the low gain) and gain control bypassing (a general common *gain_fix* bit for the sixteen channels) were checked and was found to work as predicted.

Introducing two input signals to two different readout channels, the *sum function* (on both high and low gains) was tested and was found to show the expected performance after the pedestal subtraction. Summed output is a linear function to gain control codes of the two channels whether their inputs are identical or different signals. The summed output is also a linear function to the input level.

Tests with SiPM array In these tests a blue light emitting diode was used to send light through an optical fiber into the black box including the detector. An anomaly was found in the slow control function and probe activation bits (for these tests an additional test board was used to communicate with the labview interface).

To check signal shape, a new cover was designed to allow the optical fiber to come closer to the detector. Good signal shape (similar to that found by simulation) was measured at the high gain (and that of the low gain) output of the preamplifier and at the single ended high gain (and that of the low gain) sum output.

Several improvements in the test bench including: test board, slow control, and mechanical system could be essential for complete tests and hence, for a better evaluation of the chip.

Summary and perspectives

Summary SiPM photodetectors are serious candidates to replace photomultiplier tubes (PMT) in the next generation of the LST cameras. Using SiPM detectors for the LST can reduce the energy threshold of the detected gamma rays. Characterization tests on a monolithic array of 4×4 SiPM fabricated by Hamamatsu have proved the advantage of using such detectors. SiPM matrix operates at optimal bias voltage of about $72 V$ a low bias voltage comparing to that of the PMT. An average gain of $7 \cdot 10^5$ was measured with a gain dispersion of $\sim 10\%$ among the sixteen macro pixels of the matrix. Gain of the SiPM depends on its applied voltage. As a consequence, gain dispersion in the SiPM matrix can be reduced by adjusting the applied voltage of each macro pixel. This feature was taken into account in the front-end electronic design.

ASIC design and preamplifier simulation results: An 8 – bit digital to analog converter is inserted at the beginning of each readout channel. Its role is to adjust the applied voltage of the corresponding macro pixel (SiPM).

Output signal of each SiPM is read by a current mode preamplifier of dual gain: high gain and low gain. According to simulation results, this structure makes it possible to measure a dynamic range between 1 *photo electron* and 125 *photo electrons* on the high gain. While on the low gain, the dynamic range can reach more than 2000 *photo electrons*. The two gains overlap over one decade with a gain ratio of ~ 90 . The high gain path responds to the single photo electron signal within less than $3 ns$ and measures it with a signal to noise ratio of ~ 6 . The power consumption of the sixteen preamplifiers is less than $30 mW$.

Each gain path is adjusted by an independent *R2R* structure of 8 bits. A ninth bit is added to suppress the path if it is found noisy. An additional bit common to the 32 gain paths is added to bypass these *R2R* blocks. This last function is important to avoid possible dysfunctions of these blocks.

At each gain path and after individual gain control, the sixteen preamplifier outputs are summed. ALPS gives only two analog signals: one of the high gain sum and the other is the low gain sum.

A discriminator generates a trigger signal which is the third output of the chip. it is produced by comparing the high gain sum output to a programmable threshold. A 10 – bit DAC is integrated to vary this threshold.

The proposed readout electronic was designed in AMS $0.35 \mu m$ BiCMOS, SiGe technology. ALPS stands for *ASIC de Lecture Pour SiPM*. It is a 100 – pin chip that consists in sixteen readout channels, analog sum function, and trigger function. Besides, gain control facilities.

Two test boards were designed and a Labview interface was programmed. Tests with the first test board showed added noise, oscillation and high to low gain ratio of 10. These were the reasons behind the need for the second test board. The following are results of tests that were done using the second test board.

Electrical tests, voltage pulse generator was used to produce input signals. One photo electron is estimated to be the equivalent to $385 \mu V$. The high gain path saturates at an input level of $100 mV \equiv 259 \text{ photo electrons}$. The low gain path measures input signals up to $400 mV \equiv 1039 \text{ photo electrons}$ and it is not yet saturated.

Including the linearity condition (linearity error $< 3\%$) imposed by the CTA, the high gain measures a range of $11 - 193 pe$ within the desired linearity. As for the low gain path of the preamplifier, it measures a range between $171.7 - 337.7 pe$ respecting the linearity condition.

Gain ratio was doubled: $HG/LG = 20$ was obtained with the second test board comparing to that obtained with the first test board. However, it is still less than expected. The response speed of the preamplifier could not be checked because the minimum rising time provided by the pulse generator is $2 ns$ double that of the real SiPM-generated signal ($t_{r,SiPM} = 1 ns$). Both gain ratio and response speed degradation can also be explained by the effect of the parasitic capacitive and inductive loads related to test points and lemo connectors.

As for the slow control tests, the gain control via $R2R$ blocks was found linear with the slow control codes. A gain dispersion of 5.5% among the sixteen preamplifiers was measured. This dispersion could be reduced to less than 1% ($\sim 0.2\%$ for the high gain paths and $< 0.5\%$ for the low gain paths) thanks to the $R2R$ configuration set in the Labview. The noisy channel suppression and the gain control bypassing were checked. They operate as expected. Gain equalization is a helpful mechanism to correct linearity and to boost the covered dynamic range. A correcting table should be put listing expected input levels, standard outputs and the correction codes.

The sum function tests include an additional pedestal subtraction process. The residual pedestal was defined as the output when the gain control code is set to zero. After pedestal subtraction, sum function was found a linear function to gain control codes and to input signal level.

Tests with SiPM A blue light emitting diode (LED) was used to simulate Cherenkov light. An optical fiber is used to send light into the black box including the detector. An anomaly in the slow control function was observed preventing complete tests. However, signal shape at the output of the preamplifier and at the output of the sum (chip output) was found similar to simulation.

Perspectives Outputs of the ASIC are single ended signals that should be converted into differential signals. This is required by the following acquisition system (NECTAR or DRAGON). Because of time constraints, this conversion is performed thanks to a discrete electronic devices that are welded on the test board. However, the integration of this functionality inside the ASIC is a considerable perspective for a forthcoming version.

It is important for final and more reliable evaluation of the ALPS chip to pay more attention to test bench mechanical and optical components especially for what concerns better light interaction mechanism with the different macro pixels of the SiPM array. The future perspective includes a test board composed of two small sub-boards with smaller

number of test points (less added parasitic elements) and better isolation buffers. One sub-board will be the ALPS chip holder and the other will be dedicated for the FPGA and control peripheries. This separation strategy may promise lower additional noise and less digital influence on the precision of the performance of the chip. Slow control program should be reviewed as well. Tests of the dynamic range and linearity should then be done to complete the evaluation process of ALPS.

Appendix A

Terminology of photodetector devices

Whatever type of photodetector, its performance is described in some physical and technical terms. According to the technology and structure, different terms are used to describe the performance of different photosensors. Here is a description of the most important characteristics usually used to talk about the performance of different photodetectors[41][49][116][117]:

Photo Electron (pe) It is the term used to point out one electron that will be created by an incident photon in the photo sensor.

Photon counting Light in its corpuscular definition is a stream of photons. Photon counting is a technique for measuring low light levels since in this case photons are separated from each other and can be counted.

Responsivity (R) Also called **Photo Sensitivity**, it is the ratio of the produced photocurrent to the radiant power¹ of the incident light. This ratio is called the *absolute responsivity* and is expressed in A/W .

$$R = \frac{I_e}{\Phi_r} \quad (\text{A.1})$$

The relative responsivity (%) is the normalized responsivity to its value at the peak wavelength².

Spectral response The output current (i.e, photocurrent) of the photodetector is proportional to the energy of the incident light as seen in section.2.2. Photo responsivity describes the conversion efficiency of the incident photons into photoelectrons, it varies

¹Light quantities are considered either physical quantities or photometric quantities. In the former, all wavelengths are considered while in the latter, light quantities are correlated to the visual sensation of light (human eye sensitivity). Luminous flux of light $\Phi = k_m \int \Phi_r(\lambda)V(\lambda)d\lambda$ where k_m is the maximum sensitivity of the human eye (638 lm/W), $V(\lambda)$ is the typical sensitivity of the human eye and Φ_r is the radiant power of light.

²The peak wavelength is the wavelength for which the sensitivity reaches its maximum.

according to the incident wavelength. Eq.A.2 resumes the relationship between the energy (measured in eV) and the wavelength (measured in nm).

$$E[eV] = \frac{1240}{\lambda[nm]} [34] \quad (A.2)$$

According to its energy and hence to its wavelength, the incident light can pass through the detector without any attenuation ($E < E_g$) or it can be partially or totally absorbed. The spectral response describes the photo sensitivity as a function of the wavelength. Depending on the manufacturer the spectral response range can be defined as the region in which the relative sensitivity is higher than a specific percentage (e.g, 5%) of the peak value.

Quantum Efficiency (QE) It describes the probability that an incident photon will generate an electron that will contribute to the output current. Since only a fraction of the photon flux will be effectively detected because of several issues like the reflection at the surface of the device, the absorption coefficient and depth of device material, recombination of produced charge carrier. $0 \leq QE \leq 1$. Quantum efficiency is then the number of generated electron/hole pairs N_{pe} divided by the number of the incident photons N_{hv} .

$$QE = \frac{N_e}{N_{ph}} \quad (A.3)$$

Photodetection Efficiency (PDE) It is a measure of what percentage of incident photons were detected.

$$PDE = QE * f_g * P_a \quad (A.4)$$

Where QE is the quantum efficiency defined previously, f_g is a geometric factor that depends on the effective area of the detector and P_a is the avalanche probability. Hence, photodetection efficiency is an indicator related to the type of the photodetector and to its fabrication technique. For a wave length of $\lambda \sim 450 nm$, the PDE of PMTs³ is about 20%. While, PDE is found $\sim 30\%$ in a P-on-N structure G-APD⁴ produced by Hamamatsu and operates at 1V over breakdown, while it is $\sim 18\%$ in a N-on-P G-APD fabricated by Photonique/CPTA that operates at 4V over its breakdown[36]. PDE as a function of wave length is depicted in Fig.A.1 for two different fabricators of SiPM⁵ and for different cell sizes.

Over voltage (ΔV) The avalanche process starts at a voltage known as the breakdown voltage. The over voltage is the bias voltage above the breakdown voltage that starts the geiger-mode avalanche (Geiger mode photodetectors will be discussed later in section.2.4.4). The operating voltage is then given as:

$$V_{Bias} = V_{BR} + \Delta V \quad (A.5)$$

Operating at a voltage over the breakdown optimizes the performance of the photodetector in terms of gain. However, it may increase the noise as well.

³PMT: Photo Multiplier Tube will be discussed in section.2.3.

⁴G-APD: Geiger Analanche Photo-Diode will be discussed in section.2.4.4.

⁵SiPM: Silicon Photo-Multiplier will be discussed in section.2.5.

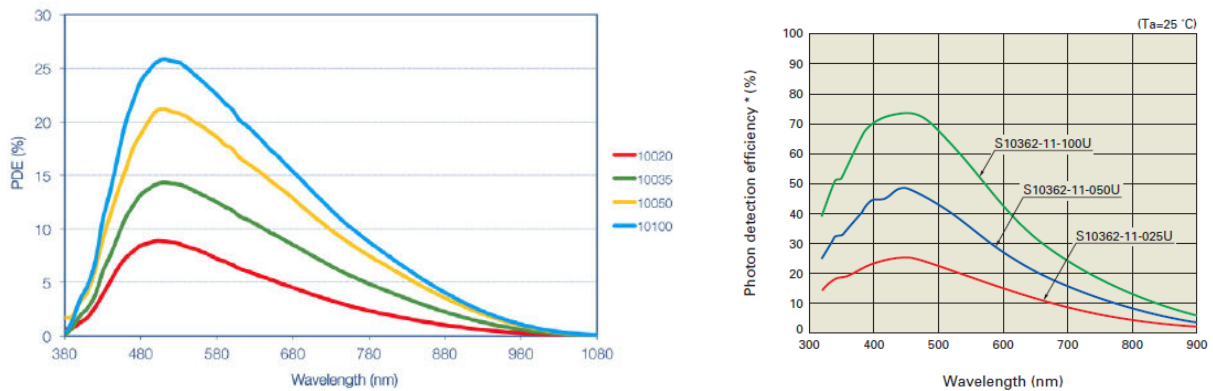


Figure A.1: PDE as a function of wavelength for different device sizes. Left, from Sensl[116]. Right, from Hamamatsu[49].

Gain (G) Internal gain of the photodetector is a characteristic related to photomultiplier tubes and semiconductor photodetectors using the avalanche phenomena. It is the ratio of the number of multiplied electrons to one electron excited by one incident photon. Or it is the total charge at the output of the detector responding to one photon divide by the charge of the electron q .

$$G = \frac{Q_{total}}{q} \quad (\text{A.6})$$

Where the total charge Q_{total} is a function to several geometrical and environmental factors represented by the detector capacitance C and the applied operating voltage δV .

$$Q_{total} = C * \Delta V \quad (\text{A.7})$$

Dark current (I_D) and Dark Count Rate (DCR) Noise in optoelectronic devices is defined as the level of their output within the absence of an incident signal, i.e, in dark. This background signal affects the minimum light quantity detected by the device.

The main source of noise is the thermal generation of charge carrier in the device material. It can be described in the dark count rate DCR which is the number of dark induced pulses per second (Hz)[37]. Fig.A.2 illustrates dark current pulses in a photodetector.

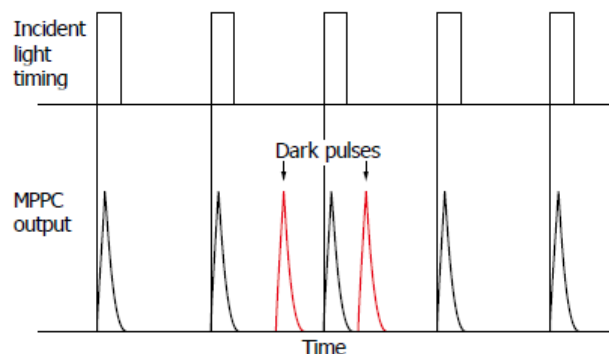


Figure A.2: Pulses of the incident light on top. On the bottom: In black, pulses due to light at the output of the photodetector (of type MPPC: Multi Pixel Photon Counter) and red pulses are dark induced pulses[50].

The DCR distribution is poissonian in time and its *rms* is the noise contribution of the detector[116]. DCR is found to depend on the detector size and area[116]. Since of thermal origin, DCR increases with temperature. DCR increases slightly with operating voltage at low temperatures but the influence of over voltage becomes very clear at high temperatures. Hence DCR can be limited by cooling to low temperatures.

After pulse It is a spurious pulse that appears in the wake of the real pulse. This phenomenon has different origins according to the type of the photodetector.

In the photomultiplier tubes (PMT), afterpulsing is caused by the elastic scattering of the electrons from the first dynode. However, the main cause of afterpulses in PMTs are the positive ions generated by the ionization of residual gases in the PMT[118][119].

In solid state photodetectors, crystal defects may trap generated charge carriers and release them after some time (some nano seconds[120]). The resulting spurious pulses cause detection errors since they have the same shape as the photo-generated pulses. The probability of the after pulse after a breakdown is $\sim 20\%$ [121].

On the contrary of the dark current, after pulse rate decreases when temperature increases since the lower the temperature is, the higher the probability that charge carriers may be trapped in crystal defects. Improving materials and process technology can reduce the after pulse rate. Which has good effect on signal to noise ratio and allow operation at wide range of bias voltages, better time resolution and better photo detection efficiency[50].

Crosstalk Secondary photons may be generated due to energetic charge carriers excited in the crystal⁶. Those photons different from incident photons may be detected in adjacent photodetectors (or in neighbor pixels in multipixel detectors).

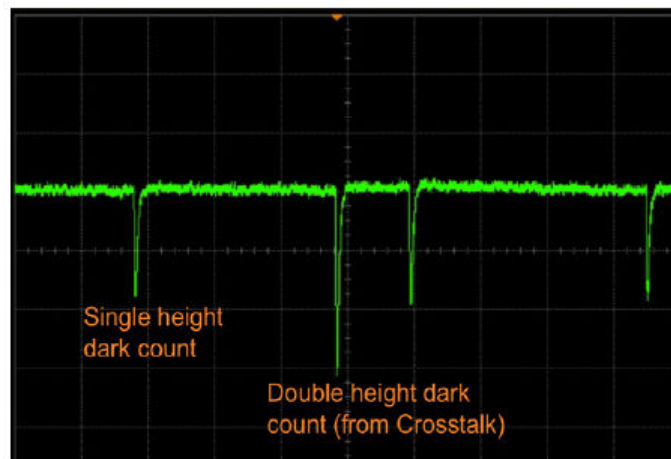


Figure A.3: Oscilloscope shot showing dark counts and we can see the crosstalk effect[116].

Crosstalk is considered as an important source of errors in photodetectors. Optical trenches or grooves are integrated in the semiconductor detectors in order to isolate pixels from each other and stop photon tunneling. Secondary photons will then be blocked from

⁶By stimulated emission pointed to in section.2.2

reaching the neighbor detectors built in the same semiconductor wafer and crosstalk is then reduced.

Rising time (t_r) For a signal to rise from 10% to 90% of its maximum, it takes some time that is known as the rising time. This criterion is very important for the electronic system in particular since it defines its response speed. Electronic circuit that will read a fast signal should have a wide band width so that to keep the characteristics of the leading edge.

Time resolution It is the width σ of the time distribution between the moment light pulse is emitted on the detector and the moment when an output pulse appears[51].

Even if photons arrive at different macro cells simultaneously, their output signals may not be at the same time. A time fluctuation called *jitter* occurs. If two photons enter macro pixels with a certain time difference shorter than this jitter, it would be impossible to be detected. The time resolution is also defined as the minimum time difference that can be detected by a SiPM. It is defined as the FWHM of the distribution of time jitter[49].

Appendix B

Electrical tests (continuation)

B.1 Residual pedestal

As was mentioned in section.4.5.1 a residual pedestal is measured on the output even if the readout channel was suppressed or that its gain control code was set to zero (R-2R code is a sequence of bits that are all zeros). This residual pedestal was showed on the low gain in Fig.4.14, but it is also measured on the high gain of the studied channel as seen in Fig.B.1.

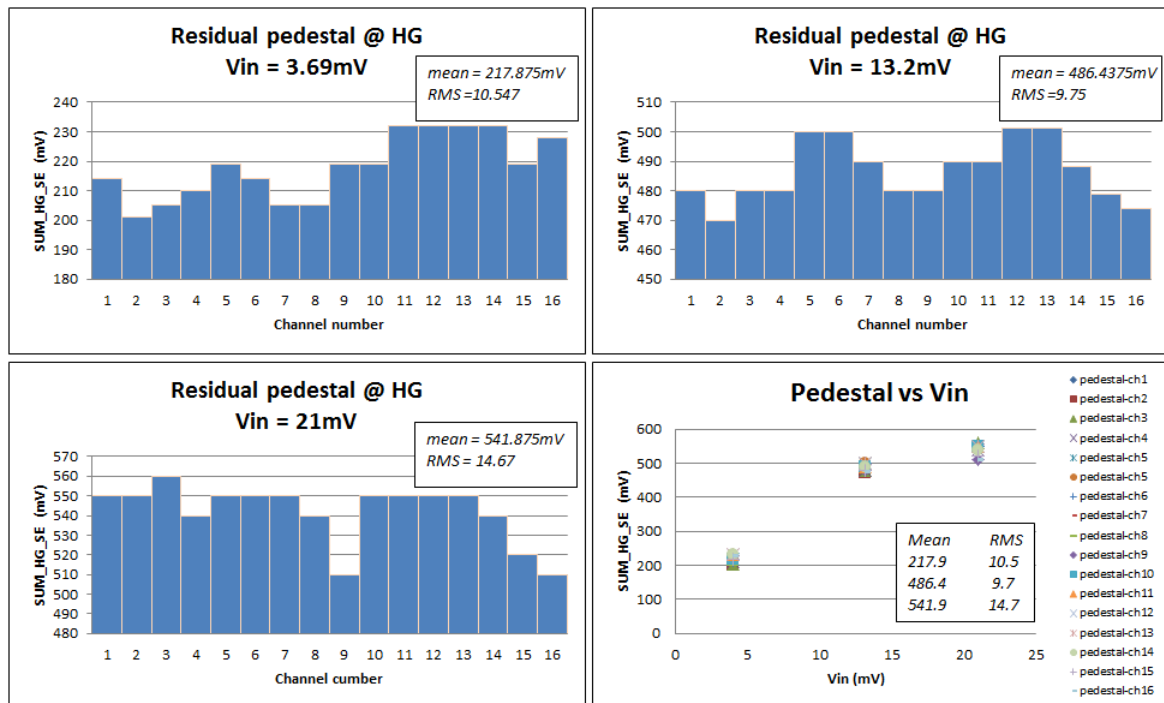


Figure B.1: Residual pedestal measured on the SUM_HG_SE for different input levels. The dispersion found to be 4.8%, 2% and 2.7% for the used input levels of 3.69 mV, 13.2 mV and 21 mV respectively.

B.2 Gain control

Another test of gain control on the high gain for an input signal of $V_{in} = 13.2\text{mV}$ ($\cong 934.2\text{photo electron}$) is shown in Fig.B.2.

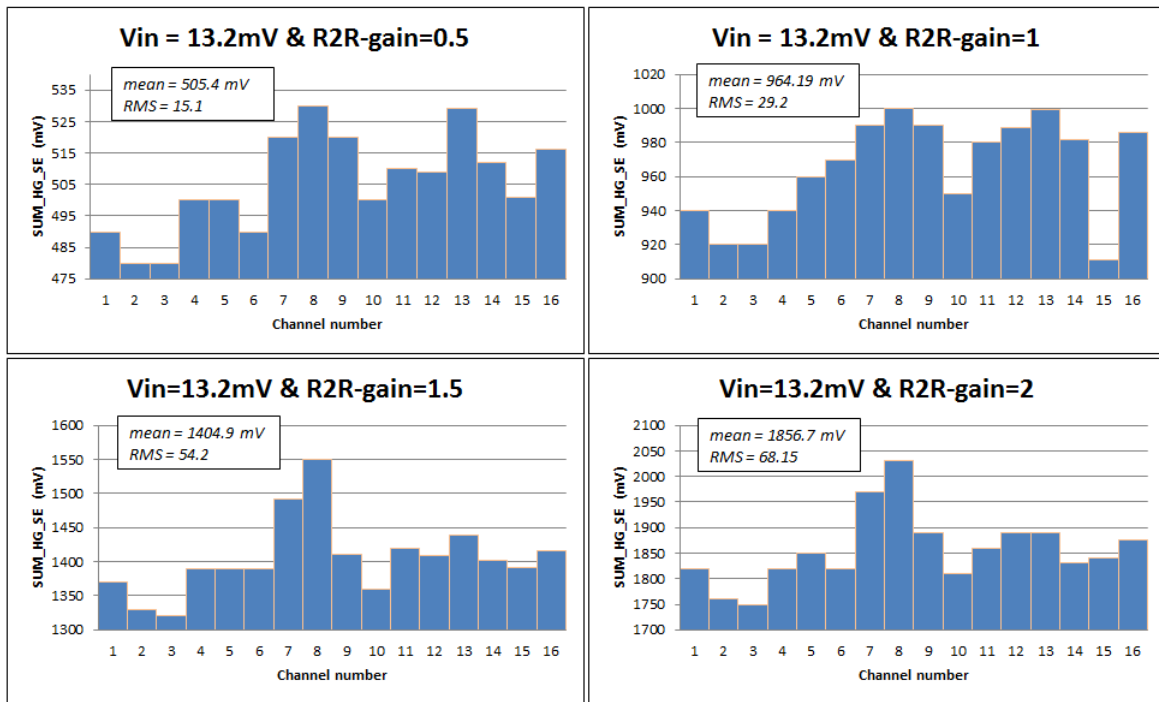


Figure B.2: Dispersion among the sixteen channels for $V_{in} = 13.2\text{mV}$ is about 3%, 3%, 3.9% and 3.7% respectively for R-2R-gain 0.5, 1, 1.5 and 2.

Turning to the low gain path, repeating the test and analyzing the measurement data gives Fig.B.3 for an input signal of $V_{in} = 75\text{mV}$ and Fig.B.4 for an input signal of $V_{in} = 146\text{mV}$. These figures show an average dispersion of around 5% among the sixteen channels for the input of $V_{in} = 75\text{mV}$ and 4.4% for $V_{in} = 146\text{mV}$.

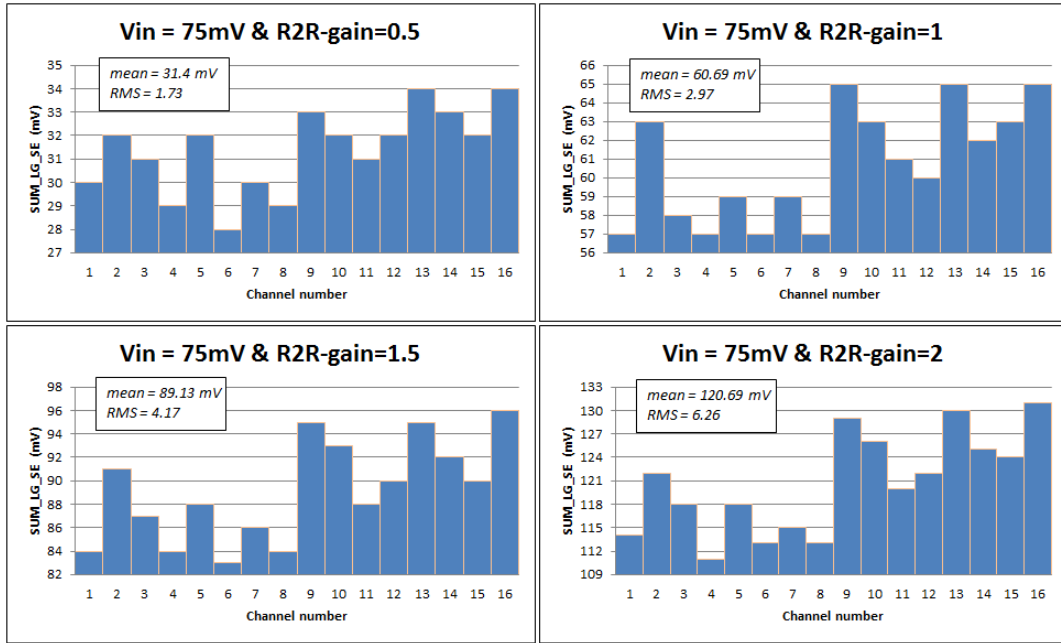


Figure B.3: Dispersion among the sixteen channels for $V_{in} = 75mV$ is about 5.5%, 4.9%, 4.7% and 5.2% respectively for R-2R-gain 0.5, 1, 1.5, 2.

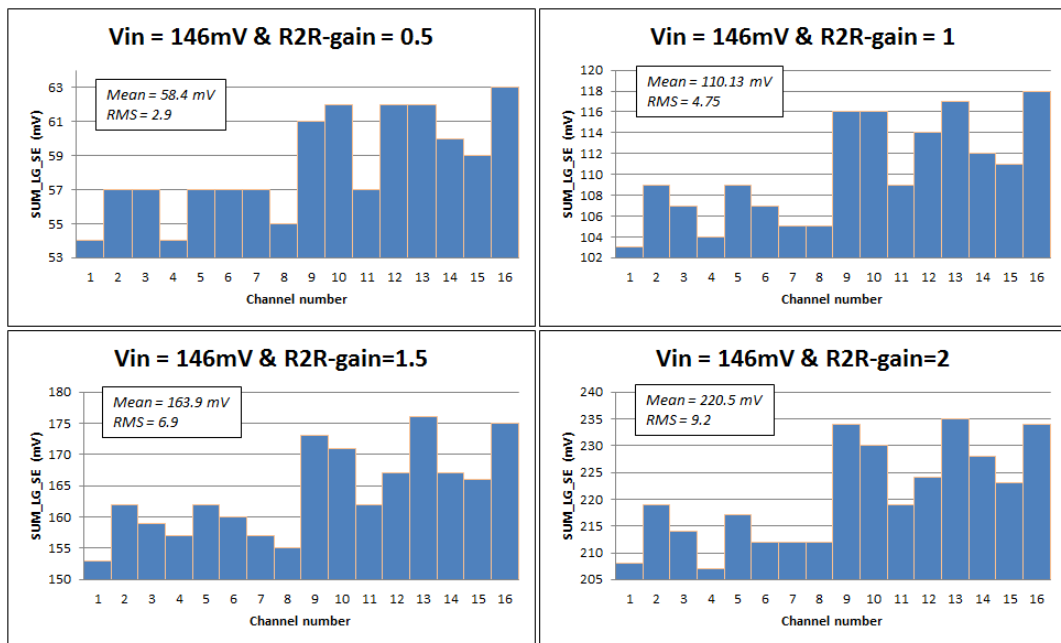


Figure B.4: Dispersion among the sixteen channels for $V_{in} = 146mV$ is about 5%, 4.3%, 4.2% and 4.2% respectively for R-2R-gain 0.5, 1, 1.5, 2.

B.3 Gain equalization

Fig.B.5 and Fig.B.6 depict the steps of gain equalization process on high gain path for two different inputs $V_{in} = 8\text{ mV}$ and $V_{in} = 21\text{ mV}$.

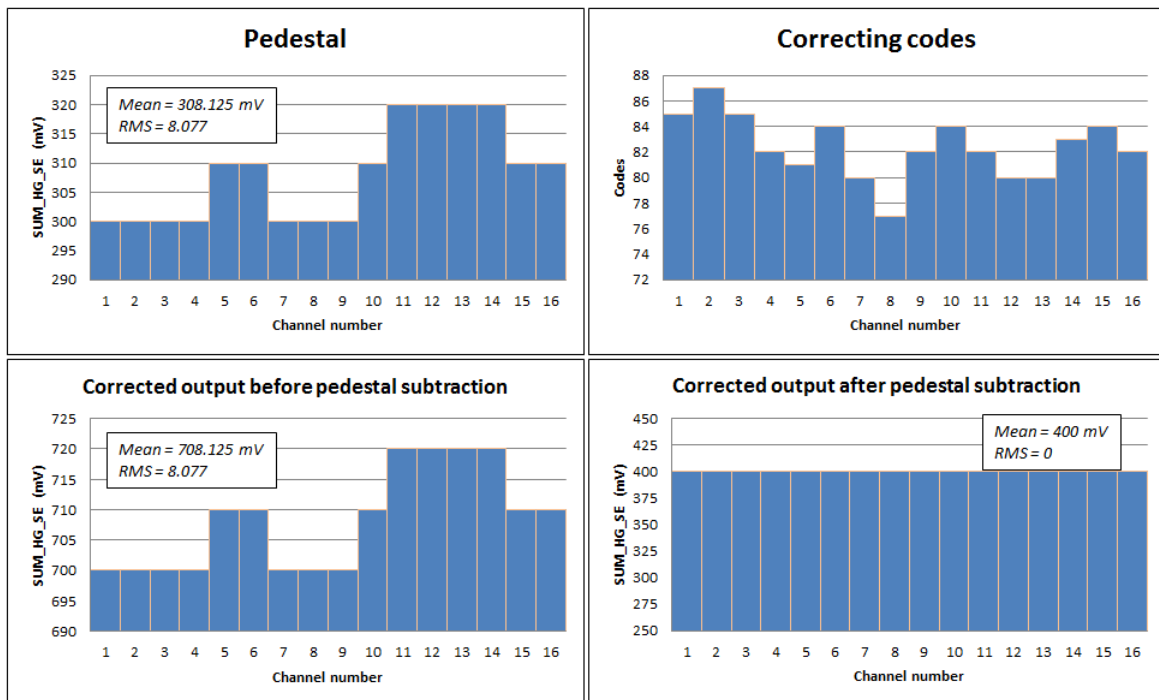


Figure B.5: High gain equalization for an input of 8 mV , the standard output was defined to 400 mV . The result shows zero dispersion among the sixteen channels.

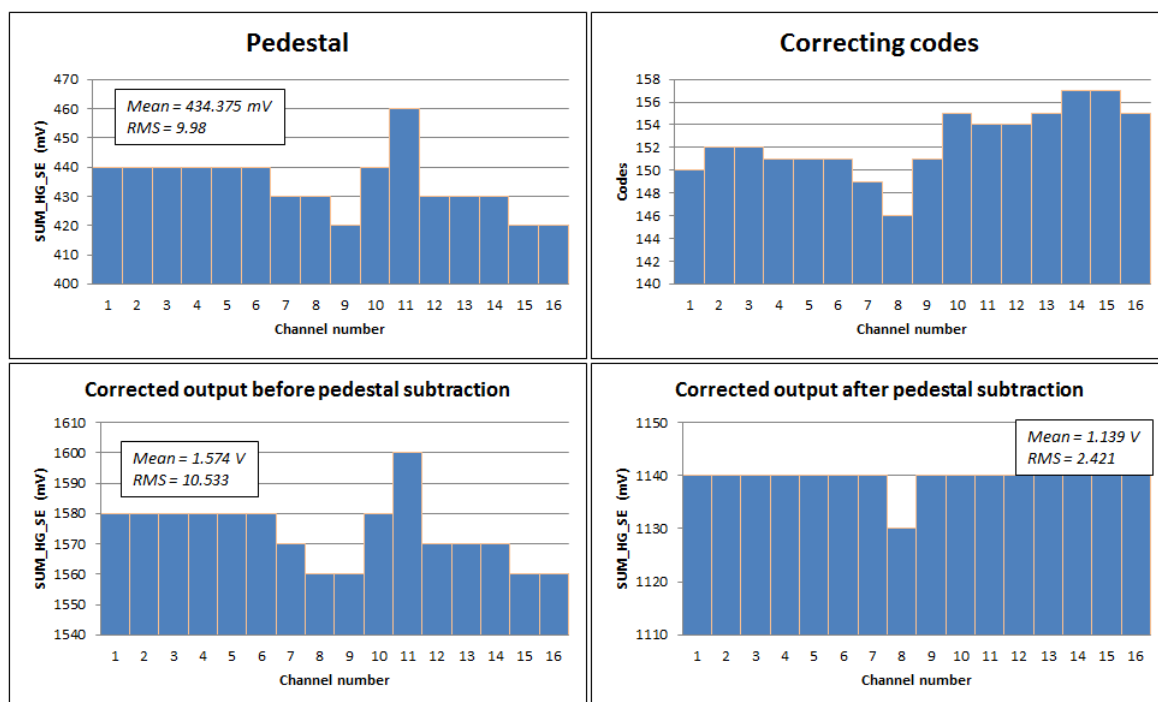


Figure B.6: High gain equalization for an input of 21 mV , the standard output was defined to 1.138 V . The result shows a dispersion of about 0.2% among the sixteen channels.

The same process was applied on the low gain for $V_{in} = 146\text{ mV}$ and $V_{in} = 292\text{ mV}$ respectively. Process details are illustrated in Fig.B.7 and in Fig.B.8.

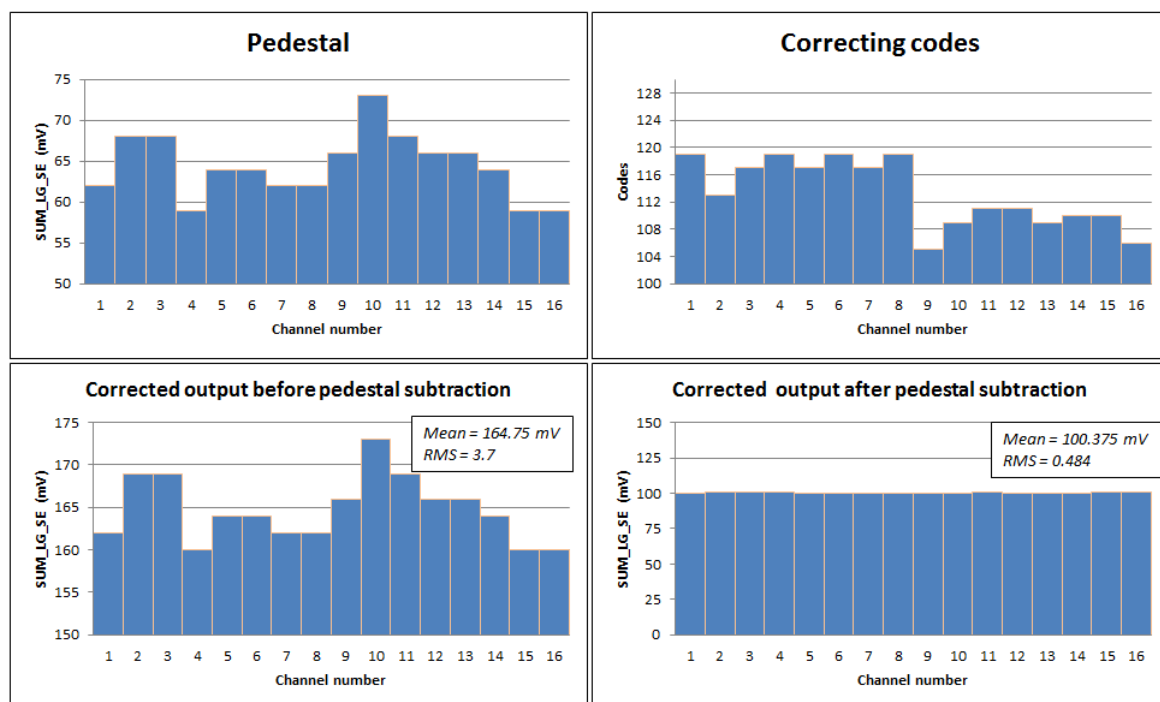


Figure B.7: Low gain equalization for an input of 146 mV , the standard output was defined to 100 mV . The result shows 0.48% of dispersion among the sixteen channels.

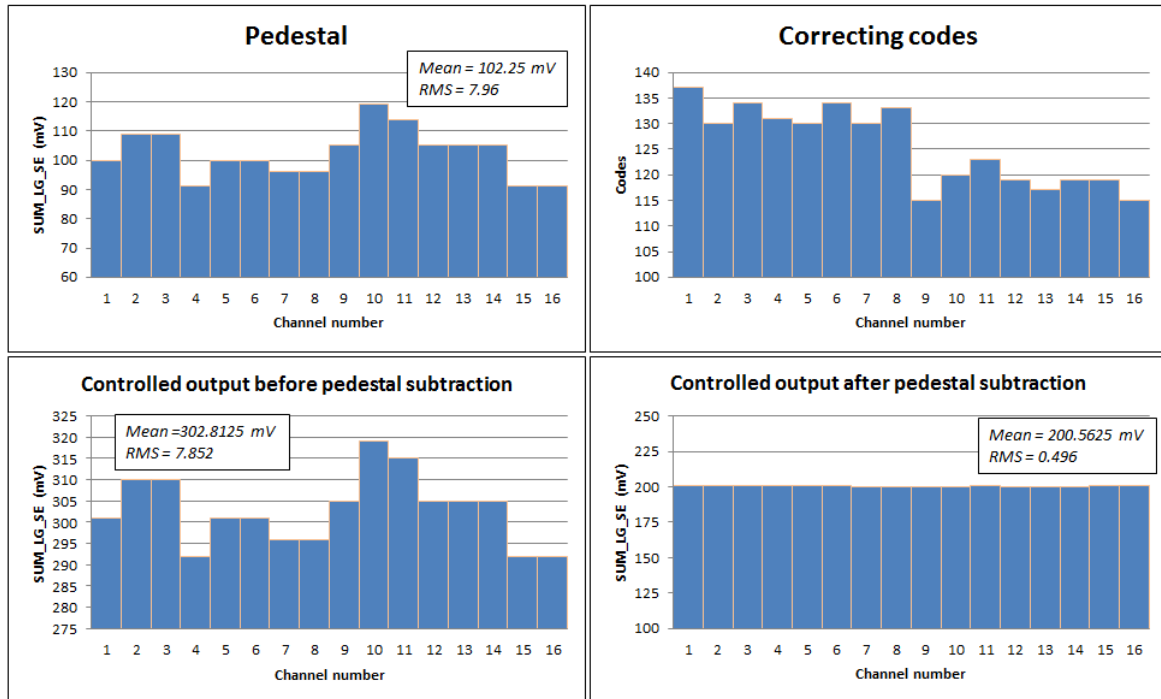


Figure B.8: Low gain equalization for an input of 292 mV , the standard output was defined to 200 mV . The result shows a dispersion of about 0.25% among the sixteen channels.

B.4 Sum as a function of the input level

For each R-2R four principle gain control codes, single ended sum output is measured as a function to the input signals. Both considered channels receive the same signal simultaneously. Fig.B.9 shows the results on the high gain sum output for input levels that are 3.6 mV , 6.6 mV , 13.2 mV , and 21 mV . Equivalent to 9.35, 17.14, 34.3, and 54.5 photo electrons respectively.

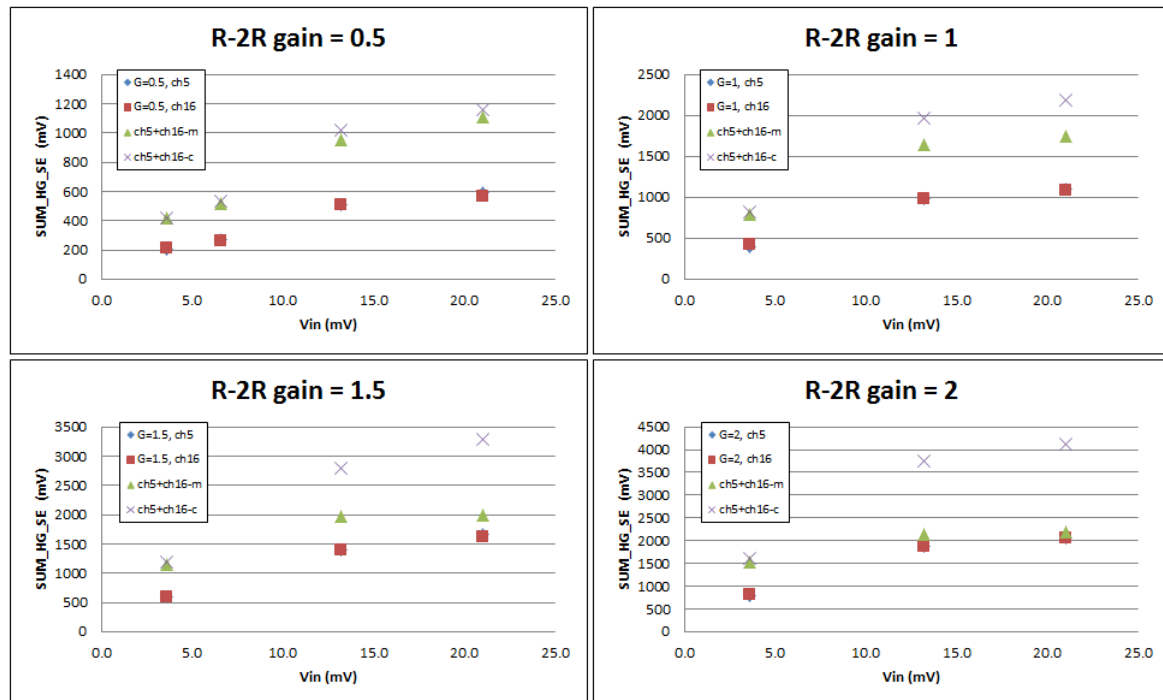


Figure B.9: Sum on high gain path of two signals as a function of the level of these input signals. Measurements are shown for different R-2R controlled gains. Results are after pedestal correction. In blue is the output when only *ch5* receives an input signal. In red, is the output when only *ch16* receives an input signal. In green, the plot labeled *ch5+ch16-m* is the measured sum output when both *ch5* and *ch16* are fed by identical inputs. The x plot labeled *ch5+ch16-c* is the arithmetic sum of the measured output when input signal is applied only on *ch5* and the measured output when the same input signal is applied only on *ch16*. For input signals that cause saturation on the high gain path, the output should be measured on the low gain path.

Fig.B.10 shows the sum on the low gain output for input signals of 37.8 mV , 74 mV and 146 mV (equivalent to 98.18, 192.2, and 379.2 photo electrons respectively) and at the four main gain control codes.

As was said in the section.4.6.4 saturation on high gain path ,and hence the damage it causes on linearity, can be postpone using gain equalization technique. It can also be compensated simply by reading the sum output on the low gain path instead.

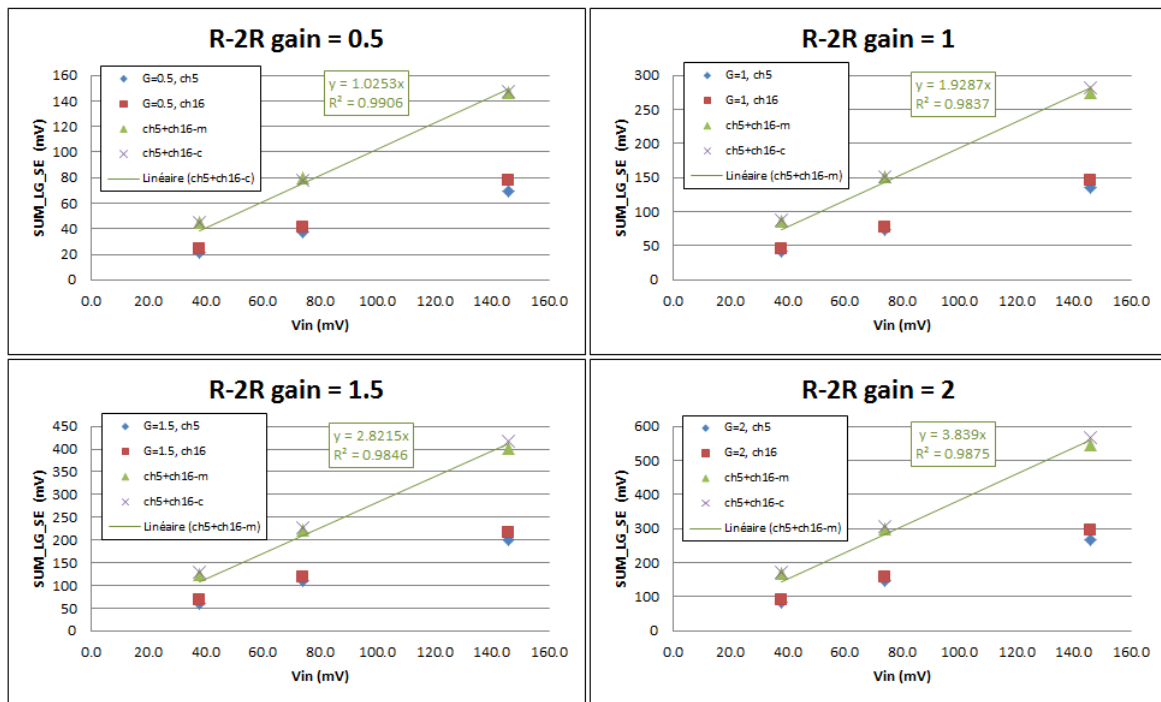


Figure B.10: Sum on low gain path of two signals as a function of the level of these input signals for different R-2R controlled gain. Results are pedestal free. $ch5+ch16-m$ is the plot of the measured sum output when both $ch5$ and $ch16$ are fed by identical input. $ch5+ch16-c$ is the plot of the manual sum of the measured output when input signal is applied only on $ch5$ and the measured output when the same input signal is applied only on $ch16$.

Appendix C

ALPS tests with SiPM (Specification)

C.1 Light emitting diode LED

The light source used to simulate Cherenkov light is a blue light emitting diode (LED). It was used to emit at $\lambda = 450\text{ nm}$. At this wave length the relative light intensity can be found from Fig.C.1 to be 0.675.

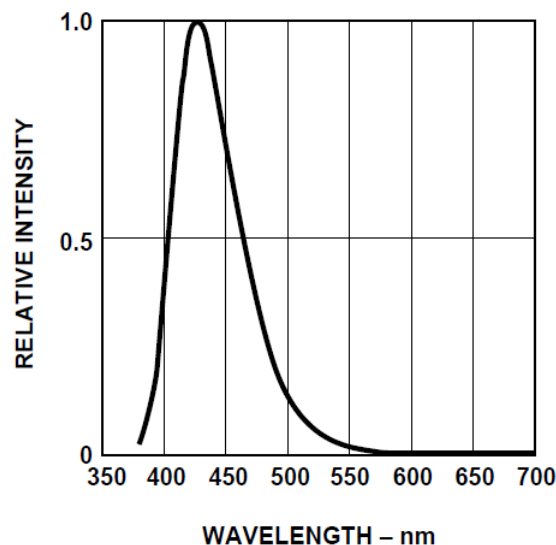


Figure C.1: Relative intensity as a function to the emitted wave length (<http://html.alldatasheet.com/html-pdf/157144/HP/HLMP-DB45-N00DD/108/3/HLMP-DB45-N00DD.html>).

This intensity was used as the primary incident value on the SiPM array ignoring all kind of possible losses in the fiber optic that leads light from the LED to the dark box of the detector. This value was then used in order to calculate the transmitted relative intensity through optical filters.

C.2 Optical filters

For varying light intensity, optical filter of the type metallic neutral density were used. These filters show invariant characteristics for various wavelengths. The opacity of these filters is defined as:

$$opacity = \frac{I_i}{I_o} = \frac{1}{T} \quad (C.1)$$

In these terms, the opacity is exactly the reciprocal of the transmittance Eq.C.1. We can conclude the transmission as given in Eq.C.2. knowing that commercially a filter is defined by its optical density as ND-D%.

$$\left. \begin{array}{l} T = \frac{I_o}{I_i}, \\ T = \frac{1}{opacity}, \end{array} \right\} \Rightarrow T = 10^{-D} \quad (C.2)$$

That is $0 \leq T \leq 1$. In terms of absorbing medium in the optical filter, the intensity of an incident light decreases exponentially as it passes through an absorber as reveals the transmittance formula depicted in Eq. C.3 called Beer's law.

$$T = 10^{-\alpha cx} \quad (C.3)$$

Where α is the absorption coefficient, c is the concentration of the absorber and x is the overall thickness of the absorber or the filter thickness in our case.

C.3 Preamplifier test

In order to change light intensity, several optical filters were used. light intensity varies from relative value of 0.68 without any filter used down to 0.0675 when using the most opaque filter. Each time the filter will be simply put on the SiPM holder (plastic cage). Output signals were measured after isolation buffers that were welded on the test board after each preamplifier in order to protect signals from noise. These outputs are called *OUT_PROBE_LG* and *OUT_PROBE_HG* respectively for the low and high gain preamplifier outputs.

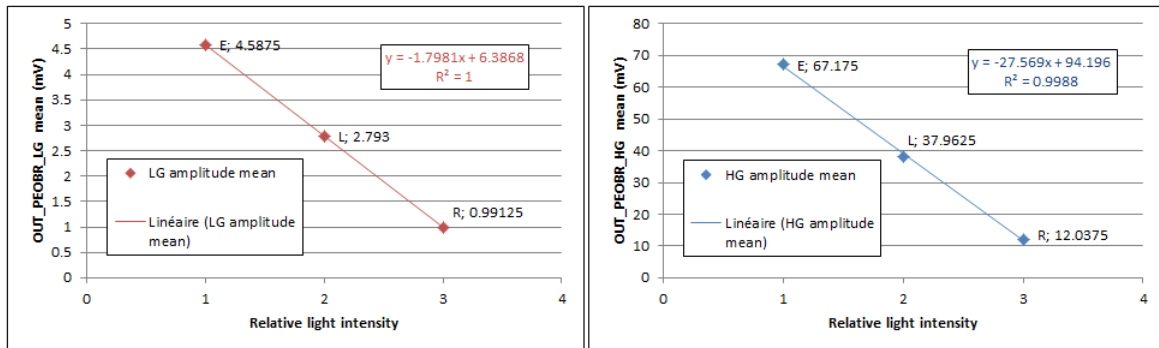


Figure C.2: Preamplifier output signals for three light intensities. Each point is the mean of the sixteen preamplifiers outputs for the considered intensity. Left, measurements on the low gain. Right, measurements on the high gain.

Fig.C.2 shows preamplifier responses to three light intensities produced using three different filters. These plots can not judge the linearity since there are no precise values for light intensity on the X-axis (Filters are labeled in letters but the output light is not known). However, these are results from the only three complete tests that could be done on the whole sixteen channels.

As a mentioned before in section.4.8, these measurements at the preamplifier outputs require probe activation by slow control intervention. Instability and several anomalies were observed in this function like for example the activation of both low and high gain outputs with sometimes one bit and other times two different bits in the probe part of the Labview program. The dysfunction of probe bits for some channels were also noticed. A review of the slow control program is an essential task for future tests.

C.4 Sum Function

Single ended sum outputs are the sum of the sixteen signals produced by the macro pixels (SiPMs of the array) being read each by the corresponding preamplifier and then being derived directly to the sum function by activating the *gain_fix* bit. Fig.C.3 shows measurements on both sum high gain and sum low gain outputs.

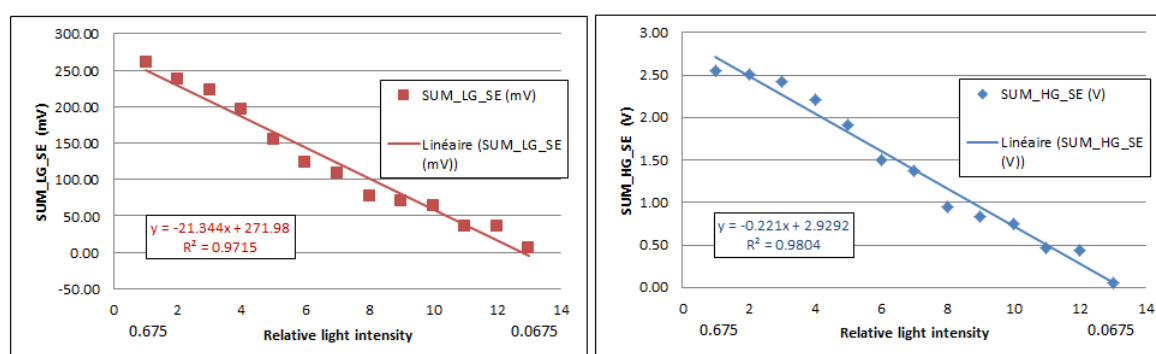


Figure C.3: Single ended sum output signals for a range of relative light intensities starting with 0.675 without an optical filter down to 0.0675 with the most opaque filter. Left, measurements on the low gain output. Right, measurements on the high gain output.

Here also the linearity can not be commented because of the unknown light intensity on the X-axis. A low high gain to low gain ratio is found. The new ratio is less than what was found during electrical tests (involving no additional boards). Moreover, this ratio is not stable at all as shown in fig.C.4. These observations could also be explained by the fact that no pedestal subtraction was done.

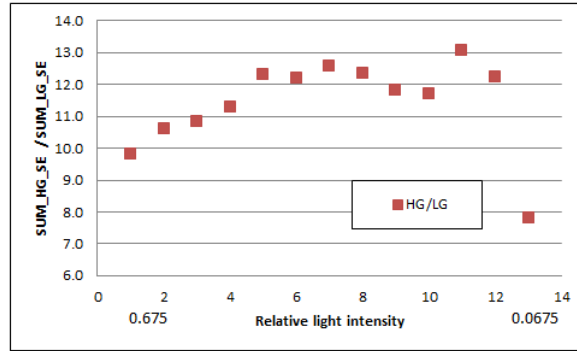


Figure C.4: Single ended sum output signals ratio over a range of light intensities from 0.675 down to 0.068.

The reason behind the difficulty of these tests may probably be the bad connection between the detector and the test board besides the bad position of the detector inside its dark box which affects the way its different macro pixels interact with the incident light.

References

- [1] Official site of the CTA: <https://www.cta-observatory.org/>
- [2] German Hermann, Towards the future Cherenkov telescope array CTA, *Nuclear Instruments and Methods in Physics Research Section A: Accelerators, Spectrometers, Detectors and Associated Equipment*, Vol. 623, No. 1, Pages. 408 - 409, 2010
- [3] B.S. Acharya, et al., Introducing the CTA concept, *Astroparticle Physics*, Vol. 43, No. 0, Pages. 3 - 18, 2013
- [4] Knoetig, M. L. et al., FACT - Long-term stability and observations during strong Moon light, *ArXiv: 1307.6116 (astro-ph.IM)*, July, 2013
- [5] H Anderhub, M Backes, A Biland, et al., Design and operation of FACT - the first G-APD Cherenkov telescope, *Journal of Instrumentation*, vol. 8, No. 06, Pages. P06008, 2013
- [6] F. Mehrez, J. M. Dubois, N. Fouque, R. Hermel, J. L. Panazol, J. Prast, S. Rosier-Lees, A SiPM readout ASIC for CTA, *The 1st SiPM advanced workshop, Max Planck Institute for Physics - Munich, July 2013*, <https://www.cta-observatory.org/indico/conferenceDisplay.py?confId=487>
- [7] C.L. Naumann, E. Delagnes, et al., New electronics for the Cherenkov Telescope Array (NECTAr), *Nuclear Instruments and Methods in Physics Research Section A: Accelerators, Spectrometers, Detectors and Associated Equipment*, Vol. 695, Pages. 44 - 51, 2012
- [8] H. Kubo, R. Paoletti, et al., Development of the Photomultiplier-Tube Readout System for the CTA Large Size Telescope, *Astrophysics - Instrumentation and Methods for Astrophysics, Physics - Instrumentation and Detectors*, July, 2013
- [9] D. Mazin, F. Mehrez, N. Fouque, R. Hermel, S. Rosier-Lees, et al., Progress towards SiPM cluster for large size telescopes, *The 2nd SiPM Advanced Workshop, Geneva March 2014*, <https://www.cta-observatory.org/indico/getFile.py/access?contribId=35&sessionId=5&resId=0&materialId=slides&confId=526>
- [10] R. Rando, F. Mehrez, N. Fouque, R. Hermel, S. Rosier-Lees, et. al, SiPM R&D report, LST general meeting, Annecy, February 2015. <https://www.cta-observatory.org/indico/getFile.py/access?contribId=6&sessionId=2&resId=0&materialId=slides&confId=788>

-
- [11] R. Rando, F. Mehzrez, et. al, Silicon Photomultiplier Research and Development Studies for the Large Size Telescope of the Cherenkov Telescope Array, *In Proceedings - the 34th International Cosmic Ray Conference (ICRC2015), Astrophysics - Instrumentation and Methods for Astrophysics, Physics - Instrumentation and Detectors, August 2015*
- [12] Malcolm S. Longair, High Energy Astrophysics, *Vol. 1 and 2, 2nd edition, Cambridge University Press*
- [13] Michael Backes, Long-term observations of the TeV blazar 1ES 1959+650: Temporal and spectral behavior in the multi-wavelength context, *Technische universität dortmund, PhD thesis 2011*
- [14] E. Lorenz, R. Wagner, Very-high energy gamma-ray astronomy. A 23-year success story in high-energy astroparticle physics. *European Physical Journal H, Vol. 37, Pages. 459-513, August 2012*
- [15] Bernard Degrange, Gérard Fontaine, Introduction to high-energy gamma-ray astronomy, *Comptes Rendus Physique*, Available online 8 September 2015, ISSN 1631-0705, <http://www.sciencedirect.com/science/article/pii/S1631070515001292>
- [16] Armand Fiasson, Recherche de l'origine des rayons cosmiques par l'étude d'associations de vestiges de supernova et de nuages moléculaires avec HESS et validation du circuit d'échantillonnage de HESS II, *PhD thesis, Université Montpellier II Sciences et Techniques du Languedoc, Laboratoire de Physique Théorique et Astroparticules (LPTA), 2008*
- [17] Aldée Charbonnier, De la recherche de matière noire à l'émission diffuse de rayons gamma dans l'expérience H.E.S.S., *Thèse de doctorat, Université Paris VI-Pierre et Marie Curie, 2010*
- [18] François Brun, Recherche de sources ténues ou transitoires dans les régions centrales de la Galaxie avec H.E.S.S. - Application à l'étude de la région du vestige de supernova W49B, *PhD thesis, Université Paris VI- Pierre et Marie Curie, 2011*
- [19] T. Suomijarvi, The Pierre Auger Observatory: Perspectives on ultra-high energy cosmic rays. *Il Nuovo Cimento B, 2005, 120, pp.793-804. <10.1393/ncb/i2005-10121-5>. <in2p3-00025344>*
- [20] Ruben Conceição, et al., The Pierre Auger Observatory: results on the highest energy particles, *Time and Matter conference, 2013, arXiv:1307.3956v1.*
- [21] J. J. Beatty for the Pierre Auger Collaboration, Results from the Pierre Auger Observatory, *33rd SLAC Summer Institute on Particle Physics (SSI 2005), 25 July - 5 August 2005*
- [22] The CTA Consortium, Design Concepts for the Cherenkov Telescope Array CTA: An advanced Facility for Ground-Based High-Energy Gamma-Ray Astronomy, *CTA Consortium, May 2010*

-
- [23] J. Rousselle, K. Byrum, R. Cameron, et al. (for the CTA Consortium), Construction of a Schwarzschild-Couder telescope as a candidate for the Cherenkov Telescope Array: status of the optical system, *In Proceedings of the 34th International Cosmic Ray Conference (ICRC2015), Astrophysics - Instrumentation and Methods for Astrophysics (astro-ph.IM); High Energy Astrophysical Phenomena (astro-ph.HE), August 2015*
- [24] Teresa Montaruli, Giovanni Pareschi, Tim Greenshaw (for the CTA Consortium and the SST-1M, ASTRI and GCT sub-consortia), The small size telescope projects for the Cherenkov Telescope Array, *In Proceedings of the 34th International Cosmic Ray Conference (ICRC2015), Astrophysics - Instrumentation and Methods for Astrophysics (astro-ph.IM); High Energy Astrophysical Phenomena (astro-ph.HE), August 2015*
- [25] H. Anderhub et al., FACT–The first Cherenkov telescope using a G-APD camera for TeV gamma-ray astronomy, *Nucl. Instru. Meth. A 639 (2011) 58-61*
- [26] G. Ambrosi, Y. Awane, H. Baba, et al., The Cherenkov Telescope Array Large Size Telescope, *Astrophysics - Instrumentation and Methods for Astrophysics, July, 2013*
- [27] M. Teshima, O. Blanch and T. Schweizer, et al., Design and study of a CTA Large Size Telescope (LST), *Proceedings, 32nd International Cosmic Ray Conference (ICRC), 2011*
- [28] A. Okumura, S. Ono, S. Tanaka, M. Hayashida, H. Katagiri, and T. Yoshida, for the CTA Consortium, Prototyping of Hexagonal Light Concentrators for the Large-Sized Telescopes of the Cherenkov Telescope Array, *Proceedings, 34nd International Cosmic Ray Conference (ICRC), Sep, 2015*
- [29] S. Masuda, Y. Konno, et al., Development of the photomultiplier tube readout system for the first Large-Sized Telescope of the Cherenkov Telescope Array, *Proceedings, 34nd International Cosmic Ray Conference (ICRC), Sep, 2015*
- [30] D. Hadasch, Development of Slow Control Boards for the Large Size Telescopes of the Cherenkov Telescope Array, *Proceedings, 34nd International Cosmic Ray Conference (ICRC), Sep, 2015*
- [31] G. Lamanna, M. Janiak, SiPM-LST camera, *LAPP-CTA Note, 2013*
- [32] B. E. A. Saleh, M. C. Teich, Fundamentals of Photonics, *Wiley, 1991*
- [33] Henri Mathieu, *Physique des semiconducteurs et des composants électroniques, DUNOD, 2004*
- [34] S. M. Sze and Kwok K. Ng, *Physics of Semiconductor Devices, Wiley interscience, 2007*
- [35] Photomultiplier Tubes - Basics and Applications, *Hamamatsu photonics, 2007*
- [36] D. Renker and E. Lorenz, Advances in solid state photon detectors, *JINST,4, P04004, 2009*

- [37] N. Dinu, Instrumentation on silicon detectors: from properties characterization to applications, *Université Paris Sud - Paris XI, 2013*
- [38] McKay, K. G. and McAfee, K. B., Electron Multiplication in Silicon and Germanium, *Phys. Rev. 91. 1079, September, 1953*
- [39] Wolff, P. A., Theory of Electron Multiplication in Silicon and Germanium, *Phys. Rev. 95. 1415, September, 1954*
- [40] Si photodiodes, *Hamamatsu photonics, KAPD9001E03, May, 2004*
- [41] Photodiode Technical Information, *Hamamatsu photonics*
- [42] Slawomir S. Piatek, Physics and Operation of a MPPC, *Hamamatsu Corporation & New Jersey Institute of Technology, February, 2014*
- [43] S. Cova and M. Ghioni and A. Lacaita and C. Samori and F. Zappa, Avalanche photodiodes and quenching circuits for single-photon detection, *Appl. Opt. vol.35, No. 12, 1956-1976, April, 1996*
- [44] Ehsan Kamrani and Frederic Lesage and Mohamad Sawan, Efficient premature edge breakdown prevention in SiAPD fabrication using the standard CMOS process, *Semiconductor Science and Technology, vol. 28, No. 4, 045008, 2013*
- [45] Haitz, Roland H., Mechanisms Contributing to the Noise Pulse Rate of Avalanche Diodes, *Journal of Applied Physics. Vol. 36, No. 10, Pages. 3123-3131, 1965*
- [46] McIntyre, R.J., Multiplication noise in uniform avalanche diodes, *IEEE Transactions on Electron Devices, Vol. 13, No. 1, Pages. 164-168, Jan 1966*
- [47] D. Renker, Geiger-mode avalanche photodiodes, history, properties and problems, *Nucl. Instrum. Meth. A 567 (2006) 48*
- [48] Golovin, V. and Savelev, V., Novel type of avalanche photodetector with Geiger mode operation, *Nucl.Instrum.Meth. A 518 (2004) 560-564*
- [49] MPPC, Multi-Pixel Photon Counter, *Hamamatsu photonics, KAPD9003E02, May, 2009*
- [50] MPPC, MPPC modules, *Hamamatsu photonics, KAPD9003E03*
- [51] Galetta, G. and Ciciriello, F. and Corsi, F. and De Leo, R. and Garibaldi, F. and others, Time and charge characterization of Hamamatsu Photonics silicon photomultipliers, *EPJ Web Conf., 66-p11028, 2014*
- [52] Kalil Jradi, Etude et Réalisation de photodétecteurs de type APD Geiger pixellisés à très hautes sensibilité pour l'astronomie gamma Très Haute Energie, *Centre d'Etude Spatiale des Rayonnements (CESR), Univertié Toulouse3 Paul Sabatier, Juillet, 2010*
- [53] Nagano, T. and Sato, K. and Ishida, A. and Baba, T. and Tsuchiya, R. and Yamamoto, K., Timing resolution improvement of MPPC for TOF-PET imaging, *IEEE Nuclear Science Symposium and Medical Imaging Conference (NSS/MIC), October, 2012*

-
- [54] H Anderhub, et al., A novel camera type for very high energy gamma-ray astronomy based on Geiger-mode avalanche photodiodes, *Journal of Instrumentation*, vol 4, No 10, pages P10010, 2009
- [55] H. Anderhub et al., Results of the prototype camera for FACT, *Nucl. Instru. Meth.* 639 (2011) 55-57
- [56] T. Krähenbühl et al., G-APDs in Cherenkov astronomy: The FACT camera, *Nucl. Instru. Meth. A* 695 (2012) 96-99
- [57] Loic Rolland, Etalonnage des caméra de l'expérience d'astronomie γ H.E.S.S. et observations du centre galactique au-delà de 100 GeV, *Université Pierre et Marie Curie - Paris VI*, 2005
- [58] F. Druillole, D. Lachartre, F. Feinstein, J. Fopma, E. Delagnes, and H. Lafoux, The Analog Ring Sampler: An ASIC for the Front-End Electronics of the ANTARES Neutrino Telescope, *IEEE TRANSACTIONS ON NUCLEAR SCIENCE*, 2002, 49, 3, June
- [59] A. Vacheret, et al., Characterization and Simulation of the Response of Multi-Pixel Photon Counters to Low Light Levels, *Nucl. Instr. and Meth. in Phys. Res. A*, 656 (2011): 69-83
- [60] Slawomir S. Piatek, Physics and Operation of an MPPC, *Hamamatsu Corporation & New Jersey institute of Technology*, February 2014
- [61] F. Corsi and A. Dragone and C. Marzocca and A. Del Guerra and P. Delizia and N. Dinu and C. Piemonte and M. Boscardin and G.F. Dalla Betta, Modeling a silicon photomultiplier (SiPM) as a signal source for optimum front-end design, *Nucl. Instrum. Med. A* 572 (2007) 416-418
- [62] Corsi, F. and Marzocca, C. and Foresta, M. and Matarrese, G. and Del Guerra, A. and Marcatili, S. and Llosa, G. and Collazuol, G. and Dalla Betta, G.-F. and Piemonte, C., Preliminary results from a current mode CMOS front-end circuit for silicon photomultiplier detectors, *Nuclear Science Symposium Conference Record, 2007. NSS '07. IEEE*, Vol. 1, Pages, 360-365, October 2007
- [63] Ronzhin, A., SiPM signal shape influence on detector time resolution, *Nuclear Science Symposium and Medical Imaging Conference (NSS/MIC), 2013 IEEE*, 2013
- [64] Seifert, S. and van Dam, H.T. and Huizenga, J. and Vinke, R. and Dendooven, P. and Lohner, H. and Schaart, D.R., Simulation of Silicon Photomultiplier Signals, *Nuclear Science, IEEE Transactions on*, Vol. 56, No. 6, Pages. 3726-3733, 2009
- [65] F. Ciciriello and F. Corsi and F. Licciulli and C. Marzocca and G. Matarrese and A. Del Guerra and M.G. Bisogni, Accurate modeling of SiPM detectors coupled to FE electronics for timing performance analysis, *Nucl. Instrum. Meth. A* 718 (2013) 331 - 333

-
- [66] C. de LA Taille, G. Martin-Chassard, L. Raux, FLC - SiPM: Front-End Chip for SiPM Readout for ILC Analog HCAL, *International Linear Collider Workshop - Stanford, U.S.A. 2005*
- [67] P. Barrillon, S. Blin, M. Bouchel, T. Caceres, C. de La Taille, member IEEE, G. Martin, P. Puzo, N. Seguin-Moreau, MAROC: Multi - Anode ReadOut Chip for MaPMTs, *IEEE Nuclear Science Symposium Conference Record, Vol. 2, Pages. 809-814, October 2006*
- [68] S. Blin, P. Barrillon, and C. de La Taille, MAROC, a generic photomultiplier readout chip, *Nuclear Science Symposium Conference Record (NSS/MIC), IEEE, pages. 1690-1693, October 2010*
- [69] P. ASSIS, P.BROGUEIRA, O.CATALANO, R&D for future SiPM cameras for Fluorescence and Cherenkov Telescopes, *In Proceedings - 32nd International Cosmic Ray Conference (ICRC2011), BEIJING 2011*
- [70] M. Bouchel, F. Dulucq, J. Fleury, C. de La Taille, G. Martin-Chassard, L. Raux, SPIROC (SiPM Integrated Read-Out Chip): Dedicated very front-end electronics for an ILC prototype hadronic calorimeter with SiPM read-out, *Nuclear Science Symposium Conference Record, 2007. NSS '07. IEEE, Vol. 3, Pages. 1857-1860, October 2007*
- [71] S. Callier, F. Dulucq, R. Fabbri, C. De La Taille, B. Lutz, G. Martin-Chassard, L. Raux, W. Shen, Silicon Photomultiplier integrated readout chip (SPIROC) for the ILC: Measurements and possible further development, *Nuclear Science Symposium Conference Record (NSS/MIC), 2009 IEEE*
- [72] S. Callier, C. Dela Taille, G. Martin-Chassard, L. Raux, EASIROC, an Easy & Versatile ReadOut Device for SiPM, *Physics Procedia, Vol. 37, Pages. 1569 - 1576, Technology and Instrumentation in Particle Physics 2011*
- [73] F. Dulucq, S. C. Di Lorenzo, C. De La Taille, S. Drouet, M. El Berni, G. Martin-Chassard, and Y. Xiongbo, PARISROC, an autonomous front-end ASIC for triggerless acquisition in next generation neutrino experiments, *Nuclear Science Symposium and Medical Imaging Conference (NSS/MIC), 2011 IEEE, Pages. 1441-1444, October 2011*
- [74] S. Conforti Di Lorenzo, J.E. Campagne, S. Drouet, F. Dulucq, M. El Berni, B. Genolini, C. de La Taille, G. Martin-Chassard, N. Seguin Moreau, E. Wanlin, and Y. Xiangbo, PARISROC, an autonomous front-end ASIC for triggerless acquisition in next generation neutrino experiments, *Nuclear Instruments and Methods in Physics Research Section A: Accelerators, Spectrometers, Detectors and Associated Equipment, Vol. 695, Pages. 373 - 378, 2012*
- [75] A. Sanuy, D. Gascón, J. M. Paredes, L. Garrido, M. Ribó and J. Sieiro, Wideband (500 MHz) 16 bit dynamic range current mode PreAmplifier for the CTA cameras (PACTA), *Journal of Instrumentation, Vol. 7, No. 01, Pages. C01100, 2012*
- [76] A. Comerma and D. Gascón et al. , Front End ASIC design for SiPM readout, *Journal of Instrumentation, Vol. 8, No. 01, Pages. C01048, 2013*

-
- [77] J. Cortina and M. Teshima for the CTA consortium, Status of the Cherenkov Telescope Array's Large Size Telescopes, *In Proceedings - the 34th International Cosmic Ray Conference (ICRC2015), Astrophysics - Instrumentation and Methods for Astrophysics, August 2015*
- [78] S. Vorobiov, J. Bolmont, et al., NECTAr: New electronics for the Cherenkov Telescope Array, *Nuclear Instruments and Methods in Physics Research Section A: Accelerators, Spectrometers, Detectors and Associated Equipment, Vol. 639, No. 1, Pages. 62 - 64, 2011*
- [79] Paweł Gryboś, Front-end Electronics for Multichannel Semiconductor Detector Systems, *Institute of Electronic Systems - Warsaw University of Technology, 2010*
- [80] J. Huizenga and S. Seifert and F. Schreuder and H.T. van Dam and P. Dendooven and H. Löhner and R. Vinke and D.R. Schaart, A fast preamplifier concept for SiPM-based time-of-flight PET detectors, *Nucl. Instrum. Meth. A 695 (2012) 379-384*
- [81] Li, C. and Palermo, S., A Low-Power 26-GHz Transformer-Based Regulated Cascode SiGe BiCMOS Transimpedance Amplifier, *IEEE Journal of Solid-State Circuits, Vol. 48, No. 5, Pages. 1264-1275, 2013*
- [82] Khoman Phang, CMOS Optical Preamplifier Design Using Graphical Circuit Analysis, *University of Toronto, 2001*
- [83] Zhenghao Lu and Kiat Seng Yeo and Wei Meng Lim and Do, A.V. and Chirn Chye Boon, Design of a CMOS Broadband Transimpedance Amplifier With Active Feedback, *IEEE Transactions on Very Large Scale Integration (VLSI) Systems, Vol. 18, No. 3, Pages. 461-472, March 2010*
- [84] Kromer, C. and Sialm, G. and Morf, T. and Schmatz, M.L. and Ellinger, F. and Erni, D. and Jackel, H., A low-power 20-GHz 52-dB Omega; transimpedance amplifier in 80-nm CMOS, *IEEE Journal of Solid-State Circuits, Vol. 39, No. 6, Pages. 885-894, June 2004*
- [85] Sung Min Park and Hoi-Jun Yoo, 1.25-Gb/s regulated cascode CMOS transimpedance amplifier for Gigabit Ethernet applications, *IEEE Journal of Solid-State Circuits, Vol. 39, No. 1, Pages. 112-121, Jan 2004*
- [86] Shekhar, S. and Walling, J.S. and Allstot, D.J., Bandwidth Extension Techniques for CMOS Amplifiers, *IEEE Journal of Solid-State Circuits, Vol.41, No. 11, Pages. 2424-2439, Nov 2006*
- [87] Kimmo Koli, CMOS Current Amplifiers: Speed versus Nonlinearity, *Helsinki University of Technology - Electronic Circuit Design Laboratory, 2000*
- [88] Behzad Razavi, Design of analog CMOS integrated circuits, *McGRAW-HILL*
- [89] Behzad Razavi, Fundamentals of microelectronics, *John Wiley & Sons, Inc*
- [90] Paul R. Gray, Paul J. Hurst, Stephen H. Lewis, Robert G. Meyer, Analysis and design of analog integrated circuits, *WILEY, 2009*

- [91] Yannis Tsvividis, Operation and Modeling of MOS Transistor, *2nd Edition, McGraw-Hill, 1999*
- [92] Nyquist, H., Thermal Agitation of Electric Charge in Conductors, *Phys. Rev., Vol. 32, Pages. 110–113, 1928*
- [93] Bing Wang and Hellums, J.R. and Sodini, C.G., MOSFET thermal noise modeling for analog integrated circuits, *IEEE Journal of Solid-State Circuits, Vol. 29, No. 7, Pages. 833-835, Jul 1994*
- [94] Tedja, S. and Van der Spiegel, J. and Williams, H.H., Analytical and experimental studies of thermal noise in MOSFET's, *IEEE Transactions on Electron Devices, Vol. 41, No. 11, Pages. 2069-2075, Nov 1994*
- [95] Chun Hu and Ji Zhao and Li, G. -P and Liu, P. and Worley, E. and White, J. and Kjar, R., The effects of plasma etching induced gate oxide degradation on MOSFET's 1/f noise, *IEEE, Electron Device Letters, Vol. 16, No. 2, Pages. 61-63, Feb 1995*
- [96] Jimmin Chang and Abidi, A.A. and Viswanathan, C.R., Flicker noise in CMOS transistors from subthreshold to strong inversion at various temperatures, *IEEE Transactions on Electron Devices, Vol.41, No. 11, Pages. 1965-1971, Nov 1994*
- [97] Chun Hu, G. P. Li, Eugene Worley, and Joe White, Consideration of low frequency noise in MOSFET's for analog performance, *IEEE Electron Device Letters, Vol. 17, No. 12, Dec 1996*
- [98] L. K. J. Vandamme, Xiaosong Li, and Dominique Rigaud, 1/f Noise in CMOS Devices Mobility or Number Fluctuations, *IEEE Transactions on Electron Devices, Vol. 41, No. 11, Nov 1994*
- [99] Abowitz, Gerald and Arnold, Emil and Leventhal, E.A., Surface states and 1/f noise in MOS transistors, *IEEE Transactions on Electron Devices, Vol. 14, No. 11, Pages. 775-777, Nov 1967*
- [100] Horng-sen Fu, and Chih-tang Sah., Theory and experiments on surface 1/f noise, *IEEE Transactions on Electron Devices, Vol. ED-19, No. 2, Feb 1972*
- [101] P. Gentil and A. Mounib, Equivalent input spectrum and drain current spectrum for 1/f noise in short channel MOS transistors, *Solid-State Electronics, Vol. 24, No. 5, Pages. 411 - 414, 1981*
- [102] Surya, C. and Hsiang, T. Y., Surface mobility fluctuations in metal-oxide-semiconductor field-effect transistors, *Phys. Rev. B, Vol. 35, Pages. 6343–6347, Apr 1987*
- [103] Chengqing Wei and Yong-Zhong Xiong and Xing Zhou, Investigation of Low-Frequency Noise in N-Channel FinFETs From Weak to Strong Inversion, *IEEE Transactions on Electron Devices, Vol. 56, No. 11, Pages. 2800-2810, Nov 2009*
- [104] Watanabe, T., Low-noise operation in buried-channel MOSFET's, *IEEE Electron Device Letters, Vol. 6, No. 7, Pages. 317-319, Jul 1985*

-
- [105] Carruthers, C. and Mavor, J., Low-noise operation of buried channel MOS transistors, *Electronics Letters*, Vol. 23, No. 22, Pages. 1173-1174, October 1987
- [106] Xiaosong Li and C. Barros and E.P. Vandamme and L.K.J. Vandamme, Parameter extraction and 1/f noise in a surface and a bulk-type, p-channel LDD MOSFET, *Solid-State Electronics*, Vol. 37, No. 11, Pages. 1853 - 1862, 1994
- [107] Chia-Yu Chen, Yang Liu, Robert W. Dutton, Junko Sato-Iwanaga, Akira Inoue, and Haruyuki Sorada, Numerical Study of Flicker Noise in P-Type $Si_{0.7}Ge_{0.3}/Si$ Heterostructure MOSFETs, *IEEE Transactions on electron devices*, Vol. 55, No. 7, July 2008
- [108] Reibold, G., Modified 1/f trapping noise theory and experiments in MOS transistors biased from weak to strong inversion - Influence of interface states, *IEEE Transactions on Electron Devices*, Vol. 31, No. 9, Pages. 1190-1198, Sep 1984
- [109] Gerard Ghibaudo, On the theory of carrier number fluctuations in MOS devices, *Solid-State Electronics*, Vol. 32, No. 7, Pages. 563 - 565, 1989
- [110] Halil I. Ozbas High Gain Differential Transimpedance Amplifier With DC Photodiode Current Rejection, *Worcester Polytechnic Institute*, 2005
- [111] A Sanuy and D Gascon and J M Paredes and L Garrido and M Ribó and J Sieiro, Wideband (500 MHz) 16 bit dynamic range current mode PreAmplifier for the CTA cameras (PACTA), *Journal of Instrumentation*, Vol. 7, No. 01, Pages. C01100, 2012
- [112] RegisGuillaume20011, Conception de circuits analogiques-numérique pour le conditionnement de microcapteurs embarqués, *Université de Grenoble, Laboratoire SYMME*, 2011
- [113] Sergio Franco, Design with operational amplifiers and analog integrated circuits, 3d edition, *McGraw-Hill*
- [114] Adel Sedra and Kenneth C. Smith, Microelectronic circuits, 6th edition, *OXFORD University Press*
- [115] Lei Wang and Fukatsu, Y. and Watanabe, K., Characterization of current-mode CMOS R-2R ladder digital-to-analog converters, *IEEE Transactions on Instrumentation and Measurement*, Vol. 50, No. 6, Pages. 1781-1786, 2001
- [116] Introduction to the SPM, *Sensl*, October, 2011
- [117] Characteristics and use of SiAPD (Avalanche Photodiode), *Hamamatsu photonics*, 2004
- [118] G.A. Morton, H. M. Smith, R. Wasserman, Afterpulses in Photomultipliers, *IEEE Transactions on Nuclear Science*, Vol. 14, No. 1, Pages. 443-448, 1967
- [119] U. Akgun, A. S. Ayan, G. Aydin, F. Duru, J. Olson, and Y. Onel, Afterpulse timing and rate investigation of three different Hamamatsu Photomultiplier Tubes, *Journal of Instrumentation*, Vol. 3, No. 1, Pages. T01001, January 2008

- [120] P. Eckert, H.-C. Schultz-Coulon, W. Shen, R. Stamen, A. Tadday, Characterisation studies of silicon photomultipliers, *Nucl. Instrum. Meth. A620 (2010) 217-226*
- [121] M. Caccia and R. Santoro and G.A. Stanizzi, A simple and robust method to study after-pulses in Silicon Photomultipliers, *Journal of Instrumentation, vol. 9, No. 10, Pages T10004, 2014*

Abstract This thesis is the R&D on front-end electronics for a second generation camera based on the SiPM detectors for the Large Size Telescope (LST) of the CTA project. It is a part of the SiPM collaboration involving the LAPP, the University of Padua, the INFN and the MPI in Munich. The first part of the thesis is the characterization of an array of 16 SiPMs from Hamamatsu. The study proves the advantages of using such detectors in the LST. It defines the specifications of the readout electronics that are the aim of this work. Especially that it should ameliorate the gain dispersion of the 16 pixels that was found of about 10%. The second part is the design of the readout ASIC. The scheme tends to measure the SiPMs' signals with minimum disturbance of the detector. It integrates slow control facilities that adjust the detector's gain, minimize the dispersion in gain and provide the possibility of deleting noisy channels or even completely jumping over the control process. These facilities could perfectly get rid of the gain dispersion. Outputs of the 16 pixels will be summed on both high gain and low gain so that only two signals are delivered to the acquisition system that follows. A trigger function will also generate a trigger signal to the acquisition system. The choice was made to realize this ASIC according to the rules of the AMS $0.35\ \mu\text{m}$ BiCMOS technology. Simulation shows a linearly-covered dynamic range up to 2000 photoelectrons with good signal to noise ratio that allows the measurement of the single photoelectron. Laboratory tests confirm a great part of these results.

Key words LST, SiPM, characterization, preamplifier, dynamic range, linearity, response speed, gain control, ASIC design and test.

Résumé Cette thèse est la R&D de l'électronique de front-end destinée à la camera de deuxième génération du télescope de grande taille LST de projet CTA, étant basée sur les détecteurs de type SiPM. Cette étude rassemble des équipes du LAPP, de l'université de Padoue, de l'INFN et du MPI de Munich. La première partie de cette thèse porte sur les tests de caractérisations d'une matrice de 16 SiPMs fabriquée par Hamamatsu. Les résultats de ces tests ont souligné les avantages qui pourraient être apportés par l'utilisation de tels détecteurs. Un cahier des charges pour l'électronique a été défini à l'issue de ces tests. Notamment, une nécessité de corriger la dispersion en gain entre les 16 pixels qui a été trouvée d'environ 10%. La seconde partie est la conception d'un circuit intégré (ASIC) qui pourrait lire les signaux des pixels -SiPM avec la moindre perturbation possible de fonctionnement du détecteur. Cet ASIC inclut des fonctions de contrôle (slow control) qui permettent l'ajustement de gain des pixels, l'amélioration de l'uniformité de gain et la possibilité de supprimer les canaux bruyants ou encore même le contournement du processus de contrôle de gain. Ces fonctionnalités peuvent unifier le gain de 16 canaux. Les sorties des 16 canaux seront sommées pour en faire deux signaux seulement à la sortie de l'ASIC. Ces deux signaux, un sur le haut gain et l'autre sur le bas gain seront fournis au système d'acquisition qui suivra l'ASIC. Une fonction de déclenchement générera un signal de trigger qui sera ainsi transmis au système d'acquisition. Cet ASIC a été réalisée avec la technologie AMS $0.35\ \mu\text{m}$ BiCMOS. Les simulations ont montré une gamme dynamique linéairement couverte jusqu'à 2000 photoélectrons et la possibilité de mesurer le photoélectron unique grâce au bon rapport signal sur bruit électronique. Les tests au laboratoire confirment une grande partie de ces résultats.

Mots clés LST, SiPM, caractérisation, préamplificateur, gamme dynamique, linéarité, temps de montée, contrôl de gain, conception et test d'un ASIC.